Impurity scattering in a helical metal

Probing the electronic surface states of a topological insulator

Michael Bjerngaard

October 1, 2011

Contents

Acknowledgements

This thesis is submitted to the faculty of science as a part of the fulfillment to obtain a master's degree in Physics at the Nanoscience Center, The Niels Bohr Institute, University of Copenhagen. The work presented in this thesis, was conducted under supervision by Associate Professor Jens Paaske.

I would like to thank my supervisor Jens Paaske for introducing me to the exciting field of topological insulators. I would also like to thank Associate Professor Brian M. Andersen for several use full discussions, but Torsten Tranum Rømer and Rune S. Frederiksen for proofreading parts of this thesis.

Abstract

On a helical metal, where the electrons spin is locked to its momentum, quantities accessible to spin-(un)resolved STM measurements, such as the modifications of the local density of states (LDOS) are studied. The distinct influence of respectively a scalar potential, a classical magnetic and a quantum magnetic impurity on the LDOS is calculated. These are shown to give rise to distinguishable features in an LDOS measurement.

The induced modifications of the LDOS by the quantum magnetic impurity has similarities with both the scalar potential and the classical magnetic impurity. This is because the first non-vanishing irreducible self energy (i.e. order J^2 in the coupling) behaves as a *complex scalar potential*. Hence an helical electron upon scattering on a quantum magnetic impurity twice, has its overall backscattering suppressed despite an arbitrary intermediate scattering.

Further the quantum magnetic impurity induce the Kondo problem for any electron-hole asymmetry and enhance the LDOS response resonances amplitudes. However for electron-hole symmetry it vanish.

Motivation

Recently a new quantum phase have been discovered theoretically and experimentally verified. This so-called *topological phase*, inhere profound new fundamental physics. For instance, the magnetic monopole[34] may be induced by an electric charge near the surface of a topological insulator. These topological insulating materials may also host the anticipated Majorana fermion, which might pave the way for topological quantum computing and in general a technical revolution in spinotronics.

Consider the 1 dimensional edge of a 2 dimensional bulk topological insulator surface. An electron propagating on the edge, can either propagate forward or backward, when scattering off an impurity on the edge. If the impurity is a scalar, then the surface electron is enforced to keep propagating in the forward direction! But instead of an edge, consider a 2 dimensional surface of a 3 dimensional bulk topological insulator. It is not at all obvious, in which direction of the 2π scattering angles the scattered surface electron will propagate.

Exactly this notion will be adopted in this thesis. That requires a scrutiny of the metallic 2 dimensional surface, dubbed the helical metal, on such a 3 dimensional topological insulator. Not only the scalar potential mentioned above will be introduced to the surface, but also two magnetic ones. A classical magnetic and a quantum magnetic impurity. The latter is the one the focus is directed towards along the whole thesis. Several articles have already investigated the properties of the helical metal contaminated with a scalar and a classical magnetic impurity, but very few regarding the quantum magnetic one. It is interesting to investigate the consequences of a helical metal embedded with a quantum magnetic impurity, because the impurity is time-reversal invariant as the non-magnetic scalar. On the other hand, it is also a magnetic impurity as the classical magnetic impurity, but this conversely is a time-reversal breaking impurity. So one may already speculate, that some of the surface electronic properties induced by the quantum impurity may be similar to those induced by the time-reversal preserving scalar. Whereas others be similar to those induced by the classical magnetic impurity.

First a gentle introduction on the topological insulators will presented in section 1.1. Here no mathematical rigor will be used, but only experiments conducted so far, in order to illustrate this new topological quantum phase, will be discussed.

In order to understand the basic electronic properties of the helical metal in presence of the impurities, the helical metal without any impurities have to be introduced, so the exciting spin-texture can be used later. This will be the beginning of section 2, where after the focus will be directed towards the impurities, and especially the dynamical spin-flip behavior of the quantum magnetic impurity.

This behavior certainly have some influence of the modification of the electron states near the the quantum impurity, which will be the topic in section 5. These modification are accessible to the local STM probe, for which it will be derived, what to be measured in an STM experiment. These modifications basically just reflect the scattered surface electrons off the impurity, which again is

a consequence of the dynamical quantum impurity spin treated in section 2. This is supposed to be envisioned by the Fourier transform of the local density of states (FT-LDOS) which section 6 deals with. But in order to derive all this, the full surface electronic Green function is needed. Therefore the T-matrix is also needed, which will be derived in section 4.

To understand these induced surface properties on the helical metal, which indeed has a special Fermi surface, it is also necessary to compare the obtained results, to the analog ones obtained on metals we have a well know knowledge of. Therefore the conventional Rashba metal, conventional Dirac metal and the conventional metal will be introduced along the development, in the relevant contexts.

Chapter 1

Introduction - basic topological concepts

In the following chapter it will be explained with words, what distinguish a topological insulator from a trivial insulator. It will be supported by a review of experiments, that confirm such a topological insulator exist. Hereafter, in section 1.1, the origin of the topological insulator will be explained by phenomenological arguments of the formation of solids. This results in an effective Hamiltonian that the describes the low-energy physics of such a topological insulator.

In condensed matter physics[33, 23] electrons and atoms organize into states of matter such as crystalline solids, magnets, superconducting states and etc. All these can be described by a certain pattern of symmetry breaking. For example a solid breaks translation symmetry (even though the interaction between unit cells are translation invariant), a magnet breaks rotation symmetry (even though the interactions are isotropic) and the superconducting state breaks the gauge symmetry. This pattern of symmetry breaking leads to a unique 'order parameter', which can be used to formulate a 'Landau-Ginzberg' effective field theory determined by the quite general properties: dimension, symmetry and the order parameter itself. This scheme captured *all* states of condensed quantum matter until the discovery, in 1980, of the Quantum Hall effect which cannot be grasped in this way.

In order to comprehend it; consider all possible Block Hamiltonians of many-body systems, all with a finite energy gap separating the ground state from the exited states. One can 'smoothly' deform the Hamiltonians into each other without closing the gap, i.e. in math lingo one interpolate continuously between them. When doing so all conventional insulators are equivalent, and equivalent to the vacuum, which according to Diracs relativistic quantum mechanics has a energy gap (for pair production) that separates the conduction band (electrons) and valence band (positrons). These Hamiltonians now define a 'topological equivalence class' which constitutes all these insulating (topologically trivial) states. The question is now whether all electronic states with a energy gap are equivalent to this class?

The answer is no, because a 3 dimensional topological insulator is uniquely characterized by four $\mathbb{Z}_2$ topological invariants $(v_0; v_1, v_2, v_3)$. The value $v_0 = 0$ or $v_1 = 1$ identifies two distinct phases of quantum matter states called weak topological insulator phase and a strong topological insulator (STI) phase, respectively. The rest (v_1, v_2, v_3) can be interpreted as Miller indices, describing the orientation of the helical surface. The 3 dimensional topological insulator (TI) refer to the 3 spatial bulk dimensions, but the helical metal surface is 2 dimensional and labeled by the crystal momentum $\mathbf{k}$. The topological properties of the surface is uniquely determined by the $\mathbb{Z}_2$

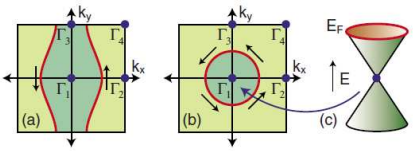

Figure 1.1: Schematic Fermi surface on the surface Brillouin zone. The simplest case is a weak topological insulator, where the Fermi surface enclose two TRIM. (b) a strong topological insulator (STI) where the Fermi surface enclose a single TRIM. (c) Illustrated the surface state of (b) which form a 2 dimensional Dirac cone in momentum space . From [23].

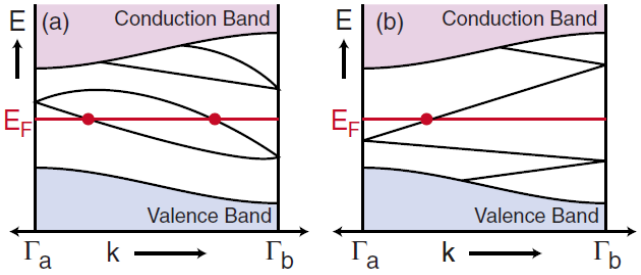

Figure 1.2: Electronic dispersion between two boundary TRIM degenerate points Γ_a and Γ_b projected into one dimension. (a) An even number of surface states crossing the Fermi level E_F are *not* topological protected. (b) An odd number of surface states crossing the Fermi level E_F are *topological protected*. From [23].

topological invariant v_0, that is solely determined by the bulk.
The surface Brillouin zone contain four time-reversal invariant momenta (TRIM) $\Gamma_1, \Gamma_2, \Gamma_3$ and Γ_4 as illustrated in figure 1.1(a) and (b), which each schematically illustrates a possible electronic configuration yet to be discussed. If surface states are present at the TRIM, then they are guaranteed to be 'Kramers' degenerate due to Kramers theorem. Away from these TRIM-points spin-orbit will lift the degeneracy, i.e. in between any two TRIM-points the surface states are non-degenerate, but at the TRIM-points they are double degenerate. Any two TRIM Γ_a and Γ_b, have to be connected by the energy dispersion curve, because they are points in the Brillouin zone. Now it is just a matter, whether the Fermi surface contour cross the Fermi level E_F an even or odd number times in between Γ_a and Γ_b. Between any two Γ_a and Γ_b, the energy dispersion of the surface state will locally look as figure 1.2(a) or (b). That is either an even number of crossings as in figure 1.2(a), or an odd number of crossings as occur in figure 1.2(b). In the case of an even number, the surface states can be eliminated by pushing them out of the gap, by some arbitrary perturbation of the system, and the surface states are thus *not* robust against perturbations. In the case of an odd number, the edge/surface states cannot be eliminated, and they are thus robust to perturbations of the system, i.e. the metallic boundary states are *topologically protected*.

The topological invariant v_0 determines whether an even ($v_0 = 0$) or odd ($v_0 = 1$) number of TRIM-points are enclosed by the Fermi surface contour. In the latter case the surface states are topologically protected, but in the former case the states are not. The 3 dimensional bulk TI determined to be $v_0 = 0$ is dubbed a 'weak topological insulator'. That which is a $v_0 = 1$ is dubbed a 'strong topological insulator' (STI), referring to the presence of robust surface states again perturbations.

The simplest possibility is a single Fermi surface enclosing the Γ-point as illustrated in figure 1.1(b) and (c), which at first hand seems to violate the *fermion doubling theorem* by Nielsen and Ninomiya. This theorem states, that for a time-reversal invariant system, the Dirac points must come in pairs. However this theorem is circumvented, since the partner Dirac point resides on

the *opposite* surface and the system is rendered a $v_0 = 1$ TI. The next simplest case is a Fermi surface enclosing two TRIM-points in the surface Brillouin zone as illustrated in figure 1.2(a). This electronic configuration can arise by stacking layers of the 2 dimensional quantum spin Hall insulator, which gives it a 3 dimensional bulk TI. However, the system is a weak topological insulator, $v_0 = 0$, and thus have no protected surface states. An already well known material for applications is graphene[20], which has four Dirac points as illustrated in figure 1.3(a). Hence it belong to the $v_0 = 0$ class.

Due to time-reversal symmetry $E^{\uparrow}(\mathbf{k}) = E^{\downarrow}(-\mathbf{k})$, i.e. except for the spin-degenerate mode at exactly $\mathbf{k} = 0$, the surface states at opposite momenta have opposite spin. This spin-momentum locked helical surface, makes the electron spin to rotate 2π, when encircling a single circular Fermi surface. This makes the electron wave function acquire a *non-trivial* π *geometric phase* called 'Berry's phase'. I.e. the $v_0 = 1$ supports a surface spin-polarized texture that underlies the π geometric phase. Conversely, the $v_0 = 0$ TI support an even multiply of π, which is a 0 or 2π electron wave function phase. The latter would be the case for a conventional spin-orbit material such as gold Au(111), where a free-electron like surface state is split into two parabolic spin-polarized sub-bands, that are shifted in $\mathbf{k}$-space relative to each other, see figure 1.3(c). This is caused by Rashba spin-orbit effect[8, 24], which creates two concentric spin-polarized Fermi surfaces. The one has opposite in-plane spin-rotation of that of the other, as in figure 1.3(b). Hence it is a $v_0 = 0$ TI. The former case is characterized by a unique π Berry phase, which has important consequences for the STI behavior in presence of magnetic field.

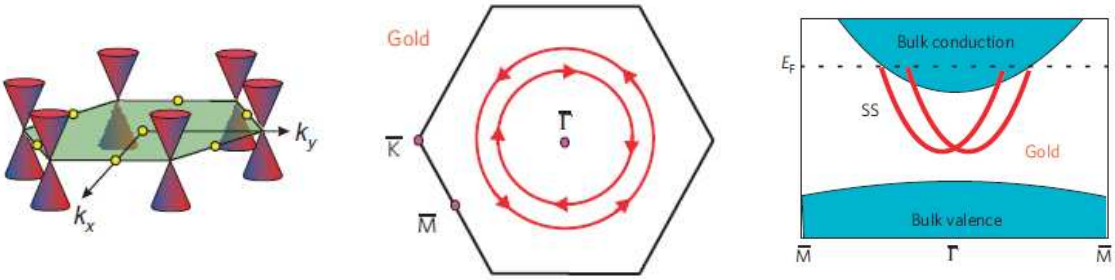

Figure 1.3: (a) Brillouin zone of graphene from ref[25], (b) Fermi surface of gold Au(111) from ref[44] and (c) surface band structure of gold Au(111) from ref[44].

A fundamental consequence of the topological classifications of gapped band structures, is the existence of gapless conducting surface states at interfaces where the topological invariant changes. I.e. at the interface between a STI ($v_0 = 1$) and the vacuum ($v_0 = 0$), topological protected gapless/massless relativistic Dirac fermions appear. For simplicity, only STI's with a single Dirac node such as the Bi_2Se_3-family[1] and its derivatives will be considered from now on. Further, only one Dirac-partner - i.e. only one surface of the 3 dimensional STI - will be investigated in the experiments to be mentioned.

Non-trivial $\mathbb{Z}_2$ topological surface states - what is called the *helical surface states* - has spin-momentum locking in a left and right helical fashion of the electron and hole states, respectively. It is this spin-momentum locking mechanism that underlies the non-trivial π phase. In this regard the spin non-degenerate helical metal posses[2] 1/2 degrees of freedom of that of a *conventional Dirac metal*. A conventional Dirac metal is in thesis defined as a 2 dimensional free-electron gas

[1] The 2nd generation of STI's referred to as the Bi_2Se_3-family consist of Sb_2Te_3, Bi_2Te_3 and Bi_2Se_3.

[2] Or phrased equivalently; the TI have 1 spin-degree of freedom on each surface - from the one Dirac partner on each surface - whereas the conventional Dirac metal has 2 degrees of freedom on each side.

with double spin-degeneracy at every state $\mathbf{k}$ and a linear Dirac dispersion[3]. Hence the Fermi surface illustrated in figure 2.4 is identical to the conventional metal (yet to be introduced), but not to that of the helical metal. Conversely the dispersion relation illustrated in figure 2.2, which is identical to the helical metal, but not to that of the conventional metal. Exactly[46, 19] these topological features: the number of Dirac nodes (i.e. the number of helical surface states) and the π Berry phase associated with these are completely fixed by the topology of the TI's bulk electronic structure which is uniquely determined by the $\mathbb{Z}_2$ invariant.

On the other hand the details of the surface band dispersion, the surface-and bulk Fermi level, the Dirac-point binding energy E_D and the helical surface spin-texture can vary significantly due to the influence on the bulk crystal symmetry and atomic potentials. These are therefore material dependent properties. Quite generally, the larger the bulk band gap is, the less pronounced warping effects it has. For example the 'small-gap' STI Bi_2Te_3 has bulk band gap ~ 0.18 eV, whereas the 'large-gap' STI Bi_2Se_3 has bulk band gap ~ 0.35 eV. The former is very warped but the latter less.

Angle resolved photoemission spectroscopy (ARPES) is an ideal tool for probing[12, 44, 27, 26, 47] the topological signatures of the non-trivial $\mathbb{Z}_2$ invariant $v_0 = 1$, which are an odd number of Dirac nodes, a spin-momentum locked Fermi surface and the π Berry phase associated with it. High-resolution ARPES performed with modulated photon energy allows for a clear isolation of the surface states from that of the bulk conductance (BCB) and valence band (BVB) states. This is so because the the former do not disperse along a direction perpendicular to the surface, whereas the latter do. ARPES cannot detect states of higher energy than the Fermi energy E_F, since the technique use a photon to kick out a occupied electron[4]. First a scan of the undoped Bi_2Te_3 over the surface Brillouin zone measures the number of Dirac nodes. As illustrated in figure 1.4(b) only a single Dirac node is present in the surface Brillouin zone, which indicates it to be a strong topological insulator (STI). In the vicinity of the node, the bulk and surface dispersion along the symmetry directions $\mathrm{K}-\Gamma-\mathrm{K}$ and $\mathrm{M}-\Gamma-\mathrm{M}$ are measured in figure 1.4(a). Clearly the bulk conductance band (BCB) dispersion is seen to have a V-shape, the bulk valence band (BVB) to be M-shaped and the surface state band (SSB) to be V-shaped with apex at the Dirac point of binding energy E_0. This indicates a linear massless Dirac fermion state with velocity of 4.05×10^5 m/s (2.67 eV·AA) and 3.87×10^5 m/s (2.55 eV·AA) along the $\Gamma-\mathrm{K}$ and $\Gamma-\mathrm{M}$ respectively. A cut of the Fermi surface illustrated in figure 1.4(c) for different photon-energies incident on the sample along k_z, shows the inner Fermi surface changing shape from being a left-pointing triangle to a snowflake like to a right-pointing triangle. This reveals that this pocket disperse with k_z (perpendicular direction to surface) and hence this is the bulk conductance band (BCB). Likewise the outer warped Fermi surface does not change and hence it belongs to the surface band.

ARPES in spin-resolution mode measures the distribution of spin-polarization on the Fermi surface, and hence enable an estimate of the geometric phase from the observed surface spin-momentum locking. The spin texture of two different Fermi surface maps - the one above the 'Dirac' Γ-point is illustrated in figure 1.7(a), and the other below as in figure 1.7(b). These show the spin momentum-locking profile. In figure 1.7(c) the evolution of the spin-texture phase is illustrated as a function of energy (left axis) away from the Dirac node and the corresponding measure of the warping factor (right axis) where $\omega = 0$, $\omega = 1$ and $\omega > 1$ imply circular, hexagonal and snowflake-shaped Fermi surface respectively. The sign $+$ and $-$ of ω indicates the spin-texture helicity for left-handed helicity (LHC) and right-handed helicity (RHC), respectively. At the zero energy and spin-degenerate Γ-point, the spin-texture inversion takes place, i.e. the Fermi surface

[3] Now three different 2 dimensional metals are introduced. The 'conventional spin-orbit metal', 'conventional Dirac metal' and the unconventional 'helical metal'. Later also a 'conventional metal' will be introduced

[4] As will be discussed later STM(S) is able to detect hole states.

turns from a + to − helicity. Far away from the Dirac node the spin-texture is highly warped. This arise from nonlinear spin-orbit terms of both the Rashba and Dresselhaus type due to the crystal symmetry and potential. Without these effects, i.e. in the low energy range near the Dirac point, the surface states form a cone that is isotropic in momentum space (k_x, k_y), and hence generates a circular Fermi contour. Spins tangentially on such a circular Fermi surface lead to a non-trivial π geometric phase and hence one can measure the topological invariant to be $v_0 = 1$.

In a trivial $v_0 = 0$ TI the surface states will be gapped away by random disorder perturbations. Hence one should not see any surface states in such a trivial TI. But if one gradually transform a trivial TI into a non-trivial $v_0 = 1$ STI, then spin non-degenerate surface states should apear together with a bulk band gap. Such a topological phase transition is actually what ref [47] show to take place at doping $\delta \sim 0.6$ for the material[5] $BiTI(S_{1-\delta}Se_\delta)_2$ as δ varies from 0.0 to 1.0. As seen in figure 1.8 for $\delta = 0.0$ the $BiTI(S_{1-\delta}Se_\delta)_2$ is a trivial $v_0 = 0$ spin-orbit band insulator with double spin degenerate bulk states and no surface states. But it changes into a non-trivial $v_0 = 1$ STI with non-gapped metallic spin non-degenerate surface states and a fully insulating bulk states at composition $\delta = 1.0$.

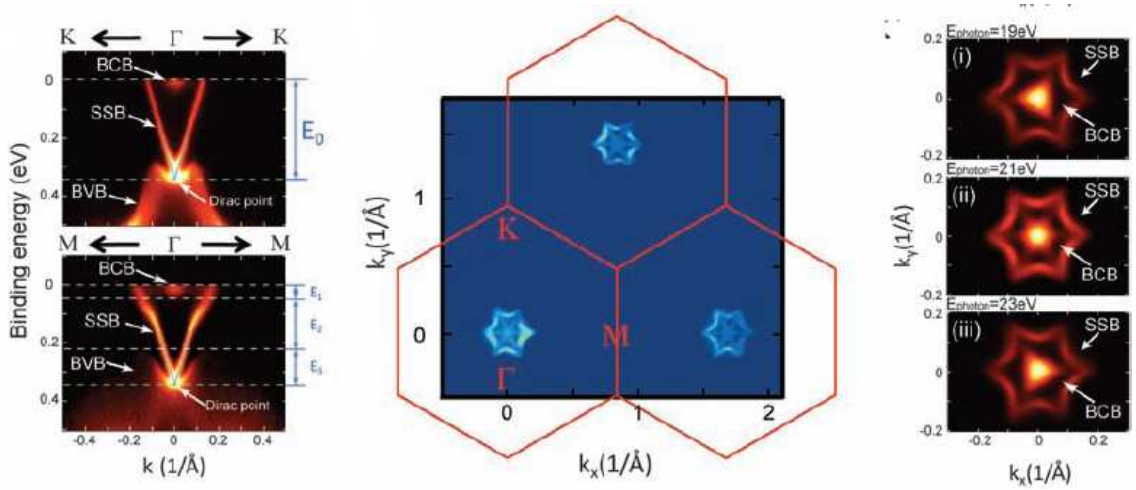

Figure 1.4: (a) Band dispersion along $K - \Gamma - K$ and $M - \Gamma - M$ directions. The energy scales are labeled: Dirac point binding energy $E_0 = 0.34$ eV, BCB bottom binding energy $E_1 = 0.045$ eV, bulk energy gap $E_2 = 0.165$ eV and energy separation between BVB top and Dirac point $E_3 = 0.13$ eV. (b) Wide-range Fermi surface maps covering three Brillouin zones, where the red hexagon represent the surface Brillouin zone. (c) Photon energy dependent Fermi surface maps. All from ref [12]

Many of the proposed exotic topological effects such as exiton condensation & charge fractionalization[36] require the system to be in the 'topological transport regime / charge neutral regime'[25, 46, 7, 45], which occur when the Fermi surface E_F lies in between the bulk conduction band minimum (BCM) and bulk valence band maximum (BVM), while exactly at or near the Dirac point which is guaranteed to be right at the Γ-point for any time-reversal-preserving perturbation. In other words, the bulk to surface carrier density has to be minimized. In a conventional quantum Hall system, the density of states at the Fermi level can be turned by a magnetic field. But this cannot be done for a STI, since it would break time-reversal symmetry, which is required in order to be a STI. So a method that respects time-reversal symmetry is needed. It is well know that

[5] $BiTI(S_{1-\delta}Se_\delta)_2$ is a fully turnable topological insulator analog of Bi_2Se_3.

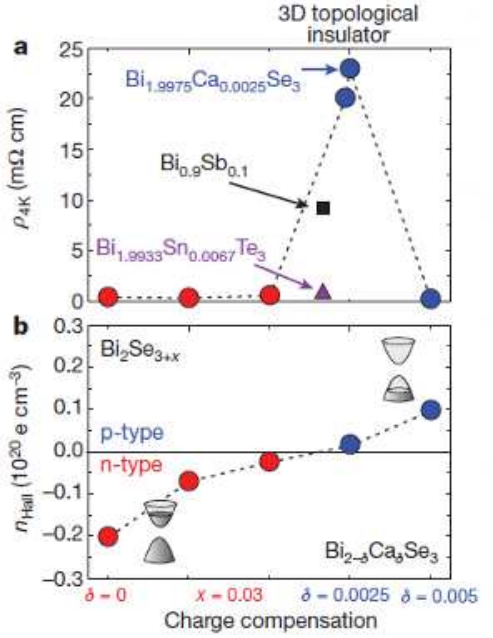

Figure 1.5: Turning of the bulk Fermi level. (a) Resistivity at temperature $T = 4$ K measured for samples of Bi_2Se_3 (filled circles, no arrow labels) that are bulk electron doped due to varying concentrations of Se vacancies (x) or bulk hole doped though Ca/Bi substitution (δ). These are compared to the bulk insulating state of $Bi_{0.9}Sb_{0.1}$ (black square), which is intrinsic and hence not due to disorder (b) Hall carrier density of the samples in (a). From ref [25]

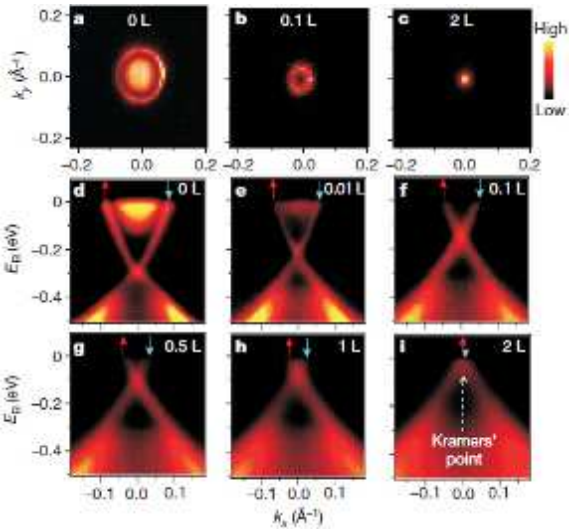

Figure 1.6: Turning the density of electrons to the spin-degenerate point. (a), (b) and (c) ARPES measurements of the Fermi surface of $Bi_{2-\delta}Ca_\delta Se_3$ (111) after doses of NO_2 from 0 L to 2 L. (d)-(i) show the band dispersion after doses. From ref [25]

undoped Bi_2Se_3 and Bi_2Te_3 are n and p-type semiconductors owning to excess of Se and Te site defects, respectively. Therefore trace amounts of carriers of opposite sign, i.e. hole and electron carries respectively, need to be introduced to compensate the carrier excess. They also need to be non-magnetic in order to respect time-reversal symmetry. By doping the Bi_2Se_3 by substitution of Ca for Bi, the bulk Fermi level can be changed, and the system undergoes a metal-insulator-metal transition as seen by monitoring the low temperature resistivity in figure 1.5(a). The resistivity peak occur for a concentration of Ca = 0.25%, and above or below the electrical conduction is supported by hole and electron carries respectively. This can be understood by the sign of the Hall carrier density measured simultaneously in figure 1.5(b). The bulk Ca doping succeeds[6] in pushing the Fermi level into the bulk band gap, so the bulk is fully insulating. But the relative position of E_F to the surface Dirac point in the ground state is about 0.35 eV and 0.18 eV for Bi_2Se_3 and Bi_2Te_3 respectively. Therefore $Bi_{1.9975}Ca_{0.0025}Se_3$ is not yet in the desired topological transport regime. Dosing NO_2 molecules on the surface does not affect the carrier density in the bulk, hence the bulk remains insulating and the binding energy of the Dirac point level is shifted towards the surface Fermi level E_F. This brings the system in the desired region as in figure 1.6. The former

[6] Actually the E_F will raise back to the $\delta = 0$ level after approximately 18 hours due to band bending effects[25, 26, 12, 46, 7] and cause problems for applications of TI's. This effect is almost non-existent in graphene for which various applications already exist[20].

method was for the large-gab STI Bi_2Se_3, and to be honest, this is actually not possible in pure Bi_2Te_3. Here an isolated Dirac node is not accessible, when tuning the chemical potential near it, since multiple bulk bands co-exist near the node. However, by intercalating some additional layers of Ge-Te into the material, then obtaining $Bi_2Te_3 \cdot (GeTe)_{0.5}$ restore an nearly ideal isolated Dirac cone and the just mentioned method is applicable.

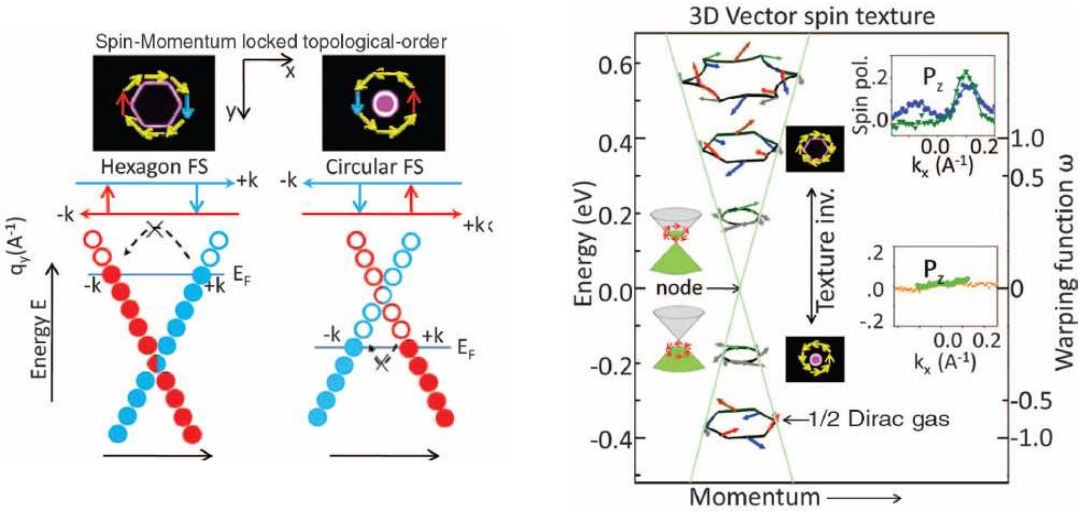

Figure 1.7: The spin-texture phase diagram (a) and (b). The spin inversion happens when the chemical potential cross the Dirac point at $\mathbf{k} = 0$. (c) The in-plane and out-of-plane (insets) spin evolution of the helical surface states. From ref [47]

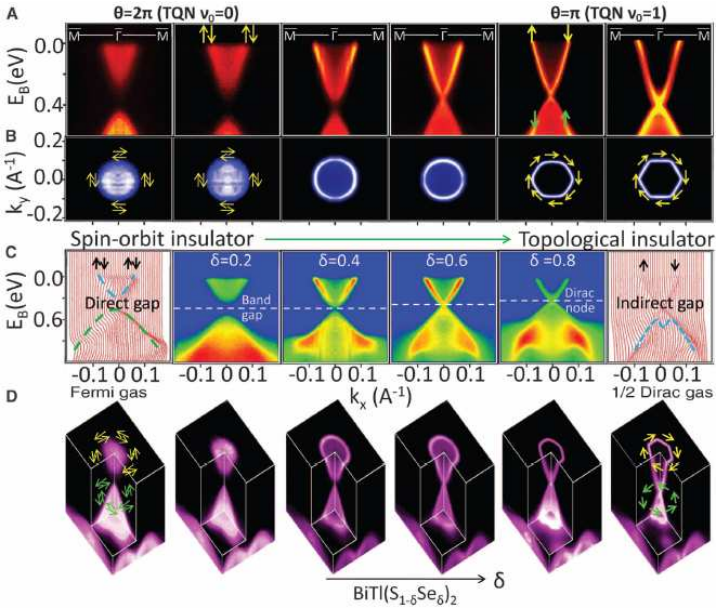

Figure 1.8: Topological phase transition. (a) ARPES dispersion maps from a spin-orbit band insulator ($v_0 = 0$) to a topological insulator ($v_0 = 1$) and (b) the corresponding Fermi surface and (c) energy dispersion curves for compositions from $\delta = 0$ to $\delta = 1$. (d) The 3 dimensional evolution of the energy groundstate with imposed spin-texture indicated by the arrows. Each arrow represent a net polarization on a $\mathbf{k}$ space point on the corresponding Fermi surface and the color yellow/ green is for a Fermi surface above/ below the Dirac node. From ref [47]

1.1 Effective model of a 3 dimensional Topological Insulator

The effective model of the 3 dimensional topological insulators presented in this section follow ref [30, 33, 48, 44] to a very large extend with the needed supplements for a novice in band theory.

By applying a simple algorithm invented in ref [19] the alloy Bi_xSb_{1-x} was the first 3 dimensional material predicted to be a STI. The algorithm is in essence able to determine the topological invariant $\mathbb{Z}_2$, that determine whether a material with an arbitrary complex electronic structure is a trivial insulator or a non-trivial insulator. However the alloy Bi_xSb_{1-x} contain random disorder, has a complex electronic structure and contain five or more dispersion branches that makes it uneasy to capture in a simple qualitative model and understand the underlying physics. Further it has a rather small bulk band gap, that makes it difficult to handle experimentally in order to reach the desired topological phase/transport regime. Hence this 1^{st} generation material is not the standard reference, but instead the 2^{nd} generation considered below due to their simplicity.

The search for a simple TI in which one is able to understand the basic physics and capture qualitatively the salient low-energy features in a effective model; one has to look for stoichiometric crystals with well-defined electronic structure, where the conduction and valence bands have opposite parity, that can be inverted by a large spin-obit coupling (SOC). The algorithm ref [19] applies *only* for such band inversion-symmetric materials and therefore theoretical and experimental focus was directed towards the Sb_2Te_3, Sb_2Se_3, Bi_2Te_3 and Bi_2Se_3 crystals. It turn out in ref [48, 44] that the spin-orbit coupling in Sb_2Se_3 is not strong enough to induce such a required band inversion, and hence it is just a trivial insulator. But the rest class Sb_2Te_3, Bi_2Te_3 and Bi_2Se_3 turn out all to be non-trivial strong topological insulators. This class is the second generation of strong topological insulators and are all very similar and therefore dubbed the Bi_2Se_3 family.

The effective model for the Bi_2Se_3 family is the same for *all*, and they will only be distincted by some parameters that enter the Hamiltonian. In what follows the reference crystal is Bi_2Se_3.

The derivation first presented in ref [48, 44] apply the algorithm in ref [19] to the electronic orbitals together with $\mathbf{k}\cdot\mathbf{p}$ theory and *ab initio* calculations to fit the parameters. The arguments presented here follow ref [30] in a phenomenological model of the electronic orbitals, but leave out the details of $\mathbf{k}\cdot\mathbf{p}$ theory and *ab initio* calculations presented in ref [30, 48, 44]. The method of ref[30] automatically incorporate the cubic k^3-order correction, that was ignored in ref [48] but derived in ref [18] first. These phenomenological arguments of the band inversion driven by spin-orbit coupling, will provide the understanding of the origin topological insulators.

The crystal structure of the Bi_2Se_3 family is rhombohedral with space group $D^2_{3d}(R\bar{3}m)$. In figure 1.9(a) is visualized the 3 dimensional bulk crystal atomic structure. Its layered structure is stacked along the z-axis in figure 1.9(c), and the x,y-plane view on a single layer is illustrated in figure 1.9(b) within which the lattice forms triangles. The three primitive lattice vectors t_1, t_2 and t_3 delimits the unit cell that contain 5 atoms; two equivalent Bi atoms (Bi1 and Bi1$'$), two equivalent Se atoms (Se1 and Se1$'$) and one inequivalent (to the other Se atoms in regard to crystal symmetry) Se atom Se2 which together form the unit cell that can be represented as a quintuple layer marked as the red box. The crystal structure is such, that the coordinate system is placed with origo Γ as inversion center. The z-axis is defined to be the trigonal axis (threefold rotation R_3 symmetry), x-axis the binary axis (twofold rotation R_2) and the y-axis as the bisectrix axis (in the reflection plane). The bulk Brillouin zone is determined by the crystal symmetries which are the following just mentioned and the bulk Brillouin zone of this lattice is shown in figure 1.9 with the four time-reversal invariant momenta (TRIM) $\Gamma(0,0,0)$, $L(\pi,0,0)$, $F(\pi,\pi,0)$ and $Z(\pi,\pi,\pi)$. The projection of these on the bulk surface fixes a hexagonal surface Brillouin zone of the (111)-surface on which the $\bar{\mathrm{M}}, \bar{\mathrm{K}}$ and $\bar{\Gamma}$ are the high-symmetry points.

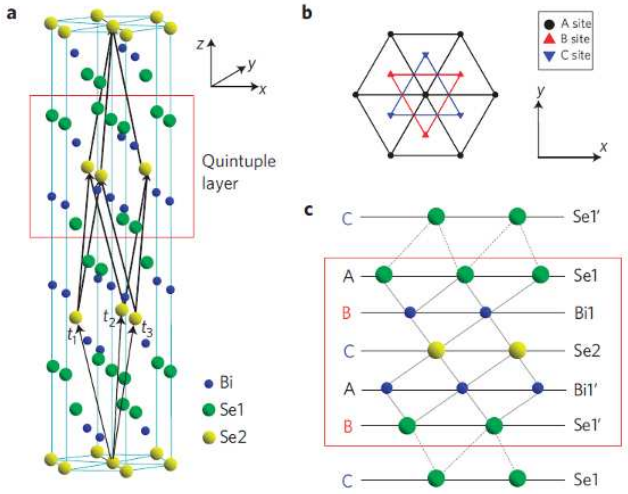

Figure 1.9: Crystal structure from ref [48]. (a) Crystal structure of Bi_2Se_3 with primitive lattice vectors t_1, t_2 and t_3 and the quintuple layer marked by a red box. (b) Top view along the z axis of the quintuple layer and (c) side view of the quintuple layer.

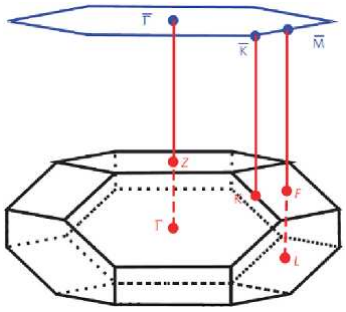

Figure 1.10: Bulk Brillouin zone of Bi_2Se_3 with four inequivalent TRIM points Γ, L, F and Z. The blue hexagon illustrate the 2 dimensional Brillouin zone of the projected $(1,1,1)$ surface in which the high-symmetry points $\bar{\Gamma}, \bar{K}$ and $\bar{M}$ are labled. From ref [48]

The bulk topology is nessecary to understand, because it is solely that, which is responsible for *all* the topological properties of the TI. The bulk topology is specified by four topological

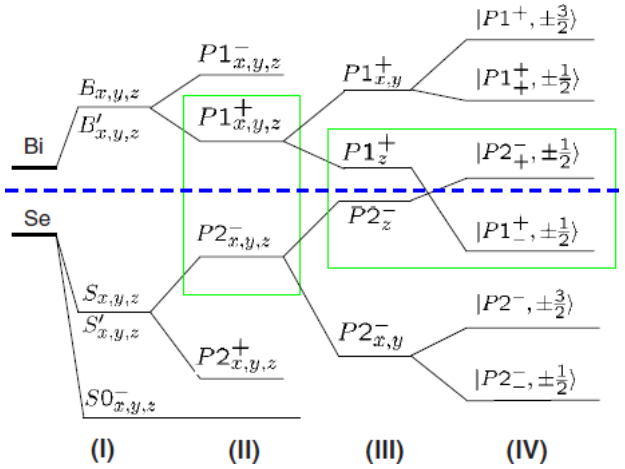

Figure 1.11: The evolution[30] of Bi_2Se_3 electronic orbitals from non-interacting Bi and Se p-orbitals to include (I) the hybridization of Bi orbitals with Se orbitals, (II) the formation of 'chemical' bonding and anti-bonding states due to inversion symmetry, (III) crystal field splitting and lastly the influence of (IV) SOC.

invariants $(v_0; v_1v_2v_3)$. The physical origin to the non-trivial $v_0 = 1$ topological nature is very nicely understood by looking at the evolution of the band structure exactly at the Γ-point. Imagine the non-interacting atoms, see figure 1.11(I) from the atomic p-orbitals of Bi and Se atoms, and subsequently adding chemical bonding, see figure 1.11(II), crystal field, see figure 1.11(III), and at last spin-orbit coupling (SOC) in figure 1.11(IV) which ends with the final configuration of conduction and valence bands. The subtle point is that, it is the states right at the Γ-point and none of the other TRIM.

As told above the electronic structure of the non-interacting atoms are p-orbitals. This is so because the electronic configuration of Bi is $6s^2p^3$ and that of Se is $4s^24p^4$, hence the outermost shells are p-orbitals and only those are taking into account. That these are the only relevant ones, is evident by acknowledge the bonding between two neighbor quintuple layers are rather weak and probably of the van der Waals type. Therefore the surface of a Bi_2Se_3 family will have such a layer as the outermost one after cleavage. On the other hand, the largest energy scale of the problem is that of strong chemical bonding within one quintuple layer, and hence the analysis simplifies to this unit cell. This contains 5 atoms each with p_x, p_y and p_z orbitals which makes 15 orbitals as long as spin is ignored. Denote the orbitals by $|\Lambda, \alpha\rangle$ with $\Lambda = \text{Bi1}, \text{Bi1}', \text{Se1}, \text{Se1}'$ and Se2 and $\alpha = p_x, p_y$ and p_z. Within the unit cell the repeated layers of Bi and Se have a large coupling in between, which results in the Bi-orbitals being pushed up in energy to form hybridized states $|B_\alpha\rangle$ and $|B'_\alpha\rangle$, but the Se-orbitals are pushed down in energy and yield three states $|S_\alpha\rangle$,$|S'_\alpha\rangle$ and $|S0_\alpha\rangle$ as illustrated in figure 1.11(I).

The existence of the inversion symmetry, makes it possible to recombine the orbitals of the unit cell according bonding and anti-bonding states of definite parity given by

$$|P1^\pm_\alpha\rangle = \frac{1}{\sqrt{2}}(|B_\alpha\rangle \mp |B'_\alpha\rangle) \quad , \quad |P2^\pm_\alpha\rangle = \frac{1}{\sqrt{2}}(|S_\alpha\rangle \mp |S'_\alpha\rangle)$$

In a real crystal there is chemical bonding between the bonding and anti-bonding states, which here is formed by a coupling between $|B_\alpha(S_\alpha)\rangle$ and $|B'_\alpha(S'_\alpha)\rangle$. When this is taking into account, the anti-bonding state is found to have higher energy than the bonding state. This is showed in figure 1.11(II), where the $|P1^+_\alpha\rangle$ and $|P2^-_\alpha\rangle$ are found to be closest to the Fermi surface and hence it is only on them the analysis focus on henceforth.

The point-group symmetry of the atomic plane, makes the z-direction different from the x,y-plane, which cause a crystal field split between p_z and $p_{x,y}$ orbitals. The end result is that $|P1^+_z\rangle$

is the lowest lying conduction state and $|P1_z^-\rangle$ the highest valence state as illustrated in figure 1.11(III). This is the atomic 'stage' before SOC is considered.

When turning on spin-orbit coupling (SOC), it becomes necessary to consider spin $\sigma = (\uparrow, \downarrow)$. Before the onset of SOC the orbitals $|P1_\alpha^+, \sigma\rangle$ and $|P2_\alpha^-, \sigma\rangle$ are all double spin-degenerate. But turning on the SOC, H_{SOC}, spin and orbital angular momentum will be coupled, since the SOC Hamiltonian $H_{SOC} = \lambda \bar{s} \cdot \bar{L}$ connects spin and ang. momentum by the coupling parameter $\lambda = \frac{1}{2m_0^2c^2}\frac{1}{r}\frac{\partial U}{\partial r}$ with U being the potential of the atoms. Therefore it is convenient to transform the p_x and p_y into orbitals with definite orbital angular momentum as

$$|\Lambda, p_+, \sigma\rangle = \frac{1}{\sqrt{2}}(|\Lambda, p_x, \sigma\rangle + i|\Lambda, p_y, \sigma\rangle) \quad , \quad |\Lambda, p_-, \sigma\rangle = \frac{1}{\sqrt{2}}(|\Lambda, p_x, \sigma\rangle - i|\Lambda, p_y, \sigma\rangle)$$

with $\Lambda = P1^+$ or $P2^-$. The basis now consists of $\{|\Lambda, p_+, \sigma\rangle, |\Lambda, p_-, \sigma\rangle, |\Lambda, p_z, \sigma\rangle\}$ out of which one can construct eigenstates by making linear combinations of these (total angular momentum along z shall be conserved) with the linear coefficients containing all the information about the SOC.

The SOC couples $|\Lambda, p_z, \uparrow\rangle(|\Lambda, p_z, \downarrow\rangle)$ to $|\Lambda, p_+, \downarrow\rangle(|\Lambda, p_-, \uparrow\rangle)$ which cause a level repulsion between these states and makes $|P2_+^-, \pm\frac{1}{2}\rangle$ go up and $|P1_-^+, \pm\frac{1}{2}\rangle$ go down in energy for the strength λ above some critical value λ_c i.e. $\lambda > \lambda_c$. Hence the state $|P1_-^+, \pm\frac{1}{2}\rangle$ is the highest valence state and $|P2_+^-, \pm\frac{1}{2}\rangle$ is the lowest conduction state, see figure 1.11(IV). Since these have opposite parity and went from being the lowest conduction state and highest valence state respectively, their bands crossed due to the strong SOC and hence a *band inversion* has occurred for $\lambda > \lambda_c$. This band inversion is the very reason why the Bi_2Se_3 family members are topological insulators! The order is reversed for $\lambda < \lambda_c$ so that $|P2_+^-, \pm\frac{1}{2}\rangle$ stay the highest valence state and $|P1_-^+, \pm\frac{1}{2}\rangle$ the lowest conduction state, and hence *no* band inversion occurs. In this case the algorithm ref [19] declare that the material in question will *not* be a TI - it is so to speak a *trivial insulator*. This is exactly the reason why Sb_2Se_3 is a trivial insulator.

By applying the symmetry operations available for this crystal, one can derive the most general bulk Hamiltonian possible. By projecting this bulk Hamiltonian into the basis consisting of $|P1_-^+, \pm\frac{1}{2}\rangle$ and $|P2_+^-, \pm\frac{1}{2}\rangle$ one can derive a effective surface Hamiltonian for the slab[7] $z > 0$. The effective Hamilton for the surface states Ψ is given by

$$H_{sur}(\mathbf{k}) = E_0(k) + v_k(\tau_x k_y - \tau_y k_x) + \frac{\lambda}{2}(k_+^3 + k_-^3)\tau_z \tag{1.1}$$

where the Pauli matrix $\bar{\tau}$ is proportional to the real spin of the surface electrons and the first term $E_0(k) = \frac{k_{||}^2}{2\,m*}$ only cause a constant shift in energy and hence generates particle-hole asymmetry. If it is set zero, $E_0(k) = 0$, then H_{sur} is particle-hole symmetric and thus zero-energy states is supposed to exist. The linear 'Rashba' term $H_0 = v_k(\tau_x k_y - \tau_y k_x)$ respects $U(1)$ rotational symmetry and hence cause isotropic 2 dimensional fermions on the surface. Due to the isotropy the Fermi surface at any energy is a circle and the Fermi velocity $v_k = v_F(1 + \alpha k^2)$ contain a square momentum dependence, but due to the C_3 symmetry it is identical in the $\Gamma - K$ and $\Gamma - M$ directions.
The warping term $H_w = \frac{\lambda}{2}(k_+^3 + k_-^3)\tau_z$ contain a $O(k^3)$ correction. This is only invariant under threefold rotation and hence it is the only term responsible for the hexagonal warping of the otherwise circular Fermi surface caused by H_0. Since τ_z is odd under mirror-operation the warping vanish along the $\Gamma - M$ but is maximum along the $\Gamma - K$.
In the limit $k \to 0$ the linear Rashba term dominates and the surface states show linear dispersion with helical spin-texture which has opposite helicity on each side of the node.

[7] Likewise for the partner Dirac node on the opposite surface

Chapter 2

Model of the homogeneous helical metal

The higher-momentum regions with the complex warped Dirac cone has very interesting physical consequences, but this also makes numerical simulations necessary. Hence the consequences due to the new energy dispersion and spin-momentum locking mechanism is easily blurred. This thesis adopts another stance towards the understanding of the consequences due to these new surface features, namely that everything is to be kept simple enough to see the new underlying mechanisms in full glory. In adopting this stance the 'warping model' will briefly be introduced and then the simpler 'Dirac model' will be invoked and used moreover. The understanding of the helical metal can be deepened further, by comparing the results on the helical metal with the analogous ones on a metal that is familiar to us. Therefore the conventional spin-orbit metal and conventional Dirac metal were considered before, when the new topological concepts were introduced. Another metal, actually the most simple and familiar one, the *conventional metal* will be introduced next and when necessary considered analog to the helical metal.

Now the simplest possible toy model of a strong topological insulator will be introduced. Consider the simplest $\mathbb{Z}_2$ STI, i.e. having the topological invariant $v_0 = 1$. It consist of a *single surface Dirac node* at the 'Kramer/Dirac' Γ-point guaranteed (by the $\mathbb{Z}_2$ inv.) to be at $\mathbf{k} = 0$ in presence of time-reversal preserving perturbations. The 2 dimensional helical metallic surface state band (SSB) form a *ideal Dirac-cone* energy dispersion centered in the Γ-point, and with symmetric momentum cut-off. Hence the surface band dispersion has a X-shaped form. Further, the surface band is filled up to the Fermi energy μ which can attain any value within the band, so the surface band may be particle-hole symmetric when $\mu = 0$ or asymmetric when $\mu \neq 0$, and hence the system can enter the topological transport regime by setting $|\mu| \approx 0$.

As explained in the introduction section 1 in figure 1.4(a), undoped Bi_2Se_3 family materials do not have a symmetric $BCB - E_D$ and $E_D - BVB$ energy distances. However, the doped onces may achieve it, if the Fermi level is placed[1] exactly mid the bulk gap and subsequently NO_2 dosing[2] drives the E_D to the vicinity of the Fermi level. Hence to achieve the X-shaped surface band for the undoped materials, the system is required to be driven into the topological transport regime. If one doesn't want this to be the experimental system; i.e. one doesn't want the Fermi level together

[1] the carrier doped, Ca and Sn substituted Bi atoms, materials only shift its Fermi level into the bulk and hence the band cut-off at the bulk valence maximum (BVM) and bulk conduction band minimum (BCM) will still not be symmetric around Γ.

[2] the NO_2 dosing cause the Dirac point to raise towards the Fermi level

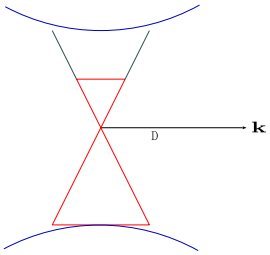

Figure 2.1: Illustration of the $\bigcap$-shaped bulk valence band and the X-shaped surface band.

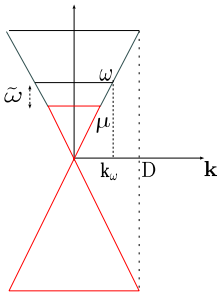

Figure 2.2: Dispersion relation of the Dirac model and the conv. Dirac metal.

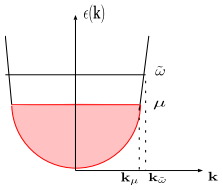

Figure 2.3: Quadratic dispersion relation of the conventional metal.

with the Dirac node to lie exactly at the gap center, or if one wants the Fermi level not to lie exactly at the Dirac node (which would have to lie exactly at the gap center), then the carrier doped and NO_2 dosed material cannot achieve the X-shaped Dirac dispersion with symmetric cut-off.
Is the chosed model of the X-shaped surface band, illustrated in figure 2.1, then experimentally unrealistic? No, a recent new compound[3] $(Sb_xBi_{1-x})Te_3$ has the X-shaped surface band as desired. Since[4] it is a desident of the mother compound Bi_2Te_3, they have the same crystal symmetries and thus the same effective model Eqn. (1.1). But the atomic potentials (the addition of Sb for Bi atoms) change the M-shaped bulk valence band (BVB) and the V-shaped surface band, into a $\bigcap$-shaped bulk valence band and a X-shaped surface band as desired. This means that even though the 2^{nd} generation Bi_2Te_3 family materials cannot provide a symmetric band cut-off, then this is realizable in the upcoming generation of materials.

The chosen model impose some constraints on the effective Hamiltonian Eqn. (1.1). These are a constant Fermi velocity $v_k \to v_F$ and $E_0(k) \to 0$, i.e. the Dirac node is defined to be the energy reference $E_D = 0$, with a negative and positive energy Dirac cone extending from this origo and a arbitrary Fermi level μ.
The symmetric cut-off mentioned above is chosen $k_x \in [-D_{SSB}/v_F, D_{SSB}/v_F]$ and $k_y \in [-D_{SSB}/v_F, D_{SSB}/v_F]$ exactly such, to include *only* momentum contributions from the surface band and no higher momenta where the surface band hybridize with the bulk valence and conduction band. Hence this model includes the warping effect and is here called the 'warping model'. However, most of the thesis further delimits the momentum range by a cut-off $k_x \in [-D/v_F, D/v_F]$ and $k_y \in [-D/v_F, D/v_F]$ to be the low-energy/long-wavelength range of the effective model, i.e. the region in momentum space (k_x, k_y) where the surface states form a cone that is isotropic, and hence generates a circular Fermi contour. In the 'Dirac model' the helical metal has only in-plane spin-momentum locking with the spins tangentially on the Fermi surface[5]. I.e. the effective Hamiltonian Eqn. (1.1) will be reduced further to the low-energy limit ($\lambda \to 0$) where only the linear 'Rashba' term H_0 governs the Hamiltonian.

[3] Presented at a talk given by Qikun Xue at the *Workshop and school on topological aspects of condensed matter physics* undertaken July 2011 in Trieste, Italy

[4] This argument was presented by Liang Fu to my question exactly on whether the effective model Hamiltonian would be the same as for the Bi_2Te_3 family materials.

[5] Such a spin-momentum lock leads to a non-trivial π geometric phase and the model of the surface band thus inhere a perfect topological invariant $v_0 = 1$

The bare Hamilton

$$\mathcal{H} = \sum_{\mathbf{k}} \sum_{\sigma,\sigma'} c^{\dagger}_{\mathbf{k},\sigma} [H(\mathbf{k})_{\sigma\sigma'} - \mu] c_{\mathbf{k},\sigma'} \tag{2.1}$$

written in the 'spin' σ-basis $\sigma = \{\uparrow, \downarrow\}$. The operator $c^{\dagger}_{\mathbf{k}\sigma}/c_{\mathbf{k}\sigma}$ creates/destroys a massless fermion on the 2 dimensional helical surface with momentum $\mathbf{k}$, which has azimuthal angle $\phi_{\mathbf{k}} = \tan^{-1}(k_y/k_x)$ and the $\mathbf{k}$ sum runs over states in the surface Brillouin zone.

2.1 The warping model

In the 'warping model' the bare Hamiltonian includes a linear 'Rashba' term H_0 and a cubic 'warping' term H_w

$$H(\mathbf{k}) = H_0(\mathbf{k}) + H_w(\mathbf{k}) = v_F(\mathbf{k} \times \bar{\tau}) \cdot \hat{z} + \lambda k^3 \cos(3\phi_{\mathbf{k}})\tau^z = \begin{pmatrix} \lambda k^3 \cos(3\phi_{\mathbf{k}}) & v_F(-ik_x - k_y) \\ v_F(ik_x - k_y) & -\lambda k^3 \cos(3\phi_{\mathbf{k}}) \end{pmatrix} \tag{2.2}$$

where $\bar{\tau}$ denotes spin Pauli-matrix vector and v_F denotes the Fermi velocity. Introducing the transformation matrix[29]

$$U(\mathbf{k}) = \begin{pmatrix} \cos\frac{\theta_{\mathbf{k}}}{2} & i\exp(-i\phi_{\mathbf{k}})\sin\frac{\theta_{\mathbf{k}}}{2} \\ i\exp(i\phi_{\mathbf{k}})\sin\frac{\theta_{\mathbf{k}}}{2} & \cos\frac{\theta_{\mathbf{k}}}{2} \end{pmatrix} \tag{2.3}$$

where $\tan\theta_{\mathbf{k}} = k_c^2/(k^2\cos 3\phi_{\mathbf{k}})$ with the characteristic wave-vector $k_c = \sqrt{v_F/\lambda}$. The transformation matrix $U(\mathbf{k})$ diagonalize $H_{\mathbf{k}}$ such that $\tilde{H}(\mathbf{k}) = U^{\dagger}(\mathbf{k})H(\mathbf{k})U(\mathbf{k}) = \epsilon(\mathbf{k})\tau^z$ with eigenvalues $\epsilon(\mathbf{k})_\eta = \eta\epsilon(\mathbf{k})$ and $\epsilon(\mathbf{k}) = \sqrt{(v_F k)^2 - (\lambda k^3 \cos\phi_{\mathbf{k}})^2}$. The bare Hamiltonian Eqn. (2.1) will be denoted in its diagonal η-basis, in which $\eta = \{+, -\}$, as

$$\tilde{\mathcal{H}}_0(\mathbf{k}) = \sum_{\mathbf{k},\eta} \xi(\mathbf{k})_\eta \tilde{c}^{\dagger}_{\mathbf{k},\eta} \tilde{c}_{\mathbf{k},\eta} \tag{2.4}$$

in terms of the new eigenvectors

$$\tilde{c}^{\dagger}_{\mathbf{k},\eta} = \sum_{\sigma} c^{\dagger}_{\mathbf{k},\sigma} U(\mathbf{k})_{\sigma\eta} \quad , \quad \tilde{c}_{\mathbf{k}',\eta'} = \sum_{\sigma'} U^{\dagger}(\mathbf{k}')_{\eta'\sigma'} c_{\mathbf{k}',\sigma'} \tag{2.5}$$

and eigenenergy $\xi(\mathbf{k})_\eta = \eta\epsilon(\mathbf{k}) - \mu$. Note that a tilde superscript $\tilde{}$ will denote a vector or matrix in η-basis $\eta = \{+, -\}$ with $\pm$ helicity of the upper and lower energy dispersion cone respectively. Vectors and matrices having no tilde superscript will denote the object being in the σ-basis with $\sigma = \{\uparrow_z, \downarrow_z\}$ where $\uparrow_z$ / $\downarrow_z$ being the eigenspinor of the s^z spin-operator. The energy spectrum is illustrated in figure 1.7(c).

2.2 The Dirac model

In what follows the 'Dirac model' will be a further simplification of the effective Hamiltonian Eqn. (2.2) by introducing $D << D_{SSB}$ a symmetric momentum cut-off $k_x \in [-D/v_F, D/v_F]$ and $k_y \in [-D/v_F, D/v_F]$ exactly such, that the dispersion is isotropic in momentum space, and the helical surface spin-momentum locking is in-plane with the spin tangentially on the circular Fermi

surface contour. I.e. instead of Eqn. (2.2), the low-energy/long-wavelength and no warping limit ($\lambda \to 0$ and $\theta_{\mathbf{k}} \to \pi/2$) the Hamiltonian reads

$$H(\mathbf{k}) = H_0(\mathbf{k}) = v_F(\mathbf{k} \times \bar{\tau}) \cdot \hat{z} \tag{2.6}$$

The transformation matrix

$$U(\phi_{\mathbf{k}}) = \frac{1}{\sqrt{2}} \begin{pmatrix} 1 & i\exp(-i\phi_{\mathbf{k}}) \\ i\exp(i\phi_{\mathbf{k}}) & 1 \end{pmatrix} \tag{2.7}$$

now only depends on the angle $\phi_{\mathbf{k}}$, and the bare Hamiltonian Eqn. (2.1) in η-basis is

$$\tilde{\mathcal{H}}_0(\mathbf{k}) = \sum_{\mathbf{k},\eta} \xi_\eta(k) \tilde{c}^\dagger_{\mathbf{k},\eta} \tilde{c}_{\mathbf{k},\eta} \tag{2.8}$$

in terms of the new eigenvectors

$$\tilde{c}^\dagger_{\mathbf{k},\eta} = \sum_\sigma c^\dagger_{\mathbf{k},\sigma} U(\phi_{\mathbf{k}})_{\sigma\eta} \quad , \quad \tilde{c}_{\mathbf{k}',\eta'} = \sum_{\sigma'} U^\dagger(\phi_{\mathbf{k}'})_{\eta'\sigma'} c_{\mathbf{k}',\sigma'} \tag{2.9}$$

and eigenenergy $\xi(k)_\eta = \epsilon(k)_\eta - \mu$ with the linear Dirac dispersion $\epsilon(k)_\eta = \eta v_F k$ only depends on $k = |\mathbf{k}|$ the magnitude of the momentum. In figure 2.2 this spectrum is illustrated; it forms a positive $\eta = +$ and negative $\eta = -$ energy cone centered at the Dirac Γ-point at $\mathbf{k} = (0,0)$ with electrons filled up to the Fermi level μ, somewhere within the surface state band truncated by $\mathbf{k} \in [-D, D]$. Also a probing frequency (in units of energy) ω and $\tilde{\omega} \equiv \omega + \mu$ is shown. For a Fermi level $\mu > 0$ a probe frequency $\omega > 0$ probe a hole-state, whereas $\omega < 0$ probe an electron-state. When $\omega = 0$ then $\tilde{\omega} = \mu$ which means, that the Fermi surface is probed, whereas $\omega = -\mu$ (for $\mu > 0$) probe the spin-degenerate point of zero energy. The cone index $\eta = \pm$ corresponds to the helicity (+ left and − right handedness of the spin-momentum locking) of the electron spin-distribution Eqn. (2.21) on the Fermi surface. For example the +helicity of a Fermi surface on a + cone is illustrated in figure 2.5.

The bare Matsubara Green function, found by standard equation of motion technique, in the σ-basis

$$G^0(\mathbf{k}\sigma, \mathbf{k}'\sigma'; i\tilde{\omega}_n) = \delta_{\mathbf{k},\mathbf{k}'} \frac{i\tilde{\omega}_n \delta_{\sigma\sigma'} + v_F(\mathbf{k} \times \bar{\tau}_{\sigma\sigma'}) \cdot \hat{z}}{(i\tilde{\omega}_n)^2 - \epsilon^2} = G^0(\mathbf{k}, \mathbf{k}'; i\tilde{\omega}_n)_{\sigma\sigma'} \tag{2.10}$$

with $\epsilon = v_F\, k$ and $\tilde{\omega} \equiv \omega + \mu$. The bare Matsubara Green function in the the η-basis

$$\begin{aligned} \tilde{G}^0(\mathbf{k}\eta, \mathbf{k}'\eta'; i\tilde{\omega}_n) &= \tilde{G}^0(\mathbf{k}, \mathbf{k}'; i\tilde{\omega}_n)_{\eta\eta'} && (2.11) \\ &= \left(\hat{U}^\dagger(\phi_{\mathbf{k}}) G^0(\mathbf{k}, \mathbf{k}'; i\tilde{\omega}_n) \hat{U}(\phi_{\mathbf{k}'})\right)_{\eta\eta'} && (2.12) \\ &= \left(\hat{U}^\dagger(\phi_{\mathbf{k}}) G^0(\mathbf{k}; i\tilde{\omega}_n) \hat{U}(\phi_{\mathbf{k}})\right)_{\eta\eta'} = \\ &= \begin{pmatrix} \frac{1}{i\tilde{\omega}_n - \epsilon} & 0 \\ 0 & \frac{1}{i\tilde{\omega}_n + \epsilon} \end{pmatrix}_{\eta\eta'} \end{aligned}$$

The first equality sign illustrate the notation, that any object as a λ, λ'-matrix component will either be written $O(\lambda, \lambda')$ or $O_{\lambda,\lambda'}$ depending on which is most convenient at hand.

2.2.1 Fermi surface on a helical metal vs. a conventional metal

In the introduction section 1 the conventional spin-orbit metal[24] was introduced. Its surface states are spin non-degenerate and have quadratic dispersion relation $\epsilon^{\uparrow,\downarrow}(\mathbf{k}) = \epsilon_0 + \frac{\hbar^2(k \pm k_0)^2}{2\,m^*}$. At that point it was convenient to use it to compare with the helical metal, because both of them have spin non-degenerate spin-momentum locked surface states. At that time it was learnt that the former is a non-trivial $v_0 = 1$ and the latter a trivial $v_0 = 0$ TI, so the desired distinction between them was clarified. Graphene was also mentioned, in order to show the difference between a $v_0 = 1$ and $v_0 = 0$ TI, but since graphene has four Dirac cones, intervalley-and intracone scattering occur, which makes the comparison to a $v_0 = 1$ TI with a single Dirac cone complicated. Therefore the helical metal will not be compared to graphene anymore.

In the rest of the thesis, it is the consequences of a non-degenerate spin-momentum locked Fermi surface that is in focus. Therefore in order to see the effects of such a Fermi surface, the helical metal will be compared to metals which doesn't have such a Fermi surface spin-texture. The conventional Dirac metal which has a linear dispersion $\epsilon(k)_\eta = \eta k$, see figure 2.2, but its surface states are double spin degenerate, as illustrated in figure 2.4. Hence is has 2 times the degrees of freedom of that, of the helical metal, and it would be the best metal to compare with in many cases. However this metal will not be used in most contexts, but instead the conventional metal.

Conventional Metal

The conventional metal is here defined as a 2 dimensional free electron gas with double spin degeneracy and quadratic dispersion relation $\epsilon^{\uparrow,\downarrow}(\mathbf{k}) = \frac{\hbar^2 k^2}{2\,m}$. The dispersion is illustrated in figure 2.3 and the Fermi surface spin-texture in figure 2.4.

Using this metal as a reference instead of the obvious choice of the conventional Dirac metal, cause the appearance of certain effects due to the difference between the energy dispersions; namely the one having a quadratic dispersion and the other two $\eta = \{+, -\}$ Dirac cones. However the effects due to the different dispersion relations will turn out not to blur the important information residing from the different spin degeneracy which is seeked. It will be clear that whenever a certain quantity of the helical metal is compared to that from the conventional, the information residing from the dispersion can be distangled from that contained in its spin degeneracy.

The volume in reciprocal $\mathbf{k}$-space associated with *one* state is $\Delta\Omega_\mathbf{k} = \frac{(2\pi)^d}{L^d}$, where d is dimension $d = 2$ and L length of surface. To convert a dimensionless sum over discrete $\mathbf{k}$ states to an integral, one substitutes

$$\sum_\mathbf{k} = \int \frac{\mathrm{d}^2\mathbf{k}}{\Delta\Omega_\mathbf{k}} = L^2 \int \frac{\mathrm{d}^2\mathbf{k}}{(2\pi)^2}$$

In an conventional metal every $\mathbf{k}$ state is $(2s+1) = 2$ spin degenerate where $s = 1/2$ denotes the spin of the surface electron. Therefore a sum over states $\{\mathbf{k}, \sigma\}$ can be converted to an integral as

$$\sum_{\mathbf{k}\sigma} = (2s+1)\,L^2 \int \frac{\mathrm{d}^2\mathbf{k}}{(2\pi)^2} = \int \mathrm{d}\epsilon\, g(\epsilon)$$

and the *density of energy states* (DOS) $g(\epsilon)$ can be obtained with the knowledge of the relation between $\mathbf{k}$ and the spectrum $\epsilon_\mathbf{k}$, i.e. $k(\epsilon_\mathbf{k})$ and $\mathrm{d}k = \frac{\partial k}{\partial \epsilon_\mathbf{k}} \mathrm{d}\epsilon$, as

$$g(\epsilon) = \sum_{\mathbf{k}\sigma} \delta(\epsilon_\mathbf{k} - \epsilon) = (2s+1)\,L^2 \int \frac{\mathrm{d}^2\mathbf{k}}{(2\pi)^2} \delta(\epsilon_\mathbf{k} - \epsilon) = \frac{2}{\pi} \frac{m\,L^2}{\hbar^2} \tag{2.13}$$

i.e. a constant in 2 dimensions and with unit of inverse energy.

The helical metal in the Dirac model

The topological insulator is different, since the surface states are *non-degenerate* and two energy cones, a positive and negative i.e. $\eta = \{+, -\}$ respectively, are linear 'Dirac' energy-spectra $\epsilon_\eta(\mathbf{p}) = \eta\, v_F\, |\mathbf{p}|$ anchored at the common 'Dirac' Γ-point in reciprocal space $\mathbf{p} = (0, 0)$.
Its linear spectrum[6] $\epsilon_\eta(\mathbf{p}) = \eta\, v_F\, |\mathbf{p}|$ where $\mathbf{p}$ denotes the linear momentum $\mathbf{p} = -i\,\hbar\nabla$ of the surface/conduction electrons.

Now define $\mathbf{k} \equiv v_F\mathbf{p}$ with units of energy and set the Fermi velocity $v_F \equiv 1$ and $\hbar \equiv 1$ will be the convention onwards. The dispersion will then be $\epsilon_\eta(k) = \eta\, k$, with $\mathbf{k}$ in units of energy and $\eta = \{+, -\}$ denote the helicity of the corresponding positive or negative energy-cones.
The volume in reciprocal (units of energy) $\mathbf{k}$-space associated with *one* state is
$\Delta\Omega_\mathbf{k} = v_F^2\, \Delta\Omega_\mathbf{p} = \frac{v_F^2\hbar^2}{L^2}(2\pi)^2$ where L is sample length and v_F the Fermi velocity. To convert a dimensionless sum over discrete $\mathbf{k}$ states to an integral, one substitutes

$$\sum_\mathbf{k} = \int \frac{\mathrm{d}^2\mathbf{k}}{\Delta\Omega_\mathbf{k}} = \frac{1}{v_F^2}\int \frac{\mathrm{d}^2\mathbf{k}}{\Delta\Omega_\mathbf{p}} = \left(\frac{L}{v_F\hbar}\right)^2 \int \frac{\mathrm{d}^2\mathbf{k}}{(2\pi)^2} \tag{2.14}$$

Note that $\frac{L^2}{(2\pi)^2 v_F^2\hbar^2}$ has dimension energy^{-2} and $\mathrm{d}^2\mathbf{k}$ has dimension energy^2 making $\sum_\mathbf{k}$ dimensionless. In a helical metal every $\mathbf{k}$ state is *non-degenerate*, with a single helicity index η corresponding to the energy cone it propagate at. Therefore a sum over states $\{\mathbf{k}, \eta\}$ can be converted to an integral as

$$\sum_{\mathbf{k}\eta} = \left(\frac{L}{v_F\hbar}\right)^2 \sum_\eta \int \frac{\mathrm{d}^2\mathbf{k}}{(2\pi)^2} = \left(\frac{L}{v_F\hbar}\right)^2 \sum_\eta \int \mathrm{d}\omega\, \tilde{g}_\eta(\omega) \tag{2.15}$$

In all calculations $(L/v_F\hbar)^2 \equiv 1$, but when an expression is returned into a physical one, it is necessary to reintroduce for ever $\mathbf{k}$-sum performed a factor $(L/v_F\hbar)^2$.

The density of energy states (DOS) per helicity η is

$$\tilde{g}_\eta(\omega) = \sum_\mathbf{k} \delta(\epsilon_\eta(k) - \omega) = \left(\frac{L}{v_F\hbar}\right)^2 \int \frac{\mathrm{d}^2\mathbf{k}}{(2\pi)^2}\delta(\omega - \epsilon_\eta(k)) \tag{2.16}$$

And the total DOS

$$\tilde{g}(\omega) = \sum_\eta g_\eta(\omega) = \left(\frac{L}{v_F\hbar}\right)^2 \frac{|\omega|}{2\pi}\Theta(D - |\omega|) \tag{2.17}$$

is linear on a 2 dimensional helical surface with unit of inverse energy.
Let the system be prepared at zero temperature, $T = 0$, and the whole surface state band filled with N electrons up to the chemical potential/Fermi level μ. The number of surface electrons

$$N = \int_\infty^\infty \mathrm{d}\omega\, \tilde{g}(\omega) n_F(\omega) = \int_{-D}^{\mu} \mathrm{d}\omega\, \tilde{g}(\omega) = \left(\frac{L}{v_F\hbar}\right)^2 \frac{D^2 + \mu^2}{4\pi} \tag{2.18}$$

[6] Here $\mathbf{p}$ is chosed to be momentum instead of the letter $\mathbf{k}$ used in the former sections. This make the shift in units more clear, than it would be if $\mathbf{k}$ was used instead of $\mathbf{p}$.

where $n_F(\omega)$ is the Fermi-Dirac distribution.

The spin-distribution on a Fermi surface with helicity η and momentum k, is the average of spin-operator $\bar{s}$ acting on the free conduction electrons in state $\eta, \mathbf{k}$, thus $\langle \eta, \mathbf{k}|\bar{s}|\mathbf{k}, \eta\rangle$. The state $|\mathbf{k}, \eta\rangle$ is a plane wave with $\langle \mathbf{k}^{'}, \eta^{'}|\mathbf{k}, \eta\rangle = \langle \eta^{'}|\eta\rangle \otimes \langle \mathbf{k}^{'}|\mathbf{k}\rangle = \delta_{\eta^{'},\eta}\delta_{\mathbf{k}^{'},\mathbf{k}}$. A general state in $\mathbf{k}, \eta$-basis, $|\mathbf{k}, \eta\rangle$, with the specific + helicity and momentum $\mathbf{k}$, $|\mathbf{k}, +\rangle$, expressed in the σ-basis spanned by the eigenstates $\{\uparrow, \downarrow\} \equiv \{\uparrow_z, \downarrow_z\}$ of the Pauli-spin operator s^z is

$$|\mathbf{k}, +\rangle = \sum_{\sigma} U^{\dagger}(\phi_{\mathbf{k}})_{+\sigma}|\mathbf{k}, \sigma\rangle = \frac{1}{\sqrt{2}}(|\mathbf{k}, \uparrow\rangle - ie^{-i\phi_{\mathbf{k}}}|\mathbf{k}, \downarrow\rangle) \tag{2.19}$$

$$\langle \mathbf{k}, +| = \sum_{\sigma} U(\phi_{\mathbf{k}})_{+\sigma}\langle \sigma, \mathbf{k}| = \frac{1}{\sqrt{2}}(\langle \mathbf{k}, \uparrow| + ie^{i\phi_{\mathbf{k}}}\langle \mathbf{k}, \downarrow|) \tag{2.20}$$

The free conduction electron spin-operator components and its expectation values are

$$s^z|\mathbf{k}, +\rangle = \frac{\hbar}{2}\frac{1}{\sqrt{2}}(|\mathbf{k}, \uparrow\rangle + ie^{-i\phi_{\mathbf{k}}}|\mathbf{k}, \downarrow\rangle), \qquad \langle \mathbf{k}, +|s^z|\mathbf{k}, +\rangle = 0$$

$$s^x|\mathbf{k}, +\rangle = \frac{\hbar}{2}\frac{1}{\sqrt{2}}(|\mathbf{k}, \downarrow\rangle - ie^{-i\phi_{\mathbf{k}}}|\mathbf{k}, \uparrow\rangle), \qquad \langle \mathbf{k}, +|s^x|\mathbf{k}, +\rangle = \frac{\hbar}{2}\sin\phi_{\mathbf{k}}$$

$$s^y|\mathbf{k}, +\rangle = \frac{\hbar}{2}\frac{1}{\sqrt{2}}(i|\mathbf{k}, \downarrow\rangle - e^{-i\phi_{\mathbf{k}}}|\mathbf{k}, \uparrow\rangle), \qquad \langle \mathbf{k}, +|s^y|\mathbf{k}, +\rangle = -\frac{\hbar}{2}\cos\phi_{\mathbf{k}}$$

so the free conduction electron spin expectation value on the circular Fermi surface with helicity $\eta = +$ and momentum $k = |\mathbf{k}|$, illustrated in figure 2.5, is given by

$$\langle \mathbf{k}, +|\bar{s}|\mathbf{k}, +\rangle = \frac{\hbar}{2}\begin{pmatrix} \sin\phi_{\mathbf{k}} \\ -\cos\phi_{\mathbf{k}} \\ 0 \end{pmatrix} \tag{2.21}$$

Notice that this is a *momentum dependent* spin expectation value. Likewise the surface of the same magnitude of momentum k, but opposite helicity $\eta = -$, has spin expectation values

$$\langle \mathbf{k}, -|\bar{s}|\mathbf{k}, -\rangle = \frac{\hbar}{2}\begin{pmatrix} -\sin\phi_{\mathbf{k}} \\ \cos\phi_{\mathbf{k}} \\ 0 \end{pmatrix} = -\langle +, \mathbf{k}|\bar{s}|\mathbf{k}, +\rangle \tag{2.22}$$

The momentum dependent spin expectation value on the +helicity surface rotates clockwise in a left-handed coordinate system (k_x, k_y), whereas on the $-$ helicity surface it rotates counter-clockwise. The coordinate system (k_x, k_y) is specified by the crystal and the $\Gamma - K$ is chosen to be the $\hat{x}$ axis and $\Gamma - M$ as the $\hat{y}$.

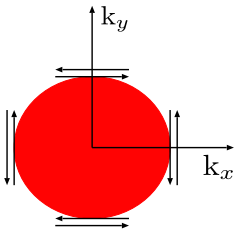

Figure 2.4: Illustration of the Fermi surface of a conventional metal and conventional Dirac metal. The double arrows on each point around the circle illustrates the double spin-degeneracy for each **k**-state on the Fermi surface.

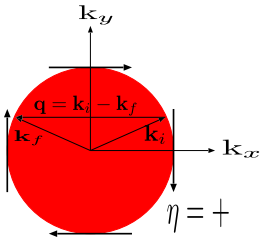

Figure 2.5: Illustration of the $\eta = +$ Fermi surface of a helical metal. The single arrow on each point around the circle illustrates the spin non-degeneracy for each **k**-state on the Fermi surface.

Chapter 3

The inhomogeneous helical metal

For a homogeneous system momentum $\mathbf{k}$ is a good quantum number. By introducing a *single local* impurity at $\mathbf{r} = 0$ translational invariance is broken due to scattering off the impurity, and hence momentum is not a good quantum number anymore. Therefore two momentum indices appear on the scattering process $V_{\mathbf{k}',\mathbf{k}}$ in an inhomogeneous system. A general impurity Hamiltonian, $\mathcal{H}_{imp}$, in σ-basis will be expressed in the η-eigenbasis as

$$\mathcal{H}_{imp} = \sum_{\substack{\mathbf{k}'\mathbf{k} \\ \sigma',\sigma}} c^{\dagger}_{\mathbf{k}',\sigma'} V^{imp.}_{\sigma',\sigma}(\mathbf{k}',\mathbf{k}) c_{\mathbf{k},\sigma} = \sum_{\substack{\mathbf{k}'\mathbf{k} \\ \eta',\eta}} \tilde{c}^{\dagger}_{\mathbf{k}',\eta'} \tilde{V}^{imp}_{\eta',\eta}(\mathbf{k}',\mathbf{k}) \tilde{c}_{\mathbf{k},\eta} = \tilde{\mathcal{H}}_{imp} \tag{3.1}$$

where the impurity expressed in the η-basis

$$\tilde{V}^{imp}(\mathbf{k}',\mathbf{k}) = U^{\dagger}(\mathbf{k}') V^{imp}(\mathbf{k}',\mathbf{k}) U(\mathbf{k}) \tag{3.2}$$

in the warping model and V^{imp} is given in units of energy. When Eqn. (3.2) is used in the Dirac model, the transformation matrix and dispersion relation defined in section 2.1 reduces to $U(\mathbf{k}) \to U(\phi_{\mathbf{k}})$ and $\epsilon(\mathbf{k}) \to \epsilon(k)$ to those defined in section 2.2.

In what is to come three types of impurities will be considered. A scalar potential, a classical magnetic and a quantum-mechanical magnetic impurity/Kondo model. The scalar (sc) potential and the quantum magnetic (qm) impurity are similar, in the sense, that they both preserve time-reversal symmetry. However, the former cannot mediate a spin flip of the conduction electrons, whereas the latter can by simultaneously flipping its own impurity spin, as long the total spin is conserved in order to respect time-reversal symmetry. The classical magnetic (cl) impurity breaks time-reversal symmetry and can flip the electron spin, but the impurity magnetic-direction stay fixed.

The scalar potential substitutes $\tilde{V}^{imp.}(\phi_{\mathbf{k}'}, \phi_{\mathbf{k}})$ in Eqn. (3.2) with

$$\tilde{V}^{sc}(\phi_{\mathbf{k}'}, \phi_{\mathbf{k}}) = V_0 \tilde{\tau}^0(\phi_{\mathbf{k}'}, \phi_{\mathbf{k}}) = V_0 U^{\dagger}(\phi_{\mathbf{k}'}) \tau^0 U(\phi_{\mathbf{k}}) = \frac{V_0}{2} \begin{pmatrix} 1 + e^{i(\phi_{\mathbf{k}} - \phi_{\mathbf{k}'})} & i\left(e^{-i\phi_{\mathbf{k}}} - e^{-i\phi_{\mathbf{k}'}}\right) \\ i\left(e^{i\phi_{\mathbf{k}}} - e^{i\phi_{\mathbf{k}'}}\right) & 1 + e^{-i(\phi_{\mathbf{k}} - \phi_{\mathbf{k}'})} \end{pmatrix} \tag{3.3}$$

Note that the scalar is *not* a identity matrix in η-basis.

The classical magnetic impurity stay fixed in the magnetic-direction $\bar{S} = |S|\hat{S}$, which couples to the electron spin σ and creates the B-field that cause the spin-flip. The impurity substitutes $\tilde{V}^{imp.}(\phi_{\mathbf{k}'}, \phi_{\mathbf{k}})$ in Eqn. (3.2) with

$$\tilde{V}^{cl}(\phi_{\mathbf{k}'}, \phi_{\mathbf{k}}) = S_i \tilde{\tau}^i(\phi_{\mathbf{k}'}, \phi_{\mathbf{k}}) \tag{3.4}$$

where the Einstein summation convention is implied.

Consider a magnetic impurity spin $\bar{S}_d$ embedded on the surface of conducting quasi-electrons. The Kondo/exchange Hamiltonian provides the exchange coupling between the free conduction electrons and the spin of the impurity. The coupling J is isotropic, since the coupling between the electrons and the impurity-spin, is the same for all incident electron momenta and spin directions. This makes the impurity substitutes $\tilde{V}^{imp.}(\phi_{\mathbf{k}'}, \phi_{\mathbf{k}})$ in Eqn. (3.2) with

$$\tilde{V}^{qm}(\phi_{\mathbf{k}'}, \phi_{\mathbf{k}}) = -J^{'} \tilde{\bar{s}}_{c.e}(\phi_{\mathbf{k}'}, \phi_{\mathbf{k}}) \cdot \bar{S}_d \tag{3.5}$$

$$= -J \tilde{\bar{\tau}}(\phi_{\mathbf{k}'}, \phi_{\mathbf{k}}) \cdot \bar{S} \tag{3.6}$$

where $\bar{S}_d = \frac{1}{2}\bar{\tau}$ is the impurity spin, allowed to be half-integer spin, independent of the electron spin space and $\bar{\tau}$ is a vector with the Pauli matrices as its components.
The $\tilde{\bar{s}}_{c.e}(\phi_{\mathbf{k}'}, \phi_{\mathbf{k}}) = \frac{1}{2}\tilde{\bar{\tau}}(\phi_{\mathbf{k}'}, \phi_{\mathbf{k}})$ is the conduction electron spin in the η-basis, which form a rotated Pauli-matrix vector $\tilde{\bar{\tau}}(\phi_{\mathbf{k}'}, \phi_{\mathbf{k}}) = U^{\dagger}(\phi_{\mathbf{k}'})\bar{\tau}U(\phi_{\mathbf{k}})$ which is momentum dependent. The subscripts on the spin operators d and $c.e$ denoting the impurity spin and conduction electron spin, respectively, will henceforth be ignored, so $\bar{S}_d \equiv \bar{S}$ and $\tilde{\bar{s}}_{c.e} \equiv \tilde{\bar{s}}$. On the form Eqn. (3.6), the factor $\frac{1}{2}$ from the electron spin operator $\tilde{\bar{s}}_{c.e}(\phi_{\mathbf{k}'}, \phi_{\mathbf{k}}) = \frac{1}{2}\tilde{\bar{\tau}}(\phi_{\mathbf{k}'}, \phi_{\mathbf{k}})$ in Eqn. (3.5) is absorbed into the coupling as $J = \frac{J^{'}}{2}$.

Further Eqn. (3.6) can be expressed on another form by defining $S^{\pm} = \frac{1}{2}(S^x \pm iS^y)$ and expanding $\tilde{V}^{qm}(\phi_{\mathbf{k}'}, \phi_{\mathbf{k}})$ on the impurity spin-flip operators S^+, S^- and the non spin-flip operator S^z. Doing this yields

$$\tilde{V}^{qm}(\phi_{\mathbf{k}'}, \phi_{\mathbf{k}}) = -J\tilde{\bar{\tau}}(\phi_{\mathbf{k}'}, \phi_{\mathbf{k}}) \cdot \bar{S} = -J\left(\tilde{\tau}^{-}(\phi_{\mathbf{k}'}, \phi_{\mathbf{k}})\, S^{-} + \tilde{\tau}^{+}(\phi_{\mathbf{k}'}, \phi_{\mathbf{k}})\, S^{+} + \tilde{\tau}^{z}(\phi_{\mathbf{k}'}, \phi_{\mathbf{k}})\, S^{z}\right) \tag{3.7}$$

where the coefficients in front of S^-, S^+ and S^z are denoted likewise $\tilde{\tau}^-, \tilde{\tau}^+$ and $\tilde{\tau}^z$, which contain the information of the conduction electrons in η-basis, when the impurity-spin is either spin-flipped or not. These are summarized in table 3.1 and given in the η-basis. They describe the spin-momentum locked relation the conduction/surface electrons are enforced to obey, when propagating on the helical surface. The impurity-spin operator $\bar{S}$ is conversely given in the σ-basis, the direction of which, is determined relative to the fixed sample orientation of k_x ($\Gamma - \mathrm{K}$) and k_y ($\Gamma - \mathrm{M}$). This means, that for a fixed direction of impurity spin magnetic moment M along the $\hat{z}$ direction (perpendicular to the surface Brillouin zone), the conduction electrons experience this impurity spin magnetic moment differently, depending on the direction of propagating inwards ($\mathbf{k}_i$) or outwards ($\mathbf{k}_f$) when scattering upon it.

$\tilde{\bar{\tau}}(\phi_{\mathbf{k}'}, \phi_{\mathbf{k}})$	$\tilde{\tau}^-$	$\tilde{\tau}^+$	$\tilde{\tau}^z$
$\tilde{\tau}_{++}$	$i\, e^{i\phi_{\mathbf{k}}}$	$-i\, e^{-i\phi_{\mathbf{k}'}}$	$\frac{1}{2}(1 - e^{i(\phi_{\mathbf{k}} - \phi_{\mathbf{k}'})})$
$\tilde{\tau}_{+-}$	1	$e^{-i(\phi_{\mathbf{k}} + \phi_{\mathbf{k}'})}$	$\frac{i}{2}\left(e^{-i\phi_{\mathbf{k}}} + e^{-i\phi_{\mathbf{k}'}}\right)$
$\tilde{\tau}_{-+}$	$e^{i(\phi_{\mathbf{k}} + \phi_{\mathbf{k}'})}$	1	$\frac{-i}{2}\left(e^{i\phi_{\mathbf{k}}} + e^{i\phi_{\mathbf{k}'}}\right)$
$\tilde{\tau}_{--}$	$-i\, e^{i\phi_{\mathbf{k}'}}$	$i\, e^{-i\phi_{\mathbf{k}}}$	$\frac{-1}{2}(1 - e^{-i(\phi_{\mathbf{k}} - \phi_{\mathbf{k}'})})$

Table 3.1: Table of the components $\tilde{\bar{\tau}}(\phi_{\mathbf{k}'}, \phi_{\mathbf{k}})$ which are the coefficients in front of S^-, S^+ and S^z, respectively. The rows corresponds to the $(\eta^{'}, \eta)$-matrix components, whereas the columns to the coefficient being $-, +$ or z. For example the $(2,2)$-entry is the $\tilde{\tau}^{+}_{+-}(\phi_{\mathbf{k}'}, \phi_{\mathbf{k}}) = e^{-i(\phi_{\mathbf{k}} + \phi_{\mathbf{k}'})}$.

3.1 Transition amplitudes

The interesting feature of the helical metal is, that the Fermi surface enforces the electron to propagate in a helical spin-texture, i.e. the electron spin point in a certain direction depending on its momentum. Further, the quantum/Kondo impurity is introduced to the surface of the helical metal. This is able to flip its impurity spin, depending on which electron with a certain spin, is scattering off it. As used in several transport experiments, one can apply an electric field, which distort the Fermi surface in **k**-momentum space and here by create an excess of electrons with some preferred momenta. But applying such an electric field to the helical Fermi surface, one creates an excess of electrons with a preferred momenta which also have a preferred spin-direction associated with the distorted helical Fermi surface. One can imagine this excess of propagating electrons with a preferred spin direction, can flip the impurity one by one. Hence it might turn out, that the helical surface with a dilute contamination of quantum impurities, all will point its impurity spin in the same direction after sufficiently many helical electrons have propagated over the surface. This will polarize the surface, because all surface impurities point in the same direction. Such an effect might be useful in applications such as spintronics. Guided by this idea, the transition amplitudes of the quantum impurity will be derived below.

In his 1964 paper[28] Kondo calculated by Eqn. (3.8) the various transition probability rates in both 1^{st} and 2^{nd} Born approximation for a conduction electron scattering off a quantum/Kondo impurity. Here only the 1^{st} Born approximation will be calculated, since it is a simple task, and it is sufficient in order to understand the consequence of the helical spin-momentum locking texture. The squared matrix element $w_{i\to f}$ given by Fermi's Golden Rule, from an initial state i to a final state f, is up to second order in perturbation given as

$$\begin{aligned} w_{i\to f} &= \frac{2\pi}{\hbar}\sum_f \left| H'_{fi} + \sum_m \frac{H'_{nm}H'_{mi}}{E_i - E_i + i\,\delta}\right|^2 \delta(E_f - E_i) \\ &= \sum_f \frac{2\pi}{\hbar}\left(\underbrace{|H'_{fi}|^2}_{1^{st}\text{ Born Approx}} + \underbrace{\sum_m \left(\frac{H'_{nm}H'_{mi}H'_{in}}{E_i - E_m + i\,\delta} + c.c\right)}_{2^{nd}\text{ Born Approx}} + O^4(H')\right)\delta(E_f - E_i) \end{aligned} \tag{3.8}$$

where the matrix element $H'_{jl} = \langle j|H'|l\rangle$ of the perturbing Hamiltonian and E_j the eigenenergy of the eigenstate $|j\rangle$ hence $H|j\rangle = E_j|j\rangle$.

The 1^{st} Born approximation involves only a single direct-energy conserving transition between states $|\mathbf{k},\eta;S,M\rangle \to |\mathbf{k}',\eta';S,M'\rangle$ where the states are product-states of the independent conduction electron state $|\mathbf{k},\eta\rangle$ and impurity state $|S,M\rangle$, thus $|\mathbf{k},\eta\rangle \otimes |S,M\rangle = |\mathbf{k},+;S,M\rangle$. The impurity spin S will be suppressed, since it does not change, whereas the impurity spin magnetic moment M is allowed to change and is therefore not suppressed.

The transition Eqn. (3.8) is restricted by $\delta(E_f - E_i)$ to occur between energy-conserved states, the energy of which, is solely determined by the electron energy dispersion. The helical metal due to its linear Dirac dispersion $\epsilon_\eta(k) = \eta k$ restricts the transition by $\delta(\epsilon_\eta(k) - \epsilon_{\eta'}(k'))$, which enforce $\eta = \eta'$ and $k = k'$, i.e. to scattering between same helicity states and $k = |\mathbf{k}| = |\mathbf{k}'| = k'$, but in general $\phi_{\mathbf{k}} \neq \phi_{\mathbf{k}'}$. As a consequence hereof *only* the transition from state $|\mathbf{k}',\eta\rangle$ to $|\mathbf{k}',\eta\rangle$ will be considered, and for simplicity only the $\eta = +$ helicity, since we imagine all the states up to the chemical potential μ filled, and the Fermi surface at $k = |\mathbf{k}|$ is somewhere in the $\eta = +$ helicity cone as illustrated in figure 2.2 and 2.5.

3.1.1 1^{st} Born approximation - an electron scattering off a scalar potential

What to expect? The common heuristic argument, presented in the introductory of most articles on topological insulators, would be: 'each momentum state $\mathbf{k}$ has a well-defined spin locked tangentially in-plane and no out-of-plane spin component. Since the scalar is only a potential, it cannot flip the spin of the conduction electron. Hence the electron cannot backscatter, but forward scattering is allowed, because the former require a spin-flip interaction whereas the latter does not. However, the spin-polarization distribution Eqn. (2.21) is actually the *average expectation value of the spin operator* $\langle +, \mathbf{k}|\bar{s}|\mathbf{k}, +\rangle$, which cause a finite overlap of spins-states not opposite of each other. But still the forward scattering is maximum and backward scattering is zero.'

The 1^{st} order matrix element squared

$$\begin{aligned} w^{sc}_{+,\mathbf{k}\to+,\mathbf{k}'} &= \frac{2\pi}{\hbar}|\langle +\mathbf{k}^{'}|\tilde{V}^{sc}(\phi_{\mathbf{k}'},\phi_{\mathbf{k}})|\mathbf{k},+\rangle|^2 \\ &= \frac{2\pi}{\hbar}|V_0\tilde{\tau}^0_{++}(\phi_{\mathbf{k}'},\phi_{\mathbf{k}})|^2 \\ &= \frac{2\pi}{\hbar}V_0^2\cos^2\left(\frac{\phi_{\mathbf{k}}-\phi_{\mathbf{k}'}}{2}\right) \end{aligned} \tag{3.9}$$

is the only diagram for an initial electron state on the + helicity cone. The argument presented above explain the case of scalar potential scattering, since by Eqn. (3.9) the scattering angle $\phi_{\mathbf{q}} = impuritynonspin - flipmatrixelementsquaredphi_{\mathbf{k}} - \phi_{\mathbf{k}'}$ in forward direction $\phi_{\mathbf{k}} = \phi_{\mathbf{k}'}$ has maximum matrix element squared, but backward scattering $\phi_{\mathbf{k}} = \pi + \phi_{\mathbf{k}'}$ has zero.

3.1.2 1^{st} Born approximation - an electron scattering off a quantum impurity

What to expect in this case? Here the common heuristic argument would be: 'the exchange coupling $-J\bar{\tau}\cdot\bar{S}$ can either make a simultaneously flip of both impurity and electron spin by $S^{\pm}$ and $\tau^{\pm}$, or make a non-flipping transition by S^z and τ^z. Both the spin non-flip and spin flip transition would be allowed.'

The 'impurity non spin-flip' matrix element squared

$$\begin{aligned} w^{qm}_{M;+,\mathbf{k}\to M;+,\mathbf{k}'} &= \frac{2\pi}{\hbar}|\langle M;+\mathbf{k}^{'}|\tilde{V}^{qm}(\phi_{\mathbf{k}'},\phi_{\mathbf{k}})|\mathbf{k},+;M\rangle|^2 \\ &= \frac{2\pi}{\hbar}|-J\langle M|S^z|M\rangle\tilde{\tau}^z_{++}(\phi_{\mathbf{k}'},\phi_{\mathbf{k}})|^2 \\ &= \frac{2\pi}{\hbar}\left(J\,M\right)^2\sin\left(\frac{\phi_{\mathbf{k}}-\phi_{\mathbf{k}'}}{2}\right)^2 \\ &= \frac{\pi}{2\hbar}J^2\sin\left(\frac{\phi_{\mathbf{k}}-\phi_{\mathbf{k}'}}{2}\right)^2 \end{aligned} \tag{3.10}$$

which is the only diagram for $S=\frac{1}{2}, M=\pm\frac{1}{2}$, when the initial state of the conduction electron is the + helicity cone, and the impurity spin is not allowed to flip. From Eqn. (3.10) the scattering angle $\phi_{\mathbf{q}} = \phi_{\mathbf{k}} - \phi_{\mathbf{k}'}$ in forward direction $\phi_{\mathbf{k}} = \phi_{\mathbf{k}'}$ has zero matrix element, but backward scattering $\phi_{\mathbf{k}} = \pi + \phi_{\mathbf{k}'}$ has maximum matrix element squared. The angle dependence of the 'non spin-flip' transitions $w^{sc}_{+,\mathbf{k}\to+,\mathbf{k}'}$ and $w^{qm}_{M;+,\mathbf{k}\to M;+,\mathbf{k}'}$ is plotted in figure 3.1. One easily concludes, that the common heuristic argument presented above, does not explain the quantum spin-flip scattering case Eqn. (3.10).

To resolve this misconception the calculation Eqn. (3.10) will be carried out again, but twice. First Eqn. (3.10) will explicitly be written as its column eigenvector $|\mathbf{k},+\rangle = \begin{pmatrix}1\\0\end{pmatrix}$ which yields

$$\begin{aligned}
|\langle M;+,\mathbf{k}^{'}|\tilde{V}^{qm}(\phi_{\mathbf{k}^{'}},\phi_{\mathbf{k}})|\mathbf{k},+;M\rangle|^2 &= |-J\langle M|S^z|M\rangle\langle+,\mathbf{k}^{'}|\tilde{\tau}^z(\phi_{\mathbf{k}^{'}},\phi_{\mathbf{k}})|\mathbf{k},+\rangle|^2 \\
&= \left|(-J\,M)^2\begin{pmatrix}1 & 0\end{pmatrix}\begin{pmatrix}\tilde{\tau}^z(\phi_{\mathbf{k}^{'}},\phi_{\mathbf{k}})_{++} & \tilde{\tau}^z(\phi_{\mathbf{k}^{'}},\phi_{\mathbf{k}})_{+-}\\ \tilde{\tau}^z(\phi_{\mathbf{k}^{'}},\phi_{\mathbf{k}})_{-+} & \tilde{\tau}^z(\phi_{\mathbf{k}^{'}},\phi_{\mathbf{k}})_{--}\end{pmatrix}\begin{pmatrix}1\\0\end{pmatrix}\right|^2 \\
&= (-J\,M)^2\left|\tilde{\tau}^z(\phi_{\mathbf{k}^{'}},\phi_{\mathbf{k}})_{++}\right|^2 \\
&= (J\,M)^2\sin^2\left(\frac{\phi_{\mathbf{k}}-\phi_{\mathbf{k}^{'}}}{2}\right) \\
&= \frac{J^2}{4}\sin^2\left(\frac{\phi_{\mathbf{k}}-\phi_{\mathbf{k}^{'}}}{2}\right) \qquad (3.11)
\end{aligned}$$

The second way will use the fact, that instead of the Hamiltonian expressed in η space as Eqn. (3.6), it could just as well have been written in σ space as

$$H = \sum_{\substack{\mathbf{k},\mathbf{k}^{'}\\ \sigma,\sigma^{'}}} V^{qm}_{\sigma^{'}\sigma}(\phi_{\mathbf{k}^{'}},\phi_{\mathbf{k}})c^{\dagger}_{\mathbf{k}^{'}\sigma^{'}}c_{\mathbf{k}\sigma} \quad , \quad V^{qm}(\phi_{\mathbf{k}^{'}},\phi_{\mathbf{k}}) = -J\bar{\tau}\cdot\bar{S} \qquad (3.12)$$

and

$$|\mathbf{k},+\rangle = \frac{1}{\sqrt{2}}\begin{pmatrix}1\\0\end{pmatrix} - \frac{ie^{-i\phi_{\mathbf{k}}}}{\sqrt{2}}\begin{pmatrix}0\\1\end{pmatrix}$$

is a superposition of eigenstates of the s^z operator in σ space. Now it is more clear how the 'non-flip' operator acts on the helical metal, since the same calculation yields

$$\begin{aligned}
|\langle M;+,\mathbf{k}^{'}|V^{qm-imp.}(\phi_{\mathbf{k}^{'}},\phi_{\mathbf{k}})|\mathbf{k},+;M\rangle|^2 &= |-J\langle M|S^z|M\rangle\langle+,\mathbf{k}^{'}|\tau^z|\mathbf{k},+\rangle|^2 \\
&= (-J\,M)^2\left|\frac{1}{\sqrt{2}}\begin{pmatrix}1 & i\,e^{i\phi_{\mathbf{k}^{'}}}\end{pmatrix}\begin{pmatrix}1 & 0\\ 0 & -1\end{pmatrix}\frac{1}{\sqrt{2}}\begin{pmatrix}1\\ i\,e^{-i\phi_{\mathbf{k}}}\end{pmatrix}\right|^2 \\
&= (J\,M)^2\sin^2\left(\frac{\phi_{\mathbf{k}}-\phi_{\mathbf{k}^{'}}}{2}\right) \\
&= \frac{J^2}{4}\sin^2\left(\frac{\phi_{\mathbf{k}}-\phi_{\mathbf{k}^{'}}}{2}\right) \qquad (3.13)
\end{aligned}$$

To see what has happened, let the state initially, for instance, be $\phi_{\mathbf{k}} = 0$ so $\mathbf{k} = k_x$ and the state is $|\mathbf{k}_x,+\rangle = \frac{1}{\sqrt{2}}(|k_x,\uparrow\rangle - i|k_x,\downarrow\rangle) \equiv |k_x,\downarrow_y\rangle$ which is an eigenstate of the τ^y operator, because $\tau^y|k_x,+\rangle = -|k_x,+\rangle$. But the 'non-flip' operator τ^z acts on this state as
$\tau^z|k_x,+\rangle = \tau^z|k_x,\downarrow_y\rangle = |k_x,\uparrow_y\rangle$, i.e. actually as a *spin-flip* operator on the state $|k_x,+\rangle$.

This is actually not that surprising since the quantization of the helical metal is in the x,y plane and not the z axis as usual. The important lesson is that the η-helicity index is a superposition of physical spin, σ, states thus the the state ket is
$|\mathbf{k},+\rangle = \sum_\sigma U^{\dagger}(\phi_{\mathbf{k}})_{+\sigma}|\mathbf{k},\sigma\rangle = \frac{1}{\sqrt{2}}(|\mathbf{k},\uparrow\rangle - ie^{-i\phi_{\mathbf{k}}}|\mathbf{k},\downarrow\rangle)$. In the σ-basis the electron spin operator s^z does *not* flip the spin of a electron in its eigenstate $|\mathbf{k},\sigma\rangle$, whereas s^x and s^y do. But a state $|\mathbf{k},+\rangle$ that is a superposition of $|\mathbf{k},\sigma\rangle$ states feels s^z as flipping according to
$s^z|\mathbf{k},+\rangle = \frac{1}{\sqrt{2}}(|\mathbf{k},\uparrow\rangle + ie^{-i\phi_{\mathbf{k}}}|\mathbf{k},\downarrow\rangle)$ the phases of its superpositioned states which cause the ket

$s^z|\mathbf{k}\rangle$ and bra $\langle +,\mathbf{k}|$ to be orthogonal and hence $\langle +,\mathbf{k}|s^z|\mathbf{k},+\rangle = 0$. Further note that neither s^i, $i = x,y,z$ flip the helicity of the $|\mathbf{k},+\rangle$ state. All this explain $\langle M;+,\mathbf{k}|S^z s^z|\mathbf{k},+,M\rangle = \underbrace{\langle M|S^z|M\rangle}_{\neq 0}\underbrace{\langle +,\mathbf{k}|s^z|\mathbf{k},+\rangle}_{0} = 0$ which say that forward scattering of the state $|\mathbf{k},+\rangle$ is not allowed.

The 'impurity spin-flip' matrix element squared

$$\begin{aligned} w^{qm}_{M;+,\mathbf{k}\to 1+M;+,\mathbf{k}'} &= \frac{2\pi}{\hbar}|\langle 1+M;+,\mathbf{k}'|\tilde{V}(\phi_{\mathbf{k}'},\phi_{\mathbf{k}})|\mathbf{k},+;M\rangle|^2 \\ &= \frac{2\pi}{\hbar}|-J\langle 1+M|S^+|M\rangle|\tilde{\tau}^+_{++}(\phi_{\mathbf{k}'},\phi_{\mathbf{k}})|^2 \\ &= \frac{2\pi}{\hbar}|-J\langle 1+M|S^+|M\rangle|^2 \\ &= \frac{2\pi}{\hbar}\frac{(-J)^2}{4} = \frac{\pi}{2\hbar}J^2 \end{aligned} \tag{3.14}$$

is the only diagram for $S = \frac{1}{2}, M = -\frac{1}{2}$, when the initial state of the conduction electron is the $+$ helicity cone, and the impurity spin is allowed to flip from $M = -\frac{1}{2}$ to $1+M = \frac{1}{2}$. Also the relation $\langle j',m'|J^{\pm}|j,m\rangle = \sqrt{(j\mp m)(j\pm m+1)}\delta_{j',j}\delta_{m',m+1}$ was used. From Eqn. (3.14) the matrix element squared $w^{qm}_{1+M;+,\mathbf{k}\to M;+,\mathbf{k}'}$ is independent of any angle.

Note that the matrix element squared Eqn. (3.10) is highly dependent on the scattering angle. This is in contrast to the case of scattering off the qm-impurity on both the conventional metal and conventional Dirac metal, which are independent of any angle. If one write down a table of the conventional metal analog to the table 3.1 of the helical metal. Then *all* the entries would be a constant independent of angles and therefore the matrix elements would also be independent of angles. In Eqn. (3.8) the 1^{st} Born approximation has *no* reference to the dispersion relation of the relevant surface nor the Fermi-Dirac distribution. So only the spin-texture of the surface in question is involved in the 1^{st} Born approximation. This is the reason why both the conventional metal and the conventional Dirac metal would give the same 1^{st} Born approximation matrix elements, since they share the same double spin-degeneracy. In the 2^{nd} Born approximation the energy dispersion and the filling (due to the Fermi-Dirac distribution) of the Fermi surface becomes relevant, so this approximation would not necessarily give the same result as for the helical metal.

However, the matrix element Eqn. (3.14) is also independent of angles like the case of a conventional metal, but the mechanism for this is of a entirely different nature. This is because the impurity spin-flip S^+ cause the electron in state $|\mathbf{k},+\rangle$ with spin in the x,y-plane to align its spin along the impurity spin z-direction by the act of $\tau^+|\mathbf{k},+\rangle = |\uparrow_z\rangle i\,e^{-i\phi_{\mathbf{k}}}$. The projection of this on the x,y-plane $\langle +\mathbf{k}|\uparrow_z\rangle i\,e^{-i\phi_{\mathbf{k}}} = i\,e^{-i\phi_{\mathbf{k}}}$ is identical up to a phase-factor $i\,e^{-i\phi_{\mathbf{k}}}$. Because the modulus square of a phase factor is a constant, then $|\langle +\mathbf{k}|\tau^+|\mathbf{k},+\rangle|^2$ is a constant independent of angles.

3.1.3 The inverse lifetime of an electron state

An electron state $|\mathbf{k},+\rangle$ can scatter out of its state to another $|\mathbf{k}',+\rangle$. The possible ways this can be done for a qm-impurity initially with $S = \frac{1}{2}$ and $M = -\frac{1}{2}$ was calculated to be $w^{qm}_{M;+,\mathbf{k}\to M;+,\mathbf{k}'}$ and $w^{qm}_{M;+,\mathbf{k}\to 1+M;+,\mathbf{k}'}$ i.e. the impurity spin not flipped and flipped, respectively. Summing over these possibilities gives the *inverse lifetime* $\frac{1}{\tau^{qm}_{\mathbf{k}+}}$ of the state $|\mathbf{k},+\rangle$. This summation corresponds to not knowing about the impurity spin polarization, since it is summed over, and hence it gives the rate the electron is scattered out of state $|\mathbf{k},+\rangle$, the in inverse of which, gives the lifetime of

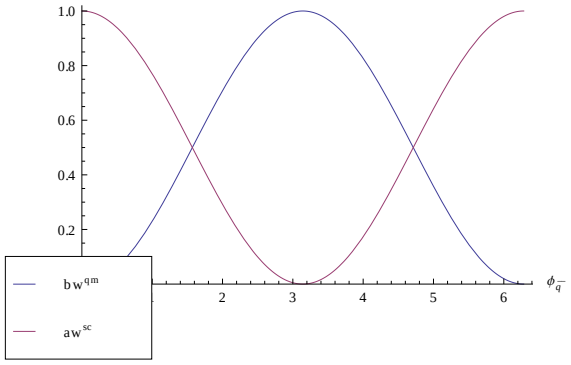

Figure 3.1: 1^{st} Born approximation matrix elements: $aw^{sc}_{+,\mathbf{k}\to+,\mathbf{k}'}$ for the scalar (purple line) with $a = \frac{4\hbar}{2\pi V_0^2}$ and $bw^{qm}_{M;+,\mathbf{k}\to M;+,\mathbf{k}'}$ quantum impurity matrix element (blue line) with $b = \frac{2\hbar}{\pi J^2}$ is plotted as a function of scattering angle $\phi_{\mathbf{q}} = \phi_{\mathbf{k}} - \phi_{\mathbf{k}'}$.

that state. Hence the inverse lifetime

$$\begin{aligned}
\frac{1}{\tau_{\mathbf{k}+}} &= \sum_{\mathbf{k}',\eta'} w^{qm}_{\mathbf{k},+\to\mathbf{k}',\eta'} = \sum_{\mathbf{k}',\eta'} \sum_{M,M'=\frac{1}{2},-\frac{1}{2}} w^{qm}_{M;\mathbf{k},+\to M';\mathbf{k}',\eta'} \\
&= \frac{2\pi}{\hbar} \sum_{\mathbf{k}',\eta'} \sum_{\substack{i=1,2,3 \\ M,M'=\frac{1}{2},-\frac{1}{2}}} \Big| -J\langle M';\mathbf{k}',\eta'|S^i\tilde{\tau}^i|M;\mathbf{k},+\rangle\Big|^2 \delta(\epsilon_{\eta'}(k') - \epsilon_+(k)) \\
&= \frac{2\pi}{\hbar} \sum_{\mathbf{k}',\eta'} \sum_{\substack{i=1,2,3 \\ M,M'=\frac{1}{2},-\frac{1}{2}}} \Big| -J\langle M'|S^i|M\rangle\langle \mathbf{k}'\eta'|\tilde{\tau}^i|\mathbf{k},+\rangle\Big|^2 \delta(\epsilon_{\eta'}(k') - \epsilon_+(k)) \\
&= \frac{2\pi}{\hbar} J^2 \sum_{\mathbf{k}',\eta'} \sum_{\substack{j,i=1,2,3 \\ M,M'=\frac{1}{2},-\frac{1}{2}}} \langle M|S^j|M'\rangle\langle M'|S^i|M\rangle\langle \mathbf{k}+|\tilde{\tau}^j|\mathbf{k}',\eta'\rangle\langle \mathbf{k}'\eta'|\tilde{\tau}^i|\mathbf{k},+\rangle \delta(\epsilon_{\eta'}(k') - \epsilon_+(k)) \\
&= \frac{2\pi}{\hbar} J^2 \sum_{\mathbf{k}',\eta'} \sum_{\substack{j,i=1,2,3 \\ M,M'=\frac{1}{2},-\frac{1}{2}}} \frac{\delta_{i,j}}{4} \tilde{\tau}^j(\phi_{\mathbf{k}},\phi_{\mathbf{k}'})_{+,\eta'} \tilde{\tau}^i(\phi_{\mathbf{k}'},\phi_{\mathbf{k}})_{\eta',+} \delta(\epsilon_{\eta'}(k') - \epsilon_+(k)) \\
&= \frac{2\pi}{\hbar} J^2 \sum_{\mathbf{k}',\eta'} \sum_{i=1,2,3} \frac{1}{4} \Big|\tilde{\tau}^i(\phi_{\mathbf{k}'},\phi_{\mathbf{k}})_{\eta',+}\Big|^2 \delta(\epsilon_{\eta'}(k') - \epsilon_+(k))
\end{aligned} \tag{3.15}$$

is the inverse lifetime of an electron in state $|\mathbf{k},+\rangle$. At the fifth equality sign above, the relation Eqn. (3.16) was used

$$\langle S^i S^j\rangle = \frac{Tr\big[\rho S^i S^j\big]}{Z} = \frac{1}{4}\frac{Tr\big[\rho\tau^i\tau^j\big]}{Z} = \frac{1}{4}\frac{Tr\big[\delta_{ij}\big]}{Z} = \frac{1}{4}\frac{2\delta_{ij}}{2} = \frac{\delta_{ij}}{4} \tag{3.16}$$

since the density operator is

$$\rho = \begin{pmatrix} e^{-\beta\epsilon_{\Uparrow}} & 0 \\ 0 & e^{-\beta\epsilon_{\Downarrow}} \end{pmatrix} = \tau^0$$

an identity operator due to the fact that the energy of the impurity spin configurations are identical $\epsilon_{\Downarrow} = \epsilon_{\Uparrow} \equiv 0$ and defined to be zero as reference energy. Hence the partition function $Z = Tr[\rho] = 2$

for a spin-half impurity.

Chapter 4

The T-matrix method

It was previously found, that both the electron spin and impurity spin can flip. The calculation was purely based on theoretical calculations of the first order matrix elements squared from Fermi's Golden rule. But can such spin flips possibly be detected in any experiments?
Since the helical metal, as it name suggests, is a metal, current flow across the surface. One obvious experimental probe would of course be transport measurements. But unfortunately the state-of-the-art transport experiments cannot reliably separate the bulk and surface carriers. Hence no reliable transport measurements have been published yet.

Therefore this experimental probe will not be considered any further in this thesis, except in section 4.1. Here the transport time of an surface electron, on the surface of a conventional and a helical metal, contaminated with a single potential or a quantum impurity, will be calculated. The different results of this physical measurable quantity, are direct manifestations by the impurities on different Fermi surfaces. Since the different Fermi surfaces have different spin-textures, the impurities allow different scattering vectors, which will reflect the previous calculated square matrix elements.

STM which is a local probe is the choice for experimental investigation that will be considered in this theses in section 5 and 6. As will be show later, the STM response signal is directly related to the surface electronic Green function. So in order to determine the Green function of the surface electrons, the T-matrix induced by the relevant impurities have to be derived. This T-matrix is the primary aim of the forthcoming section 4.

The T-matrix for multiple scatterings on a single local $\delta(\mathbf{r})$ impurity is determined by solving

$$T_{\mathbf{k}\mathbf{k}'} = \Sigma_{\mathbf{k}\mathbf{k}'} + \Sigma_{\mathbf{k}\mathbf{k}_1} G^0_{\mathbf{k}_1\mathbf{k}_2} T_{\mathbf{k}_2\mathbf{k}'} \tag{4.1}$$

with $\Sigma_{\mathbf{k}\mathbf{k}'}$ being the irreducible impurity induced self-energy and repeated indices is implicit summed over.

The retarded T-matrix (superscript R will be suppressed in all relevant quantities) derived in appendix D for the scalar and classical magnetic impurity follow immediately ref[9, 22], since the first order self-energy $\Sigma^{(1),imp} = V^{imp}$ is the only irreducible one. Hence

$$\tilde{T}^{sc}_{\mathbf{k}'\mathbf{k}}(\tilde{\omega}, V_0) = \frac{V_0}{1 + V_0 g(\tilde{\omega})} U^\dagger(\phi_{\mathbf{k}'}) U(\phi_{\mathbf{k}}) \tag{4.2}$$

and

$$\tilde{T}^{cl}_{\mathbf{k}'\mathbf{k}}(\tilde{\omega}, S) = U^{\dagger}(\phi_{\mathbf{k}'})\frac{\bar{S}\cdot\bar{\tau} - g(\tilde{\omega})|S|^2}{1 - g(\tilde{\omega})^2|S|^2}U(\phi_{\mathbf{k}}) \tag{4.3}$$

As will be shown in section 5, STM directly probe the local density of states (LDOS) which is solely determined by the T-matrix of the conduction electrons. Therefore STM is a direct (indirectly though the FT-LDOS i.e. Fourier transformed LDOS) probe of the electrons scattering off the impurity.

It is exactly this dynamical information of the impurity, that is the interest in this thesis, so the ordinary Kondo physics will be left out[1]. Hence the energy and momentum dependence of the T-matrix is the primary goal to obtain in section 4.1 and the 2^{nd} order in the coupling J i.e. 2^{nd} order in the T-matrix will suffice. Further in section 4.2, the 3^{rd} order T-matrix will be derived, because this will reveal whether the Kondo problem arise on the helical surface or not. When this is the case the STM signal will be enhanced, which might pave the way to possibly detect the presence of a quantum impurity on the helical surface. The relevant information for this, is solely contained in the imaginary part of the self-energy. Therefore a scrutiny of this part will be given, but the real part of the self-energy will be left, in A.3.5, without any comments except a consistency check of the symmetries it is required to obey, in appendix A.3.4.

To my knowledge, no literature treating the Kondo problem with the perturbative method on the helical surface has been published yet. This will be derived here.

4.1 Quantum impurity induced 2^{nd} order self-energy

The strategy[17] is to expand the full Green function[2] $\tilde{G}(\mathbf{k}\eta\tau;\mathbf{k}'\eta'\tau') =< T_\tau[\Psi_{\eta\mathbf{k}}(\tau)\Psi^{\dagger}_{\eta'\mathbf{k}'}(\tau')] >$ in powers of the exchange coupling Eqn. (3.6) where $\Psi^{\dagger}(\mathbf{k}) = \psi^{\dagger}(\mathbf{k})\hat{U}(\mathbf{k})$ is the eigenvector in η-basis and $\psi(\mathbf{k}) = \{c_{\mathbf{k}\uparrow}, c_{\mathbf{k}\downarrow}\}$ in the σ-basis. Both external and internal states are labled identical, with the convention that an incoming state is primed, whereas an outgoing state is unprimed. Thus the full Green function is given by the formal expression

$$\begin{aligned}
&\tilde{G}(\mathbf{k}\eta\tau;\mathbf{k}'\eta'\tau') \\
&= \sum_{n=0}^{\infty}\sum_{\mathbf{k}_1\cdots\mathbf{k}_n}\sum_{\mathbf{k}'_1\cdots\mathbf{k}'_n}\sum_{\eta_1\cdots\eta_n}\sum_{\eta'_1\cdots\eta'_n}\sum_{i_1\cdots i_n}\int_0^\beta \mathrm{d}\tau_1\cdots\int_0^\beta \mathrm{d}\tau_n(-J)^n \ < T_\tau[S_d^{i_1}(\tau_1)\ldots S_d^{i_n}(\tau_n)] > \\
&\times < T_\tau[\Psi^{\dagger}_{\eta_1}(\mathbf{k}_1)\tilde{\tau}^{i_1}_{\eta_1\eta'_1}(\mathbf{k}_1,\mathbf{k}'_1)\Psi_{\eta'_1}(\mathbf{k}'_1)\ldots\Psi^{\dagger}_{\eta_n}(\mathbf{k}_n)\tilde{\tau}^{i_n}_{\eta_n\eta'_n}(\mathbf{k}_n,\mathbf{k}'_n)\Psi_{\eta'_n}(\mathbf{k}'_n)\times\Psi_{\eta}(\mathbf{k})\Psi^{\dagger}_{\eta'}(\mathbf{k}')] >_{0,cdd}
\end{aligned}$$

In figure 4.1 the diagrams up to and including 3^{rd} order is illustrated. The zeroth order term ($n = 0$) is the bare Green function. The first order in the coupling J ($n = 1$) vanish, because it is the average of the impurity spin $< T_\tau[S^i_d] >=< S^i_d >= 0$ and due to the same reason all diagrams containing a fermion loop also vanish. In second order such a diagram with a Fermi loop exist, and 2 of these diagrams are shown in the third order diagrams. Hence the second order contribution

[1] For example the physics of Kondo screening and spin-spin correlations have been published in ref[41, 14, 15, 39]. But still, the Kondo problem has not been investigated much on the surface of a STI. Rather the attention have been directed towards the WTI graphene.

[2] Note that that any Green function is denoted $C(\nu;\nu') =< T_\tau[A(\nu)B(\nu')] >$ for any incoming quantum number ν' and outgoing ν

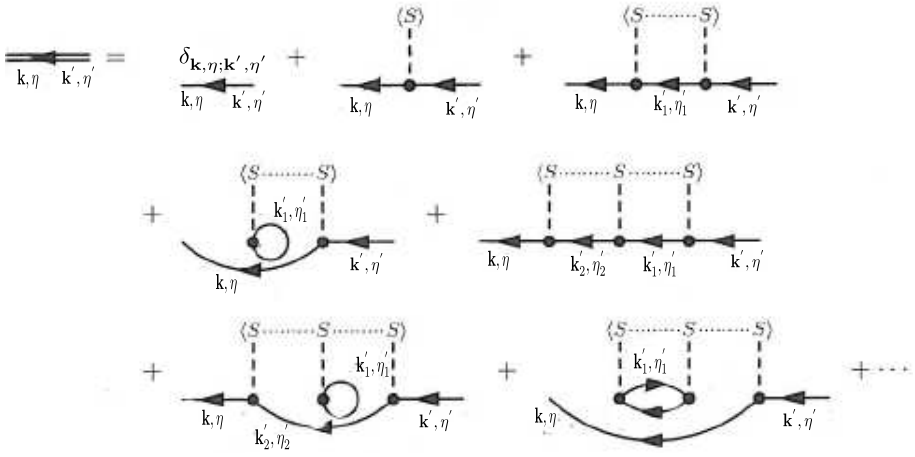

Figure 4.1: The expansion including zeroth, 1^{st} ,2^{nd} and some of the 3^{rd} order contributions. Modified[17]

to the full Green function is formally

$$\begin{aligned}
&\tilde{G}^{(2)}(\mathbf{k}\eta,\mathbf{k}^{'}\eta^{'};\tau-\tau^{'}) \\
&= \sum_{\mathbf{k}_1\mathbf{k}_2}\sum_{\mathbf{k}_1^{'}\mathbf{k}_2^{'}}\sum_{\eta_1\eta_2}\sum_{\eta_1^{'}\eta_2^{'}}\sum_{i,k=1}^{3}\int_0^\beta \mathrm{d}\tau_1\int_0^\beta \mathrm{d}\tau_2\times(-J)^2 \;< T_\tau[S_d^i(\tau_1)S_d^k(\tau_2)] > \\
&\times < T_\tau[\Psi^\dagger_{\eta_1}(\mathbf{k}_1)\tilde{\tau}^i_{\eta_1\eta_1^{'}}(\mathbf{k}_1,\mathbf{k}_1^{'})\Psi_{\eta_1^{'}}(\mathbf{k}_1^{'})\,\Psi^\dagger_{\eta_2}(\mathbf{k}_2)\tilde{\tau}^k_{\eta_1\eta_2^{'}}(\mathbf{k}_2,\mathbf{k}_2^{'})\Psi_{\eta_2^{'}}(\mathbf{k}_2^{'})\times\Psi_\eta(\mathbf{k})\Psi^\dagger_{\eta^{'}}(\mathbf{k}^{'})] >_{0,cdd}
\end{aligned}$$

which only include a single diagram. It will be used that the bare Green function is diagonal in both momentum space $\mathbf{k}$ and η quantum number and also depends only on the time-difference and momentum magnitude, i.e. the bare Green function has the form
$\tilde{G}^0(k_1\eta_1;k_2\eta_2;\tau_1,\tau_2)=\tilde{G}^0(k_1\eta_1,k_2\eta_2;\tau_1-\tau_2)=\tilde{G}^0_{\eta_1\eta_2}(k_1;\tau_1-\tau_2),\ s=\tau_1-\tau_2$. Therefore the irreducible self-energy to second order is

$$\begin{aligned}
\tilde{\Sigma}^{(2)}(\mathbf{k}\eta,\mathbf{k}^{'}\eta^{'};\tau_1-\tau_2) &= \sum_{\mathbf{k}_1}\sum_{\eta_1\eta_2}\sum_{ik}(-J)^2\underbrace{< T_\tau[S_d^i(\tau_1)S_d^k(\tau_2)] >}_{\frac{\delta_{ki}}{4}}\times\tilde{\tau}^i_{\eta\eta_1}(\phi_{\mathbf{k}},\phi_{\mathbf{k}_1})\tilde{G}^0_{\eta_1\eta_2}(k_1;s)\tilde{\tau}^k_{\eta_2\eta^{'}}(\phi_{\mathbf{k}_1},\phi_{\mathbf{k}^{'}}) \\
&= \frac{(-J)^2}{4}\sum_{\mathbf{k}_1}\sum_{\eta_1\eta_2}\sum_{i,k=0}^{3}\delta_{ki}\tilde{\tau}^i_{\eta\eta_1}(\phi_{\mathbf{k}},\phi_{\mathbf{k}_1})\tilde{G}^0_{\eta_1\eta_2}(k_1;s)\tilde{\tau}^k_{\eta_2\eta^{'}}(\phi_{\mathbf{k}_1},\phi_{\mathbf{k}^{'}}) \\
&= \frac{(-J)^2}{4}\sum_{\mathbf{k}_1}\sum_{\eta_1\eta_2}\sum_{i=0}^{3}\tilde{\tau}^i_{\eta\eta_1}(\phi_{\mathbf{k}},\phi_{\mathbf{k}_1})\tilde{G}^0_{\eta_1\eta_2}(k_1;s)\tilde{\tau}^i_{\eta_2\eta^{'}}(\phi_{\mathbf{k}_1},\phi_{\mathbf{k}^{'}})
\end{aligned}$$

where the time-difference is $s=\tau_1-\tau_2$ and Eqn. (3.16) was used in the first equality sign. The only term dependent on time is the bare Green function. Since it is only on time-difference, a single Matsubare frequency will appear, and thus the 2^{nd} order self-energy in Matsubare frequency

is

$$\begin{aligned}
\tilde{\Sigma}^{(2)}(\mathbf{k}\eta,\mathbf{k}'\eta';i\omega_n) &= \int_0^\beta \mathrm{d}s\, e^{i\omega_n s}\,\tilde{\Sigma}^{(2)}(\mathbf{k}\eta,\mathbf{k}'\eta';s)\\
&= \frac{(-J)^2}{4}\sum_{\mathbf{k}_1}\sum_{\eta_1\eta_2}\sum_{i=1}^{3}\tilde{\tau}^i_{\eta\eta_1}(\phi_{\mathbf{k}},\phi_{\mathbf{k}_1})\tilde{G}^0_{\eta_1\eta_2}(k_1;i\,\tilde{\omega}_n)\tilde{\tau}^i_{\eta_2\eta'}(\phi_{\mathbf{k}_1},\phi_{\mathbf{k}'})\\
&= \frac{(-J)^2}{4}\sum_{\eta_1\eta_2}\sum_{\sigma\sigma'}\sum_{i=1}^{3}\left(U^\dagger(\phi_{\mathbf{k}})\tau^i\right)_{\eta\sigma}\sum_{\mathbf{k}_1}\left(U(\phi_{\mathbf{k}_1})\tilde{G}^0(k_1;i\,\tilde{\omega}_n)U^\dagger(\phi_{\mathbf{k}_1})\right)_{\sigma\sigma'}\left(\tau^i U(\phi_{\mathbf{k}'})\right)_{\sigma'\eta'}\\
&= (-g(i\,\tilde{\omega}_n))\frac{(-J)^2}{4}\sum_{\sigma\sigma'}\sum_{i=1}^{3}\left(U^\dagger(\phi_{\mathbf{k}})\tau^i\right)_{\eta\sigma}\delta_{\sigma\sigma'}\left(\tau^i U(\phi_{\mathbf{k}'})\right)_{\sigma'\eta'}\\
&= (-g(i\,\tilde{\omega}_n))\frac{(-J)^2}{4}\sum_{i=1}^{3}\left(U^\dagger(\phi_{\mathbf{k}})\tau^i\tau^i U(\phi_{\mathbf{k}'})\right)_{\eta\eta'}\\
&= -g(i\,\tilde{\omega}_n)J^2\frac{3}{4}\left(U^\dagger(\phi_{\mathbf{k}})U(\phi_{\mathbf{k}'})\right)_{\eta\eta'}
\end{aligned}$$

where it was used that

$$\begin{aligned}
-g(i\,\tilde{\omega}_n)\tau^0 &= \sum_{\mathbf{k}_1}U(\mathbf{k}_1)\tilde{G}^0(k_1;i\,\tilde{\omega}_n)U^\dagger(\mathbf{k}_1) = \int_0^{\mathrm{D}}\frac{\mathrm{d}k_1}{2\pi}\,k_1\left(\int_0^{2\pi}\frac{\mathrm{d}\phi_{k_1}}{2\pi}U(\mathbf{k}_1)\tilde{G}^0(k_1;i\,\tilde{\omega}_n)U^\dagger(\mathbf{k}_1)\right)\\
&= \int_0^{\mathrm{D}}\frac{\mathrm{d}k_1}{2\pi}\,k_1\frac{1}{2}\mathrm{Tr}[\tilde{G}^0(k_1;i\tilde{\omega}_n)]\tau^0 \qquad (4.4)
\end{aligned}$$

and $\frac{1}{2}\mathrm{Tr}[\tilde{G}^0(\mathbf{k}_1;i\tilde{\omega}_n)] = \frac{i\,\tilde{\omega}_n}{(i\,\tilde{\omega}_n)^2-k_1^2}$ will be left unintegrated for a moment.

The self-energy in real frequency space is the analytic continuation of the Matsubara frequency dependent self-energy, thus *the retarded irreducible self-energy to* 2^{nd} *order*

$$\tilde{\Sigma}^{(2)}(\mathbf{k}\eta,\mathbf{k}'\eta';\tilde{\omega}) = \tilde{\Sigma}^{(2)}(\mathbf{k}\eta,\mathbf{k}'\eta';i\tilde{\omega}_n\to\tilde{\omega}+i\,0^+) = -g(\tilde{\omega})J^2\frac{3}{4}\left(U^\dagger(\phi_{\mathbf{k}})U(\phi_{\mathbf{k}'})\right)_{\eta\eta'} \qquad (4.5)$$

with the notation $g(\tilde{\omega})$ used in ref[9], which is the retarded and integrated function Eqn. (4.4)

$$\begin{aligned}
-g(\tilde{\omega}) &\equiv -g(i\tilde{\omega}\to\tilde{\omega}+i\,0^+)\\
&= \int_0^{\mathrm{D}}\frac{\mathrm{d}k_1}{2\pi}\,k_1\,\frac{1}{2}\mathrm{Tr}[\tilde{G}^0(\mathbf{k}_1;i\tilde{\omega}_n\to\omega+i\,0^+)]\\
&= \int_0^{\mathrm{D}}\frac{\mathrm{d}k_1}{2\pi}\,k_1\,\frac{\omega+i\,0^+}{(\omega+i\,0^+)^2-k_1^2}\\
&= \frac{-\tilde{\omega}}{4\pi}\left(\ln(\frac{\mathrm{D}^2-\tilde{\omega}^2}{\tilde{\omega}^2})\Theta(\mathrm{D}-|\tilde{\omega}|)+\ln(\frac{\tilde{\omega}^2-\mathrm{D}^2}{\tilde{\omega}^2})\Theta(|\tilde{\omega}|-\mathrm{D})\right)\\
&\quad -\frac{i\,|\tilde{\omega}|}{4}\Theta(\mathrm{D}-|\tilde{\omega}|)\\
&= -\left(\frac{\tilde{\omega}}{4\pi}\ln\left|\frac{\mathrm{D}^2}{\tilde{\omega}^2}-1\right|+\frac{i\,|\tilde{\omega}|}{4}\right)\Theta(\mathrm{D}-|\tilde{\omega}|) \qquad (4.6)
\end{aligned}$$

The remarkable simple expression Eqn. (4.5) can be used to analytically calculate the T-matrix

in η-basis to 2^{nd} order in the coupling strength J, by noting that

$$\int_0^{\mathrm{D}} \frac{\mathrm{d}k}{2\pi}\, k \int_0^{2\pi} \frac{\mathrm{d}\phi_{\mathbf{k}}}{2\pi}\, U^\dagger(\phi_{\mathbf{k}}) \tilde{G}^0(k; i\tilde{\omega}_n \to \tilde{\omega} + i\,0^+) U(\phi_{\mathbf{k}}) = -g(\tilde{\omega})\tau^0 \tag{4.7}$$

as just described by Eqn. (4.4) and (4.6).
The Einstein summation convention is implicit used when repeated internal indices appear and each internal momentum-variable sum are carried out as just mentioned.

$$\begin{aligned}
\tilde{\mathrm{T}}^{(2)}_{\mathbf{k}'\mathbf{k}}(\tilde{\omega}) &= \tilde{\Sigma}^{(2)}_{\mathbf{k}'\mathbf{k}}(\tilde{\omega}) + \tilde{\Sigma}^{(2)}_{\mathbf{k}'\mathbf{k}_1}(\tilde{\omega})\, \tilde{G}^0_{\mathbf{k}_1}(\tilde{\omega})\, \tilde{\Sigma}^{(2)}_{\mathbf{k}_1\mathbf{k}}(\tilde{\omega}) + \tilde{\Sigma}^{(2)}_{\mathbf{k}'\mathbf{k}_1}(\tilde{\omega})\, \tilde{G}^0_{\mathbf{k}_1}(\tilde{\omega})\, \tilde{\Sigma}^{(2)}_{\mathbf{k}_1\mathbf{k}_2}(\tilde{\omega})\, \tilde{G}^0_{\mathbf{k}_2}(\tilde{\omega})\, \tilde{\Sigma}^{(2)}_{\mathbf{k}_2\mathbf{k}}(\tilde{\omega}) + \cdots \\
&= -g(\tilde{\omega}) J^2 \frac{3}{4} U^\dagger(\phi_{\mathbf{k}'}) U(\phi_{\mathbf{k}}) + \left(-g(\tilde{\omega}) J^2 \frac{3}{4}\right)^2 U^\dagger(\phi_{\mathbf{k}'}) \underbrace{\left(U(\phi_{\mathbf{k}_1}) \tilde{G}^{0,R}_{k_1} U^\dagger(\phi_{\mathbf{k}_1})\right)}_{=-g(\tilde{\omega})\tau^0} U(\phi_{\mathbf{k}}) + \cdots \\
&= -g(\tilde{\omega}) J^2 \frac{3}{4} U^\dagger(\phi_{\mathbf{k}'}) U(\phi_{\mathbf{k}}) \left(1 + \frac{3}{4}\left((-g(\tilde{\omega}))^2 J^2\right) + (\frac{3}{4})^2 \left((-g(\tilde{\omega}))^2 J^2\right)^2 + \cdots\right) \\
&= -g(\tilde{\omega}) J^2 \frac{3/4}{1 - \frac{3}{4} g(\tilde{\omega})^2\, J^2}\, U^\dagger(\phi_{\mathbf{k}'}) U(\phi_{\mathbf{k}})
\end{aligned} \tag{4.8}$$

To summarize the results with real physical units; the retarded 2^{nd} order irreducible self-energy[3]

$$\tilde{\Sigma}^{(2)}(\mathbf{k}', \mathbf{k}; \tilde{\omega}) = -\frac{3}{4} g(\tilde{\omega})\, J^2\, U^\dagger(\phi_{\mathbf{k}'}) U(\phi_{\mathbf{k}}) \tag{4.9}$$

$$\Sigma^{(2)}(\mathbf{k}, \mathbf{k}'; \tilde{\omega}) = -\frac{3}{4} g(\tilde{\omega})\, J^2\, \tau^0 \tag{4.10}$$

where τ^0 is the identity matrix. $\tilde{\Sigma}^{(2)}$ is in unit of energy due to the g-function Eqn. (4.13) which has unit of inverse energy and the coupling J with unit energy. The retarded T-matrix[4] to 2^{nd} order is

$$\tilde{\mathrm{T}}^{(2)}_{\mathbf{k}'\mathbf{k}}(\tilde{\omega}, J) = -\frac{\frac{3}{4} g(\tilde{\omega})\, J^2}{1 - \frac{3}{4} g(\tilde{\omega})^2\, J^2}\, U^\dagger(\phi_{\mathbf{k}'}) U(\phi_{\mathbf{k}}) \tag{4.11}$$

$$\mathrm{T}^{(2)}_{\mathbf{k}'\mathbf{k}}(\tilde{\omega}, J) = -\frac{\frac{3}{4} g(\tilde{\omega})\, J^2}{1 - \frac{3}{4} g(\tilde{\omega})^2\, J^2}\, \tau^0 \tag{4.12}$$

in unit of energy. Note that the sole frequency dependence is contained in the g-function[5]

$$g(\tilde{\omega}) = \left(\frac{L}{\hbar v_F}\right)^2 \left(\frac{\tilde{\omega}}{4\pi} \ln\left|\frac{\mathrm{D}^2}{\tilde{\omega}^2} - 1\right| + \frac{i\,|\tilde{\omega}|}{4}\right) \Theta(\mathrm{D} - |\tilde{\omega}|) \tag{4.13}$$

with $\tilde{\omega} \equiv \omega + \mu$ in unit of energy, L^2 surface area, V_F Fermi velocity and D being the ultra-violet energy (unit of energy) cut-off chosen to be the symmetric bandwidth in the Dirac model. The factor $(L/v_F\hbar)$ has unit of inverse energy and the characteristic energy is defined $\epsilon_c \equiv (v_F\hbar/L)$.

By noting that the quantum impurity induced T-matrix in σ-basis Eqn. (4.12) is diagonal in spin σ, it may be tempting to conclude, that no spin-flip can occur and hence no backscattering as well. But the calculated square matrix elements $w^{imp.}_{M;+,\mathbf{k}\to M;+,\mathbf{k}'}$ and $w^{qm}_{M;+,\mathbf{k}\to 1+M;+,\mathbf{k}'}$ show that,

[3] note that $\Sigma^{(2)}_{\mathbf{k}'\mathbf{k}}(\tilde{\omega}) = U(\phi_{\mathbf{k}'})\, \tilde{\Sigma}^{(2)}_{\mathbf{k}'\mathbf{k}}(\tilde{\omega}) U(\phi_{\mathbf{k}})^\dagger$.

[4] note that $\mathrm{T}^{(2)}_{\mathbf{k}'\mathbf{k}}(\tilde{\omega}) = U(\phi_{\mathbf{k}'})\, \tilde{\mathrm{T}}^{(2)}_{\mathbf{k}'\mathbf{k}}(\tilde{\omega}) U(\phi_{\mathbf{k}})^\dagger$.

[5] Note that in ref[9, 22] $g^{[9,\,22]}(\tilde{\omega}) = -g(\tilde{\omega})$

this is indeed not the case. As explained in section (3.1.3), summing over these gives the inverse lifetime of the state $|\mathbf{k},+\rangle$. In the 1^{st} Born approximation the quantum impurity induced T-matrix is $\tilde{T}(\mathbf{k},\eta;\mathbf{k}^{'},\eta^{'};\tilde{\omega}) = \tilde{\Sigma}^{(2)}(\mathbf{k},\eta;\mathbf{k}^{'},\eta^{'};\tilde{\omega})$ (since the leading order $\tilde{\Sigma}^{(1),R} = 0$ vanish) and the inverse lifetime of the state $|\mathbf{k},\eta\rangle$ on the energy-shell $\tilde{\omega}$ is defined as $\frac{1}{\tau_{\eta\mathbf{k}}(\tilde{\omega})} = -(2/\hbar)\,\Im[\tilde{\Sigma}^{(2)}(\mathbf{k}\eta;\mathbf{k}\eta;\tilde{\omega})]$ i.e. connecting only same initial and final eigenstates $\{\mathbf{k},\eta\}$. Therefore

$$\begin{aligned}\Im[\tilde{\Sigma}^{(2)}(\mathbf{k}\eta;\mathbf{k}\eta;\tilde{\omega})] &= \frac{J^2}{4}\,\Im[\sum_{\mathbf{k}^{'},\eta^{'}}\sum_{i=1}^{3}\tilde{\tau}^{i}(\phi_{\mathbf{k}},\phi_{\mathbf{k}^{'}})_{\eta\eta^{'}}\tilde{G}^{0}(k^{'};i\tilde{\omega}_n\rightarrow\tilde{\omega}+i\,0^{+})_{\eta^{'}\eta^{'}}\tilde{\tau}^{i}(\phi_{\mathbf{k}^{'}},\phi_{\mathbf{k}})_{\eta^{'}\eta}] \\ &= \frac{J^2}{4}\sum_{\mathbf{k}^{'}\eta^{'}}\sum_{i=1}^{3}|\tilde{\tau}^{i}(\phi_{\mathbf{k}},\phi_{\mathbf{k}^{'}})|^2_{\eta\eta^{'}}\,\Im[\tilde{G}^{0}(k^{'};i\tilde{\omega}_n\rightarrow\tilde{\omega}+i\,0^{+})_{\eta^{'}\eta^{'}}] \\ &= \frac{-J^2\pi}{4}\sum_{\mathbf{k}^{'}\eta^{'}}\sum_{i=1}^{3}|\tilde{\tau}^{i}(\phi_{\mathbf{k}},\phi_{\mathbf{k}^{'}})|^2_{\eta\eta^{'}}\,\delta(\tilde{\omega}-\epsilon_{\eta^{'}}(k^{'})) \qquad (4.14)\end{aligned}$$

When setting on-shell ($\tilde{\omega} = \mu = \epsilon_{\eta}(k)$) the inverse lifetime of state $|\mathbf{k},\eta\rangle$

$$\begin{aligned}\frac{1}{\tau_{\eta\mathbf{k}}(\epsilon_{\eta}(k))} &= -\frac{2}{\hbar}\Im[\tilde{\Sigma}^{(2)}(\mathbf{k}\eta;\mathbf{k}\eta;\epsilon_{\eta}(k))] \\ &= \frac{2\pi J^2}{\hbar}\sum_{\mathbf{k}^{'}\eta^{'}}\sum_{i=1}^{3}\frac{1}{4}|\tilde{\tau}^{i}(\phi_{\mathbf{k}},\phi_{\mathbf{k}^{'}})|^2_{\eta\eta^{'}}\,\delta(\epsilon_{\eta}(k)-\epsilon_{\eta^{'}}(k^{'})) \qquad (4.15)\end{aligned}$$

This is exactly Eqn. (3.15) if also the $1/\tau_{\mathbf{k},-}$ was calculated.
From Eqn. (4.15) the square matrix elements[6] from state $|\mathbf{k},\eta\rangle$ to $|\mathbf{k}^{'},\eta\rangle$ can be extracted to yield

$$w^{qm}_{\mathbf{k},\eta\rightarrow\mathbf{k}^{'},\eta} = \frac{2\pi J^2}{\hbar}\sum_{i=1}^{3}\frac{1}{4}|\tilde{\tau}^{i}(\phi_{\mathbf{k}},\phi_{\mathbf{k}^{'}})_{\eta\eta}|^2 = \frac{2\pi J^2}{4\hbar}\left(1+\sin^2\left(\frac{\phi_{\mathbf{k}}-\phi_{\mathbf{k}^{'}}}{2}\right)\right) \qquad (4.16)$$

off a quantum impurity and

$$w^{sc}_{\mathbf{k},\eta\rightarrow\mathbf{k}^{'},\eta} = \frac{2\pi V_0^2}{\hbar}\,\frac{1}{4}|\tilde{\tau}^{0}(\phi_{\mathbf{k}},\phi_{\mathbf{k}^{'}})_{\eta\eta}|^2 = \frac{2\pi V_0^2}{4\hbar}\cos^2\left(\frac{\phi_{\mathbf{k}}-\phi_{\mathbf{k}^{'}}}{2}\right) \qquad (4.17)$$

off a scalar potential.

As noticed above, only matrix elements between eigenstates on the energy-shell occur i.e. $\eta = \eta^{'}$ so the diagonal elements $|\tilde{\tau}^{\lambda}(\phi_{\mathbf{k}},\phi_{\mathbf{k}^{'}})_{\eta\eta^{'}}|^2$ for $\lambda = 0,1,2,3$ are allowed, but the non-diagonal elements are forbidden due to the delta function $\delta(\epsilon_{\eta}(k)-\epsilon_{\eta^{'}}(k^{'}))$. This direct-energy conserving delta function is the same for the conventional Dirac metal (but not the conventional metal) and the the vercities of the helical metal reduces to $\sum_{i=1}^{3}|\tilde{\tau}^{i}(\phi_{\mathbf{k}},\phi_{\mathbf{k}^{'}})_{\eta\eta^{'}}|^2 \rightarrow 3\tau^{0}_{\eta\eta^{'}}$ and
$\tilde{\tau}^{0}(\phi_{\mathbf{k}},\phi_{\mathbf{k}^{'}})_{\eta\eta^{'}}|^2 \rightarrow \tau^{0}_{\eta\eta^{'}}$ on a conventional Dirac metal. I.e. no angle dependence is present for both impurities and hence the square matrix elements on the conventional Dirac metal

$$W^{qm}_{\mathbf{k},\eta\rightarrow\mathbf{k}^{'},\eta} = 3\frac{2\pi J^2}{4\hbar}\tau^{0}_{\eta\eta^{'}} \qquad (4.18)$$

off a quantum impurity and

$$W^{sc}_{\mathbf{k},\eta\rightarrow\mathbf{k}^{'},\eta} = \frac{2\pi V_0^2}{4\hbar}\tau^{0}_{\eta\eta^{'}} \qquad (4.19)$$

[6] The Eqn. (4.17) can be derived by use of the optical theorem.

off a scalar potential. So on the conventional Dirac metal, except for the couplings J and V_0, then no difference between Eqn. (4.19) and Eqn. (4.18) appears, which is obvious not the case on the helical metal Eqn. (4.17) and Eqn. (4.16), where the scalar forbid backscattering, but the qm-impurity explicitly enhance it. In figure 4.2 the square matrix elements as a function of scattering angle are plotted for the scalar and qm-impurity, respectively. This agree with the theory of topological insulators. This in supposed to be understood in the sense that, the modulus square matrix elements reflects the fact, that the helical surface lock momentum orthogonal to spin, and the scalar potential and the quantum-impurity both preserve time-reversal symmetry, but the former cannot flip spin whereas the latter can.

- For same helicity $\eta = \eta^{'}$:
  - The scalar *cannot* (zero matrix element) backscatter, whereas the quantum-impurity *can* (maximum square modulus matrix element). This is due to the former cannot flip the spin, whereas the latter can.
  - Both the scalar potential and the quantum-impurity *can* (finite matrix element squared) forward scatter, since it does not require a spin-flip.

If this degradation did not happen, the lifetime (the inverse of Eqn. (4.15)) would be infinite, but due to Eqn. (4.16) it is finite, which for an electron on the +helicity Fermi surface acquires a inverse life time

$$\frac{1}{\tau^{sc}_{+\mathbf{k}}(\mu)} = \sum_{\eta^{'},\mathbf{k}'} w^{sc}_{\mathbf{k},\eta\to\mathbf{k}',\eta} = \frac{1}{8}\frac{2\pi V_0^2}{\hbar}\left(\frac{L}{\hbar v_F}\right)^2 \frac{\mu}{2\pi} \tag{4.20}$$

for the scalar case, and scattering off the qm-impurity yields an inverse lifetime

$$\frac{1}{\tau^{qm}_{+\mathbf{k}}(\mu)} = \sum_{\eta^{'},\mathbf{k}'} w^{qm}_{\mathbf{k},\eta\to\mathbf{k}',\eta} = \frac{3}{8}\frac{2\pi J^2}{\hbar}\left(\frac{L}{\hbar v_F}\right)^2 \frac{\mu}{2\pi} \tag{4.21}$$

which is 3 times longer than the scalar case. This inverse lifetime only tell how fast the $|\mathbf{k},+\rangle$ state is lost, but not how much momentum is degraded in the process.

Therefore a factor $(1-\cos(\phi_{\mathbf{k}}-\phi_{\mathbf{k}'}))$ is inserted into the expression for the relaxation rate entering the Bolzman Eqn. descriptive of transport. If the electron forward scatter, the $\mathbf{k}$ state is destroyed, but momentum is almost conserved. Conversely if the electron backscatter the momentum is changed a lot. In the latter case the conductivity is largely affected, but in the former it is not. The inverse transport time $\frac{1}{\tau^{tr}}$, i.e. the time entering the expression for conductivity, is given by

$$\frac{1}{\tau^{tr,sc}_{+\mathbf{k}}(\mu)} = \sum_{\eta^{'},\mathbf{k}'} w^{sc}_{\mathbf{k},\eta\to\mathbf{k}',\eta}\left(1-\cos(\phi_{\mathbf{k}}-\phi_{\mathbf{k}'})\right) = \frac{1}{16}\frac{2\pi V_0^2}{\hbar}\left(\frac{L}{\hbar v_F}\right)^2 \frac{\mu}{2\pi} \tag{4.22}$$

for the scalar case and

$$\frac{1}{\tau^{tr,qm}_{+\mathbf{k}}(\mu)} = \sum_{\eta^{'},\mathbf{k}'} w^{qm}_{\mathbf{k},\eta\to\mathbf{k}',\eta}\left(1-\cos(\phi_{\mathbf{k}}-\phi_{\mathbf{k}'})\right) = \frac{7}{16}\frac{2\pi J^2}{\hbar}\left(\frac{L}{\hbar v_F}\right)^2 \frac{\mu}{2\pi} \tag{4.23}$$

for the quantum case. Since the qm-impurity allow backscattering, it is 7 times larger than the scalar case, which does not allow backscattering. In the $\mathbf{k}$ integral it was used that

$\int_0^D \frac{\mathrm{d}k',k'}{2\pi}\delta(\mu-k') = \frac{\mu}{2\pi}$. Since $\int_0^{2\pi}\frac{\mathrm{d}\phi_{\mathbf{k}'}}{2\pi} = \int_0^{2\pi}\frac{\mathrm{d}\phi_{\mathbf{k}'}}{2\pi}\left(1-\cos\left(\phi_{\mathbf{k}}-\phi_{\mathbf{k}'}\right)\right) = 1$ the inverse transport time is identical to inverse the lifetime for the conventional Dirac metal

$$\frac{1}{\tau^{sc}_{+\mathbf{k}}(\mu)} = \frac{1}{\tau^{tr,sc}_{+\mathbf{k}}(\mu)} = \sum_{\eta',\mathbf{k}'} W^{sc}_{\mathbf{k},\eta\to\mathbf{k}',\eta}\left(1-\cos\left(\phi_{\mathbf{k}}-\phi_{\mathbf{k}'}\right)\right) = \frac{1}{4}\frac{2\pi V_0^2}{\hbar}\left(\frac{L}{\hbar v_F}\right)^2\frac{\mu}{2\pi} \tag{4.24}$$

for the scalar case and

$$\frac{1}{\tau^{qm}_{+\mathbf{k}}(\mu)} = \frac{1}{\tau^{tr,qm}_{+\mathbf{k}}(\mu)} = \sum_{\eta',\mathbf{k}'} W^{qm}_{\mathbf{k},\eta\to\mathbf{k}',\eta}\left(1-\cos\left(\phi_{\mathbf{k}}-\phi_{\mathbf{k}'}\right)\right) = \frac{3}{4}\frac{2\pi J^2}{\hbar}\left(\frac{L}{\hbar v_F}\right)^2\frac{\mu}{2\pi} \tag{4.25}$$

for the quantum case.

In the case of a scalar potential, the transport lifetime on the helical metal is a factor 4 larger than on the conventional Dirac metal! For the quantum impurity this difference is not quite that remarkable, but a factor $\frac{12}{7}$ larger on the helical metal than the conventional Dirac metal. In any case, this enhancement is solely due to the helical metal Fermi surface. This have non-degenerate surface states with spin locked tangentially to the Fermi surface momentum, which is inherent in the transformation matrix $U(\phi_{\mathbf{k}})$.

In the introduction to this section, it was speculated whether the helical metal could be used in any applications as spintronics. Now it is clear, that it might be. The factor of 16 times larger transport lifetime on the helical metal, than on the conventional metal, makes such necessary concepts as a large coherence time possible. Also the angle dependent square matrix elements $w^{qm}_{M;\mathbf{k},+\to M;\mathbf{k}',+}$ and $w^{qm}_{M;\mathbf{k},+\to M+1;\mathbf{k}',+}$ suggest that it might be possible to control the impurity.

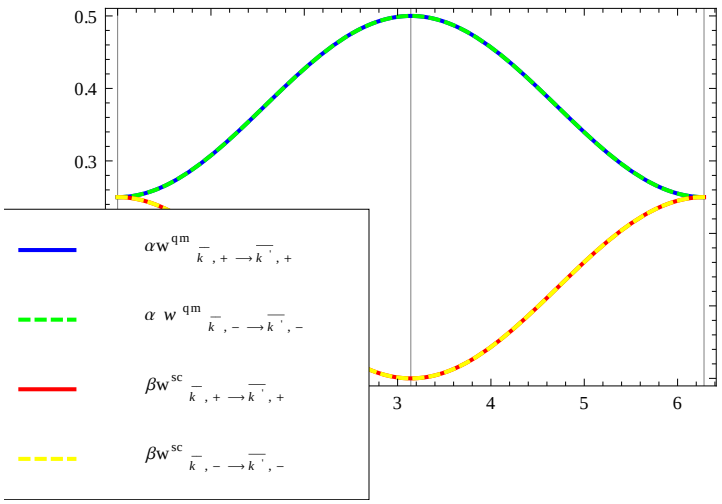

Figure 4.2: Plot of the square matrix element $\alpha w_{\mathbf{k},\eta\to\mathbf{k}',\eta}$ of the qm-impurity with $\alpha = 4\hbar/2\pi J^2$ and $\beta w^{sc}_{\mathbf{k},\eta\to\mathbf{k}',\eta}$ for the scalar potential with $\beta = 4\hbar/2\pi V_0^2$ as function of scattering angle $\phi_{\mathbf{q}} = \phi_{\mathbf{k}} - \phi_{\mathbf{k}'}$. Blue/red line is for $\eta = \eta' = +$ and green/yellow line is for $\eta = \eta' = -$ of the qm-impurity/scalar.

4.2 Quantum impurity induced 3^{rd} order self-energy

The 3. order irreducible self-energy (the one surving diagram in third order in figure 4.1) is

$$\tilde{\Sigma}^{(3)}_{\mathbf{k}\eta,\mathbf{k}'\eta'}(\tau_2;\tau_3) = \sum_{\mathbf{k}_1\mathbf{k}_2\mathbf{k}_3\mathbf{k}_4}\sum_{\eta_1\eta_2\eta_3\eta_4}\sum_{i,j,l=1}^{3}\int_0^\beta \mathrm{d}\tau_3(-J)^3 \underbrace{< T_\tau[S^i_d(\tau_1)S^j_d(\tau_3)S^l_d(\tau_2)] >}_{\frac{i}{8}s(\tau_{13})\epsilon^{ijl}}$$
$$\times\, \tilde{\tau}^i_{\eta\eta_1}(\phi\mathbf{k},\phi\mathbf{k}_1)\tilde{G}^0_{\eta_1\eta_2}(k_1,k_2;\tau_{13})\tilde{\tau}^j_{\eta_2\eta_3}(\phi\mathbf{k}_2,\phi\mathbf{k}_3)\tilde{G}^0_{\eta_3\eta_4}(k_3,k_4;\tau_{32})\tilde{\tau}^l_{\eta_4\eta'}(\phi\mathbf{k}_4,\phi\mathbf{k}^{'}) \quad (4.26)$$

where[7] $\tau_\alpha - \tau_\beta \equiv \tau_{\alpha\beta}$ and define $\tau_2 = 0$ as reference and the notation $s(\cdot) = sign(\cdot)$. Using that the η-basis is eigenbasis and homogeneity of the bare propagator thus

$$\begin{aligned}\tilde{G^0}_{\eta_\alpha\eta_\beta}(k_\alpha,k_\beta;\tau_{\alpha\beta}) &= \tilde{G^0}_{\eta_\alpha}(k_\alpha;\tau_{\alpha\beta})\delta(\xi_\alpha-\xi_\beta)\\ &= \tilde{G^0}_{\eta_\alpha}(k_\alpha;\tau_{\alpha\beta})\delta_{\eta_\alpha\eta_\beta}\delta(k_\alpha-k_\beta)\end{aligned} \quad (4.27)$$

and[17]

$$\tilde{G^0}_{\eta_\alpha}(k_\alpha;\tau_{\alpha\beta}) = -\left[\Theta_{\alpha\beta}(1-n_\alpha)+\Theta_{\beta\alpha}n_\alpha\right]e^{-\xi_\alpha\tau_{\alpha\beta}} \quad (4.28)$$

with shorthand notation $\xi_\alpha \equiv \xi_{\eta_\alpha}(k_\alpha) = \epsilon_{\eta_\alpha}(k_\alpha)-\mu$, $n_\alpha = n_F(\xi_\alpha) = 1/(e^{\beta\xi_\alpha}+1)$ and $\Theta_{\alpha\beta} = \Theta(\tau_{\alpha\beta})$ where $\Theta(\cdot)$ is the Heaviside step-function. After performing the $\mathbf{k}_1$ and $\mathbf{k}_4$ sums the τ_3 dependent part of Eqn. (4.27) is separated from the rest, which is lumped together with the $\tilde{\tau}$ vercities, then

$$\begin{aligned}&\tilde{\Sigma}^{(3)}_{\mathbf{k}\eta,\mathbf{k}'\eta'}(\tau_1;\tau_2)\\ &= (-J)^3\sum_{\mathbf{k}_1\mathbf{k}_3}\sum_{\eta_1\eta_2\eta_3\eta_4}\sum_{i,j,l=1}^{3}\frac{i}{8}\epsilon^{ijl}\left(\int_0^\beta \mathrm{d}\tau_3\,\tilde{G^0}_{\eta_1}(k_1;\tau_{13})\,\tilde{G^0}_{\eta_3}(k_3;\tau_{30})\,s(\tau_{13})\right)\\ &\quad\times\tilde{\tau}^i_{\eta\eta_1}(\phi\mathbf{k},\phi\mathbf{k}_1)\delta_{\eta_1\eta_2}\tilde{\tau}^j_{\eta_2\eta_3}(\phi\mathbf{k}_1,\phi\mathbf{k}_3)\delta_{\eta_3\eta_4}\tilde{\tau}^l_{\eta_4\eta'}(\phi\mathbf{k}_3,\phi\mathbf{k}^{'})\\ &= (-J)^3\sum_{\mathbf{k}_1\mathbf{k}_3}\sum_{\eta_1\eta_2\eta_3\eta_4}\sum_{i,j,l=1}^{3}\frac{i}{8}\epsilon^{ijl}\,\mathbb{M}_{\eta_1\eta_3}(k_1,k_3)\\ &\quad\times\tilde{\tau}^i_{\eta\eta_1}(\phi\mathbf{k},\phi\mathbf{k}_1)\delta_{\eta_1\eta_2}\tilde{\tau}^j_{\eta_2\eta_3}(\phi\mathbf{k}_1,\phi\mathbf{k}_3)\delta_{\eta_3\eta_4}\tilde{\tau}^l_{\eta_4\eta'}(\phi\mathbf{k}_3,\phi\mathbf{k}^{'})\end{aligned}$$

Where the τ_3 integration will be carried by using Eqn. (4.28), $s(\tau_{13}) = \Theta_{13}-\Theta_{31}$ and that only terms $\Theta_{13}\Theta_{30}\Theta_{13} = \Theta_{13}$ and $\Theta_{31}\Theta_{30}\Theta_{31} = \Theta_{31}$ contribute, when τ_3 integrating since terms $-\Theta_{13}\Theta_{30}\Theta_{31} = -\Theta_{31}\Theta_3\Theta_{13} = 0$

$$\begin{aligned}\mathbb{M}_{\eta_1\eta_3}(k_1,k_3;\tau_1) &\equiv \int_0^\beta \mathrm{d}\tau_3\,\tilde{G^0}_{\eta_1}(k_1;\tau_{13})\,\tilde{G^0}_{\eta_3}(k_3;\tau_{30})\,sgn(\tau_{13})\\ &= (1-n_1)(1-n_2)e^{-\xi_1\tau_1}\int_0^{\tau_1}\mathrm{d}\tau_3\left(e^{(\xi_1-\xi_3)\tau_3}-1\right)+n_1(1-n_2)e^{-\xi_1\tau_1}\int_{\tau_1}^\beta\mathrm{d}\tau_3\left(e^{(\xi_1-\xi_3)\tau_3}-1\right)\\ &= \frac{(1-n_1)(1-n_2)}{\xi_1-\xi_3}\left(e^{-\xi_3\tau_1}-e^{-\xi_1\tau_1}\right)+\frac{n_1(1-n_2)}{\xi_1-\xi_3}\left(e^{\xi_1(\beta-\tau_1)}e^{-\xi_2\beta}-e^{-\xi_3\tau_1}\right)\end{aligned} \quad (4.29)$$

[7] If not the Hamilton (2.6) was diagonalized, then the 3^{rd} order self-energy imaginary time-integration would not be possible to carrie out. This was the lesson to be learnt, after the first attempt to calculate $\Sigma^{(3)}$ by using (2.6) undiagonalized. The form of the bare Green function, when using (2.6), made the **k**-integration very easy and hence it was a tempting strategy, but unfortunately it left the imaginary time-integration undefined.

Now, define

$$\tilde{g}^0_\alpha(\tau_1) = -(1-n_\alpha)e^{-\xi_\alpha \tau_1} \tag{4.30}$$

and using $(1-n_\alpha)e^{-\xi_\alpha\beta} = n_\alpha$ and $n_\alpha e^{\xi_\alpha\beta} = 1-n_\alpha$ then

$$\mathbb{M}_{\eta_1\eta_3}(k_1,k_3;\tau_1) = \frac{1}{\xi_1-\xi_3}\left((1-2\,n_3)\tilde{g}^0_1(\tau_1) - (1-2\,n_1)\tilde{g}^0_2(\tau_3)\right) \tag{4.31}$$

and the definition of a eigenstate Green function propagator in Matsubara frequency

$$\tilde{g}^0_\alpha(i\,\omega_n) = \int_0^\beta \mathrm{d}\tau_1 \tilde{g}^0_\alpha(\tau_1)\, e^{i\,\omega_n\tau_1} = \frac{1}{i\,\omega_n - \xi_\alpha} \tag{4.32}$$

therefore

$$\mathbb{M}_{\eta_1\eta_3}(k_1,k_3;i\,\omega_n) = \int_0^\beta \mathrm{d}\tau_1\, \mathbb{M}_{\eta_1\eta_3}(k_1,k_3;\tau_1)\, e^{i\,\omega_n\tau_1} = \frac{1}{\xi_1-\xi_3}\left(\frac{1-2\,n_3}{i\,\omega_n-\xi_1} - \frac{1-2\,n_1}{i\,\omega_n-\xi_3}\right) \tag{4.33}$$

The symmetry of the dummy labels $\eta_1, \eta_3, \mathbf{k}_1$ and $\mathbf{k}_3$ makes

$$\sum_{\eta_1\eta_3}\sum_{\mathbf{k}_1,\mathbf{k}_3} \mathbb{M}_{\eta_1\eta_3}(k_1,k_3;i\,\omega_n) = 2\sum_{\eta_1\eta_3}\sum_{\mathbf{k}_1,\mathbf{k}_3} \frac{1-2\,n_3}{\xi_1-\xi_3}\frac{1}{i\,\omega_n-\xi_1} \tag{4.34}$$

Beside a factor 2, Eqn. (4.34) is on the same form as that of the conventional metal[17], except that the energy dependence ξ_η is the Dirac spectrum, whereas that of the the conv. metal is the quadratic one independent of spin $\xi_\sigma = \xi$. However, this factor 2 may very well be an error, because the diagram is identical for both the helical and conventional metals and yet only Eqn. (4.29) the time-integration over time-ordered bare Green function matrix components has been performed. These are both diagonal, the helical metal in η and the conventional metal in σ, so the result Eqn. (4.34) should be that of the conventional metal, if one substitutes $\eta \to \sigma$ and $\xi_\eta \to \xi_\sigma$. Anyway, this factor is kept even though it might be an error. First because the possible error cannot be found, and secondly leaving it in the expression doesn't change the physics of the final result $\Sigma^{(3)}(\mu,\omega)$ except for a real constant.

Equation Eqn. (4.34) is inserted back into Eqn. (4.29) as the Matsubare frequency dependence of the self-energy and summed over η_2 and η_4

$$\begin{aligned}
\tilde{\Sigma}^{(3)}_{\mathbf{k}\eta,\mathbf{k}'\eta'}(i\,k_n) &= (-J)^3 \sum_{\mathbf{k}_1\mathbf{k}_3}\sum_{\eta_1\eta_2\eta_3\eta_4}\sum_{i,j,l=1}^{3} \frac{i}{8}\epsilon^{ijl}\mathbb{M}_{\eta_1\eta_3}(k_1,k_3;i\,\omega_n) \\
&\quad\times\tilde{\tau}^i_{\eta\eta_1}(\phi\mathbf{k},\phi\mathbf{k}_1)\delta_{\eta_1\eta_2}\tilde{\tau}^j_{\eta_2\eta_3}(\phi\mathbf{k}_1,\phi\mathbf{k}_3)\delta_{\eta_3\eta_4}\tilde{\tau}^l_{\eta_4\eta'}(\phi\mathbf{k}_3,\phi\mathbf{k}') \\
&= (-J)^3 \sum_{\mathbf{k}_1\mathbf{k}_3}\sum_{\eta_1\eta_3}\sum_{i,j,l=1}^{3} \frac{i}{8}\epsilon^{ijl}\mathbb{M}_{\eta_1\eta_3}(k_1,k_3;i\,\omega_n)\tilde{\tau}^i_{\eta\eta_1}(\phi\mathbf{k},\phi\mathbf{k}_1)\tilde{\tau}^j_{\eta_1\eta_3}(\phi\mathbf{k}_1,\phi\mathbf{k}_3)\tilde{\tau}^l_{\eta_3\eta'}(\phi\mathbf{k}_3,\phi\mathbf{k}')
\end{aligned}$$

Since[8] the transformation matrix *only* depends on azimuthal angle $\phi_{\mathbf{k}_\alpha}$ and $\mathbb{M}_{\eta_1\eta_3}(k_1,k_3;i\,\omega_n)$ *only* depends on magnitude $k_\alpha = |\mathbf{k}_\alpha|$, the 2D polar $\mathbf{k}$-integration is carried out in two steps - first the angle integration leaving the magnitude integration to come after the η sums have been carried out. The relation

$$\sum_{\eta_\alpha}\int_0^{2\pi}\frac{\mathrm{d}\phi_{\mathbf{k}_\alpha}}{2\pi}\mathbb{M}_{\eta_1\eta_3}(k_1,k_3;i\,\omega_n)U_{\sigma\eta_\alpha}(\phi_{\mathbf{k}_\alpha})U^\dagger_{\eta_\alpha\sigma'}(\phi_{\mathbf{k}_\alpha}) = \frac{\delta_{\sigma\sigma'}}{2}\sum_{\eta_\alpha}\mathbb{M}_{\eta_1\eta_3}(k_1,k_3;i\,\omega_n) \tag{4.35}$$

[8] Note that this simplification of the integration can only be done when no warping is present.

valid for α being 1 or 3 will be used twice subsequently in Eqn. (4.35) after the vercities are written explicitly as $\tilde{\tau}^{\alpha} = U^{\dagger}(\phi\mathbf{k}_{\alpha})\tau^{\alpha}U(\phi\mathbf{k}_{\alpha})$ as will be elucidated now

$$
\begin{aligned}
\tilde{\Sigma}^{(3)}_{\mathbf{k}\eta,\mathbf{k}'\eta'}(i\,\omega_n) &= (-J)^3 \sum_{\mathbf{k}_1\mathbf{k}_3}\sum_{\eta_1\eta_3}\sum_{i,j,l=1}^{3}\frac{i}{8}\epsilon^{ijl}\mathbb{M}_{\eta_1\eta_3}(k_1,k_3;i\,\omega_n) \\
&\quad\times\left(U^{\dagger}(\phi_{\mathbf{k}})\tau^i U(\phi_{\mathbf{k}_1})\right)_{\eta\eta_1}\left(U^{\dagger}(\phi_{\mathbf{k}_1})\tau^j U(\phi_{\mathbf{k}_3})\right)_{\eta_2\eta_3}\left(U^{\dagger}(\phi_{\mathbf{k}_3})\tau^l U(\phi_{\mathbf{k}'})\right)_{\eta_3\eta'} \\
&= -J^3\int\frac{\mathrm{d}k_1}{2\pi}k_1\int\frac{\mathrm{d}k_3}{2\pi}k_3\sum_{i,j,l=1}^{3}\frac{i}{8}\epsilon^{ijl}\sum_{\substack{\sigma\sigma_1\\ \sigma_2\sigma_3}} \\
&\quad\times\left(U^{\dagger}(\phi_{\mathbf{k}})\tau^i\right)_{\eta\sigma}\underbrace{\left(\sum_{\eta_1}\int\frac{\mathrm{d}\phi_{\mathbf{k}_1}}{2\pi}\mathbb{M}_{\eta_1\eta_3}(k_1,k_3;i\,\omega_n)\left(U_{\sigma\eta_1}(\phi_{\mathbf{k}_1})U^{\dagger}_{\eta_1\sigma_1}(\phi_{\mathbf{k}_1})\right)\right)}_{\frac{\delta_{\sigma\sigma_1}}{2}\sum_{\eta_1}\mathbb{M}_{\eta_1\eta_3}(k_1,k_3;i\,\omega_n)} \\
&\quad\times\tau^j_{\sigma_1\sigma_2}\left(\sum_{\eta_3}\int\frac{\mathrm{d}\phi_{\mathbf{k}_3}}{2\pi}\left(U_{\sigma_2\eta_3}(\phi_{\mathbf{k}_3})U^{\dagger}_{\eta_3\sigma_3}(\phi_{\mathbf{k}_3})\right)\right)\left(\tau^l U(\phi_{\mathbf{k}'})\right)_{\sigma_3\eta'} \\
&= -J^3\int\frac{\mathrm{d}k_1}{2\pi}k_1\int\frac{\mathrm{d}k_3}{2\pi}k_3\sum_{i,j,l=1}^{3}\frac{i}{8}\epsilon^{ijl}\sum_{\substack{\sigma\sigma_1\\ \sigma_2\sigma_3}}\left(U^{\dagger}(\phi_{\mathbf{k}})\tau^i\right)_{\eta\sigma}\frac{\delta_{\sigma\sigma_1}}{2}\sum_{\eta_1} \\
&\quad\times\tau^j_{\sigma_1\sigma_2}\underbrace{\left(\sum_{\eta_3}\int\frac{\mathrm{d}\phi_{\mathbf{k}_3}}{2\pi}\mathbb{M}_{\eta_1\eta_3}(k_1,k_3;i\,\omega_n)\left(U_{\sigma_2\eta_3}(\phi_{\mathbf{k}_3})U^{\dagger}_{\eta_3\sigma_3}(\phi_{\mathbf{k}_3})\right)\right)}_{\frac{\delta_{\sigma_2\sigma_3}}{2}\sum_{\eta_3}\mathbb{M}_{\eta_1\eta_3}(k_1,k_3;i\,\omega_n)}\left(\tau^l U(\phi_{\mathbf{k}'})\right)_{\sigma_3\eta'} \\
&= -J^3\int\frac{\mathrm{d}k_1}{2\pi}k_1\int\frac{\mathrm{d}k_3}{2\pi}k_3\sum_{i,j,l=1}^{3}\frac{i}{8}\epsilon^{ijl}\sum_{\substack{\sigma\sigma_1\\ \sigma_2\sigma_3}}\sum_{\eta_1\eta_3}\mathbb{M}_{\eta_1\eta_3}(k_1,k_3;i\,\omega_n) \\
&\quad\times\frac{\delta_{\sigma\sigma_1}}{2}\frac{\delta_{\sigma_2\sigma_3}}{2}\left(U^{\dagger}(\phi_{\mathbf{k}})\tau^i\right)_{\eta\sigma}\tau^j_{\sigma_1\sigma_2}\left(\tau^l U(\phi_{\mathbf{k}'})\right)_{\sigma_3\eta'} \\
&= -J^3\int\frac{\mathrm{d}k_1}{2\pi}k_1\int\frac{\mathrm{d}k_3}{2\pi}k_3\sum_{\eta_1\eta_3}\mathbb{M}_{\eta_1\eta_3}(k_1,k_3;i\,\omega_n) \\
&\quad\times\sum_{i,j,l=1}^{3}\frac{i}{4\cdot 8}\epsilon^{ijl}\left(U^{\dagger}(\phi_{\mathbf{k}})\tau^i\tau^j\tau^l U(\phi_{\mathbf{k}'})\right)_{\eta\eta'} \\
&= -J^3\int\frac{\mathrm{d}k_1}{2\pi}k_1\int\frac{\mathrm{d}k_3}{2\pi}k_3\sum_{\eta_1\eta_3}\mathbb{M}_{\eta_1\eta_3}(k_1,k_3;i\,\omega_n) \\
&\quad\times\underbrace{\sum_{i,j,l=1}^{3}\frac{i^2}{4\cdot 8}\left(\epsilon^{ijl}\right)^2}_{=-\frac{6}{4\cdot 8}}\left(U^{\dagger}(\phi_{\mathbf{k}})\tau^0 U(\phi_{\mathbf{k}'})\right)_{\eta\eta'} \\
&= \frac{6}{4\cdot 8}J^3\int\frac{\mathrm{d}k_1}{2\pi}k_1\int\frac{\mathrm{d}k_3}{2\pi}k_3\sum_{\eta_1\eta_3}\mathbb{M}_{\eta_1\eta_3}(k_1,k_3;i\,\omega_n)\left(U^{\dagger}(\phi_{\mathbf{k}})U(\phi_{\mathbf{k}'})\right)_{\eta\eta'} \\
&= \frac{S(S+1)}{4}J^3\int\frac{\mathrm{d}k_1}{2\pi}k_1\int\frac{\mathrm{d}k_3}{2\pi}k_3\sum_{\eta_1\eta_3}\mathbb{M}_{\eta_1\eta_3}(k_1,k_3;i\,\omega_n)\left(U^{\dagger}(\phi_{\mathbf{k}})U(\phi_{\mathbf{k}'})\right)_{\eta\eta'}
\end{aligned}
$$

and it was used that $\sum_{i,j,l=1}^{3}\epsilon^{ijl}\tau^i\tau^j\tau^l = \sum_{i,j,l=1}^{3} i\left(\epsilon^{ijl}\right)^2\tau^0 = i\,6\tau^0$. Using explicitly $\xi_\alpha = \xi_{\eta_\alpha}(k_\alpha) = \eta_\alpha\,k_\alpha - \mu$ and $i\,\omega_n + \mu \equiv i\,\tilde{\omega}_n$ with $\tilde{\omega}_n = \omega_n - i\mu$ and the anti-symmetry $(1-2\,n(-x)) = -(1-2\,n(x))$ (since $n(-x) = 1 - n(-x)$) where $(1-2\,n(x)) = \tanh(x/2T)$ which at near zero temperature ($T = 0$)
$\tanh(x/2T) = s(x)$ the sum becomes

$$\begin{aligned}
\sum_{\eta_1\eta_3}\mathbb{M}_{\eta_1\eta_3}(k_1,k_3;i\,\omega_n) &= 2\sum_{\eta_1\eta_3}\frac{1-2\,n_3}{\xi_1-\xi_3}\frac{1}{i\,\omega_n-\xi_1}\\
&= 2\sum_{\eta_1\eta_3}\frac{s(\eta_3\,k_3-\mu)}{\eta_1\,k_1-\eta_3\,k_3}\frac{1}{i\,\tilde{\omega}_n-\eta_1\,k_1}\\
&= 2\frac{1}{D^2}\sum_{\eta_1\eta_3}\frac{s(\eta_3\,q_3-\lambda)}{\eta_1\,q_1-\eta_3\,q_3}\frac{1}{i\,\tilde{\phi}_n-\eta_1\,q_1}\\
&= 2\frac{1}{D^2}\underbrace{\sum_{\eta_1\eta_3}\mathbb{M}_{\eta_1\eta_3}(\mathbf{q}_1,\mathbf{q}_3;i\,\tilde{\phi}_n)}_{\equiv\rho(i\tilde{\phi}_n)} \equiv \frac{2}{D^2}\rho(i\tilde{\phi}_n)
\end{aligned} \tag{4.36}$$

which is a factor, $\frac{1}{D^2}$, with dimension energy square-inverse times a dimensionless sum of the parameters 'dimensionless momentum' $q_i = \frac{k_i}{D}$ in the range $q_i \in [0,1]$, 'dimensionless chemical potential' $\lambda = \frac{\mu}{D}$ in the range $\lambda \in]-1,1[$ and 'dimensionless Matsubara frequency' $i\tilde{\phi}_n \to \tilde{\phi} + i\,0^+$ when performing the analytic continuation with $\tilde{\phi} = \frac{\tilde{\omega}}{D} = \frac{\omega}{D} + \frac{\mu}{D} = \phi + \lambda$ in the range $\tilde{\phi} \in]-1,1[$ with 'dimensionless probe frequency' $\phi = \frac{\omega}{D}$ in the range $\phi \in]-1,1[$. However, for a certain chemical potential μ only probing frequencies ϕ that obey $|\tilde{\phi}| < 1$ are allowed in the subsequently derivations. Nevertheless only values $\phi, \lambda << 1$ are sensible when the model are to resemble the low-energy approximation of the real physical systems Bi_2X_3, $X = \mathrm{Se}, \mathrm{Te}$. Define

$$\begin{aligned}
R(i\,\tilde{\omega}_n) &\equiv \frac{1}{2}\int_0^D\frac{\mathrm{d}k_1}{2\pi}k_1\int_0^D\frac{\mathrm{d}k_3}{2\pi}k_3\sum_{\eta_1\eta_3}\mathbb{M}_{\eta_1\eta_3}(k_1,k_3;i\,\tilde{\omega}_n)\\
&= D^4\int_0^1\frac{\mathrm{d}q_1}{2\pi}q_1\int_0^1\frac{\mathrm{d}q_3}{2\pi}q_3\frac{1}{D^2}\sum_{\eta_1\eta_3}\mathbb{M}_{\eta_1\eta_3}(q_1,q_3;i\,\tilde{\phi}_n)\\
&= D^2\int_0^1\frac{\mathrm{d}q_1}{2\pi}q_1\int_0^1\frac{\mathrm{d}q_3}{2\pi}q_3\,\rho(i\,\tilde{\phi}_n) \equiv R(i\,\tilde{\phi}_n)
\end{aligned} \tag{4.37}$$

then the 3.order self-energy, with Eqn. (4.36) and Eqn. (4.36), is expressed shortly as

$$\begin{aligned}
\Sigma^{(3)}_{\mathbf{k},\mathbf{k}'}(i\,\tilde{\phi}_n) &= \frac{S(S+1)}{2}J^3\left(\frac{L}{\hbar v_F}\right)^4 D^2\int_0^1\frac{\mathrm{d}q_1}{2\pi}q_1\int_0^1\frac{\mathrm{d}q_3}{2\pi}q_2\,\rho(i\,\tilde{\phi}_n)\,\tau^0\\
&= \frac{S(S+1)}{2}J^3\left(\frac{L}{\hbar v_F}\right)^4 R(i\,\tilde{\phi}_n)\,\tau^0
\end{aligned} \tag{4.38}$$

For both integrals a factor $\left(\frac{L}{\hbar v_F}\right)^2$ has been reintroduced - one for each dimensionless $\mathbf{k}$-sum $\sum_{\mathbf{k}}$ performed - in order to express it in right dimension of energy.

The $\Im\Sigma^{(3)}$ will come from $\Im\rho$ whereas $\Re\Sigma^{(3)}$ from $\Re\rho$ which are given formally by

$$\Im\rho(\phi,\lambda) = \sum_{\eta_1\eta_3} \frac{s(\eta_3\, q_3 - \lambda)}{\eta_1\, q_1 - \eta_3\, q_3}(-\pi)\delta(\tilde{\phi} - \eta_1\, q_1) \tag{4.39}$$

$$\Re\rho(\phi,\lambda) = \sum_{\eta_1\eta_3} \frac{s(\eta_3\, q_3 - \lambda)}{\eta_1\, q_1 - \eta_3\, q_3}\frac{1}{\tilde{\phi} - \eta_1\, q_1} \tag{4.40}$$

where $\tilde{\phi}$ is parametrized as $\tilde{\phi} = \tilde{\phi}(\phi,\lambda) = \phi + \lambda$. The derivation of $R(i\,\tilde{\phi}_n)$ in (4.38) is carried out in the appendix A. The resulting imaginary and real part are summerized in section 4.2.1 and A.3.5 respectively.

4.2.1 Imaginary part of the self-energy

The imaginary part of the retarded *3. order self-energy* in the σ-basis[9] is finally (Eqn. (4.38) with Eqn. (A.3.9))

$$\Sigma^{(3)}_{\mathbf{k},\mathbf{k}'}(\mu,\omega,T) = \frac{S(S+1)}{4}\, J^3 \left(\frac{L}{\hbar v_F}\right)^4 \Im\Upsilon(\mu,\omega,T)\Theta(D - |\tilde{\omega}|)\,\tau^0 \tag{4.41}$$

where

$$\Im\Upsilon(\mu,\omega,T) = \frac{|\tilde{\omega}|D}{\pi}\left[1 - \frac{|\mu|}{D} - \frac{|\tilde{\omega}|}{D}\frac{1}{2}\log\frac{D+|\tilde{\omega}|}{D-|\tilde{\omega}|} - s(\mu)\frac{\tilde{\omega}}{D}\left(\log\frac{\sqrt{\omega^2+T^2}}{D} - \log\frac{\sqrt{\tilde{\omega}^2+T^2}}{D}\right)\right] \tag{4.42}$$

Remember the retarded *2. order self-energy* in the σ-basis

$$\Sigma^{(2)}_{\mathbf{k},\mathbf{k}'}(\mu,\omega) = -S(S+1)J^2 g^R(\tilde{\omega})\,\Theta(D - |\tilde{\omega}|)\,\tau^0 \tag{4.43}$$

with

$$g(\tilde{\omega}) \equiv \left(\frac{L}{\hbar v_F}\right)^2 \left(\frac{\tilde{\omega}}{4\pi}\ln\left(\frac{D^2}{\tilde{\omega}^2} - 1\right) + i\,\frac{1}{4}\,|\tilde{\omega}|\right) \tag{4.44}$$

thus the imaginary part of the retarded 2. order self-energy in the σ-basis is

$$\Im\Sigma^{(2)}_{\mathbf{k},\mathbf{k}'}(\mu,\omega) = -\frac{S(S+1)}{4}\, J^2 \left(\frac{L}{\hbar v_F}\right)^2 |\tilde{\omega}|\,\Theta(D - |\tilde{\omega}|)\,\tau^0 \tag{4.45}$$

The imaginary part of the *total irreducible self-energy up to 3. order* is

$$\begin{aligned}
\Im\Sigma^{(1,2,3)}_{\mathbf{k},\mathbf{k}'}(\mu,\omega,T) &= \Im\Sigma^{(2)}_{\mathbf{k},\mathbf{k}'}(\mu,\omega) + \Im\Sigma^{(3)}_{\mathbf{k},\mathbf{k}'}(\mu,\omega) \\
&= -\frac{S(S+1)}{4}J^2\left(\frac{L}{\hbar v_F}\right)^2 |\tilde{\omega}|\Theta(D - |\tilde{\omega}|) \\
&\quad \times\left[1 - J\left(\frac{L}{\hbar v_F}\right)^2 \frac{D}{\pi}\left(1 - \frac{|\mu|}{D} - \frac{|\tilde{\omega}|}{D}\frac{1}{2}\log\frac{D+|\tilde{\omega}|}{D-|\tilde{\omega}|}\right.\right. \\
&\quad \left.\left. -s(\mu)\frac{\tilde{\omega}}{D}\left(\log\frac{\sqrt{\omega^2+T^2}}{D} - \log\frac{\sqrt{\tilde{\omega}^2+T^2}}{D}\right)\right)\right]\tau^0
\end{aligned} \tag{4.46}$$

[9] $\Sigma^{(3),R}_{\mathbf{k},\mathbf{k}'}(\mu,\omega) = U_{\mathbf{k}}\tilde{\Sigma}^{(3),R}_{\mathbf{k},\mathbf{k}'}(\mu,\omega)U^{\dagger}_{\mathbf{k}'}$

Kondo[28, 40, 17] showed that, at low temperatures conventional metals contaminated with dillute magnetic impurities,, show non-trivial resistance behaviour due to the conduction electrons scatter off the impurities. In this low temperature regime, the low-energy physics of an isolated impurity is determined by a single energy scale T_K being the Kondo temperature (in units of energy). In the conventional metal for temperatures $T << T_K$ the impurity is fully screened by the conduction electrons which form a collective many-body state of spin zero with the impurity spin. The Kondo temperature $T_K \propto g(\mu)^{-1} e^{\frac{1}{2g(\mu)J}}$ is proportional to the inverse DOS $g(\mu)$ at the Fermi level and depends exponentially on the inverse coupling J and inverse $g(\mu)$. But for systems[40, 43] with a vanishing DOS at the Fermi level, this standard picture has to be revised. These concern[10] pseudo-gap systems[11] which has a power-law DOS $\tilde{g}(\omega) \sim |\omega|^r$ for $r > 0$ and hence also include the helical metal, since it has exponent $r = 1$.

Here a perturbation expansion of the Green function were used, hence it really doesn't make sense to compare the result with for example a renormalization-group flow diagram. Such matters are carried out elsewhere[41, 14, 15, 39]. But instead Eqn. (4.46) can be compared to the similar perturbation result of a conventional metal. For the conventional metal, the imaginary part of the self-energy up to third order goes as

$$\Im\Sigma^{(2)+(3)}_{conv.metal}(\mathbf{k},\mathbf{k}') = -J^2 g(\mu)\left(1 - 2\,J\,g(\mu)\ln\left(\frac{1}{T\,g(\mu)}\right)\right) \tag{4.47}$$

with $g(\mu) = g_0$ a constant (units of inverse energy), Eqn. (2.13), independent on the Fermi level μ. This leads to the Kondo temperature

$$T \ll T_K^{conv.metal} \equiv g(\mu)^{-1} e^{\frac{1}{2\,g(\mu)\,J}} \tag{4.48}$$

It is seen that Eqn. (4.46) on the Fermi surface ($\omega \to 0$) goes as

$$\begin{aligned}&\Im\Sigma^{(1,2,3)}_{\mathbf{k},\mathbf{k}'}(\mu,0,T)\\ &\propto \underbrace{-J^2\tilde{g}(\mu)}_{\varrho_1}\left(\underbrace{1}_{\Pi_1} - J\underbrace{\left[2\tilde{g}(D) - 2\tilde{g}(\mu)\right]}_{\Delta_1} + \underbrace{J\tilde{g}(\mu)\log\frac{D+|\mu|}{D-|\mu|}}_{\Phi_1} - \underbrace{\underbrace{2\,J\tilde{g}(\mu)}_{\rho_1}\underbrace{\ln\sqrt{\frac{\mu^2+T^2}{T^2}}}_{\lambda_1}}_{\Gamma_1}\right)\end{aligned} \tag{4.49}$$

when written in terms of the DOS, Eqn. (2.17), at the Fermi surface $\tilde{g}(\mu) = \frac{|\mu|}{2\pi}\left(\frac{L}{\hbar v_F}\right)^2\Theta(D-\mu)$ depending on the Fermi level μ and on a constant DOS $\tilde{g}(D) = \frac{|D|}{2\pi}\left(\frac{L}{\hbar v_F}\right)^2$ determined by the cut-off D. Notice that every term in Eqn. (4.49) are marked by a Greek letter, because we need to keep track on the different terms.

It is seen that Eqn. (4.49) has a large similarity to Eqn. (4.47). The overall prefactor ϱ_1 and that ρ_1 of the logarithmic correction λ_1 both have same negative sign, and depends linearly on the DOS at the Fermi surface of the respective metals. The 2^{nd} order term, i.e. ρ_1 and Π_1, is

[10] The hard-gap system, such as s-wave superconductors, with $g(\mu) = 0$ for energies smaller than the energy gap Δ, i.e. $\omega < \Delta$, belong to these systems.

[11] Pseudo-gap systems include some zero-gap semiconductors and p & d-wave superconductors($r = 2$ and $r = 1$ respectively).

$\Im\Sigma^{(2)}(\mu,0)$ identical to the $\Im\Sigma^{(2)}_{conv.metal}$ with a substitution of the DOS at the Fermi level of the respective metals. However, since $g(\mu)=g_0$ is a constant independent of the Fermi surface, then for a given coupling J the $\Im\Sigma^{(2)}_{conv.metal}$ is a constant independent on the Fermi level μ. But since the helical DOS $\tilde{g}(\mu)$ depends linear on μ for a given J the $\Im\Sigma^{(2),R}(\mu,0)\to 0$ for $\mu\to 0$ i.e. turning the system in the topological regime. This is indeed reasonable, since the phase-space at $\mu=0$ consist of a single $\mathbf{k}$-state and thus no scattering to other states can occur.

The 3^{rd} order expansion, however, distinguish the metals with more than a substitution of the DOS at the Fermi surface of the respective metals which characterize the 2^{nd} oder self-energy. This discrepancy is due to the Δ_1 and Φ_1 terms and the log-correction dependence λ_1. The Δ_1 term is a new feature which for $|\mu|<|D|$ enhance the log-correction effect Γ_1 since they share the same sign. For a Fermi level $|\mu|=|D|$ at the cut-off D, it vanish and the logarithmic correction λ_1 and Φ_1 are left as the only 3^{rd} order terms. The Φ_1 term is also a new feature, which for $|\mu|<<|D|$ vanish and the log-correction λ_1 and Δ_1 are left as the only 3^{rd} order terms. But for a Fermi level $|\mu|=|D|$, at the cut-off D it blows up and compete with the log-correction Γ_1. Φ_1 has a different sign than both Δ_1 and Γ_1, hence it compete with them, on determine the effective sign of the 3^{rd} order contribution. When Φ_1 is absent the sign in front of the 3^{rd} order, i.e. Δ_1 and Γ_1, is negative, thus having a negative, $J<0$, coupling increases the effective coupling $|J_{eff}|>|J|$ which leads to anti-ferromagnetic ordering. And having a positive coupling, $J>0$, decrease the effective coupling $J_{eff}<J$ which leads to ferromagnetic ordering. This is in accord with the definition of the Kondo Hamilton, Eqn. (3.6), $-J\tilde{\tilde{\tau}}(\phi_{\mathbf{k}'},\phi_{\mathbf{k}})\cdot\bar{S}$ which favor anti-ferromagnetic ordering for negative couplings $J<0$, and favor ferromagnetic ordering for positive couplings $J>0$. The former tend to drive the system into the phase, where the conduction electrons screen the impurity, whereas the latter drives it into the unscreened phase. The above scenario was when Φ_1 is zero, but because of its opposite sign, the scenario of the resulting effective coupling J_{eff} may be different when Φ_1 is non-zero, which only happens for $|\mu|\sim|D|$. In this case it may change the sign of the effective coupling otherwise determined by Δ_1 and Γ_1.

Because we're about to scrutinize $\Im\Sigma$ for the Kondo problem, i.e. the breakdown of the perturbation expansion of the Green propagator, the 3^{rd} order terms are required to be less than the 2^{nd} order Π_1-term in Eqn. (4.49) in order to find the breakdown. This gives the Kondo temperature T_K and a restriction on the possible coupling J values. Due to the rather akward 3^{rd} order terms Δ_1, Φ_1 and Γ_1, which each dominates in the different domains of $|\tilde{\omega}|\lesseqgtr|D|$, the analysis have to be devided into three cases: $\mu=0$, $|\mu|=|D|$ and $0<|\mu|<<|D|$ and further only the effect *on the Fermi surface*,[12] i.e. only $\omega=0$, will be treated. The other cases for a general $\omega\neq 0$ can be seen on the plots of $\frac{\Im\Sigma^{(3),R}(\mu,\omega)}{(-(s(s+1)/4)J^3)\epsilon_c^{-4}}$ in figure A.1(a) and (b) where (a) is for high temperature $T=D$ and (b) is for low temperature $T=0.0005\,D$.

Instead of expressing Eqn. (4.49) in terms of DOS it reads

$$\Im\Sigma^{(1,2,3)}_{\mathbf{k},\mathbf{k}'}(\mu,0,T)$$
$$\propto \underbrace{-J^2|\mu|}_{\varrho_2}\left(\underbrace{1}_{\Pi_2}-\underbrace{J\left[\frac{D-|\mu|}{\pi}\left(\frac{L}{\hbar v_F}\right)^2\right]}_{\Delta_2}+\underbrace{J\frac{|\mu|}{2\pi}\left(\frac{L}{\hbar v_F}\right)^2\log\frac{D+|\mu|}{D-|\mu|}}_{\Phi_2}-\underbrace{\underbrace{J\left(\frac{L}{\hbar v_F}\right)^2\frac{|\mu|}{\pi}}_{\rho_2}\underbrace{\ln\sqrt{\frac{\mu^2+T^2}{T^2}}}_{\lambda_2}}_{\Gamma_2}\right) \quad (4.50)$$

[12] For a given $\mu=\mu_0$ ARPES is actually *only* able to probe the occupied electronic states $\omega\leq 0$ but STM(S) also the empty hole states $\omega>0$.

Case $\mu = 0$: Setting the Fermi level at the spin degenerate Dirac Γ-point and probing it $\omega \to 0$ makes $\Phi_2 \to 0$, $\Gamma_2 \to 0$ and Δ_2 a constant $J\tilde{g}(D)$, but the overall prefactor $\varrho_2 \to 0$ hence $\Im\Sigma^{(1,2,3),R}_{\mathbf{k},\mathbf{k}'}(0,0,T) = 0$. The temperature dependence (the figure A.1(a) and (b) are identical here) is absent and no restriction on J is required which makes the Kondo problem non-existing.

Case $|\mu| = |D|$: Setting the Fermi level at the cut-off $\mu = D$ makes $\Delta_2 \to 0$ and the denominator in Φ_2 to $D - |\mu| \to \delta$ a infinitesimal δ ultraviolet divergence and $\lambda_2 \to \ln\sqrt{\frac{D^2+T^2}{T^2}}$. Now the overall sign of the 3^{rd} order is determined by a competition between Π_2 and Γ_2 dependent on temperature T since each having opposite signs.
If the temperature is high as $T = D$ in figure A.1(a) $\Gamma_2 << \Pi_2$ and Γ_2 can be ignored. Thus

$$\Im\Sigma^{(1,2,3)}_{\mathbf{k},\mathbf{k}'}(D,0) \propto \underbrace{-J^2|D|}_{\varrho_2}\left(\underbrace{1}_{\Pi_2} + \underbrace{J\frac{D}{2\pi}\left(\frac{L}{\hbar v_F}\right)^2 \log\frac{2D}{\delta}}_{\Phi_2}\right)$$

The Φ_2 blows up and the Kondo problem is present even for a large temperature. Requiring the 2^{nd} order term Π_2 to be larger than the 3^{rd} term Φ_2 leads to the restriction

$$J << \frac{2\pi}{D}\left(\frac{\hbar v_F}{L}\right)^2 \frac{1}{\log\frac{2D}{\delta}} = \frac{\tilde{g}(D)}{\log\frac{2D}{\delta}} \tag{4.51}$$

that the coupling have to be smaller than a infinite large positive number. That $J > 0$ is required in this limit, makes the effective coupling J_{eff} (of adding the contribution from Π_2 to Δ_2) $J_{eff} > J$ increase. This enhance the screening phase, and that is in accord with the definition of the Kondo Hamilton mentioned above.
If instead the temperature is low $D >> T \to 0$ as in figure A.1(b) $\Gamma_2 >> \Pi_2$ and Π_2 can be ignored. Thus

$$\Im\Sigma^{(1,2,3),R}_{\mathbf{k},\mathbf{k}'}(D,0,T) \propto \underbrace{-J^2|D|}_{\varrho_2}\left(\underbrace{1}_{\Pi_2} - \underbrace{\underbrace{J\left(\frac{L}{\hbar v_F}\right)^2\frac{|\mu|}{\pi}}_{\rho_2}\underbrace{\ln\sqrt{\frac{\mu^2+T^2}{T^2}}}_{\lambda_2}}_{\Gamma_2}\right)$$

The Γ_2 blows up and the Kondo problem is present for low temperature. Requiring the 2^{nd} order term Π_2 to be larger than the 3^{rd} term Γ_2 leads to Kondo temperature

$$T << T_K \equiv D\, e^{\frac{\pi}{D(L/\hbar v_F)^2 J}} \tag{4.52}$$

$$= \frac{\tilde{g}(D)}{(L/\hbar v_F)^2} e^{\frac{1}{2\tilde{g}(D)J}} \tag{4.53}$$

Case $0 < |\mu| << |D|$**:** This is the physical and experimental realistic situation, where the Fermi level is much less than the cut-off $|\mu| << |D|$ which makes the $\Phi_2 \to 0$ and Δ_2 to a constant

$$\Im\Sigma^{(1,2,3),R}_{\mathbf{k},\mathbf{k}'}(\mu,0,T) \propto \underbrace{-J^2|\mu|}_{\varrho_2}\left(\underbrace{\frac{1}{\Pi_2} - \underbrace{J\left[\frac{D}{\pi}\left(\frac{L}{\hbar v_F}\right)^2\right]}_{\Delta_2}}_{\Gamma_2} - \underbrace{\underbrace{J\left(\frac{L}{\hbar v_F}\right)^2\frac{|\mu|}{\pi}}_{\rho_2}\underbrace{\ln\sqrt{\frac{\mu^2+T^2}{T^2}}}_{\lambda_2}}_{\Gamma_2}\right)$$

For higher temperatures $T >> |\mu|$ one may neglect Γ_2, and requiring the 2^{nd} order term Π_2 to be larger than the 3^{rd} term Δ_2 leads to the restriction

$$J >> -\frac{\pi}{D}\left(\frac{\hbar v_F}{L}\right)^2 = -2\tilde{g}(D) << 0 \tag{4.54}$$

being less than a very large negative number. For low temperatures $T << |\mu|$ one may neglect Δ_2 and requiring the 2^{nd} order term Π_2 to be larger, than the 3^{rd} term Γ_2 leads to the Kondo temperature

$$T << T_K \equiv |\mu|\, e^{\frac{\pi}{|\mu|(L/\hbar v_F)^2 J}} = \frac{\tilde{g}(\mu)}{(L/\hbar v_F)^2} e^{\frac{1}{2\tilde{g}(\mu)J}} \tag{4.55}$$

The new terms Δ_1 and Φ_1 (or identically Δ_2 and Φ_2) are unwanted artifacts of the theory, which arise due the ultraviolet cut-off D. These could possibly be removed from the theory if higher orders were summed. In the real physical situation where $0 \leq |\mu| << |D|$ and for low temperatures these artifacts becomes negligible as shown above and hence the 3^{rd} order contribution is only the log-singularity Γ_2 which give rise the the Kondo problem & temperature Eqn. (4.55) in the helical metal. This Eqn. (4.55) is very similar to the Kondo temperature Eqn. (4.48) on the conventional Metal. Both depends exponentially on the inverse coupling and inverse DOS at the Fermi level of the respective metals but Eqn. (4.55) is inverse proportional to DOS at the Fermi level whereas Eqn. (4.55) depends linearly.

4.3 Analysis of T-matrix

In principle the irreducible self-energy $\Sigma^{\text{irr.}} = \Sigma^{(2)} + \Sigma^{(3)}$ including the 2^{nd} and 3^{rd} order contributions, should be used to construct the T-matrix upto 3^{rd} order, which again determine the full Green function as desired. The value of the coupling strength J, should be sufficiently small, such that the 3^{rd} order term is just a correction to the 2^{nd} oder, because otherwise the full Green function cannot be expanded as treated in this thesis. However, in all quantities to be calculated the correction from the $\Sigma^{(3)}$ will be ignored and only $\Sigma^{(2)}$ will be used, and hence the T-matrix is Eqn. (4.12) or Eqn. (4.11) with a J determined below.

The reason for this is two-fold; first the 2^{nd} order T-matrix is much more simple, than that including the 3^{rd} order, and if the 3^{rd} order contribution should be included, it would be nothing but a slight correction to the 2^{nd} order term. So it can just as well be ignored. More importantly; the 3^{rd} order term was calculated in order to show, whether the Kondo problem arise on the helical metal or not. In section 4.2.1 it was found, that for a $|\mu| \neq 0$ the Kondo problem arise, which has the overall effect of changing the coupling J to a effective J_{eff}. Thus for a given temperature

T and a chosed coupling J, then by lowering temperature T, has the equivalent effect, of using a effective J_{eff} which $|J_{eff}| > |J|$, instead of J.

This is the important point; for a coupling J, the 2^{nd} order T-matrix is used too calculate the relevant quantities. But having in mind ,that the onset of the Kondo problem, by imagine the temperature T, enforce a new coupling $|J_{eff}| > |J|$. So this enforce the simplification argued in the first reason, which at first hand seemed quite superficial. So instead of carrying a temperature T and coupling coupling J along in all calculations and plots in addition to μ and ω, now only a single effective coupling J is the parameter, which can be enhance by a effective $|J_{eff}| > |J|$. If the temperature T is lowered. In section 5 and 6 it will be learnt what this enhancement of the coupling has on the physical quantities LDOS and FT-LDOS which is detected in the lab by the experimental STM(S) probe.

The T-matrices Eqn. (4.11), (4.3) and (4.2) are all on the form $\tilde{T}^{imp.}_{\mathbf{k}',\mathbf{k}} = t^{imp.}(\tilde{\omega}, J)U^{\dagger}(\phi_{\mathbf{k}'})U(\phi_{\mathbf{k}'})$ with J substituted by either V_0 or S for the scalar and classical magnetic impurity respectively. define the t-factor as the energy dependent part of the T-matrix, which can be completely separated from the momentum matrix, which in σ-basis is τ^0 and in η-basis $U^{\dagger}(\phi_{\mathbf{k}'})U(\phi_{\mathbf{k}'})$. That is for the scalar impurity

$$t_{sc}(\tilde{\omega}, V_0) = \frac{V_0\tau^0}{1 + V_0 g(\tilde{\omega})} \tag{4.56}$$

for the quantum impurity

$$t_{qm}(\tilde{\omega}, J) = \frac{-\frac{3}{4}J^2 g(\tilde{\omega})}{1 - \frac{3}{4}J^2 g(\tilde{\omega})^2} \tag{4.57}$$

for the magnetic impurity only the part of $t(\tilde{\omega}, S)$, which is identical to that of the quantum-impurity, t_{qm}, when the magnetic strength is scaled $S^2 = \frac{3}{4}J^2$ will be considered. The reason for this, will actually be very obvious in section 6. Hence for the classical magnetic impurity

$$t_{cl}(\tilde{\omega}, S) = \left(\frac{-\frac{3}{4}J^2 g(\tilde{\omega})}{1 - \frac{3}{4}J^2 g(\tilde{\omega}^2}\right) \tag{4.58}$$

$$= t_{qm}(\tilde{\omega}, J) \tag{4.59}$$

Therefore no analysis of $t_{cl}(\tilde{\omega}, S)$ will be carried out independently, but indirectly though the analysis of $t_{qm}(\tilde{\omega}, J)$ All t-factors have the common g-function dependency Eqn. (4.13).

4.3.1 The t-function

In figure 4.3(a) a contour plot of the $\Im$ and $\Re$ parts of the denominators of $t_{qm}(\tilde{\omega}, J)$ as a function of $\tilde{\omega}$ and J. Because $\Re[1 - \frac{3}{4}(g(\tilde{\omega})J)^2] = \Re[1 - \frac{3}{4}(g(-\tilde{\omega})J)^2]$ and $\Im[1 - \frac{3}{4}(g(\tilde{\omega})J)^2] = -\Im[1 - \frac{3}{4}(g(-\tilde{\omega})J)^2]$ only the blue contours of $\Re[1 - \frac{3}{4}(g(\tilde{\omega})J)^2]$ is plotted for positive $\tilde{\omega}/\epsilon_c > 0$ and red contours of $\Im[1 - \frac{3}{4}(g(\tilde{\omega})J)^2]$ for $\tilde{\omega} < 0$ due to the simplicity of the plot. Also the solution $\Re[1 - \frac{3}{4}(g(\tilde{\omega})J)^2] = 0$ is drawn as a black dashed line whereas $\Im[1 - \frac{3}{4}(g(\tilde{\omega})J)^2] = 0$ is drawn as green dashed line.
Large-energy/frequency solutions near the cut-off D/ϵ_c i.e. $|\tilde{\omega}| \sim 90 - 100$ exist, however, since only experimentally realistic situations restricts $|\tilde{\omega}| << D$, only low-frequency solutions $|\tilde{\omega}| \lesssim 30$ is considered and hence shown. The same reason applies in the scalar case shown in figure 4.4. The quantum magnetic impurity t_{qm}-function has singularities where $\Re[1 - \frac{3}{4}(g(\tilde{\omega})J)^2] = 0$ if also the imaginary part $\Im[1 - \frac{3}{4}(g(\tilde{\omega})J)^2]$ is close to zero. A bound state exist, when such a singularity

is encountered. But from figure 4.3(a) for $J < 0.426$ no solutions of $\Re[1 - \frac{3}{4}g^R(\tilde{\omega})J)^2] = 0$ exists, and hence no bound states can exist for these values. For $J > 0.426$ solutions (black dashed line) to $\Re[1 - \frac{3}{4}(g(\tilde{\omega})J)^2] = 0$ exists, but only for $\tilde{\omega} = 0$ is $\Im[1 - \frac{3}{4}(g(\tilde{\omega})J)^2] = 0$. Hence for $\tilde{\omega} \neq 0$ no bound states really exist, however, for the coupling strength J becoming stronger, quasi-bound states can exist since $\Im[1 - \frac{3}{4}(g(\tilde{\omega})J)^2] = 0$ and $\Re[1 - \frac{3}{4}(g(\tilde{\omega})J)^2] = 0$ approach each other. In the scalar case the situation much similar as seen in figure 4.4.

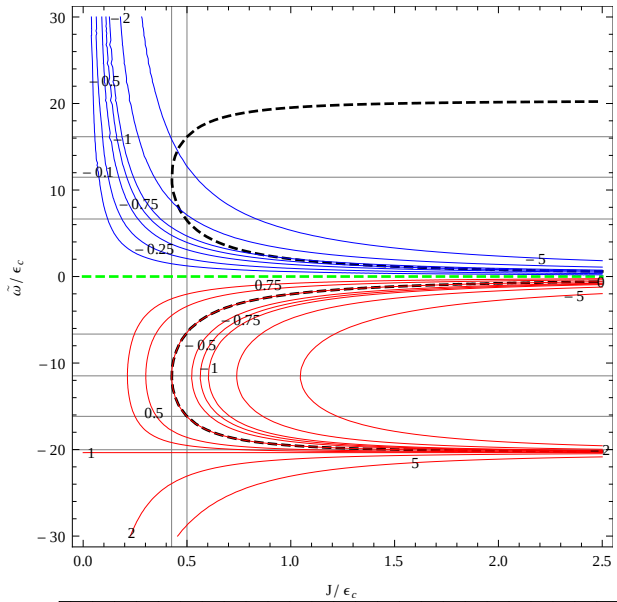

Figure 4.3: Contours of (black dashed) $\Re[1 - \frac{3}{4}(g(\tilde{\omega})J)^2] = 0$ and (green dashed) $\Im[1 - \frac{3}{4}(g(\tilde{\omega})J)^2] = 0$ plotted for $|\tilde{\omega}|/\epsilon_c < 30$. The contours of (blue) $\Re[1 - \frac{3}{4}(g(\tilde{\omega})J)^2]$ and (red) $\Im[1 - \frac{3}{4}(g(\tilde{\omega})J)^2]$ are plotted for $0 < \tilde{\omega}/\epsilon_c < 30$ and $0 > \tilde{\omega}/\epsilon_c > -30$, respectively, and as a function of J/ϵ_c. All contours have $D/\epsilon_c = 100$ and as a function of J/ϵ_c. The straight black lines lines $J/\epsilon_c = 0.426$ and $\tilde{\omega}/\epsilon_c = 11.48$ together and for $J/\epsilon_c = 0.5$ and $\tilde{\omega}/\epsilon_c = \pm 11.48, \pm 16.16$ together are to guide the eye for the solution $Re[1 - \frac{3}{4}(g(\tilde{\omega})J)^2] = 0$.

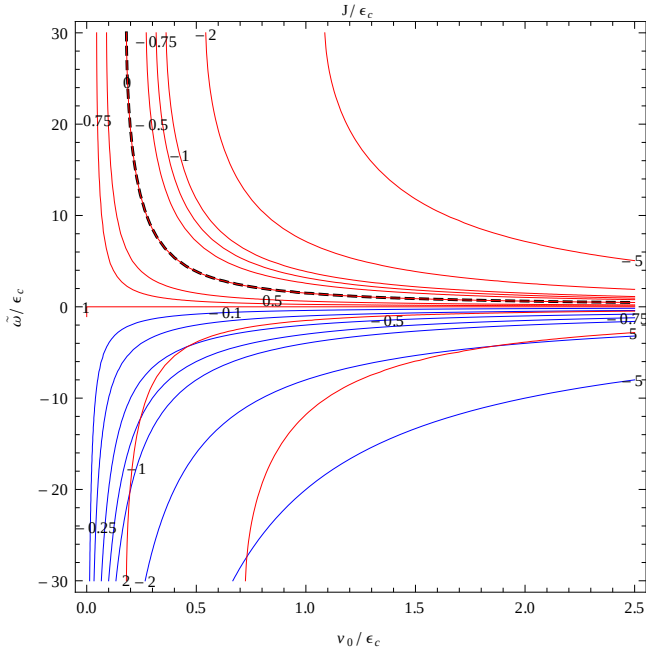

Figure 4.4: Contour of (black dashed) $\Re[1 + U\, g(\tilde{\omega})] = 0$, (green dashed) $\Im[1 + U\, g(\tilde{\omega})] = 0$, (red) $\Re[1 + U\, g(\tilde{\omega})]$ for $|\tilde{\omega}/\epsilon_c| < 30$ and (blue) $\Im[1 + U\, g(\tilde{\omega})]$ as function of $0 > \tilde{\omega}/\epsilon_c < 30$ all as a function of v_0/ϵ_c for $D\epsilon_c = 100$.

The value $J = 0.5$ is chosen, because a solution $\Re[1 - \frac{3}{4}(g(\tilde{\omega})J)^2] = 0$ exist for $\tilde{\omega} = \pm 11.48$ and $\tilde{\omega} = \pm 16.16$ as illustrated by the straight lines in figure 4.3. The $\Re[1 - \frac{3}{4}(g(\tilde{\omega})J)^2]$ and

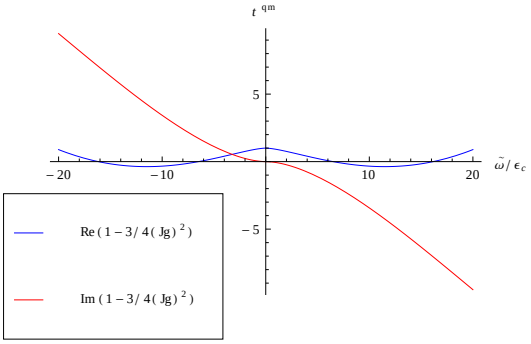

Figure 4.5: t^{qm}-function: Blue line $\Re[1 - \frac{3}{4}(g(\tilde{\omega})J)^2]$ and red $\Im[1 - \frac{3}{4}(g(\tilde{\omega})J)^2]$ as a function of $\tilde{\omega}/\epsilon_c$ for $J/\epsilon_c = 0.5$.

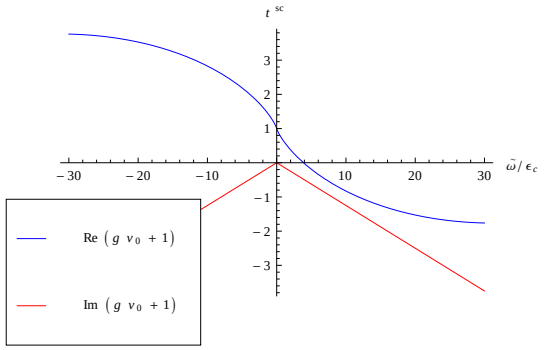

Figure 4.6: t^{sc}-function: Blue line $\Re[1+g(\tilde{\omega})V_0]$ and red line $\Im[1+g(\tilde{\omega})V_0]$ as a function of $\tilde{\omega}/\epsilon_c$ for $V_0/\epsilon_c = 0.5$.

$\Im[1 - \frac{3}{4}(g(\tilde{\omega})J)^2]$ for the specific $J = 0.5$ is plotted in figure 4.5(a) Likewise the scalar strength $V_0 = 0.5$ is chosen to be the same as the quantum impurity coupling, since it neither encounter any singularities in the denominator which is reflected in figure 4.4 by the fact that $\Re[1 + g(\tilde{\omega})v_0] \neq 0$ when $\Im[1 + g(\tilde{\omega})v_0] = 0$ and vise versa. The only values for which $\Im[1 - \frac{3}{4}(g(\tilde{\omega})J)^2] = 0$ exist, is for $\tilde{\omega} = 0$, but here $\Re[1 - \frac{3}{4}(g(\tilde{\omega})J)^2] \neq 0$. If a larger $J > 0.5$ was choosen, the $\Re[1 - \frac{3}{4}(g(\tilde{\omega})J)^2]$ would approach zero.

A plot of the real and imaginary parts of the total factor $t(\tilde{\omega}, J)$ is presented in figure 4.7 for the qm-impurity and the scalar in figure 4.8, both for $J = V_0 = 0.5$. This show that the t-function does not encounter a singularity. Again if a larger value $J = V_0 > 0.5$ was chosen, the hills/ valleys would be larger positive/negative and approach/get further away from the $\tilde{\omega} = 0$ point and reverse if a smaller value $J = V_0 < 0.5$ was chosen.

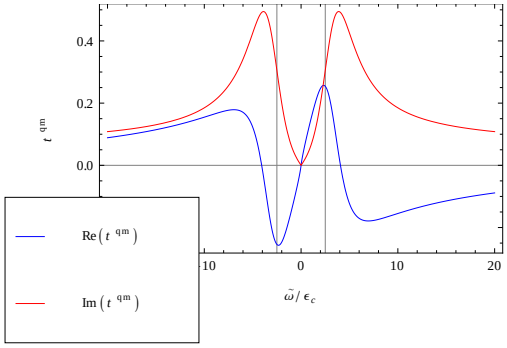

Figure 4.7: t^{qm}-function: blue line $\Re[t^{qm}(\tilde{\omega}, J)]$ and red line $\Im[t^{qm}(\tilde{\omega}, J)]$ for $J/\epsilon_c = 0.5$.

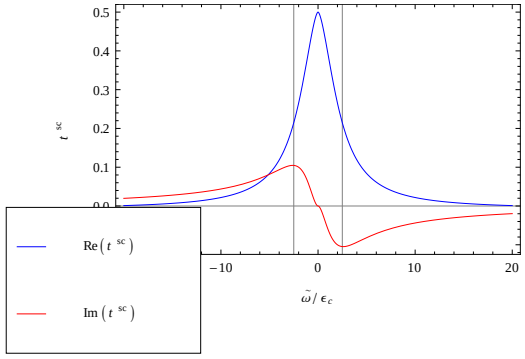

Figure 4.8: t^{sc}-function: blue line $\Re[t^{sc}(\tilde{\omega}, V_0)]$ and red line $\Im[t^{sc}(\tilde{\omega}, V_0)]$ for $V_0/\epsilon_c = 0.5$.

Chapter 5

Basic STM

In 1981 Binning and Roher developed the scanning tunneling microscope (STM) and spectroscopy (STS) which consist of a sharp metallic tip mounted on a piezoelectric drive. The tip acts as a *local probe* which can be scanned in the x, y-plane by the X and Y actuators in a given height z above the sample by the Z actuator, see figure 5.1(b). Applying a bias voltage, eV, between the

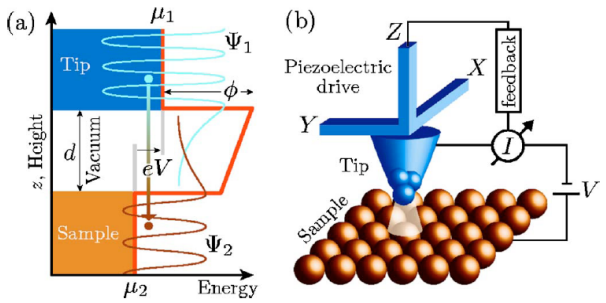

Figure 5.1: Principle of STM/STS, (a) tunneling process and (b) Schematic setup of the STM/STS. Adapted from ref [16]

metallic tip and the conducting sample while approaching the tip within a few angstroms from the sample surface results in a measurable tunneling current.
Hence, see figure 5.1(a), the phenomenon behind STM(S) is quantum tunneling of electrons between two electrodes (i.e. the tip and sample which for simplicity are assumed to have same work function ϕ) separated by a thin potential barrier (e.g. the vacuum) of width d and also height ϕ.
The electron wave functions, Ψ_1 and Ψ_2, decays exponentially into the vacuum barrier and overlaps spatially allowing electrons to tunnel between electrodes. Applying a bias voltage determines the relative heights of the electrodes chemical potential, μ_1 and μ_2, thus determining the preferred tunneling direction. A positive bias voltage applied to the sample, drives the electrons to tunnel from tip into unoccupied electron-states in the sample and vice verse.

The tunneling Hamilton formalism[4, 16, 17] launched by Bardeen[5] and Tersoff & Harmann[38] provides to understand tunneling of single-particle states through a junction. If the temperature and applied bias is sufficiently low, the tunneling of quasipariticles from the two isolated materials can reasonably be treated as in thermal equilibrium. Further, the current amplitude is so low that the tunneling process can be described by a single-particle electron process and correlations in the barrier can be neglected, thus a linear-response technique can be used to calculate the current.

The transfer of particles across the barrier is then described by the phenomenological tunneling Hamilton

$$H_T = \sum_{\lambda,\rho} T_{\lambda\rho} c_\rho^\dagger c_\lambda + H.c. \tag{5.1}$$

where c_λ destroys a particle in the quantum state λ in the sample whereas $c_\rho^\dagger$ creates an particle in state ρ in the tip. The tunneling matrix $T_{\lambda\rho}$ depends on the specific tunneling junction geometry and the electronic-state quantum numbers. Linear-response gives a tunneling current

$$I \propto \int \mathrm{d}\omega \left[f(\omega - eV) - f(\omega) \right] \sum_{\lambda,\rho} |T_{\lambda\rho}|^2 A_\rho^{tip}(\omega - eV) A_\lambda^{sample}(\omega) \tag{5.2}$$

The current Eqn. (5.2) is determined by three factors: the tunneling matrix, $|T_{\lambda\rho}|^2$, that measures the overlap of wave-functions. The energy window $[f(\omega - eV) - f(\omega)]$ of available states weighted by the respective density of states $A_\rho^{tip}(\omega - eV) A_\lambda^{sample}(\omega)$ in the tip and sample at the relevant energies. The single-particle spectral function of the isolated tip (A_ρ^{tip}) and sample (A_λ^{sample}) materials in principle *a priori* convey *all* tip-geometry and surface effects.

The expression Eqn. (5.2) is phenomenological and applies to any type of tunneling junction. If the tip is a simple metal where one can assume the tip density of states to be constant and tunneling matrix independent of λ so

$$\sum_\rho |T_{\lambda\rho}|^2 A_\rho^{tip}(\omega - eV) \approx \text{constant}$$

then the *differential conductance* - the derivative of the current with respect to the bias voltage - becomes

$$\frac{\mathrm{d}I}{\mathrm{d}V} \propto \int \mathrm{d}\omega \left(-\frac{\partial f(\omega - eV)}{\partial \omega} \right) \sum_\lambda A_\lambda^{sample}(\omega) \tag{5.3}$$

For low temperatures $T \to 0$, $-\frac{\partial f(\omega - eV)}{\partial \omega} \approx \delta(\omega - eV)$ then Eqn. (5.3) becomes

$$\frac{\mathrm{d}I}{\mathrm{d}V} \propto \sum_\lambda A_\lambda^{sample}(\omega = eV) \tag{5.4}$$

However, in order to understand a local probe such as STM(S), it is convenient to express it in terms of the sample real-space spectral function. The *differential tunneling conductance*

$$\frac{\mathrm{d}I}{\mathrm{d}V(\mathbf{r})} \propto \sum_\lambda A_\lambda^{sample}(\mathbf{r}, \mathbf{r}; \omega = eV) = \rho(\mathbf{r}; \omega = eV) \tag{5.5}$$

is proportional to the LDOS, $\rho(eV, \mathbf{r})$, at bias energy eV and the tip position $\mathbf{r}$.
The LDOS is in turn related to the *sample electronic Green function*

$$\rho(\mathbf{r}, \omega)\big|_{\omega = eV} = \sum_\lambda A_\lambda^{sample}(\mathbf{r}, \mathbf{r}; \omega)|_{\omega = eV} = \frac{-1}{\pi} \sum_\lambda \Im G_\lambda^{sample}(\mathbf{r}, \mathbf{r}; \omega + i\,0^+)|_{\omega = eV} \tag{5.6}$$

Hence STM(S) by measuring the tunneling current between metallic tip and sample as function of bias voltage and tip position (which is controlled with atomic resolution) provides a real-space 'topological' image[1] of the sample LDOS.

[1] topology here is not to be confused with any topological aspects mentioned before. This has only to do with the $\mathbf{r}$-image topological landscape of the electronic LDOS.

A STM(S) measurement of the local tunneling conductance $\frac{\mathrm{d}I}{\mathrm{d}V(\mathbf{r})}$ is taken over a predetermined $L\times L$ grid of points that cover a region approximately $600AA\times 600AA$. Assuming that the tunneling conductance is proportional to the underlying density of states of the sample layer the expression (5.5) is valid[2]. These measurements, (5.5), give a STM(S) map of the local tunneling density of states $\rho(\mathbf{r};\omega)$ for probing frequencies $\omega =$ eV of the external bias voltage. The Fourier transformed, *FT-LDOS*, of this LDOS map in a continuum limit

$$\rho(\mathbf{q};\omega) = \int \mathrm{d}^2\mathbf{r} e^{-i\mathbf{q}\cdot\mathbf{r}}\rho(\mathbf{r};\omega) \tag{5.7}$$

What will be discussed in the section 6 is the $|\rho(\mathbf{q};\omega)|$ factorization into a quasi particle spectrum Ω-structure and a t-function of the scattering impurity and in section 5.1 the LDOS (5.5). Note that appendix C in detail explain the connection between the long distance expansion of the LDOS oscillations and the FT-LDOS. Hence it connects this chapter 5 with chapter 6.

After decades of STM(S) investigation of superconducting materials, it is by now a well accepted interpretation[13] that LDOS oscillations results from surface quasi particle interference due to impurity induced scatterings. FT-LDOS data can be analyzed in terms of a set of probe frequency-dependent wave vectors $\mathbf{q}_\alpha(\omega)$ which connect the tips of the *constant energy contour (CEC)* specified by the quasi particle dispersion relation $\omega = \epsilon_{\eta,\mathbf{k}}$. That this is necessarily so becomes clear when considering the full retarded Green function

$$G(\mathbf{r},\mathbf{r}';\omega) = G_0(\mathbf{r},\mathbf{r}';\omega) + \delta G(\mathbf{r},\mathbf{r}';\omega) \tag{5.8}$$

where the homogeneous (impurity free surface) bare Green function in Dirac model approximation[9]

$$G_0(\mathbf{r},\mathbf{r}';\tilde{\omega}) = \frac{|\tilde{\omega}|}{4}\left(f_0(\tilde{\omega},\rho) + f_1(\tilde{\omega},\rho)\left(\hat{\boldsymbol{\rho}}\times\bar{\tau}\right)_z\right)\left(\frac{1}{v_F\hbar}\right)^2 \quad \tilde{\omega} = \omega + \mu \tag{5.9}$$

in units of $L^{-2}\,\mathrm{energy}^{-1}$. The unnormalized distance (probe to local impurity) vector is denoted $\boldsymbol{\rho} = \mathbf{r} - \mathbf{r}'$ which normalized has the unit vector $\hat{\boldsymbol{\rho}} = \frac{\boldsymbol{\rho}}{\rho}$ and the magnitude denoted $\rho = |\boldsymbol{\rho}|$. The functions

$$\begin{aligned} f_0(\tilde{\omega},\rho) &= s(\tilde{\omega})Y_0(|\tilde{\omega}|\rho) - iJ_0(|\tilde{\omega}|\rho)\Theta(D-|\tilde{\omega}|), \\ f_1(\tilde{\omega},\rho) &= iY_1(|\tilde{\omega}|\rho) + s(\tilde{\omega})J_1(|\tilde{\omega}|\rho)\Theta(D-|\tilde{\omega}|) \end{aligned} \tag{5.10}$$

$$\tag{5.11}$$

are both symmetric in frequency $\tilde{\omega}$. The J_n and Y_n denote the Bessel functions of first and second kind of order n. The local bare propagator for $\mathbf{r} = \mathbf{r}'$

$$G_0(\mathbf{r},\mathbf{r};\tilde{\omega}) = -g(\tilde{\omega})\mathbb{I} \tag{5.12}$$

since $\rho = 0$ whenever $\mathbf{r} = \mathbf{r}'$ and this holds for all $\mathbf{r} = \mathbf{r}'$ and $g(\tilde{\omega})$ is given by Eqn. (4.13). This give a bare spin-unresolved LDOS

$$\rho_0(\mathbf{r},\tilde{\omega}) \equiv \frac{-1}{\pi}\Im\, Tr\, G_0(\mathbf{r},\mathbf{r};\tilde{\omega}) = \frac{|\tilde{\omega}|}{2\pi}\Theta(D-|\tilde{\omega}|)\left(\frac{1}{v_F\hbar}\right)^2 = \rho_0(\tilde{\omega}) \tag{5.13}$$

[2] If this is not the case a momentum-dependent tunneling matrix element would enter in (5.3) and give rise to a *tunneling matrix element form factor* in the FT-LDOS.

i.e. independent on distance r from the impurity site but linear dependent on frequency $|\tilde{\omega}|$ so $\rho_0(\tilde{\omega})$ is a *homogeneous shift* for a given frequency and given in units of in units of L^{-2} energy^{-1}. On the other hand the bare FT-LDOS

$$\rho_0(\mathbf{k},\omega) \propto \delta(\mathbf{k})$$

has *no* **k**-*resolution* in units of energy^{-1}.

On the contrary, the qm-correction Green function which contain the information on multiple scatterings of the local $\delta(\mathbf{r})$ impurity

$$\delta G(\mathbf{r},\mathbf{r};\tilde{\omega}) = G_0(\mathbf{r};\tilde{\omega}) T_{imp.}(\tilde{\omega}) G_0(-\mathbf{r};\tilde{\omega}) \tag{5.14}$$

arise due to scatterings (described by the T-matrix) induced by impurity and is given in units of energy^{-1}. Thus, it's now rather obvious that the spin-unresolved FT-LDOS (the Fourier transformed LDOS Eqn. (5.6)) [3]

$$\begin{aligned}\delta\rho(\mathbf{q},i\tilde{\omega}_n) &\equiv \int \mathrm{d}\mathbf{r} \exp\left(i\,\mathbf{q}\cdot\mathbf{r}\right) Tr\left[\delta\rho(\mathbf{r},\mathbf{r};i\tilde{\omega}_n)\right] \\ &= \left(\frac{L}{\hbar v_F}\right)^2 \frac{1}{2\,i} \int \frac{\mathrm{d}^2\mathbf{k}}{(2\pi)^2} Tr\left[\delta\, G(\mathbf{k},\mathbf{k}+\mathbf{q};i\tilde{\omega}_n) - (\delta\, G(\mathbf{k},\mathbf{k}-\mathbf{q};i\tilde{\omega}_n))^*\right]\end{aligned} \tag{5.15}$$

inhere the information of scattering between quasi particle-states with wave vector $\mathbf{q} = \mathbf{k}_i - \mathbf{k}_f$ (and wavelength $\lambda = 2\pi/q$). These scatterings modulate the LDOS in **r**-space in a manner which corresponds to this interference pattern produced by the quasi particle scattering. Since the STM can measure the differential conductance Eqn. (5.5) that is proportional to the LDOS, the STM(S) observes these spatial modulations and thus indirectly reveal the scattering vectors by its Fourier transform.

To summarize; a FT-LDOS of STM(S) image from a homogeneous(impurity free) surface does not have any **k**-space resolution at all since no quasi particle interference pattern is produced. Only when impurities are introduced to a surface interference pattern which modulate the electronic state LDOS appear and hence a FT-LDOS with **k**-resolution as well. An impurity is needed in order to induce scatterings and this information is contained in the T-matrix and hence in the full Green propagator which determine the LDOS Eqn. (5.6). FT-STM data can be analyzed in terms of a set of frequency-dependent wave vectors $\mathbf{q}_\alpha(\omega)$ which connect the tips of the CEC (since energy-conservation has to be respected by requirement) specified by the quasi particle dispersion relation $\omega = \epsilon_{\eta,\mathbf{k}}$.

[3] Note the Green function depends on two **k**-momenta which in necessary since the presence of the impurity break translation-invariance of the sample. Since the scattering is *energy-elastic* all fermion lines have the same frequency label ω therefore it enters $\delta G(\mathbf{r},\mathbf{r};\tilde{\omega})$. But the trace(Tr) over spin is necessary because the scattering allow for *spin-inelastic* processes. However, the total (electron and impurity) spin is conserved so the perturbation from the impurity preserve TR-symmetry

5.1 LDOS

The system properties directly accessible to STM(S) measurements that will be treated here are obtained by spin-unresolved and spin-resolved LDOS. By knowing the modifications to the bare Eqn. (5.13) LDOS surface electron LDOS induced by the different impurities it will be possible to determine

(i) the stability of the LDOS near the Dirac-point, in the sense, whether the presence of impurities open a gab in the LDOS or not.

(ii) whether quasi-bound states appear or not. These can only be *quasi-bound* states and not real bound-states, because the analysis of $t^{imp.}$-function in section 4.3.1 showed that neither $t^{imp.}$ had any singularities for a finite coupling.

(iii) the difference between the nature of the impurities on the surface.

(iv) Friedel oscillations in the LDOS which are intimately related to the possible scattering vectors.

The first two subjects of investigation (i) and (ii) are relevant[9, 10, 3, 2, 1] for the proposed applications of TIs to spintronics and to perform topological quantum computing. Because these are supposed to exploit the 'topological protection' enjoyed by the Dirac node and surface states in presence of time-reversal symmetric perturbations. In that regard it is also useful to know the stability when a time-reversal breaking perturbation is introduced. Knowing about (iii) make it possible to determine the nature, i.e. being magnetic or non-magnetic, of the impurities embedded on a given helical surface. This is possible because the spin-unresolved and spin-resolved LDOS will tell the difference between them, and hence experimental STM map data can fit to these expressions, which will tell the nature of the impurities at the sample surface at hand.

The LDOS Friedel oscillations (iv) attenuate in a power-law decay rate, and hence this decay rate reveal which scattering pairs $(\mathbf{k}_f, \mathbf{k}_i)$ that contribute to the LDOS interference pattern. This together with (iii) should be reflected in the FT-LDOS analysis which is also interpreted to reveal the possible scattering channels.

The relevant derived quantities that answer these questions (i), (ii) and (iii) all depend on the given impurity energy dependence which as shown in section 4.3 is completely determined by the t-function for the impurity in question. As shown, it depends solely on the probing frequency/bias voltage ω and Fermi level μ though $\tilde{\omega}$ and the impurity strength V_0,S or J. Therefore these quantities for the quantum magnetic impurity may be changed by the appearance of the Kondo problem for $|\mu| \neq 0$, which is modulated here by an enhancement of the effective coupling J. Conversely (iv) will not be affected by the arise of the Kondo problem, because it only depends on the long-distance behavior of Eqn. (5.5).

These questions (i),(ii),(iii) and (iv) have been published in ref [9, 10, 3, 2, 1, 49, 42, 31] on the scalar potential and the classical magnetic impurity. For the quantum-impurity only (iv) has been analyzed by slave-boson mean-field theory in ref [39]. To my knowledge, on the questions (i),(ii) and (iii) regarding the quantum impurity, no published work exist so far. Therefore these matters concerning the quantum magnetic impurity presented in this thesis will be the first published.

The inclusion of the 3^{rd} order term to the self-energy of the qm-impurity will show a strong dependence of the μ and ω which is not present in the 2^{nd} order. If the T-matrix to 3^{rd} order $T = T^{(2)} + T^{(3)}$ had been calculated and used, the t^{qm}-function would inhere this information and hence the LDOS as well. But only $T = T^{(2)}$ is calculated, because the difference in LDOS spin-unresolved and spin-resolved turn out to be able to differentiate between all the impurities and hence $T = T^{(2)} + T^{(3)}$ is not needed. Therefore the effect of the Kondo problem will be modulated

by increasing J which suffice to answer (i),(ii) and (iii) in this physical condition of temperatures below the Kondo temperature.

The quantities directly accessible to STM that will be considered here are the following ones: *full spin-unresolved LDOS*

$$\rho(\mathbf{r},\omega) \equiv \frac{-1}{\pi}\Im Tr\, G(\mathbf{r},\mathbf{r};\omega) = \frac{-1}{\pi}\Im Tr\, G_0(\mathbf{r},\mathbf{r};\omega) - \frac{1}{\pi}\Im Tr\, \delta G(\mathbf{r},\mathbf{r};\omega) = \rho_0(\omega) + \delta\rho(\mathbf{r};\omega)$$

with $\rho_0(\omega)$ given by Eqn. (5.13). The *correction* - $\delta\rho(\mathbf{r},\omega)$ - *spin-unresolved LDOS*

$$\delta\rho(\mathbf{r};\omega) = \frac{-1}{\pi}\Im Tr\, \delta G(\mathbf{r},\mathbf{r};\omega) \tag{5.16}$$

and further the *LDOS of spin up(+)/down(-) states in spatial direction* $i = 1,2,3$

$$\rho^i_{\pm}(\mathbf{r};\omega) \equiv \frac{-1}{\pi}\Im Tr\left[G(\mathbf{r},\mathbf{r};\omega)\left(\frac{\tau^0 \pm \tau^i}{2}\right)\right] = \frac{\rho(\mathbf{r};\omega)}{2} \mp \frac{1}{\pi}\Im Tr\left[G(\mathbf{r},\mathbf{r};\omega)\frac{\tau^i}{2}\right] \tag{5.17}$$

so the spin $\pm$-resolved LDOS in the i'th-spin direction projected onto the j'th axis is $\rho^i_{\pm}(\mathbf{r}_j;\tilde{\omega})$ at a given probe energy/frequency $\tilde{\omega}$.

In order to calculate Eqn. (5.16) and (5.17) which is in the $\mathbf{r}$-representation the T-matrix in $\mathbf{k}$-representation for the scalar potential Eqn. (4.2), classical magnetic impurity Eqn. (4.3) and the quantum magnetic impurity Eqn. (4.11) need to be Fourier transformed because it enter Eqn. (5.8) though

$$\delta G(\mathbf{r},\mathbf{r}';\tilde{\omega}) = \int \mathrm{d}^2\mathbf{r}_1 \int \mathrm{d}^2\mathbf{r}_2 G_0(\mathbf{r},\mathbf{r}_1;\tilde{\omega}) T_{imp.}(\mathbf{r}_1,\mathbf{r}_2;\tilde{\omega}) G_0(\mathbf{r}_2,\mathbf{r}';\tilde{\omega}) \tag{5.18}$$

The scalar potential and classical magnetic impurity are readily Fourier transformed because their bare propagators are in the σ-basis. Hence

$$T^{imp.}(\mathbf{r},\mathbf{r}';\tilde{\omega},U) = \int \frac{\mathrm{d}^2\mathbf{k}}{(2\pi)^2}\int \frac{\mathrm{d}^2\mathbf{k}'}{(2\pi)^2} e^{i\mathbf{k}\cdot\mathbf{r}} e^{-i\mathbf{k}'\cdot\mathbf{r}'} T^{imp.}(\mathbf{k},\mathbf{k}';\tilde{\omega},U) = t^{imp.}(\tilde{\omega},U)\delta(\mathbf{r})\delta(\mathbf{r}') \tag{5.19}$$

where U symbolize the strength of the scalar v_0 or classical magnetic S for the representative impurity considered. Also $t^{imp.}(\tilde{\omega},U)$ represent the t-function for Eqn. (4.56) for the scalar, but for the classical magentic impurity it has the expression

$$t^{cl}(\tilde{\omega},S) = t^{cl}_1(\tilde{\omega},S) + t^{cl}_2(\tilde{\omega},S) \quad , \quad t^{cl}_1(\tilde{\omega},S) = \frac{S}{1-(S\,g(\tilde{\omega}))^2} \quad , \quad t^{cl}_2(\tilde{\omega},S) = -\frac{S^2 g(\tilde{\omega})}{1-(S\,g(\tilde{\omega}))^2} \tag{5.20}$$

and $t^{cl}_2(\tilde{\omega},S)$ is t-function Eqn. (4.58) for the classical magnetic impurity.

The correction to the local full Green function in $\mathbf{r}$-representation is then

$$\begin{aligned}\delta G^{imp.}(\mathbf{r},\mathbf{r},\tilde{\omega},U) &= \int \mathrm{d}^2\mathbf{r}_1 \int \mathrm{d}^2\mathbf{r}_2 G^0(\mathbf{r},\mathbf{r}_1,\tilde{\omega}) T^{imp.}(\mathbf{r}_1,\mathbf{r}_2,\tilde{\omega},U) G^0(\mathbf{r}_2,\mathbf{r},\tilde{\omega}) \\ &= t^{imp.}(\tilde{\omega},U)\, G^0(\mathbf{r},0,\tilde{\omega}) G^0(0,\mathbf{r},\tilde{\omega})\end{aligned} \tag{5.21}$$

where from Eqn. (5.9)

$$\begin{aligned}G^0(\mathbf{r},0,\tilde{\omega}) &= \frac{|\tilde{\omega}|}{4}\left(f_0(\tilde{\omega},r) + f_1(\tilde{\omega},r)\,(\hat{\mathbf{r}}\times\bar{\tau})_z\right) \\ G^0(0,\mathbf{r},\tilde{\omega}) &= \frac{|\tilde{\omega}|}{4}\left(f_0(\tilde{\omega},r) - f_1(\tilde{\omega},r)\,(\hat{\mathbf{r}}\times\bar{\tau})_z\right)\end{aligned}$$

By doing this for the scalar potential its correction to the full Green function in **r**-representation becomes

$$\delta G^{sc}(\mathbf{r},\mathbf{r},\tilde{\omega},J) = t^{sc}(\omega,J)\frac{|\tilde{\omega}|^2}{16}\left(f_0^2(\tilde{\omega},r) - f_1^2(\tilde{\omega},r)\right) \tag{5.22}$$

Likewise for the classical magnetic impurity

$$\delta G^{cl}(\mathbf{r},\mathbf{r},\tilde{\omega},S) = t_1^{cl}(\omega,S)\frac{|\tilde{\omega}|^2}{16}\left(f_0^2(\tilde{\omega},r) - f_1^2(\tilde{\omega},r)\right) + \Delta\delta G^{cl}(\tilde{\omega},\bar{S},\hat{\mathbf{r}}) \tag{5.23}$$

where

$$\Delta\delta G^{cl}(\tilde{\omega},\bar{S},\hat{\mathbf{r}}) = t_1^{cl}(\omega,S)\frac{|\tilde{\omega}|^2}{16}$$
$$\left[f_0^2(\bar{\tau}\cdot\hat{S}) + f_1^2\left[(\bar{\tau}\cdot\hat{z})(\hat{S}\cdot\hat{z}) + (\bar{\tau}\cdot\hat{\mathbf{r}})(\hat{S}\cdot\hat{\mathbf{r}}) - (\hat{\mathbf{r}}\times\hat{z}\cdot\bar{\tau})((\hat{\mathbf{r}}\times\hat{z})\cdot\hat{S})\right] + 2if_0f_1\left[(\bar{\tau}\cdot\hat{\mathbf{r}})(\hat{S}\cdot\hat{z}) - (\bar{\tau}\cdot\hat{z})(\hat{S}\cdot\hat{\mathbf{r}})\right]\right] \tag{5.24}$$

depends on the frequency $\tilde{\omega}$ but also in addition of the magnetic direction $\bar{S}$ and the position of the probe $\hat{r} = (\hat{r}_x, \hat{r}_x, 0)$ in the x,y-plane.

The quantities Eqn. (5.16) and (5.17) are the physical ones in the σ-basis. However, the Green function for the quantum impurity is only expressible in terms of the Greens functions in the η-basis.

$$\begin{aligned}\delta\, G^{qm}(\mathbf{k},\mathbf{k}^{'};\tilde{\omega}) &= U(\phi_{\mathbf{k}})\delta\,\tilde{G}^{qm}(\mathbf{k},\mathbf{k}^{'};\tilde{\omega})U^{\dagger}(\phi_{\mathbf{k}^{'}}) = U(\phi_{\mathbf{k}})\tilde{G}^{0}(k;\tilde{\omega})\tilde{T}^{qm}(\mathbf{k},\mathbf{k}^{'};\tilde{\omega})\tilde{G}^{0}(k^{'};\tilde{\omega})U^{\dagger}(\phi_{\mathbf{k}^{'}}) \\ &= t^{qm}(\tilde{\omega},J)G^{0}(k;\tilde{\omega})G^{0}(k^{'};\tilde{\omega}) = t^{qm}(\tilde{\omega},J)\int\frac{\mathrm{d}^2\mathbf{k}_1}{(2\pi)^2}\int\frac{\mathrm{d}^2\mathbf{k}_2}{(2\pi)^2}G^{0}(k,k_1;\tilde{\omega})G^{0}(k_2,k^{'};\tilde{\omega})\end{aligned} \tag{5.25}$$

since $\tilde{T}^{qm}(\mathbf{k},\mathbf{k}^{'};\tilde{\omega}) = t^{qm}(\tilde{\omega},J)U^{\dagger}(\phi_{\mathbf{k}})U(\phi_{\mathbf{k}^{'}})$ and the bare Green function $G^0(k;\tilde{\omega}) = \delta_{\mathbf{k},\mathbf{k}_i}G^0(k,k_i;\tilde{\omega})$ as is evident by Eqn. (2.10). Now

$$\begin{aligned}\delta G^{qm}(\mathbf{r},\mathbf{r},\tilde{\omega},J) &= t^{qm}(\tilde{\omega},J)\int\frac{\mathrm{d}^2\mathbf{k}}{(2\pi)^2}\int\frac{\mathrm{d}^2\mathbf{k}_1}{(2\pi)^2}e^{i(\mathbf{k}\cdot\mathbf{r}-\mathbf{k}_1\cdot 0)}G^{0}(k,k_1;\tilde{\omega})\int\frac{\mathrm{d}^2\mathbf{k}^{'}}{(2\pi)^2}\int\frac{\mathrm{d}^2\mathbf{k}_2}{(2\pi)^2}e^{i(\mathbf{k}_2\cdot 0-\mathbf{k}^{'}\cdot\mathbf{r})}G^{0}(k_2,k^{'};\tilde{\omega}) \\ &= t^{qm}(\tilde{\omega},J)G^{0}(\mathbf{r},0;\tilde{\omega})G^{0}(0,\mathbf{r};\tilde{\omega}) = t^{qm}(\omega,J)\frac{|\tilde{\omega}|^2}{16}\left(f_0^2(\tilde{\omega},r) - f_1^2(\tilde{\omega},r)\right)\end{aligned} \tag{5.26}$$

The Green function of quantum impurity Eqn. (5.26) and the scalar potential Eqn. (5.22) is on the same form, but differentiated by the t-function belonging to the respective impurity. This is of cause necessarily so, because the T-matrix was on the same form only differentiated by the t-function carrying the information of energies $\tilde{\omega}$ and the impurity strength J and V_0, respectively. The correction of the full Green function of the classical magnetic impurity Eqn. (5.23) is, on the other hand, on a different form than the two others by the same argument.

5.1.1 ρ charge/spin-unresolved LDOS:

The scalar potential:

The spin-unresolved/charge channel LDOS for the scalar potential

$$\rho_{sc}(\mathbf{r};\tilde{\omega},J) = \rho_0(\tilde{\omega}) + \delta\rho_{sc}(\mathbf{r};\tilde{\omega},J) \tag{5.27}$$

with the change in the LDOS

$$\delta\rho_{sc}(\mathbf{r};\tilde{\omega},J) = -\frac{2}{\pi}\Im\left[t^{sc}(\tilde{\omega},J)\frac{|\tilde{\omega}|^2}{16}\left(f_0^2(\tilde{\omega},r) - f_1^2(\tilde{\omega},r)\right)\left(\frac{L}{v_F\hbar}\right)^4\frac{1}{L^2}\right] \tag{5.28}$$

which is neither symmetric or anti-symmetric in frequency $\tilde{\omega}$ nor strength J. Here and in rest of the thesis the potential strength V_0 will be set equal to the quantum coupling J, so $V_0 = J$ to simplify the forthcoming analysis.

The quantum magnetic impurity:

The spin-unresolved LDOS for the qm-magnetic impurity

$$\rho_{qm}(\mathbf{r};\tilde{\omega},J) = \rho_0(\tilde{\omega}) + \delta\rho_{qm}(\mathbf{r};\tilde{\omega},J) \tag{5.29}$$

with the change in LDOS

$$\delta\rho_{qm}(\mathbf{r};\tilde{\omega},J) = -\frac{2}{\pi}\Im\left[t^{qm}(\tilde{\omega},J)\frac{|\tilde{\omega}|^2}{16}\left(f_0^2(\tilde{\omega},r) - f_1^2(\tilde{\omega},r)\right)\left(\frac{L}{v_F\hbar}\right)^4\frac{1}{L^2}\right] \tag{5.30}$$

being symmetric in both frequency $\tilde{\omega}$ and coupling strength J.

The classical magnetic impurity:

When the classical magnetic strength is scaled $S^2 \to \frac{3}{4}J^2$ (this will be the convention in the rest of the thesis) then Eqn. (5.23)

$$\delta G^{cl}(\mathbf{r},\mathbf{r};\tilde{\omega},J) = \delta G^{qm}(\mathbf{r},\mathbf{r};\tilde{\omega},J) + \Delta\delta G^{cl}(\tilde{\omega},\sqrt{3/4}J\hat{S},\hat{\mathbf{r}}) \tag{5.31}$$

and $t_2^{cl}(\tilde{\omega},\sqrt{3/4}J) = t^{qm}(\tilde{\omega},J)$. The change in the LDOS becomes

$$\delta\rho_{cl}(\mathbf{r};\tilde{\omega},J) = \delta\rho_{qm}(\mathbf{r};\tilde{\omega},J) \tag{5.32}$$

since $Tr\left[\Delta\delta G^{cl}(\tilde{\omega},\sqrt{3/4}J\hat{S},\hat{\mathbf{r}})\right] = 0$ because each term involves a $Tr[\tau^i] = 0$ for $i = 1,2,3$. Hence the classical and quantum magnetic impurities have *identical* spin-unresolved LDOS responses Eqn. (5.30).

$$\rho_{cl}(\mathbf{r};\tilde{\omega}) = \rho_{qm}(\mathbf{r};\tilde{\omega}) \tag{5.33}$$

Since $\rho_0(r,\tilde{\omega}) = \rho_0(\tilde{\omega})$ is independent of distance, all LDOS' dependence on magnitude distance $r = \sqrt{r_x^2 + r_y^2}$ only appear in $\delta\rho_{imp.}$ as $f_0^2(\tilde{\omega},r) - f_1^2(\tilde{\omega},r)$ and gives rapid oscillations in $\delta\rho_{imp.}$ as a function of $\tilde{\omega}$ for a given distance r. However, these 'Friedel' oscillations only appear slow in the total LDOS $\rho = \rho_0 + \delta\rho_{imp.}$ due to the much larger magnitude of ρ_0 than $\delta\rho_{imp.}$.

The effect of prolonging/shrinking the distance $|\mathbf{r}|$ is to diminish/enlarge the magnitude of the amplitudes of the oscillations. Likewise by turning the coupling strengths J up/down shift the resonances to smaller/larger $|\tilde{\omega}|$ i.e. towards/away the $\tilde{\omega}$, and amplify/attenuate the resonance peak magnitudes.

For larger values of the $f_{0/1}$ argument $|\tilde{\omega}|r$ the total LDOS approach the bare, i.e. $\rho_{imp.} \to \rho_0$ and the oscillations disappear. These considerations make it natural to plot LDOS only in the low distance and low frequency ranges while keeping the coupling strength J fixed at a representative value.

These effects mentioned are visualized in figure 5.2 which show total-LDOS $\rho_{imp}(\mathbf{r};\tilde{\omega})$ along an arbitrary line ($\delta\rho_{imp.}(r;\tilde{\omega})$ is rotational symmetric) in the (r_x, r_y)-plane. Figures 5.2(a) to (e) exhibits the effect of turning the impurity strength J for a fixed distances $\epsilon_c r = 1$. For lager coupling J, resonance peaks for all impurities arise; the scalar $L^2\epsilon_c\rho_{sc}$ has for all J a larger resonance peak than that of the classical and quantum magnetic ones $L^2\epsilon_c\rho_{cl}$ and $L^2\epsilon_c\rho_{qm}$. Remember that these are identical in the unresolved case and hence only the $L^2\epsilon_c\rho_{Qm}$ is plotted. The resonance peaks are solely determined by the minimum of the denominator of the t^{imp}-function. From figure 4.3 and 4.4 it is evident that the zero-solution to the real part of the t-function denominator for lager J need smaller $\tilde{\omega}$. This is exactly reflected in the figures 5.2(a) to (e). From figure 4.6 and 4.5 for a larger J, the $\Re[t^{imp}]$ approach zero while $\Im[t^{imp}]$ stay unchanged and therefor the peak intensity amplifies. The effect of prolonging the distance from $r = 1$ to $r = 4$ while keeping fixed a certain strength $J = 4$ is showed in figures 5.2(e) to (h), and is solely determined by the functions $f_{0/1}(\tilde{\omega}, r)$.

The results Eqn. (5.27) and (5.32) first derived in ref [9] and the Fridel oscillation in ref [10] (to be discussed lated) have been extended from a local impurity $\delta(\mathbf{r})$ to a finite one. This properly account[3, 2, 1, 49] for the experimental date for certain triangle defects appearing in the topology map of Bi_2Se_3. Also the the low-energy resonances that disrupt but not destroy the LDOS near the defect appearing in figure 5.2 agree with the experimental data.

If the quantum impurity exist on the surface of a STI its coupling would have to be very small and probably no resonance peaks would appear in an STM measurement. However, as shown in section 4.2.1 the Kondo problem arise when lowering the temperature which is effectively the same as enhance the coupling value J. So as the LDOS Eqn. (5.33) shown in figure 5.2, resonance peaks arise for sufficiently high values of J and hence resonance peaks might be detectable for temperatures $T < T_K$ below the Kondo temperature.

5.1.2 $\rho^i_{\pm}$ spin-resolved LDOS:

The scalar potential:

For the scalar potential the spin-resolved LDOS

$$\rho^i_{sc,\pm}(\mathbf{r};\tilde{\omega}, J) = \frac{\rho_{sc}(\mathbf{r};\tilde{\omega}), J}{2} \tag{5.34}$$

Notice that any $\rho^i_{sc,\pm}(\mathbf{r}_j;\tilde{\omega}, J)$, i.e. LDOS $\pm$-spin resolution in *every* i'th-direction ($i = x, y, z$) projected onto *anywhere* in the (r_x, r_y)-plane are identical. Due to Eqn. (5.34) the resonance peak in Eqn. (5.27), which was showed to appear in figure 5.2 for a sufficient large J, is double spin-degenerate.

The quantum magnetic impurity:

The $\pm$ spin-resolved LDOS $\rho^i_{qm,\pm}$ in spin-direction i for the quantum impurity is

$$\rho^i_{qm,\pm}(\mathbf{r};\tilde{\omega}, J) = \frac{\rho_{qm}(\mathbf{r};\tilde{\omega};J)}{2} \tag{5.35}$$

As for the scalar, all the $\rho^i_{qm,\pm}(\mathbf{r}_j;\tilde{\omega}, J)$, i.e LDOS $\pm$-spin in *every* i'th-direction ($i = x, y, z$) projected onto the (r_x, r_y)-plane are identical. But different from the scalar case, the spin-resolved LDOS is symmetric in frequency

$$\rho^i_{qm,\pm}(\mathbf{r}_j;\tilde{\omega}, J) = \rho^i_{qm,\pm}(\mathbf{r}_j;-\tilde{\omega}, J)$$

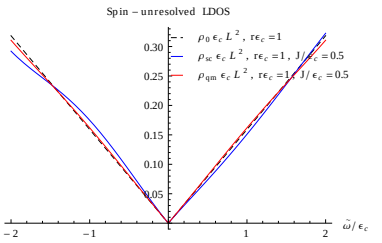

(a) r=1,J=0.5

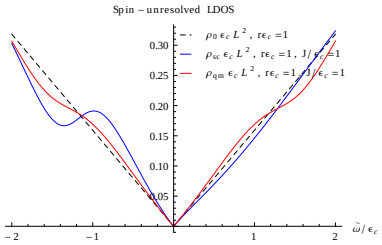

(b) r=1,J=1

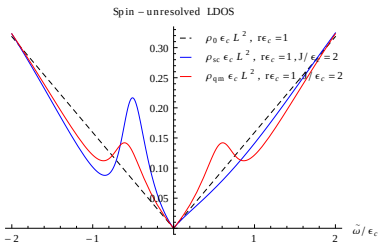

(c) r=1,J=2

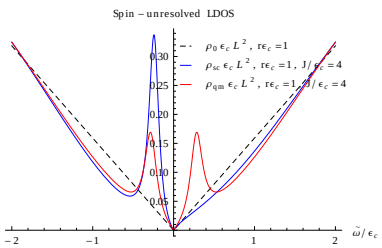

(d) r=1,J=4

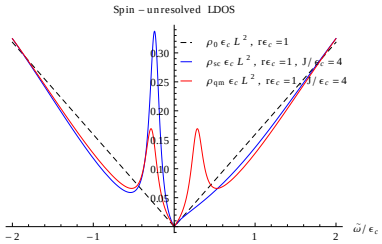

(e) r=1,J=4

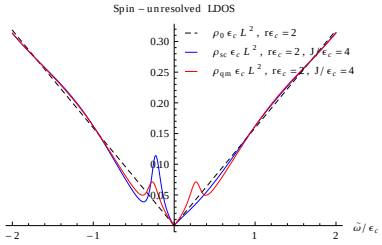

(f) r=2,J=4

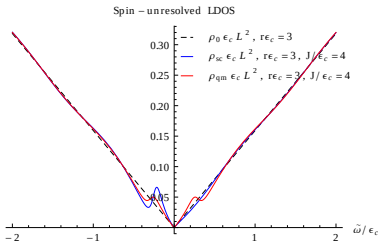

(g) r=3,J=4

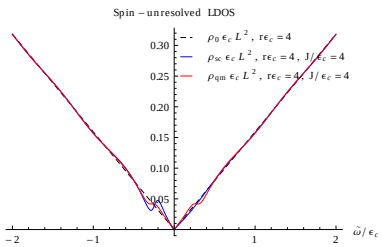

(h) r=4,J=4

Figure 5.2: Plot of LDOS $L^2\epsilon_c\rho_0, L^2\epsilon_c\rho_{sc}$ and $L^2\epsilon_c\rho_{Qm}$ as a function of $\tilde{\omega}/\epsilon_c$ with $D/\epsilon_c = 100$. Figures (a) to (e) have a fixed distance $r/\epsilon_c = 1$ but increasing J, whereas figures (e) to (h) have a fixed coupling J but increasing distance r/ϵ_c.

and coupling

$$\rho^i_{qm,\pm}(\mathbf{r}_j;\tilde{\omega},J) = \rho^i_{qm,\pm}(\mathbf{r}_j;\tilde{\omega},-J)$$

but also notice that (which will be evident below)

$$\rho^i_{qm,\pm}(\mathbf{r};\tilde{\omega},J) \neq \rho^i_{cl,\pm}(\mathbf{r};\tilde{\omega},J)$$

which is the first discrepancy between the the quantum and the classical magnetic impurity considered until now. Due to Eqn. (5.35) the resonance peak in Eqn. (5.29), which was showed to appear in figure 5.2 for a sufficient large J, is double degenerate.

The classically magnetic impurity:

For the classical magnetic impurity[4] the spin-resolved LDOS

$$\begin{aligned}\rho^i_{cl,\pm}(\mathbf{r};\tilde{\omega},J) &= \frac{\rho_{qm}(\mathbf{r};\tilde{\omega},J)}{2} \\ &\mp \frac{1}{\pi}\underbrace{\Im Tr\left[G_{cl}(\mathbf{r},\mathbf{r};\omega,J)\frac{\tau^i}{2}\right]}_{\neq 0}\end{aligned} \tag{5.36}$$

Notice that the $\rho^i_{cl,\pm}(\mathbf{r}_j;\tilde{\omega},J)$ depends on the $\pm$-spin in the i'th direction and the j'th axis to which it's projected onto. This feature is different from both the scalar potential and quantum magnetic impurity. The Eqn. (5.36) means that the resonance peaks are split into two spin-polarized resonance state peaks on either side of $\tilde{\omega}=0$, i.e. appear symmetric on the electron and hole side.
First, $\rho^z_{cl,\pm}(\mathbf{r}_{x,y-plane};\tilde{\omega},J)$ both the $+$ and $-$ z-spin projected LDOS are indifferent onto anywhere in the x,y-plane, which is exhibited in figure 5.3 together with the sum of the spin-resolved along the same direction $\rho^z_{cl}(\mathbf{r}_{x,y-plane};\tilde{\omega},J) = \rho^z_{cl,+}(\mathbf{r}_{x,y-plane};\tilde{\omega},J) + \rho^z_{cl,-}(\mathbf{r}_{x,y-plane};\tilde{\omega},J)$.
Second, $\rho^x_{cl,\pm}(\mathbf{r}_x;\tilde{\omega},J)$ the $\pm$ x-spin projected onto the x-axis is exhibited in figure 5.4 together with the sum of the spin-resolved along the same direction $\rho^x_{cl,\pm}(\mathbf{r}_x;\tilde{\omega},J) = \rho^x_{cl,+}(\mathbf{r}_x;\tilde{\omega},J) + \rho^x_{cl,-}(\mathbf{r}_x;\tilde{\omega},J)$.
Third, $\rho^x_{cl,\pm}(\mathbf{r}_y;\tilde{\omega},J)$ the $\pm$ x-spin projected onto the y-axis is exhibited in figure 5.5 together with the sum of the spin-resolved along the same direction $\rho^x_{cl,\pm}(\mathbf{r}_y;\tilde{\omega},J) = \rho^x_{cl,+}(\mathbf{r}_y;\tilde{\omega},J) + \rho^x_{cl,-}(\mathbf{r}_y;\tilde{\omega},J)$.
At last, in figure 5.6 is illustrated the transformation of $\rho^x_{+,cl}(r_x;\tilde{\omega},J)$ into $\rho^x_{+,cl}(r_y;\tilde{\omega},J)$ and in figure 5.7 the transformation $\rho^x_{-,cl}(r_x;\tilde{\omega},J)$ into $\rho^x_{-,cl}(r_y;\tilde{\omega},J)$. Each graph is for a fixed distance magnitude $\epsilon_c r = \epsilon_c|\mathbf{r}| = 1$ but at different azimuthal angle $\phi_{\mathbf{r}} = \tan^{-1}\left(\frac{r_y}{r_x}\right)$.

For Eqn. (5.35) and Eqn. (5.36) all resonance peaks appear symmetric around $\tilde{\omega}=0$ determined by the t^{imp}-function, which is a result of the Dirac model having a symmetric band cut-off. This is not the case for real Bi_2Se_3 and Bi_2Te_3 materials, and further the Fermi level may be $\mu \neq 0$. Both are effects that cause the resonance peaks not to be situated symmetric on the electron and hole side.

Depending on the probe, using either the spin-unresolved or spin-resolved LDOS makes it possible to distinguish between a scalar potential, classical-and quantum magnetic impurities in which a experiment can use to fit. For the scalar and classical magnetic impurity this have been done as

[4] The results are derived from the Hamilton $H = (\mathbf{k}\times\bar{\tau})_z$ whereas Biswas[9] use $H = \bar{\tau}\cdot\mathbf{k}$. The results $\rho^x_{\pm}(\mathbf{r}_x,\tilde{\omega})$ and $\rho^x_{\pm}(\mathbf{r}_y,\tilde{\omega})$ derived below is the reverse results, i.e. $\rho^x_{\pm}(\mathbf{r}_y,\tilde{\omega})$ and $\rho^x_{\pm}(\mathbf{r}_x,\tilde{\omega})$ respectively, of those of Biswas. However this cause no trouble since as noticed by Zitko[41], the results are identical for both STI low-energy Hamiltonians. I.e. for $H = (\mathbf{k}\times\bar{\tau})_z$ where the spins are rotated by 90 degrees around the z-axis as compared to $H = \bar{\tau}\cdot\mathbf{k}$.

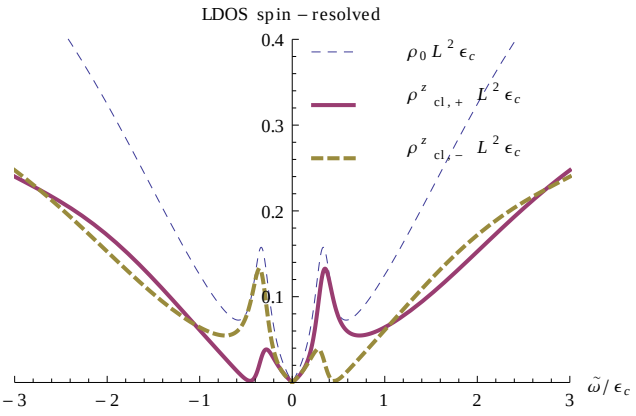

Figure 5.3: Dashed blue: $L^2\epsilon_c\rho^z_{cl.}$, thick purple: $L^2\epsilon_c\rho^z_{+,cl}$, thick dashed green: $L^2\epsilon_c\rho^z_{-,cl}$ as a function of $\tilde{\omega}/\epsilon_c$ for $D/\epsilon_c = 100$, $\epsilon_c r = 1$ and coupling constant $J/\epsilon_c = 3$. Notice that both z-spins $\pm$ retain the same values when projected everywhere in x,y-plane (here at the x-axis).

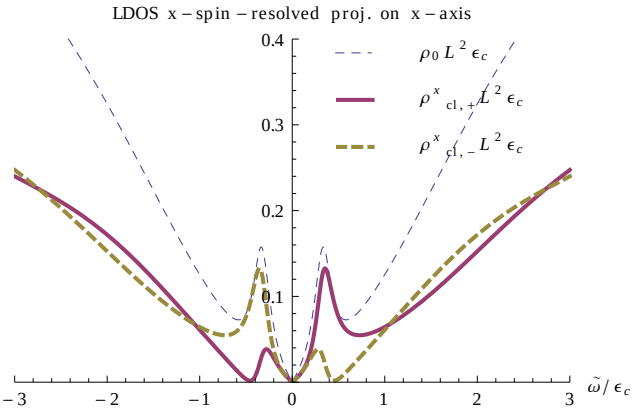

Figure 5.4: Show the x-spin projected LDOS at point on the x-axis. Dashed blue: $L^2\epsilon_c\rho^x_{cl}$, thick purple: $L^2\epsilon_c\rho^x_{+,cl}$, thick dashed green: $L^2\epsilon_c\rho^x_{-,cl}$ as a function of $\tilde{\omega}/\epsilon_c$ for $D/\epsilon_c = 100$, $\epsilon_c r = 1$ and coupling constant $J/\epsilon_c = 3$.

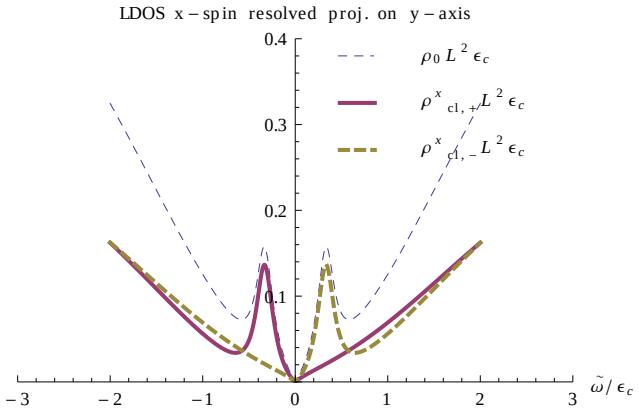

Figure 5.5: Show the x-spin projected LDOS at point on the y-axis. Dashed blue: $L^2\epsilon_c\rho^x_{cl}$, thick purple: $L^2\epsilon_c\rho^x_{+,cl}$, thick dashed green: $L^2\epsilon_c\rho^x_{-,cl}$ as a function of $\tilde{\omega}/\epsilon_c$ for $D/\epsilon_c = 100$, $\epsilon_c r = 1$ and coupling constant $J/\epsilon_c = 3$.

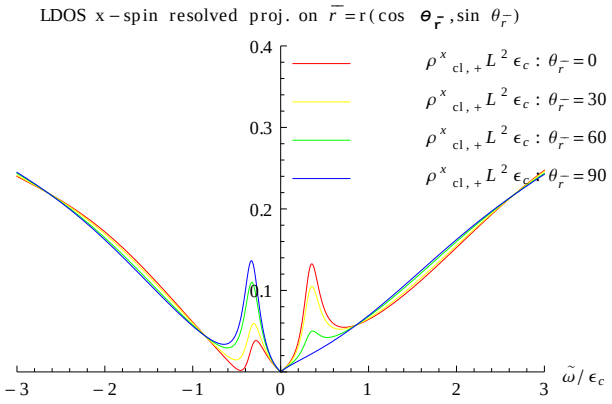

Figure 5.6: Show the x-spin projected LDOS $L^2\epsilon_c\rho^x_{+,cl}$ at point $(r_x, r_y) = (r\cos\phi_{\mathbf{r}}, r\sin\phi_{\mathbf{r}})$ in the r_x, r_y-plane as a function of $\tilde{\omega}/\epsilon_c$ for $D/\epsilon_c = 100$, $\epsilon_c r = 1$ and coupling constant $J/\epsilon_c = 3$. Red: $\phi_{\mathbf{r}} = 0$, yellow: $\phi_{\mathbf{r}} = \pi/6$, green: $\phi_{\mathbf{r}} = \pi/3$ and blue: $\phi_{\mathbf{r}} = \pi/2$.

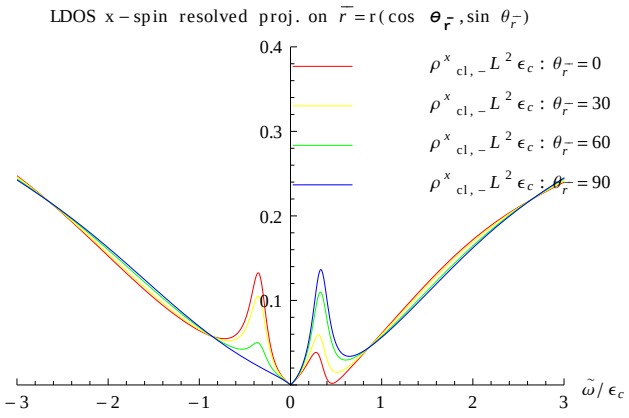

Figure 5.7: Show the x-spin projected LDOS $L^2\epsilon_c\rho^x_{-,cl}$ at point $(r_x, r_y) = (r\cos\phi_{\mathbf{r}}, r\sin\phi_{\mathbf{r}})$ in the r_x, r_y-plane as a function of $\tilde{\omega}/\epsilon_c$ for $D/\epsilon_c = 100$, $\epsilon_c r = 1$ and coupling constant $J/\epsilon_c = 3$. Red: $\phi_{\mathbf{r}} = 0$, yellow: $\phi_{\mathbf{r}} = \pi/6$, green: $\phi_{\mathbf{r}} = \pi/3$ and blue: $\phi_{\mathbf{r}} = \pi/2$.

mentioned above.

Even though the impurities considered here are point-like, then to simplify the arguments for the results obtained, consider two counter-propegating helical wave-vectors: As illustrated in figure 5.8 a magnetic wall with edge along the y-axis and a incoming wave Ψ_1 along the x-direction with spin pointing in the negative y-direction is flipped by the magnetic wall to be aligned in the positive y-direction and traveling back Ψ_2 in the negative x-direction.

The interference $\Psi = \Psi_1 + \Psi_2$, indicated with dark blue spiral-arrows, between these two helical wave-vectors can be shown to have a constant spin-unresolved LDOS, but a spin-spiral LDOS in the xz-plane as illustrated in figure 5.8 by the dark blue spinning arrows. The former STM probe - the charge/spin-unresolved LDOS measures the charge density at a given point $\mathbf{r}$ for a bias energy/probe frequency $\tilde{\omega}$. The latter STM probe - the spin-resolved LDOS $\delta\rho^i_\pm$ measures the interference in the i'th spin channel of the $\pm$ spin-polarization for a bias energy/probe frequency $\tilde{\omega}$.

Since the magnetic wall break time-reversal symmetry by allowing a spin-flip process, then the interference pattern of the two orthogonal waves cause a standing wave that is open in a spin-channel, but is constant in the charge channel. Conversely for the scalar that respect time-reversal symmetry but cannot flip the spin, this interference result in a constant charge density/spin-unresolved LDOS but the spin-channel annihilates to zero.

This considerations make it plausible that $\delta\rho$ for Eqn. (5.27),(5.30) and Eqn. (5.32) together with the vanishing of $\delta\rho^i_\pm$ in Eqn. (5.34) and Eqn. (5.35) but oscillations in Eqn. (5.36).

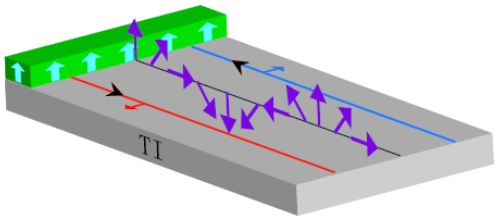

Figure 5.8: A magnetic wall setup from ref [31]: Incoming (blue line) Ψ_1 along x-direction with spin in negative y-direction. It scatter off the wall, with magnetic moment pointing in positive z-direction, which flips its spin to point along the positive y-direction and to propagate Ψ_2 back (red line) along the negative x-direction. The interference (purple line) $\Psi = \Psi_1 + \Psi_1$ cause a constant charge channel but standing wave in the spin-channel.

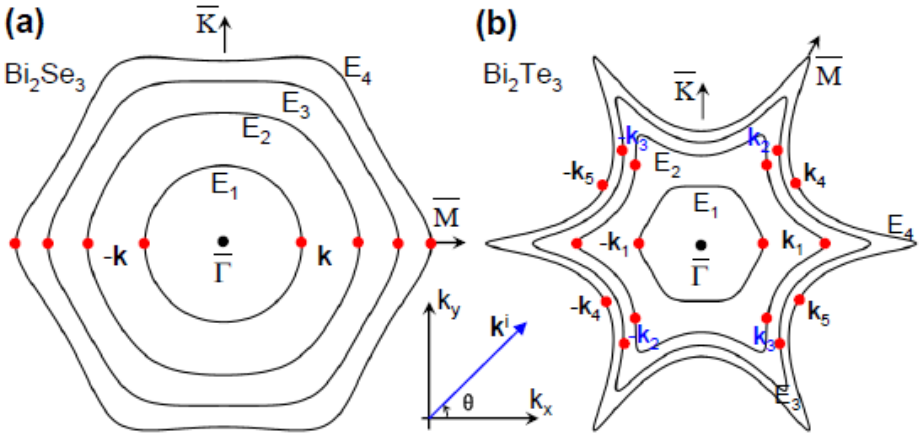

Figure 5.9: Constant energy contours (CEC) with energy E_i of Bi_2Se_3 in (a) and Bi_2Te_3 in (b). (a): $E_1/mV = 380$, $E_2/mV = 700$, $E_3/mV = 740$, $E_4/mV = 860$. (b): $E_1/mV = -50$, $E_2/mV = 110$, $E_3/mV = 230$, $E_4/mV = 340$. Note that ref[42] have $k_x(\Gamma - M)$ and $k_y(\Gamma - K)$ whereas I have $k_y(\Gamma - M)$ and $k_x(\Gamma - K)$.

Bi_2Se_3

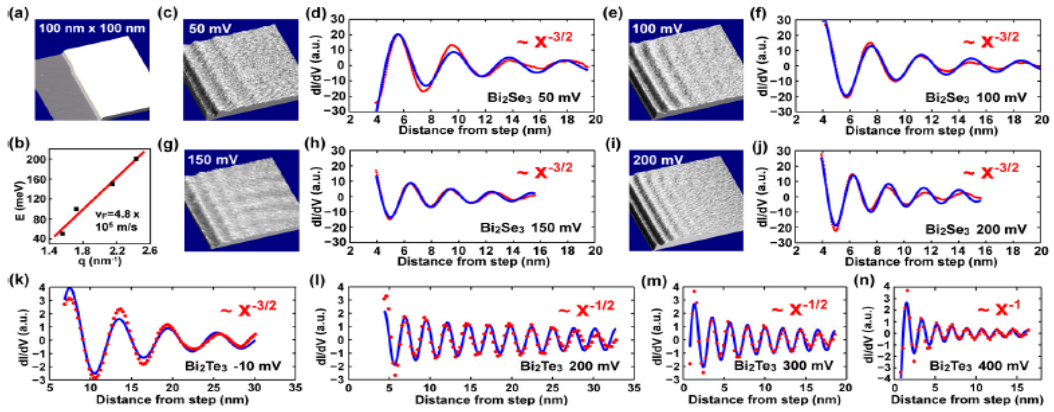

Figure 5.10: Experiment in ref[42]. (a) STM topography of Bi_2Se_3(111) film, (b) Energy disp. deduced from standing waves on the step-edge, (c)-(j) dI/dV maps and LDOS oscillations for different bias voltages of (a). (k)-(n) LDOS oscillations of Bi_2Te_3 for different bias voltages. The red lines in (d),(f),(h),(j),(k),(l),(m) and (n) are fitted curves to the respective LDOS oscillations.

5.2 The importance of the CEC geometry on possible scattering pair states $(\mathbf{k}_f, \mathbf{k}_i)$

The interference pattern between an incoming $\mathbf{k}_i$ and outgoing $\mathbf{k}_f$ wave-vector leads to 'Friedel oscillations' that modify the LDOS at scattering vectors $\mathbf{q} = \mathbf{k}_i - \mathbf{k}_i$. The experiments in ref[1] of Sn and Cd-doped single crystals of Bi_2Te_3, which are widely believed to be of scalar nature, show strongly damped oscillations in the spin-unresolved/charge density LDOS. This feature together with (see section 6.2) the absence of the scattering angle $\mathbf{q} = 2\mathbf{k}_F$ at twice the Fermi momentum vector [22, 21, 50, 35, 31, 37], and the 'anomalies' in the FT-LDOS along $\Gamma - K$ different from the $\Gamma - M$ direction, when the warping effect is present, are all attributed to the forbidden backscattering vector $\mathbf{q}$ in the FT-LDOS. In topological lingo, this strongly suggest that the surface states enjoy a topological protection by time-reversal symmetry on the helical metal for time-reversal preserving disorder like the scalar.

The last two notions, the absence of backscattering and the anomalies when the FS is non-circular, bear to mind, that the geometry of the Fermi surface at constant energy contour (CEC) has an important influence on the possible scattering vectors between pair of states $(\mathbf{k}_f, \mathbf{k}_i)$ that contribute to the LDOS response. Such pairs $(\mathbf{k}_f, \mathbf{k}_i)$ can either be time-reversal pairs, i.e. $|\mathbf{k}_f, \uparrow\rangle = |-\mathbf{k}_i, \downarrow\rangle$, denoted TRP, or they are non-time-reversal pairs, i.e. $|\mathbf{k}_f, \uparrow\rangle \neq |-\mathbf{k}_i, \downarrow\rangle$, denoted non-TRP.

In order to establish the connection between the strong attenuation/damping and the possible scattering vectors; first a review of the possible LDOS attenuations/decay rates for a helical metal will be presented and compared with a conventional metal. Next in section 6 an explanation of the quasi particle interference (QPI) will be presented - an explanation that tacitly takes for granted the common interpretation of the notion of 'absence of backscattering' associated with the suppression standing wave-osculations in the LDOS. Finally, in section 6, the very notion of the absence of backscattering will be examined in detail both of the helical and the conventional metal.

Note that the notion of the absence of the scattering vector $\mathbf{q}$ rely on a interpretation of FT-LDOS, which is crucial to investigate since the scalar and qm-impurity have the same attenuation of the Friedel oscillations, which should mean by ref[31], that they both do not backscatter. But

remember that it was derived in section 3.1 and 4.2, that the qm-impurity *does* indeed backscatter and the scalar *doesn't*, hence the above picture seems misleading.

The helical 2 dimensional surface band dispersion has $\epsilon_\eta(\mathbf{k}) = \eta\sqrt{k^2 + (\lambda k^3 \cos(3\theta_\mathbf{k}))^2}$ when the warping is included. Let the lower $\eta = -$ band be filled completely and the upper $\eta = +$ band partly, then the CECs with energy E_i for Bi_2Se_3 and Bi_2Te_3 are illustrated in figure 5.9(a) and (b), respectively. Scattering on the helical 2 dimensional surface requires a $\delta(\epsilon_+(\mathbf{k}_i) - \epsilon_+(\mathbf{k}_f))$ between incoming $\mathbf{k}_i$ and outgoing $\mathbf{k}_f$ wave-vectors, due to which the energy-elastic scattering enforce $\mathbf{k}_i$ and $\mathbf{k}_f$ to be on the same contour of constant energy (CEC).

Instead of considering a point-like impurity scattering as this thesis only concerns, then for the sake of argument, lets consider an 'edge-setup'. This will make the physical scattering situation much more simple and therefore the physical arguments about the 'influence of the CEC-geometry on possible scattering pairs $(\mathbf{k}_f, \mathbf{k}_i)$' easier. The edge-setup where the edge step

$$V(k_x) = \begin{cases} -V & \text{for} \quad k_x > 0 \\ 0 & \text{for} \quad k_x < 0 \end{cases}$$

a positive constant $V > 0$.
The main difference between an edge-setup from that of a point-impurity scatter, is the requirement of conservation of momentum along the edge, which is along k_y in this example, and the dominant contribution to LDOS comes from *pairs of stationary points*, where the momentum transfer $\mathbf{q} = \mathbf{k}_f - \mathbf{k}_i$ is orthogonal to the edge, i.e. $q_x = k_x^f - k_x^i$ in this example. These constraints give more possible stationary scattering pairs $(\mathbf{k}^f, \mathbf{k}^i)$, but make the calculations easier.

The stationary-phase approximation[37] says, that the pairs $(\mathbf{k}_f, \mathbf{k}_i)$ such that $\bar{\nabla}_{\mathbf{k}_f}\epsilon_+(\mathbf{k}_f)$ and $\bar{\nabla}_{\mathbf{k}_i}\epsilon_+(\mathbf{k}_i)$ are parallel contribute most to the LDOS response. In other words, pairs composed of points whose tangents to the CEC are parallel will dominate the LDOS response. Further due to the edge-setup, scattering vectors $\mathbf{q} = \mathbf{k}_f - \mathbf{k}_i$ which are orthogonal to the edge will contribute to the LDOS response. I.e. the scattering vectors in this setup have to be $q_x = k_x^f - k_x^i$, and all the possible pairs for Bi_2Se_3 and Bi_2Te_3 in this setup, are indicated by red dots on the CEC for each energy E_i in figure 5.9 and will be discussed below.

So along the edge $k_y^f - k_y^i = q_y$ is conserved and interference between $\mathbf{k}^f$ and $\mathbf{k}^i$ creates a standing wave oscillation in the k_x direction with a spatial period of $\frac{2\pi}{k_x^f - k_x^i}$ for a given k_y. The spin-unresolved/charge density LDOS $\delta\rho(\tilde{\omega}, \mathbf{r})$ with the generic form[5] Eqn. (5.37) is in principle a sum over *all* the possible oscillations from the scattered surface state pairs($\mathbf{k}^i, \mathbf{k}^f$) on the CEC.

$$\delta\rho(\tilde{\omega}, \mathbf{r}) = -\frac{1}{\pi}\Im\int \frac{\mathrm{d}^2\mathbf{k}}{(2\pi)^2}\frac{\mathrm{d}^2\mathbf{k}'}{(2\pi)^2}e^{i(\mathbf{k}-\mathbf{k}')\cdot\mathbf{r}}Tr[G_0(\tilde{\omega};\mathbf{k})T(\tilde{\omega};\mathbf{k},\mathbf{k}')[G_0(\tilde{\omega};\mathbf{k}')] \tag{5.37}$$

Hence those pairs who varies much over a small range in k_y will have rapid phase $e^{i(\mathbf{k}_f - \mathbf{k}_i)}$ oscillations in the LDOS Eqn. (5.37) contribution and cancel each other at large k_x. But those whom are *stationary* in respect to small variations in k_y will have slow-varing phases $e^{i(\mathbf{k}_f - \mathbf{k}_i)}$ that add constructively and contribute to the final LDOS.
In figure 5.9(a) are marked the contributing scattering pairs in this setup for Bi_2Se_3 and in Eqn. (5.38) the pairs are listed for the E_i'th CEC. Likewise in figure 5.9(b) are marked the contributing scattering pairs in this setup for Bi_2Te_3 which for the E_i'th CEC and listed in Eqn. (5.39). For the last two CECs E_3 and E_4 the pair $(\mathbf{k}_1, -\mathbf{k}_1)$ vanish because the SSs along $\Gamma - M$ hybridize

[5] which is actually the retarded expression of (5.15).

into the BCB states and hence cannot be separated from them anymore.

$$\mathrm{Bi_2Se_3}\begin{cases} E_1: & (\mathbf{k},-\mathbf{k}) \\ E_2: & (\mathbf{k},-\mathbf{k}) \\ E_3: & (\mathbf{k},-\mathbf{k}) \\ E_4: & (\mathbf{k},-\mathbf{k}) \end{cases} \tag{5.38}$$

and

$$\mathrm{Bi_2Te_3}\begin{cases} E_1: & (\mathbf{k}_1,-\mathbf{k}_1) & & & & \\ E_2: & (\mathbf{k}_1,-\mathbf{k}_1) & , & (\mathbf{k}_2,-\mathbf{k}_3) & , & (\mathbf{k}_3,-\mathbf{k}_2) \\ E_3: & (\mathbf{k}_2,-\mathbf{k}_3) & , & (\mathbf{k}_3,-\mathbf{k}_2) & & \\ E_4: & (\mathbf{k}_4,-\mathbf{k}_5) & , & (\mathbf{k}_5,-\mathbf{k}_4) & & \end{cases} \tag{5.39}$$

Now ref [42] expand the LDOS Eqn. (5.37) in k_y around the stationary scattering pairs listed above, and obtain a power-law decay of the standing waves for each pair $(\mathbf{k}_f, \mathbf{k}_i)$. The exponent index α of the power-law is the decay rate which goes as $x^{-\alpha}$ along the x-axis of the spin-unresolved LDOS. The stationary scattering pairs $(\mathbf{k}_f, \mathbf{k}_i)$ are found to decay with rate α as

$$(\mathbf{k},-\mathbf{k}) \text{ and } (\mathbf{k}_1,-\mathbf{k}_1) \quad , \quad \text{with} \quad \alpha = \frac{3}{2} \tag{5.40}$$

$$(\mathbf{k}_2,-\mathbf{k}_3) \text{ and } (\mathbf{k}_3,-\mathbf{k}_2) \quad , \quad \text{with} \quad \alpha = \frac{1}{2} \tag{5.41}$$

$$(\mathbf{k}_4,-\mathbf{k}_5) \text{ and } (\mathbf{k}_5,-\mathbf{k}_6) \quad , \quad \text{with} \quad \alpha = 1 \tag{5.42}$$

respectively. Hence in an experiment for bias/probe energies[6] ω the LDOS oscillation in x-direction should show power-law rate α as

$$\mathrm{Bi_2Se_3}\left\{\omega \leqq E_4 \quad , \quad \alpha = \tfrac{3}{2}\right. \tag{5.43}$$

and for

$$\mathrm{Bi_2Te_3}\begin{cases} \omega \leqq E_1 & , \quad \alpha = \frac{3}{2} & & \\ \omega \leqq E_3 & , \quad \alpha = \frac{3}{2} & \text{co-exist with} & \alpha = \frac{1}{2} \\ \omega \geqq E_4 & , \quad \alpha = 1 & & \end{cases} \tag{5.44}$$

which is in agreement with the experimental STM differential conductance measurements Eqn. (5.5) resented in figure 5.10 for several bias voltage ω . In figure 5.10 the standing Friedel oscillations are measured for Bi_2Se_3 in figure 5.10(c) to 5.10(j) and for Bi_2Te_3 in figure 5.10(k) to 5.10(n). For each bias voltage ω a red curve is fitted to the experimental measured oscillation. One can see that for bias voltage ω in figure 5.10(c) to 5.10(j) of Bi_2Se_3 fits well/perfect with the predicted decay rate values of α in Eqn. (5.43). Likewise for Bi_2Te_3, one can see that for bias voltage ω in figure 5.10(k) to 5.10(n) the fitted curve agree well with the predicted decay rate values of α in Eqn. (5.44).

The conventional metal reported in ref [13] has $\alpha = \frac{1}{2}$, which is attributed *backscattering* at $\mathbf{q} = 2\mathbf{k}_F$. Hence the decay rate for Bi_2Se_3, which is much faster in a wide energy range than

[6] Note that it is only ω and not $\tilde{\omega}$ because the CECs in figure 5.9(a) and (b) already have been added and subtracted the Dirac point level energy of Bi_2Se_3 and Bi_2Te_3 respectively.

the conventional metal, is attributed to the *absence of the backscattering* vector $\mathbf{q} = 2\mathbf{k}_F$. This suppression of the oscillating standing wave reveal the topological protection of the SSs on the helical metal, which do not occur for the conventional metal. This is not the case for Bi_2Te_3 which has the same decay rate as the conventional metal for some energies.

As mentioned above, the stationary-phase approximation[37] just used, only take into account pairs of $\mathbf{k}_f$ and $\mathbf{k}_i$ such that $\bar{\nabla}_{\mathbf{k}_f}\epsilon_+(\mathbf{k}_f)$ and $\bar{\nabla}_{\mathbf{k}_i}\epsilon_+(\mathbf{k}_i)$ are parallel, i.e. a pair is composed of two points on CEC whose tangents are parallel. Such a pair can either be between a time-reversal symmetric pair (denoted TRP) for which $|\mathbf{k}_f,\uparrow\rangle = |-\mathbf{k}_i,\downarrow\rangle$, or a non time-reversal symmetric pair (denoted non-TRP) in which $|\mathbf{k}_f,\uparrow\rangle \neq |-\mathbf{k}_i,\downarrow\rangle$,

By introducing this discrepancy between the contributing scattering pairs on the CEC, ref [31] extend the analysis of ref [42] presented above, to be able to determine the dominant leading term in the LDOS decay rate for both TRPs and non-TRPs These are summarized in table 5.1 for the edge-setup. This agree with the results presented before, since only the pairs Eqn.(5.40) are TRP and the rest Eqn.(5.41) and Eqn.(5.42) are non-TRP. From the α determined in Eqn.(5.40),Eqn.(5.41) and Eqn.(5.42) one can see in table 5.1 that these agree with each other on the spin-unresolved LDOS decay rates. Ref[31] also calculated the decay rates α for a point-impurity scattering which are summarized in table 5.2. In both tables the conventional metal decay rate is also tabulated.

This distinction between TRP and non-TRP is only introduced, in order to illustrate the simple Fermi surface (or CEC) of the Dirac model considered in this thesis. In this Dirac model, the Fermi surface is circular and only *one* TRP exist and none of the non-TRPs, because only one pair of states with parallel tangents to the circular Fermi surface can be found. Or one can say that many exist, but they are identical because no particular can be picked out. The table 5.2 of the decay rates from pairs in an point-impurity scattering, can now be reduced to table 5.3 for the circular Fermi surface and with the quantum magnetic impurity included form the derivations developed in this thesis.

Table 5.1: Table from ref [31] of α for edge impurities

change in LDOS	$(\mathbf{k}_f, \mathbf{k}_i)$	α for spin-unresolved $\delta\rho$	α for spin-resolved $\delta\rho^i$
scalar	TRP	3/2	-
	non-TRP	1/2	-
classical magnetic	TRP	3/2	1/2
	non-TRP	1/2	1/2
conv.metal		1/2	

Table 5.2: Table from ref [31] of α for point impurities.

change in LDOS	$(\mathbf{k}_f, \mathbf{k}_i)$	α for spin-unresolved $\delta\rho$	α for spin-resolved $\delta\rho^i$
scalar	TRP	2	-
	non-TRP	1	-
classical magnetic	TRP	2	1
	non-TRP	1	1
conv.metal		1	

The decay index α tabulated in table 5.3 for the quantum impurity induced oscillations are the long-distance and low-frequency behavior of the derived Eqn. (5.30) $\delta\rho_{qm}$. And notice that Eqn. (5.35) is tabulated as a blank, because it is only the change in the spin-resolved LDOS that is of significance, i.e. $\delta\rho^i_{qm} = 0$.

Table 5.3: Table of α for point-impurities in the Dirac model.

change in LDOS	$(\mathbf{k}_f, \mathbf{k}_i)$	α for spin-unresolved $\delta\rho$	α for spin-resolved $\delta\rho^i$
scalar	TRP	2	-
classical magnetic	TRP	2	1
quantum magnetic	TRP	2	-
conv.metal		1	

The fast decay rate $\alpha = 2$ of the spin-unresolved LDOS for the scalar potential and quantum magnetic impurity are identical and none of them are spin-resolvable $\delta\rho^i_{sc} = \delta\rho^i_{qm} = 0$. The only published paper treating the quantum impurity regarding this subject is in ref [39], who perform a slave-boson mean-field analysis in the no-warping limit, i.e. the Dirac model as tabulated in table 5.3. Quoting the abstract of ref [39]

> ... the pattern of Friedel oscillation in the helical surface is identical to that of the graphene surface, displaying the inverse-square behavior $\sim r^{-2}$ if the intervally scattering is not introduced in the graphene case. However, introduction of the magnetic field leads the electron density of states from the inverse-square physics to the inverse behavior $\sim r^{-1}$ in the topological insulator's surface while it still remains as $\sim r^{-2}$ in the graphene Kondo effect.

This is partly in agreement with table 5.3, that the quantum-impurity behaves as the scalar, i.e. $\alpha = 2$, when no magnetic field is applied. However, ref [39] find that it behaves as $\alpha = 1$ when applying a finite magnetic field in the z-direction. Under such a field the quantum magnetic impurity should intuitively transform into that of the classical magnetic impurity, and hence keep the decay index $\alpha = 2$ according to table 5.3 of the classical magnetic impurity. But instead, according to the abstract of ref [39], they find the decay index to be $\alpha = 1$. No more comments will be said regarding the result in ref[39], since only the absence of magnetic field is considered in this thesis.

In the literature, the $\alpha = 2$ decay rate is completely attributed to the *absence of backscattering*. As calculated in section 3.1.1 the scalar makes no backscattering transitions, and hence to attribute the $\alpha = 2$ to the absence of backscattering is plausible. However, in section 3.1.2, 3.1.3 and 4.1 it was derived, that the quantum magnetic impurity indeed backscatter, and hence the argument presentended in literature of a $\alpha = 2$ decay as *necessarily* being caused by a absence of backscattering seems to be wrong.
To try to resolve this paradox the understanding of how FT-LDOS is supposed to reveal scattering vectors will be treated in section 6, but here an explanation on why the quantum impurity resemble the scalar in regard to LDOS is presented.

Both the spin-unresolved and spin-resolved LDOS are determined by the full Green function and hence by the T-matrix. Both the scalar and quantum magnetic impurity T-matrix could be expressed as

$$T^{imp}_{\mathbf{k},\mathbf{k}'}(\tilde{\omega}, J) = t^{imp.}(\tilde{\omega}, J) U^\dagger(\phi_{\mathbf{k}}) U(\phi_{\mathbf{k}'}) \tag{5.45}$$

with 'imp.' denoting either 'scalar' or 'qm-imp.'. I.e. a separation into a t-function $t^{imp.}(\tilde{\omega}, J)$ containing the whole frequency $\tilde{\omega}$ and impurity strength J dependence, and a matrix $U^\dagger(\phi_{\mathbf{k}}) U(\phi_{\mathbf{k}'})$ in η containing the whole information on the incoming $\mathbf{k}$ and outgoing $\mathbf{k}'$ scattering vectors. So the T-matrix for the scalar and qm-impurity, have the same momentum and spin part $U^\dagger(\phi_{\mathbf{k}}) U(\phi_{\mathbf{k}'})$ in

common, but are differentiated in the energy t-function being either t^{sc} or t^{qm}. This is the reason why, the correction Green function for both the scalar and the qm-impurity could be written

$$\delta G^{imp.}(\mathbf{r},\mathbf{r},\tilde{\omega},J) = t^{imp.}(\omega,J)\frac{|\tilde{\omega}|^2}{16}\left(f_0^2(\tilde{\omega},r) - f_1^2(\tilde{\omega},r)\right) \tag{5.46}$$

which is again a separation into the t^{imp}-function (still the only quantity that differentiates them) but now a distance $\mathbf{r}$ dependent identity matrix $\frac{|\tilde{\omega}|^2}{16}\left(f_0^2(\tilde{\omega},r) - f_1^2(\tilde{\omega},r)\right)$. It is the latter that determines the LDOS Friedel oscillating behavior, whereas it is the denominator of the t^{imp}-function that determines the resonance peaks in Eqn. (5.27) and Eqn. (5.30) or Eqn. (5.34) and Eqn. (5.35). Therefore the decay rate α of the oscillations are the same in both the spin-unresolved and spin-resolved LDOS.

Chapter 6

Spin-unresolved FT-LDOS on a helical metal

Note that appendix C explain in detail the connection between the long distance LDOS expansion with leading decay rate α and the FT-LDOS. Hence it connects chapter 5 with this chapter 6..

The LDOS indirectly gives the quasi-particle interference (QPI) image by its Fourier transform (FT-LDOS). For simplicity only the spin-unresolved FT-LDOS is derived. This should, according to the literature, reveal the information of scattering vectors on the helical surface for a constant energy contour.

A signature revealing a backscattered wave is seeked. Because if such one undoubtedly exist, a FT-LDOS plot would be expected to distinguish, between a scalar and a quantum magnetic impurity on the surface of a helical metal, since the former does not backscatter whereas the latter does. Since a scalar on a conventional metal backscatter, it might reveal such a signature. Therefore the case of scattering off a scalar potential on the conventional and helical metal in the simple Born approximation will be considered. This will result in a desired signature of the FT-LDOS response for each metal. This is used widely in the literature to argue for the absence of backscattering on a helical metal in the presence of time-reversal symmetric perturbations.

Using this signature, an explanation of a experimental recorded QPI will be presented - an explanation that tacitly take for granted the common interpretation of the notion of 'absence of backscattering' associated with the suppression standing wave-oscillations in the LDOS.

At last the FT-LDOS response for the scalar and magnetic impurities will be treated in with the full T-matrix.

In principle all that is needed is the *spin-unresolved FT-LDOS* defined as the retarded quantity

$$\delta\rho(\mathbf{q},\omega) = \delta\rho(\mathbf{q}, i\omega_n \to \omega + i\,0^+) \tag{6.1}$$

where by definition

$$\begin{aligned}\delta\rho(\mathbf{q}, i\omega_n) &\equiv \int \mathrm{d}\mathbf{r} \exp\left(i\,\mathbf{q}\cdot\mathbf{r}\right) Tr\left[\delta\rho(\mathbf{r},\mathbf{r}; i\omega_n)\right] \\ &= \frac{1}{2\,i}\int \frac{\mathrm{d}^2\mathbf{k}}{(2\pi)^2} Tr\left[\delta\, G(\mathbf{k},\mathbf{k}+\mathbf{q}; i\omega_n) - (\delta\, G(\mathbf{k},\mathbf{k}-\mathbf{q}; i\omega_n))^*\right]\left(\frac{L}{\hbar v_F}\right)^2\end{aligned} \tag{6.2}$$

is in units of inverse energy and $*$ denotes complex conjugation. This is derived in appendix B.

The FT-LDOS above is the physical one in the σ-basis. However, the qm-impurity Green function is only expressible in the η-basis. Hence the Green function in η-basis shall be transformed back to the σ-basis as

$$\begin{aligned}\delta G(\mathbf{k},\mathbf{k}\pm\mathbf{q};i\tilde{\omega}_n) &= U(\phi_{\mathbf{k}})\delta\tilde{G}(\mathbf{k},\mathbf{k}\pm\mathbf{q};i\tilde{\omega}_n)U^{\dagger}(\phi_{\mathbf{k}\pm\mathbf{q}}) \\ &= U(\phi_{\mathbf{k}})\tilde{G}^0(k;i\tilde{\omega}_n)\,\tilde{T}(\mathbf{k},\mathbf{k}\pm\mathbf{q};i\tilde{\omega}_n,J)\,\tilde{G}^0(k\pm q;i\tilde{\omega}_n)U^{\dagger}(\phi_{\mathbf{k}\pm\mathbf{q}}) \\ &= t^{imp.}(i\tilde{\omega}_n,J)G^0(k;i\tilde{\omega}_n)G^0(k\pm q;i\tilde{\omega}_n) \end{aligned} \tag{6.3}$$

To account for *all* impurities Eqn. (6.3) is inserted in Eqn. (6.2) which gives the FT-LDOS for *all* impurities on the same form

$$\delta\rho(q,i\omega_n) = \Im\big[t^{imp.}(i\tilde{\omega}_n,J)\Omega(q,i\tilde{\omega}_n)\big]\left(\frac{L}{\hbar v_F}\right)^2 \tag{6.4}$$

Both the $t^{imp.}(i\omega_n,J)$-function and the Ω-structure depend on the Matsubara frequency $\tilde{\omega}_n$ and bandwidth cut-off which is $D/\epsilon_c = 100$. This will not be a label in neither the t-function nor Ω-structure. However, the Ω-structure is the only quantity depending on momentum $\mathbf{q}$, but solely as $|\mathbf{q}| = q$ i.e. it is *isotropic* in momentum space. This is obvious, because the Fermi surface is circular, hence no specific points on the circle circumference can be distinguished from the others. Due to the isotropy the quasi particle interference image (QPI) will be plotted along some arbitrary direction in the (q_x,q_y)-plane. The Ω-structure is identical for *all* impurities and is expressed as

$$\Omega(\mathbf{q},i\tilde{\omega}_n) \equiv \int\frac{\mathrm{d}^2\mathbf{k}}{(2\pi)^2}\,Tr[G_0(\mathbf{k};i\tilde{\omega}_n)G_0(\mathbf{k}+\mathbf{q};i\tilde{\omega}_n)] = \frac{1}{2\pi}\left(-F(z)+\ln\left(\frac{\mathrm{D}^2}{\tilde{\omega}_n^2}+1\right)\right) \tag{6.5}$$

with $z=\frac{2\tilde{\omega}_n}{q}$, $F(z)=(-1-z^2)g(z)$ and $g(z)=\frac{2}{\sqrt{-1-z^2}}\tan^{-1}\left(\frac{1}{\sqrt{-1-z^2}}\right)$.
However, the t-function contain only frequency the $\tilde{\omega}$ and impurity the strength J. It is solely this t-function that differentiates the scalar from the magnetic ones. The scalar has retarded t-factor

$$t_{sc}(\tilde{\omega},J) = \frac{J}{1+g(\tilde{\omega})J} \tag{6.6}$$

and the two magnetic impurities have identical retarded t-functions

$$t_{qm}(\tilde{\omega},J) = \frac{-\frac{3}{4}g(\tilde{\omega})J^2}{1-\frac{3}{4}g(\tilde{\omega})^2J^2} = t_{cl}(\tilde{\omega},J) \tag{6.7}$$

when the classical magnetic strength is scaled $S^2 \to \frac{3}{4}J^2$ and therefore the magnetic impurities are considered together as one.

6.1 FT-LDOS in the Born approximation

We seek a fingerprint that reveal whether an electron has backscattered upon a given impurity or not. This information is stored in the FT-LDOS response signal, and for the scalar, luckily all what's needed is the information inherent in the Ω-structure. The basic different characteristics of the FT-LDOS response $\Omega(q,\tilde{\omega})$ for a scalar on the conventional and helical metals in the Born approximation will be derived.

The scalar T-matrix in this approximation becomes $T = J$ i.e. equal to the scalar potential J and hence the scalar t-factor becomes $t_{sc}(\tilde{\omega},J) = J$ a real constant. In this approximation - valid

for weak scatters - the difference is simply and easily understood, since only the real potential J and $\Im\Omega$ is needed. If instead a strong scatter was considered both the real and imaginary parts of full T-matrix t-factor $\Re t(\tilde{\omega}, J)$ and $\Im t(\tilde{\omega}, J)$ would sample with $\Im\Omega$ and $\Re\Omega$, thus blurring the FT-LDOS response for $q \leq 2k_F$ which will turn out to be the region of interest. The difference in FT-LDOS response between the helical and conventional metal is thus easily to grasp in the this approximation.

6.1.1 On a conventional metal

The conventional metal[11, 4] is defined as a gas of free conduction electrons, where the surface states have a quadratic dispersion relation $\epsilon(k) = \frac{k^2}{2\,m}$, $\xi(k) = \epsilon(k) - \mu$ and each $\mathbf{k}$-state is double spin degenerate. In appendix B.3 the FT-LDOS is derived to be on the same form as that of the helical metal Eqn. (6.4). The FT-LDOS response on a conventional metal is

$$\delta\rho_{Conv.Metal}(q, i\omega_n) = \Im\big[t^{sc}(i\tilde{\omega}_n, J)\Omega_{Conv.Metal}(q, i\tilde{\omega}_n)\big] = J\Im\big[\Omega_{Conv.Metal}(q, i\tilde{\omega}_n)\big] \tag{6.8}$$

where the last equality sign is valid only in the Born approximation for a scalar potential. Further the retarded Ω-structure is

$$\Im[\Omega_{Conv.Metal}(\mathbf{q}; \omega)] = \begin{cases} \frac{8\pi^2 N_0^2}{|q|\sqrt{q^2 - 4\,k_\omega^2}} & \text{for } q > 2k_\omega \\ 0 & \text{for } q < 2k_\omega \end{cases} \tag{6.9}$$

with $k_\omega = k_F\sqrt{\omega/\mu + 1}$ and $N_0 = \frac{m}{2\pi}$ being the single spin electron density of states. When probing the Fermi surface on a conventional metal, i.e. $\omega = 0$ then $k_\omega = k_F$, and the FT-LDOS response *vanish* because

$$\Im\Omega_{Conv.Metal}(q; \omega)\big|_{\omega=0} = 0 \quad \text{for} \quad q < 2k_F$$

and it has a *singularity* exactly at $q = 2k_F$ as illustrated in figure 6.1. This turn out to be quite a different signature than that on helical metal as explained in section 6.1.2.

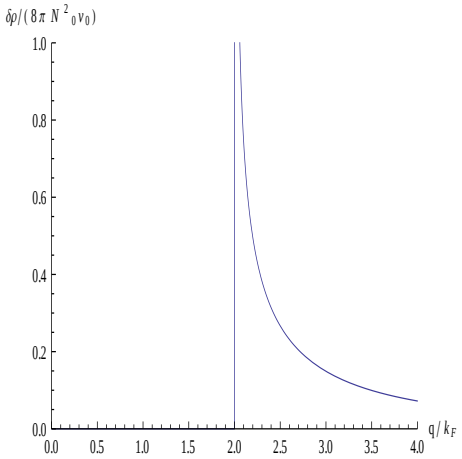

Figure 6.1: Plot of $\rho_{Conv.Metal}(q, 0)/8\pi^2 N_0^2 J$ as a function of q/k_F.

This *singularity* at $q = 2k_F$ is in the conventional metal case a direct manifestation of backscattering from state $\mathbf{k}$ to $-\mathbf{k}$ through scattering vector $q = 2k_F$. To see this, lets begin the derivation

of Eqn. (6.4) in another way, than that undertaken in appendix B.3.

$$\begin{aligned}\delta\rho_{Conv.Metal}(q,\omega,J) &= \Im\left[t_{sc}(\omega,J)\Omega(q;\omega)\right] = J\Im\left[\Omega(q;\omega)\right] \\ &= J\,4\pi\int\frac{\mathrm{d}^2\mathbf{k}}{(2\pi)^2}\,\delta(\varpi-\epsilon(k))\frac{1}{\epsilon(k-q)-\epsilon(k)} \quad , \quad \varpi=\omega+\mu\end{aligned}$$

This show directly that the resonance peak singularity of $\frac{1}{\epsilon(k-q)-\epsilon(k)}$ is exactly where $\epsilon(k-q)=\epsilon(k)$ i.e. for scattering vector $q=2k_F$ between states $\mathbf{k}$ to $-\mathbf{k}$.

6.1.2 On a helical metal

The t-function and Ω-structure in Eqn. (6.5) depends on the Matsubara frequency $\tilde{\omega}_n$. Since the physical FT-LDOS response Eqn. (6.4) is a retarded quantity, then analytic continuation of the t-function and Ω-structure is necessary to perform. The analytic continuation of the Matsubare frequency reads $i\tilde{\omega}_n \to \tilde{\omega}+i\,0^+$ in which $t^{imp.}(i\tilde{\omega}_n \to \tilde{\omega}+i0^+) = t^{imp.}(\tilde{\omega})$ are the retarded t-functions discussed in section 4.3. The same analytic continuation prescription reads $\tilde{\omega}_n \to -i\tilde{\omega}+0^+$, which means when performing the analytic continuation the z-parameter

$$z = \frac{2\,\tilde{\omega}_n}{q} \to \frac{-i\,2\tilde{\omega}}{q} + \frac{2\cdot 0^+}{q} \approx \frac{-i\,2\tilde{\omega}}{q} \tag{6.10}$$

which is valid for $q\neq 0$. This will always be the case for Eqn. (6.4), since the contribution $q=0$ is solely contained in the impurity free FT-LDOS response $\rho_0(\mathbf{k},\tilde{\omega})$. In the Born approximation for a scalar $t_{sc}(\tilde{\omega},J)=J$ and the FT-LDOS response simplifies to

$$\delta\rho(q,i\omega) = J\Im\big[\Omega_{helical}(q,i\tilde{\omega})\big]\left(\frac{L}{v_F\hbar}\right)^2 \tag{6.11}$$

where the retarded Ω-structure on a helical metal Eqn. (6.5) is given by

$$\begin{aligned}\Im\left[\Omega_{helical}(q,\tilde{\omega})\right] &= \Im\left[\int\frac{\mathrm{d}^2\mathbf{k}}{2\pi}\,Tr[G_0(k;i\tilde{\omega}_n\to\tilde{\omega}+i\,0^+)G_0(k-q;i\tilde{\omega}_n\to\tilde{\omega}+i\,0^+)]\right] \\ &= \begin{cases}\pi & \text{for } q\leq 2\tilde{\omega} \\ \Im[F(z\to -i\frac{2\tilde{\omega}}{q})]+\pi & \text{for } q>2\tilde{\omega}\end{cases}\end{aligned} \tag{6.12}$$

What one should notice is that, the FT-LDOS response $\Im\left[\Omega_{helical}(q,\tilde{\omega})\right]$ is a constant $\neq 0$ for $q\leq 2\tilde{\omega}$ and exactly at $q=2\tilde{\omega}$ has a *no singularity*. This is FT-LDOS response (or QPI) is illustrated in figure 6.2 for two frequencies $\tilde{\omega}=0.1$ and $\tilde{\omega}=0.4$. Exactly the momentum $\mathbf{q}_\omega=2\tilde{\omega}$ is that, at probe bias ω, which $\xi_{helical}(\frac{\mathbf{q}_\omega}{2})=\omega \leftrightarrow \mathbf{q}_\omega = 2(\omega+\mu)=2\tilde{\omega}$ the FT-LDOS responce is *not singular*. When probing the Fermi surface $\omega=0$ then $\tilde{\omega}=\mu$ and this scattering vector is $\mathbf{q}=2\mu$ i.e. in other words equal to twice Fermi energy.

This is completely in contrast to the FT-LDOS response on a conventional metal analyzed in section 6.1.1. Here the $\Im\left[\Omega_{Conv.Metal}(q,\tilde{\omega})\right]$ is $=0$ for $q\leq 2k_\omega$ and exactly at $q=2k_\omega$ entertain a *singularity* as illustrated in figure 6.1. For exactly this scattering vector, the FT-LDOS response on the conventional metal is *singular*, since this momentum q_ω is the one $\xi(\frac{q_\omega}{2})=\omega$ at probe bias ω so $\xi_{conv.metal}(\frac{q_\omega}{2})=\omega \leftrightarrow q_\omega = 2k_\omega$. At this momentum both the real and imaginary part of $\Omega_{conv.metal}(q;\omega)$ has a *singularity* as derived in appendix B.3. When probing the Fermi surface this is also exactly the $q=2k_F$.

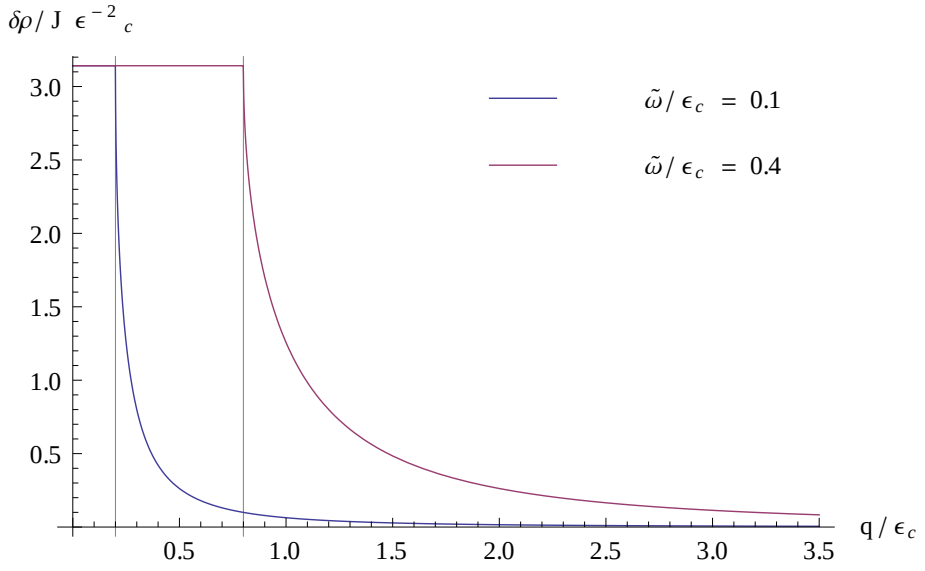

Figure 6.2: Plot of $\delta\rho(q;\tilde{\omega})/J\epsilon_c^{-2}$ as a function of non-scaled momentum q/ϵ_c. The vertical lines are $q/\epsilon_c = 2\cdot 0.1 = 0.2$ and $q/\epsilon_c = 2\cdot 0.4 = 0.8$ and hence marks the important $q = 2\tilde{\omega}$. $D/\epsilon_c = 100$.

Due to the linear Dirac spectrum it will be convenient to scale the the momentum $q \to q\,2\tilde{\omega}$ which cause all FT-LDOS responses to have the $q = 2\tilde{\omega}$ point to be at $q = 1$ for *all* probing frequencies $\tilde{\omega}$. This scaling makes the helical FT-LDOS response, i.e $\Im\left[\Omega_{helical}(q\,2\tilde{\omega}, \tilde{\omega})\right]$, a *finite constant* $\neq 0$, for $q \leq 1$ and exactly at $q = 1$ to have *no singularity* i.e. being finite. So instead of figure 6.2, the FT-LDOS response when momentum scaled as $q \to q\,2\tilde{\omega}$ becomes as illustrated in 6.3.

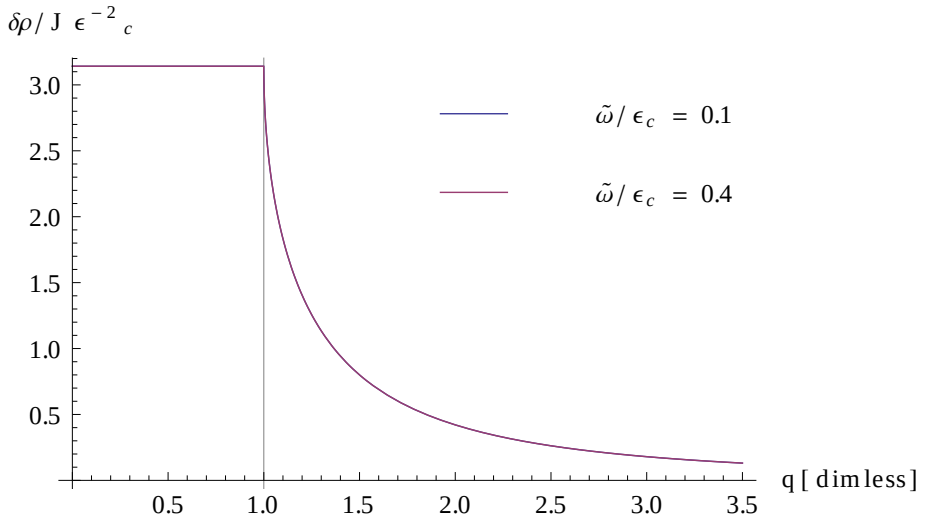

Figure 6.3: Plot of $\delta\rho(q \cdot 2\tilde{\omega}; \tilde{\omega})/J\epsilon_c^{-2}$ as a function of scaled dimensionless q momentum. The vertical line is $q = 1$ and $D/\epsilon_c = 100$.

To conclude about the response FT-LDOS for backscattering upon the two metal surfaces. On the conventional metal the *singularity* at $q_\omega = 2k_\omega$ is a direct manifestation of backscattering from state $\mathbf{k}$ to $-\mathbf{k}$ through scattering vector $\mathbf{q}_\omega = 2\mathbf{k}_\omega$, as illustrated in figure 6.1. The reverse is true when scattering upon a scalar impurity (i.e. a time-reversal invariant perturbation) on a helical metal surface, i.e backscattering is suppressed and hence the FT-LDOS response at backscattering vector $q_\omega = 2\omega$ is *not singular* as is exhibited in figure 6.2.

This is consistent with the common heuristic argument presented in section 3.1.1 and 3.1.2, that on a helical metal a time-reversal-invariant impurity, is not able of mediate a electron spin-flip - such as a scalar potential - cannot backscatter from state $\mathbf{k}$ to $-\mathbf{k}$. However, in the conventional metal a scalar may backscatter. Thus the presence of a singularity at q_ω in the FT-LDOS response signal is, in the literature, widely accepted to signify a backscattering vector q_ω.

6.2 Quasi particle interference image on a helical metal

The QPI intensity patterns from ref [6] in figure 6.4(f)-(j) of Mn-and Ca doped Bi_2Te_3 including warping effects, are seen to be isotropic in the low-energy regime in figures 6.4(i) and (j). These originate from the conic Fermi surface in figure 6.5(c), which has only one stationary scattering vector marked with the red arrow. Note that the pink arrow marked in figure 6.5(c) do not contribute (in the stationary phase approximation), because as discussed in section 5.2 only one time-reversal symmetric pair (TRP) exist on the circular Fermi surface in the Dirac model as tabulated in table 5.3. The pink arrow is a non time-reversal symmetric pair (non-TRP) and hence its contribution is vanishing, compared to the only TRP which is the red arrow figure 6.5(c). However, for higher energies on the warped Fermi surface in figure 6.4(f)-(h), the QPI patterns are anisotropic with intensity peaks along the $\Gamma - M$ directions, but absent peaks along the $\Gamma - K$ directions. This is the 'anomaly' mentioned in the introduction of section 5.2. These originate from the anisotropic and warped Fermi surface in figure 6.5(c), which have several stationary scattering vectors (marked 6.5(c)) nesting points on the Fermi surface connected by high JDOS intensities marked in figure 6.5(d), with a green arrow along $\Gamma - M$ while indicated with a dark-and light blue arrow in figure 6.5(c). These green,blue and red arrows are the dominant scattering vectors, because as discussed in section 5.2, they connect 'stationary' points on the warped and conic Fermi surfaces (i.e. the CEC's in the terminology of section 5.2).

Consider the high-energy warped Fermi surface first, i.e. the QPI patterns in the figures 6.4(f)-(h) and the corresponding possible scattering vectors in figure 6.5(c). The contribution these green and blue scattering vectors give to the QPI pattern can be calculated with JDOS (join density of states) with the approximation $JDOS(E, \mathbf{q}) = \int_{BZ} \mathrm{d}^2\mathbf{k}\rho(E, \mathbf{k})\rho(E, \mathbf{k} + \mathbf{q})$ with $\rho(E, \mathbf{k})$ being the energy and momentum resolved LDOS. This approximation completely ignores the warped surface spin-texture/dependence illustrated with grey symbols in figure 6.5(c). However, the JDOS calculation gives the QPI pattern in 6.5(d) with high intensities along both the $\Gamma - K$ and $\Gamma - M$ direction.

The absence of QPI intensity peaks along the $\Gamma - K$ direction in figure 6.4(f)-(h), are attributed to the full spin-texture marked with grey symbols in figure 6.5(c). This can be captured by calculating the spin-dependent scattering probability $SSP(E, \mathbf{q})$ in the 'warping model' introduced in section 2.1. This is given by $SSP(E, \mathbf{q}) = \int_{BZ} \mathrm{d}^2\mathbf{k}|\langle +; \mathbf{k}|\mathbf{k} + \mathbf{q}; +\rangle|^2\rho(E, \mathbf{k} + \mathbf{p})$ where $|\mathbf{k}, +\rangle = \sum_\sigma U^\dagger(\mathbf{k})_{+\sigma}|\mathbf{k}, \sigma\rangle$ denotes the helical spin state with the transformation matrix $U(\mathbf{k})$ that diagonalize the full Hamiltonian $H_0(\mathbf{k}) + H_w(\mathbf{k})$ containing both the Rashba $H_0(\mathbf{k})$ and warping $H_w(\mathbf{k})$ Hamiltonians and given by Eqn. (2.3). The resulting SSP calculation is given in figure 6.5(e). This SSP produced QPI pattern have peaks along $\Gamma - M$, but those along $\Gamma - K$ are absent. This QPI pattern resembles pretty well the observed QPI in figure 6.4(f)-(h).

6.2.1 QPI on a helical metal in the Dirac model

Now consider the low-energy conic Fermi surface, i.e. the QPI pattern in figure 6.4(i) and (j) of the scalar Ca-doped Bi_2Te_3 in the top row of figure 6.4(i) and (j), and the magnetic Mn-doped Bi_2Te_3 in the mid row of figure 6.4(i) and (j).

As already noticed above, it is pretty clear that the the QPI is isotropic for a point-like scalar impurity. But in the case of a classical magnetic impurity, it is not intuitively clear, that this is also the case and it produce the same QPI as the scalar even when warping is included. Because it break time-reversal symmetry by allowing the surface electrons to backscatter and hence one expects it to show interference. But remember, it was derived in section 5.1.1, that in the charge/spin-unresolved LDOS channel no such constructive interference occur - the standing wave is strongly attenuated with a decay rate of $\alpha = 2$ as both the scalar and qm-impurity. It was derived that for

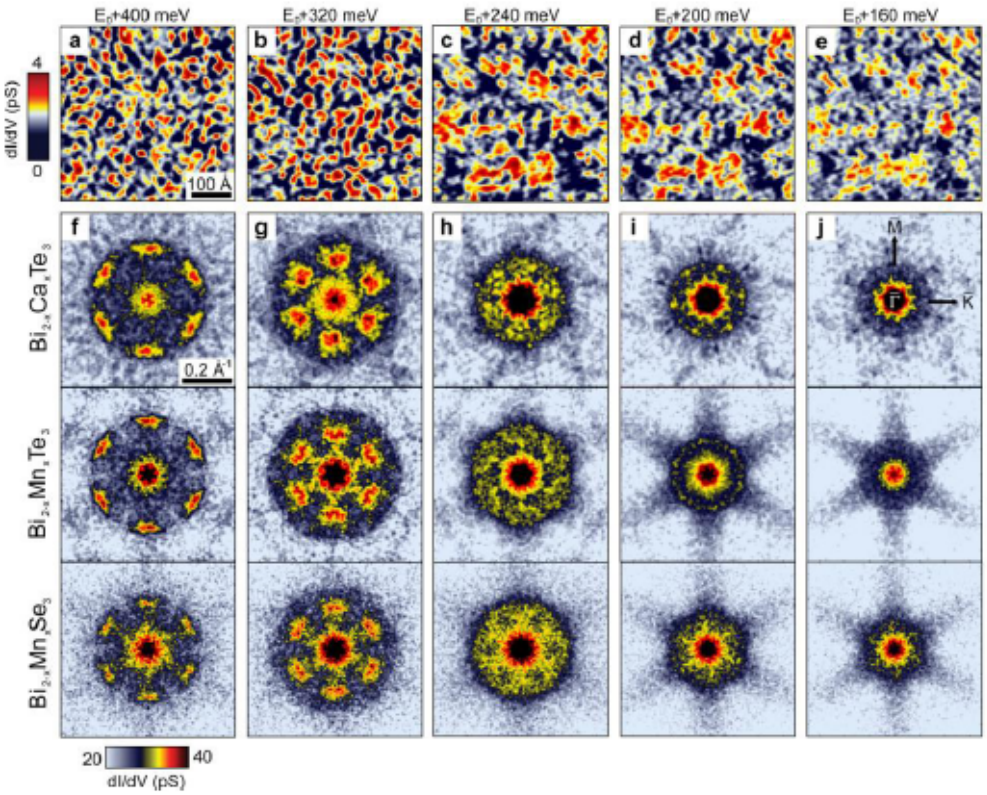

Figure 6.4: From ref [6]. (a) to (e) Show real space LDOS on the surface of Ca-doped Bi_2Te_3 at different energies. (f) to (j) The Fourier transform of the LDOS (FT-LDOS) of the Ca-and Mn doped Bi_2Te_3 and Mn-doped Bi_2Se_3.

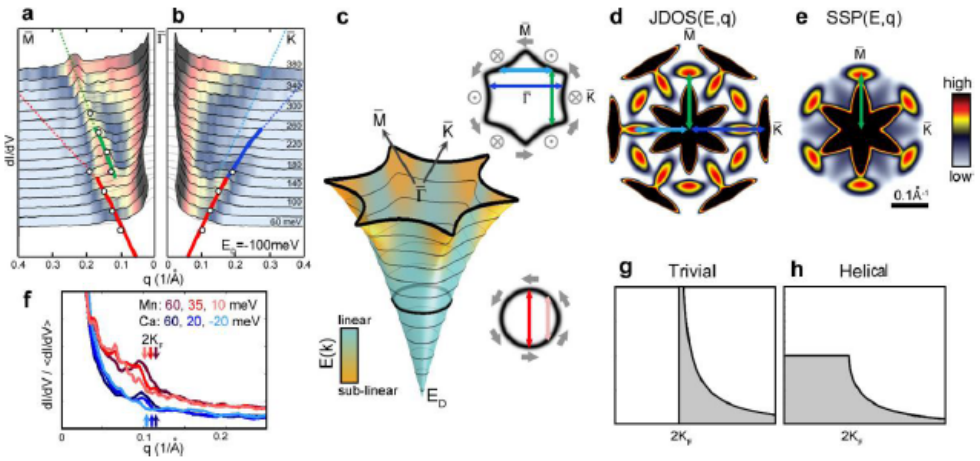

Figure 6.5: Origin of QPI patterns in figure ref 6.4 from ref [6]. FT-LDOS (FT of STM measured dI/dV) maps of Mn and Ca doped Bi_2Te_3 (a) along $(\Gamma - M)$ and (b) along $(\Gamma - K)$. (a) and (b) is a map of the full warping dispersion relation. (c) The band structure measured by ARPES from conic to hexagonally warped constant energy contours of Bi_2Te_3. The associated spin-texture is imposed with gray symbols in the inputs describing the Fermi surface of the conic and warped. The red arrow on the conic Fermi surface transform into symmetric modes in the $(\Gamma - M)$ and $(\Gamma - K)$ directions shown in (a) and (b), respectively, which is seen in (a) and (b) where the red arrow is imposed on the dispersion. On the warped Fermi surface, the dark and light blue arrows indicate scattering vectors along $\Gamma - K$ calculated by JDOS are shown in (b). Also the scattering vector marked with a green arrow along $\Gamma - M$ is shown in (a). The scattering peaks calculated with JDOS (d) and SSP (e). (f) Azimuthally averaged radial QPI profile on the conic Fermi surface in Mn-and Ca doped Bi_2Te_3. The theoretical calculated FT-LDOS on (g) a trivial(conventional in figure 6.1) metal and (h) a helical metal as illustrated in figure 6.3.

a classical magnetic impurity in the charge/spin-unresolved LDOS Eqn. (5.30)

$$\delta\rho_{cl}(\mathbf{r};\tilde{\omega},J) = -\frac{2}{\pi}\Im\left[t^{cl}(\tilde{\omega},J)\frac{|\tilde{\omega}|^2}{16}\left(f_0^2(\tilde{\omega},r) - f_1^2(\tilde{\omega},r)\right)\left(\frac{L}{v_F\hbar}\right)^2\right] = \delta\rho_{qm}(\mathbf{r};\tilde{\omega},J) \tag{6.13}$$

which except for the t^{cl} function is the same as that of a scalar Eqn. (5.28)

$$\delta\rho_{sc}(\mathbf{r};\tilde{\omega},J) = -\frac{2}{\pi}\Im\left[t^{sc}(\tilde{\omega},J)\frac{|\tilde{\omega}|^2}{16}\left(f_0^2(\tilde{\omega},r) - f_1^2(\tilde{\omega},r)\right)\left(\frac{L}{v_F\hbar}\right)^2\right] \tag{6.14}$$

and all the impurities, in the charge/spin-unresolved channel, share the same distance $|\tilde{\omega}|\left(f_0^2(\tilde{\omega},r) - f_1^2(\tilde{\omega},r)\right)$ dependence that determines the decay rate to be $\alpha = 2$.
But in the spin-resolved mode calculated in section 5.1.2 the spin-resolved LDOS Eqn. (5.36) $\rho^i_{cl,\pm}(\mathbf{r}_j;\tilde{\omega},J)$ depends on the $\pm$-spin polarization in the i'th direction and the j'th axis to which it's projected onto. This feature is different from both the scalar potential and quantum magnetic impurity and was illustrated in figure 5.3,5.4 and 5.5. In this STM spin-resolved mode calculated in ref [22], standing waves are not suppressed and hence the decay rate is $\alpha = 1$ as tabulated in table 5.3. However, in a spin-resolved FT-LDOS response *singularities* would occur for the classical magnetic case, but not for the scalar (and quantum magnetic case). This would show a different QPI pattern than that observed in the spin-unresolved one in figure 6.4. So in summery; the classical magnetic impurity keep the isotropic QPI as the scalar which is illustrated in figure 6.4(i) and (j). For the same reason, the QPI pattern in the higher-energy regime in figure 6.4(f) - (h) for the scalar and magnetic doped materials have the same QPI pattern when probed with spin-unresolved FT-LDOS.

Now take a look on the radial QPI profile on the conic Fermi surface in figure 6.5(f), which exhibits a small cusp at the $q = 2k_F$ for both scalar Ca and magnetic Mn doped Bi_2Te_3. The reddish curves in figure 6.5(f) are from the Mn doped Bi_2Te_3 of the mid row in figure 6.4(i) and (j), and blueish curves in figure 6.5(f) are from the Ca doped Bi_2Te_3 of the top row in figure 6.4(i) and (j).

The FT-LDOS response at $q = 2k_F$ is a certain signature, that depends strongly on the type of metal with a circular Fermi surface. This is illustrated in figure 6.5(g) for a conventional metal and in figure 6.5(h) on a helical metal. It is pretty clear that the cusps in figure 6.5(f) does not originate from a FT-LDOS response from a conventional metal but on a helical metal, since the intensity peak of a conventional metal reported in ref [32] are much more strongly peaked and resembles that of figure 6.5(g). As shown in section 6.1.1 FT-LDOS with a *singularity* peak as in figure 6.5(g) for a conventional metal is associated directly with a backscattering and it simply follows as the Fourier transform of a LDOS with a decay rate $\alpha = 1$. The other FT-LDOS response with *no singularity* peak as in 6.5(h), simply follows as the Fourier transform of a LDOS with a decay rate $\alpha = 2$. In the literature regarding a helical metal, exactly this is often associated with the absence of backscattering.

In order to understand this cusp, we'll have to calculate the full FT-LDOS Eqn. 6.4

$$\delta\rho(q,i\omega_n,J) = \Im\left[t^{imp.}(i\tilde{\omega}_n,J)\Omega(q,i\tilde{\omega}_n)\right]\left(\frac{L}{\hbar v_F}\right)^2 \tag{6.15}$$

with the retarded $t^{imp.}(\tilde{\omega},J) = t^{imp.}(i\tilde{\omega}_n \to \tilde{\omega} + i0^+,J)$ coming from the full T-matrix series of the respective impurities. Since it is not the Born approximation anymore, but the full T-matrix

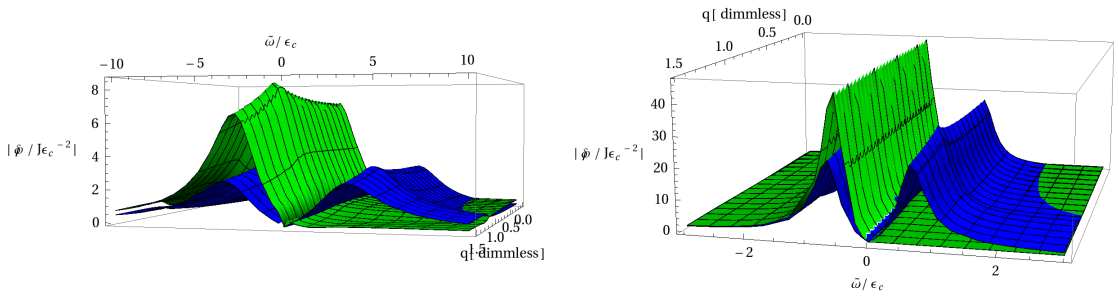

(a) scalar: $J/\epsilon_c = 0.5$

(b) qm-imp. $J/\epsilon_c = 0.5$

Figure 6.6: Plot of FT-LDOS along a line in the q_x, q_y plane as a function of $\tilde{\omega}$ for $J/\epsilon_c = 0.5$ in figure 6.6(a) and $J/\epsilon_c = 2$ in figure 6.6(b) . Green contour $|\delta_{sc}\rho(q\,2\tilde{\omega}, \tilde{\omega})|/J\epsilon_c^{-2}$ and blue contour $|\delta_{qm}\rho(q\,2\tilde{\omega}, \tilde{\omega})|/J\epsilon_c^{-2}$.

now, then the t-factor is restored as $t_{imp.}(\tilde{\omega}, J)$ given in section 4.3 which for the scalar impurity

$$t_{sc}(\tilde{\omega}, J) = \frac{J}{1 + J\, g(\tilde{\omega})} \tag{6.16}$$

and the quantum impurity

$$t_{qm}(\tilde{\omega}, J) = \frac{-\frac{3}{4}J^2 g(\tilde{\omega})}{1 - \frac{3}{4}J^2 g(\tilde{\omega})^2} \tag{6.17}$$

and the classical magnetic impurity $t_{cl}(\tilde{\omega}, J) = t_{qm}(\tilde{\omega}, J)$ is the same as the quantum magnetic impurity and hence their spin-unresolved FT-LDOS QPI plots are identical, hence only one of them is shown. The t-factor thus contains both a real and imaginary part, which samples with the imaginary and real part of the Ω-structure.

The radial FT-LDOS responce plots along any line in the q_x, q_y-plane of scalar and magnetic (the quantum and classical have same response) impurities are illustrated in figure 6.6(a) for $J/\epsilon_c = 0.5$. and figure 6.6(b) for $J/\epsilon_c = 2$. From figure 6.6(a) and 6.6(b) one see, that the resonance peak at some $\tilde{\omega} < 0$ is at the same frequency for both the scalar and magnetic impurities. This peak occur closer to $\tilde{\omega} = 0$ for larger couplings J. For a given coupling J the response of the scalar and magnetic impurities are almost identical away from the resonance peak. Regardless the coupling J, for $\tilde{\omega} > 0$ the scalar has *no* resonance peak but the magnetic peak has a *resonance peak* symmetric around $\tilde{\omega} = 0$. These resonance peak intensities grow as the coupling J increases. This means, for low temperature the Kondo problem sets in and raise the effective coupling, which gives rise to a larger peak intensities.

From figure 6.6(a) and 6.6(b) the cusp at $q = 2k_F$(i.e. $q = 1$ in the figure) very difficult to see. Therefore the radial FT-LDOS response plots along any line in the q_x, q_y-plane of scalar and magnetic impurities in figure 6.7 for $J/\epsilon_c = 0.5$. The figure 6.7(a) and 6.7(b) show the scalar FT-LDOS $|\delta\rho_{sc}(q\,2\tilde{\omega}, \tilde{\omega})|$ as a function of scaled $q \to q\,2\tilde{\omega}$ for positive $\tilde{\omega} > 0$ and negative $\tilde{\omega} < 0$ frequencies $\tilde{\omega}$, respectively. The figures 6.7(c) and 6.7(d) show the magnetic FT-LDOS

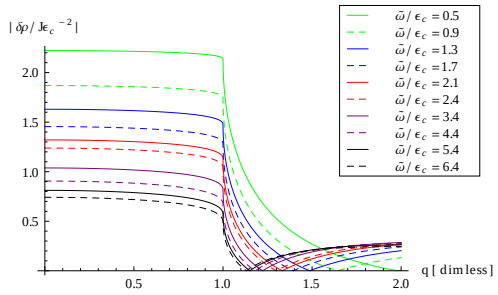

(a) scalar: $J/\epsilon_c = 0.5$, $\tilde{\omega} > 0$

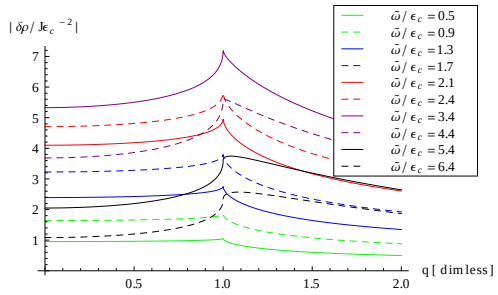

(c) qm-imp. $J/\epsilon_c = 0.5$, $\tilde{\omega} > 0$

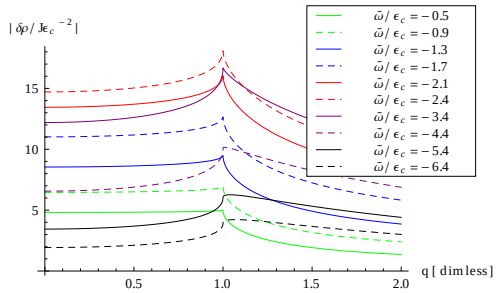

(b) scalar: $J/\epsilon_c = 0.5$, $\tilde{\omega} < 0$

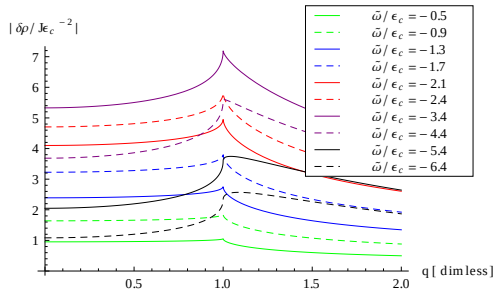

(d) qm-imp. $J/\epsilon_c = 0.5$, $\tilde{\omega} < 0$

Figure 6.7: Plot of $|\delta_{sc}\rho(q\,2\tilde{\omega},\tilde{\omega})|$ in 6.7(a) for $\tilde{\omega} > 0$ and 6.7(b) for $\tilde{\omega} < 0$. Plot of $|\delta_{mag}\rho(q\,2\tilde{\omega},\tilde{\omega})|$ in 6.7(c) for $\tilde{\omega} > 0$ and 6.7(d) for $\tilde{\omega} < 0$. Note that $\delta_{mag}\rho(q\,2\tilde{\omega},\tilde{\omega}) \equiv \delta_{qm}\rho(q\,2\tilde{\omega},\tilde{\omega}) = \delta_{cl}\rho(q\,2\tilde{\omega},\tilde{\omega})$ and all are for $J/\epsilon_c = 0.5$

$|\delta\rho_{mag.}(q\,2\tilde{\omega},\tilde{\omega})|$ as a function of scaled $q \to q\,2\tilde{\omega}$ for positive $\tilde{\omega} > 0$ and negative $\tilde{\omega} < 0$ frequencies $\tilde{\omega}$, respectively.

The radial FT-LDOS response plots along any line in the q_x, q_y-plane of scalar and magnetic impurities in figure 6.8 for $J/\epsilon_c = 2$. The figures 6.8(a) and 6.8(b) show the scalar FT-LDOS $|\delta\rho_{sc}(q\,2\tilde{\omega},\tilde{\omega})|$ as a function of scaled $q \to q\,2\tilde{\omega}$ for positive $\tilde{\omega} > 0$ and negative $\tilde{\omega} < 0$ frequencies $\tilde{\omega}$, respectively. The figures 6.8(c) and 6.8(d) show the magnetic FT-LDOS $|\delta\rho_{mag.}(q\,2\tilde{\omega},\tilde{\omega})|$ as a function of scaled $q \to q\,2\tilde{\omega}$ for positive $\tilde{\omega} > 0$ and negative $\tilde{\omega} < 0$ frequencies $\tilde{\omega}$, respectively.

In summery; if one is to be able to distinguish between a scalar potential and a magnetic FT-LDOS response for a given Fermi level μ, one have to probe frequencies ω such that $\tilde{\omega} = \mu + \omega > 0$. These possibilities are summarized in table 6.1.
This is also what have been done experimentally in ref [6] as seen in figure 6.5(f). From figure 6.5(b) one read that the Dirac energy is $E_D = -100$ mV and the Fermi level is $\mu = 140$mV, which is just before warping sets in as seen in figure 6.5(a) and (b). The blueish curves and reddish curves in figure 6.5(f) are for $\omega > -|\mu|$, which is the crucial condition derived above. Hence the theoretical prediction of the radial FT-LDOS plot, would be, that the scalar and classical magnetic cusp should resemble those depicted in figure 6.6(a) and 6.6(b), i.e. figure 6.7 and 6.8, depending on the strength of the impurity couplings. However, from figure 6.5(f) one can hardly distinguish

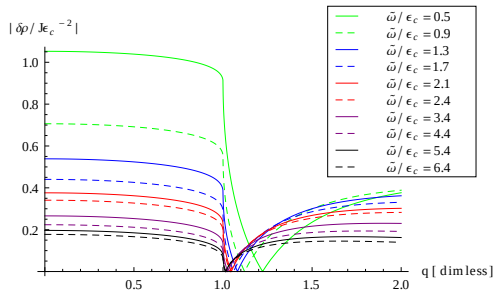

(a) scalar: $J/\epsilon_c = 2$, $\tilde{\omega} > 0$

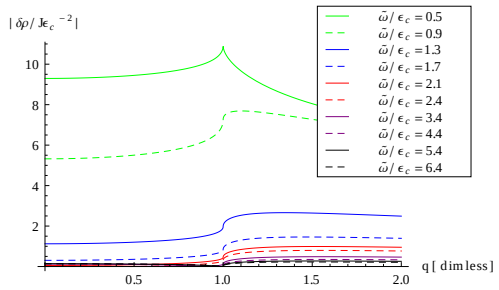

(c) qm-imp. $J/\epsilon_c = 2$, $\tilde{\omega} > 0$

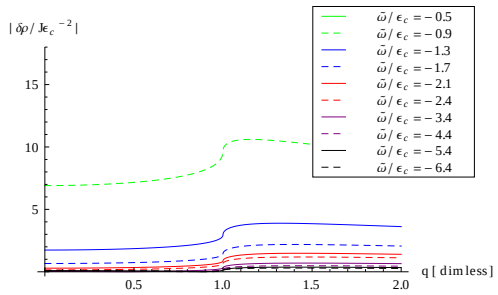

(b) scalar: $J/\epsilon_c = 2$, $\tilde{\omega} < 0$

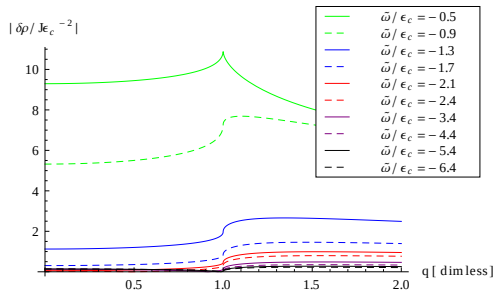

(d) qm-imp. $J/\epsilon_c = 2$, $\tilde{\omega} < 0$

Figure 6.8: Plot of $|\delta_{sc}\rho(q\,2\tilde{\omega},\tilde{\omega})|$ in 6.8(a) for $\tilde{\omega} > 0$ and 6.8(b) for $\tilde{\omega} < 0$. Plot of $|\delta_{mag}\rho(q\,2\tilde{\omega},\tilde{\omega})|$ in 6.8(c) for $\tilde{\omega} > 0$ and 6.8(d) for $\tilde{\omega} < 0$. Note that $\delta_{mag}\rho(q\,2\tilde{\omega},\tilde{\omega}) \equiv \delta_{qm}\rho(q\,2\tilde{\omega},\tilde{\omega}) = \delta_{cl}\rho(q\,2\tilde{\omega},\tilde{\omega})$ and all are for $J/\epsilon_c = 2$

Table 6.1: Table of probing possibilities when $\tilde{\omega} > 0$

Fermi level	ω	probing states
$\mu = 0$	$\omega > 0$	unocc. states (electrons)
$\mu > 0$	$\omega > -\mu$	occ. states (electrons), Fermi surface or unocc. states (electrons)
$\mu < 0$	$\omega > \|\mu\|$	unocc. states (high placed holes)
μ	$\omega > -\mu$	

the cusp deformation of the scalar (Ca) doped from that of the magnetic (Mn) doped material, in the conic Fermi surface regime. So the conclusion must be, that it is too difficult experimentally to determine the difference between a scalar and a classical magnetic impurity in the conic Fermi surface regime at the present state of the art experiments. To my knowledge, ref [6] is the only experimental article of STM(S) in this regime, and they discuss the experimental difficulties of probing these states. But one should notice, as discussed in section 5.1, that it is necessary to understand and experimentally control these low-energy states, if one wish to exploit the helical metal for technical applications and to provoke exotic topological quantum phenomena not yet discovered.

Further ref [22] show that the spin-resolved FT-LDOS of both the scalar and the quantum magnetic impurity vanish completely, but the classical magnetic impurity has FT-LDOS response with singularity at $q = 2k_F$ for every spin-polarization. As for the LDOS response this happens because the T-matrix for the scalar and quantum impurity have the same spin and momentum dependence $U^{\dagger}(\mathbf{k})U(\mathbf{k}')$. However, the T-matrix are differentiated by an energy dependent t-function $t^{sc}(\tilde{\omega}, J)$ and $t^{qm}(\tilde{\omega}, J)$, which in the case of the quantum impurity contain the information about the intermediate scatterings. Notice that these intermediate scatterings are allowed to scatter in any direction.

Chapter 7

Discussion

In this chapter, some of the physical features induced by the impurities will be repeated. This will be done, while keeping track of the similarities or differences between the non-magnetic opposed to magnetic impurities and the time-reversal preserving opposed to time-reversal breaking impurities.

The resonance peaks in the spin-unresolved LDOS response in Eqn. (5.34) for the scalar, Eqn. (5.35) for the quantum magnetic impurity and Eqn. (5.36) for the classical magnetic impurity are fully determined by the t-functions: $t_{sc}(\tilde{\omega}, J)$ Eqn. 4.56, $t_{qm}(\tilde{\omega}, J)$ Eqn. 4.57 and $t_{cl}(\tilde{\omega}, J)$ Eqn. (4.58). None of these encounter any singularities, and therefore are the resonance states not real bound states, but quasi-bound states that depend strongly on the coupling J.

It the was found, that both the quantum magnetic and the classical magnetic impurity backscatter, but the scalar does not. Therefore, at first hand, one would expect the interference of the classical and quantum magnetic impurities relative to the scalar would be enhanced, because they both backscatter, but the latter not. The classical magnetic impurity backscatter, because it break time-reversal symmetry, whereas the quantum impurity preserve time-reversal symmetry while it backscatter. The backscattering vector is the crucial in this context, as explained in section 5.2, since this vector connect points on the Fermi surface, that are time-reversal pairs (TRP). Scattering between such time-reversal pairs dominate the power-low in LDOS and hence also the FT-LDOS response. However, it was found that this, is not the case, but the charge/spin-unresolved LDOS interference is suppressed as a decay rate $\alpha = 2$ for all of the impurities, because they all share the generic form

$$\delta\rho_{sc/qm/cl}(\mathbf{r}; \tilde{\omega}, J) = -\frac{2}{\pi}\Im\left[t^{sc/qm/cl}(\tilde{\omega}, J)\frac{|\tilde{\omega}|^2}{16}\left(f_0^2(\tilde{\omega}, r) - f_1^2(\tilde{\omega}, r)\right)\left(\frac{L}{v_F\hbar}\right)^2\right] \tag{7.1}$$

But the energy dependence $\tilde{\omega}$ and J that appear as $t^{sc/qm/cl}(\tilde{\omega}, J)$ differentiates the scalar by $t^{sc}(\tilde{\omega}, J)$ from the magnetic impurities $t^{qm}(\tilde{\omega}, J) = t^{cl}(\tilde{\omega}, J)$. In figure 5.2 the spin-unresolved LDOS for the impurities are illustrated.

This cause the scalar to have a single spin double-degenerate resonance peak, because it cannot be spin-resolved due to

$$\rho^i_{sc,\pm}(\mathbf{r}; \tilde{\omega}, J) = \frac{\rho_{sc}(\mathbf{r}; \tilde{\omega}; J)}{2} \tag{7.2}$$

The magnetic impurities have two resonance peaks located symmetric around $\tilde{\omega} = 0$, i.e. symmetric on the electron and hole side. As for the scalar, the two quantum magnetic impurity resonance

peaks are also spin double-degenerate, since it cannot be spin-resolved due to

$$\rho^i_{qm,\pm}(\mathbf{r};\tilde{\omega},J) = \frac{\rho_{qm}(\mathbf{r};\tilde{\omega};J)}{2} \tag{7.3}$$

For a given coupling J the two resonance peaks of the magnetic impurities are merging each other due to $t^{qm}(\tilde{\omega},J) = t^{cl}(\tilde{\omega},J)$. Unlike the time-reversal preserving impurities, the scalar and quantum impurity, the two resonance peaks of the classical magnetic impurity split into two spin-polarized peaks, since the spin-resolved LDOS is

$$\rho^i_{cl,\pm}(\mathbf{r};\tilde{\omega},J) = \frac{\rho_{qm}(\mathbf{r};\tilde{\omega},J)}{2} \mp \frac{1}{\pi}\underbrace{\Im Tr\left[G_{cl}(\mathbf{r},\mathbf{r};\omega,J)\frac{\tau^i}{2}\right]}_{\neq 0} \tag{7.4}$$

This strongly depends on projection into (r_x, r_y)-plane of the spin $i = x, y, z$ polarization. The $\delta\rho^i_{cl,\pm}(\mathbf{r};\tilde{\omega},J)$ decay with $\alpha = 1$ which is associated with a backscattering channel that has opened via a spin-flip process due to the classical magnet breaking time-reversal symmetry.

Since the quantum impurity is allowed to backscatter, it would be expected that this would be reflected in the spin-channel as $\delta\rho^i_{qm,\pm}$ hence having a decay $\alpha = 1$ in which the standing waves in the spin-channel is slowly attenuated. But instead $\delta\rho^i_{qm,\pm}(\mathbf{r};\tilde{\omega},J) = 0$ because of Eqn. (7.3), and hence the oscillations in the spin channel is strongly damped as $\alpha = 2$. This is the same decay rate as for the scalar case.

The unresolved-LDOS measure the charge or spin-unresolved interference. The attenuation/decay of these 'Friedel' oscillations progress in a power-law long-distance expansion as $r^{-\alpha}$ with distance r and decay rate index α. The interference of scattering vectors (off the impurity on the surface) creates these standing waves. If they interfere destructively, the standing wave will be suppressed and hence decay faster than a standing wave that is not suppressed. The Fourier transform of this real-space LDOS interference pattern is the FT-LDOS. This reveal which scattering vectors that was involved in the LDOS oscillations.

On the conventional metal in the 1^{st} Born approximation, electrons scattering off a point-like scalar potential creates a spin-unresolved LDOS oscillation, which has a long-distance asymptotic expansion with *slow* decay rate $\alpha = 1$ (as tabulated in table 5.2 section5.2 and in table C.1 sectionC.1) due to its generic form $h_{sc,conv.}(\mathbf{r},\mu) = \frac{\cos(2|\mu|r)}{\epsilon_c r}$. The Fourier transform of this has the characteristic shape, as illustrated by the blue curve in figure C.2, of a singularity peak at $q = 2k_F$ (i.e. $q = 1$ in the figure). This resembles the FT-LDOS (of the full distance dependent LDOS) plotted as the blue curve in figure C.3. Therefore one associate a LDOS decay rate $\alpha = 1$ with a *singularity* at $q = 2k_F$ in the FT-LDOS response as illustrated in figure C.3.

The *singular* resonance peak at $q = 2k_F$ is the resonance peak singularity of $\frac{1}{\epsilon(k-q)-\epsilon(k)}$ which occur for a scattering vector $\mathbf{q} = 2\mathbf{k}_F$ between states $\mathbf{k}$ to $-\mathbf{k}$.

On the other hand, in the 1^{st} Born approximation scattering off a point-like scalar potential on the helical metal creates a LDOS oscillation which has a long-distance asymptotic expansion with *fast* decay rate $\alpha = 2$ (as tabulated in table 5.2 section5.2 and in table C.1 sectionC.1) due to its generic form Eqn. (C.1.7) $h_{sc}(\mathbf{r},\mu) = \frac{\sin(2|\mu|r)}{\epsilon_c^2 r^2}$. The Fourier transform of this has the characteristic shape, as illustrated by the red curve in figure C.2, of a *not singular cusp* at $q = 2k_F$ (i.e. $q = 1$ in the figure) in the FT-LDOS response. This resembles the FT-LDOS (of the full distance dependent LDOS) plotted as the red curve in figure C.4. Therefore one associate a LDOS decay rate $\alpha = 2$ induced by a scalar potential with a *not singular cusp* at $q = 2k_F$ in the FT-LDOS response as illustrated bu the red line in figure C.4.

It has *not a singular* resonance peak at $q = 2k_F$, because the backscattering vector $\mathbf{q} = 2\mathbf{k}_F$ has been suppressed by the helical spin-texture, since the backscattering vector is between states which are time-reversal partners and hence orthogonal.

In the 1^{st} Born approximation scattering off a local quantum magnetic impurity on the helical metal creates a LDOS oscillation which has a long-distance asymptotic expansion with a *fast* decay rate $\alpha = 2$ (as tabulated in table 5.2 section5.2 and in table C.1 sectionC.1) due to its generic form Eqn. (C.1.13) $h_{qm}(\mathbf{r},\mu) = \frac{3J\mu}{4\epsilon_c^2}\left(\frac{\cos(2|\mu|r)}{4\epsilon_c^2 r^2} - \frac{\log\left((D/\mu)^2-1\right)}{4\pi}\frac{\sin(2|\mu|r)}{\epsilon_c^2 r^2}\right)$. The Fourier transform of this has the characteristic shape, as illustrated by the black curve in figure C.2, of a *not singular but deformed cusp* at $q = 2k_F$ (i.e. $q = 1$ in the figure) in the FT-LDOS response. This resembles the FT-LDOS (of the full distance dependent LDOS) plotted as the black curve in figure C.4. Therefore one can associate a LDOS decay rate $\alpha = 2$ induced by a quantum magnetic impurity with a *deformed cusp* at $q = 2k_F$ in the FT-LDOS response as illustrated by the black line in figure C.4.

The reason why the quantum magnetic impurity decay with $\alpha = 2$ as the scalar, but have a cusp deformation instead of a cusp, is because of the second order irreducible self-energy (see the diagram in figure 7.1)

$$\begin{aligned}\tilde{\Sigma}^{(2)}(\mathbf{k},\mathbf{k}^{'};\omega) &\propto J^2\sum_{\mathbf{k}_1}\sum_{i,j=1}^{3}\underbrace{\langle S^iS^j\rangle}_{\propto\delta_{i,j}}\tilde{\tau}^i(\phi_{\mathbf{k}},\phi_{\mathbf{k}_1})\tilde{G}^0(k_1;i\,\tilde{\omega}_n\to\tilde{\omega}+i0^+)\tilde{\tau}^j(\phi_{\mathbf{k}_1},\phi_{\mathbf{k}'})\\ &\propto -g(\tilde{\omega})J^2U^\dagger(\phi_{\mathbf{k}})U(\phi_{\mathbf{k}'})\end{aligned}$$

This quantum impurity induced self-energy has momentum and spin dependence $U^\dagger(\phi_{\mathbf{k}})U(\phi_{\mathbf{k}'})$, which is the *same* as the scalar induced $\Sigma^{(1)}$. However, its *energy dependence* $g(\tilde{\omega})$ is complex function of $\tilde{\omega}$ whereas the scalar energy dependence is a real constant.
This effect arise due to the sum over impurity configurations. The average of impurity spin $< S_d^iS_d^j > \propto \delta_{i,j}$, cause an incoming surface electron $\mathbf{k}^{'}$ interacting with the vertex in η-basis $\tilde{\tau}^i(\phi_{\mathbf{k}_1},\phi_{\mathbf{k}'})$ going out into a intermediate fermion state $\mathbf{k}_1$ in an arbitrary direction and spin, but on hitting the next vertex $\tilde{\tau}^i(\phi_{\mathbf{k}},\phi_{\mathbf{k}_1})$, it is rotated back to same helicity η. The $\int\frac{\mathrm{d}\phi_{\mathbf{k}_1}}{2\pi}$ sum the contributions from all intermediate states, and the sum over vertex $i = 1,2,3$ ensures that all the possible spin-rotations in-and-out are included. However, this ends effectively with $g(\tilde{\omega})J^2U^\dagger(\phi_{\mathbf{k}})U(\phi_{\mathbf{k}'})$ which resembles that of the scalar, except for the energy dependence $g(\tilde{\omega})$ which arise because of all the intermediate scatterings. It is exactly this sum over intermediate states and spin-flippings, that differentiates the quantum magnetic impurity from the scalar. Therefore this energy dependence manifest itself in the T-matrix Eqn. (5.45) as the t-function $t_{qm}(\tilde{\omega},J) = \frac{-\frac{3}{4}J^2g(\tilde{\omega})}{1-\frac{3}{4}J^2g(\tilde{\omega})^2}$ which is different from $t_{sc}(\tilde{\omega},J) = \frac{J}{1+J\,g(\tilde{\omega})}$ since the scalar did not sum over intermediate states.

To conclude: because the T-matrix for the scalar and the quantum impurity have $\tilde{T}_{\mathbf{k}\mathbf{k}'} \propto t_{sc/qm}(\tilde{\omega},J)U^\dagger(\phi_{\mathbf{k}})U(\phi_{\mathbf{k}'})$, the spin-unresolved LDOS for them both can be expressed as

$$\delta\rho_{sc/qm/cl}(\mathbf{r};\tilde{\omega},J) = -\frac{2}{\pi}\Im\left[t^{sc/qm/cl}(\tilde{\omega},J)\frac{|\tilde{\omega}|^2}{16}\left(f_0^2(\tilde{\omega},r) - f_1^2(\tilde{\omega},r)\right)\left(\frac{L}{v_F\hbar}\right)^4\right] \tag{7.5}$$

and likewise the spin-unresolved FT-LDOS as

$$\delta\rho(q,i\omega_n)_{sc/cl/qm} = \Im\left[t^{sc/cl/qm}(i\tilde{\omega}_n,J)\Omega(q,i\tilde{\omega}_n)\right]\left(\frac{L}{\hbar v_F}\right)^2 \tag{7.6}$$

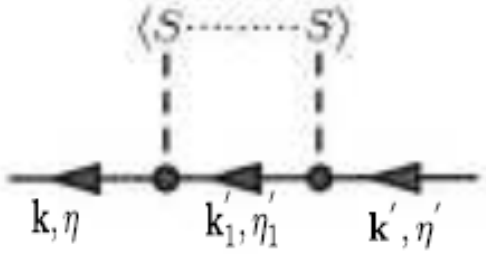

Figure 7.1: Diagram of the quantum impurity second order irreducible self-energy $\Sigma^{(2)}(\mathbf{k},\mathbf{k}^{'})_{\eta\eta'}$.

Also the spin-unresolved LDOS and FT-LDOS response for classical magnetic impurity is Eqn. (7.5) and (7.6), respectively, in the Full T-matrix expansion since only the part $\tilde{T}_{\mathbf{k}\mathbf{k}'} \propto t_{cl}(\tilde{\omega},J)U^{\dagger}(\phi_{\mathbf{k}})U(\phi_{\mathbf{k}'})$ of its T-matrix is picked out and $t_{cl}(\tilde{\omega},J) = t_{qm}(\tilde{\omega},J)$.

In the 1^{st} Born Approximation the induced the surface properties of the quantum magnetic impurity compared to the scalar and classical magnetic imp.:

- Since $\tilde{T}^{sc}_{\mathbf{k}\mathbf{k}'} = JU^{\dagger}(\phi_{\mathbf{k}})U(\phi_{\mathbf{k}'})$ (i.e. $t_{sc}(\tilde{\omega},J) = J$) and $\tilde{T}^{qm}_{\mathbf{k}\mathbf{k}'} = \Sigma^{(2)}(\tilde{\omega},J) \propto J^2U^{\dagger}(\phi_{\mathbf{k}})U(\phi_{\mathbf{k}'})$ spin-unresolved LDOS response Eqn. (7.5) of the scalar and the quantum magnetic impurity has the long-distance generic form $h_{sc}(\mathbf{r},\mu)$ (Eqn. (C.1.7)) and $h_{qm}(\mathbf{r},\mu)$ (Eqn. (C.1.13)), respectively, and both have *fast* decay rate $\alpha = 2$ which gives a *not singularity* at $q = 2k_F$ in the FT-LDOS as illustrated by the black and red lines in figure C.2 and C.4. These long-distance LDOS expansions are plotted in figure C.1, and for both time-reversal invariant impurities on the helical metal, i.e $h_{sc}(\mathbf{r},\mu)$ and $h_{qm}(\mathbf{r},\mu)$, decay faster than the scalar on the conventional metal $h_{sc,qm}(\mathbf{r},\mu)$ with $\alpha = 1$ which gives a *singularity* at $q = 2k_F$ in the FT-LDOS as illustrated by the blue black and red lines in figure C.2 and C.3.

  - The T-matrix $\tilde{T}^{sc/qm}_{\mathbf{k}\mathbf{k}'} \propto U^{\dagger}(\phi_{\mathbf{k}})U(\phi_{\mathbf{k}'})$ makes both *time-reversal preserving* impurities to have vanishing spin-resolved LDOS $\delta\rho^{i}_{sc/qm}(\mathbf{r},\tilde{\omega}) = 0$ and FT-LDOS $\delta\rho^{i}_{sc,qm}(\mathbf{q},\tilde{\omega}) = 0$ as opposed to the *time-reversal breaking* impurity $\delta\rho^{i}_{cl}(\mathbf{r},\tilde{\omega}) \neq 0$ which decays *slow* as $\alpha = 1$ and FT-LDOS $\delta\rho^{i}_{cl}(\mathbf{q},\tilde{\omega}) \neq 0$. Further the *time-reversal breaking* impurity have vanishing spin-unresolved LDOS $\delta\rho_{cl}(\mathbf{r},\tilde{\omega}) = 0$ and FT-LDOS $\delta\rho_{cl}(\mathbf{q},\tilde{\omega}) = 0$ in the 1^{st} Born approximation.

- However, the energy dependence of the self-energy $\Sigma^{(2)}(\tilde{\omega},J) \propto g(\tilde{\omega})$ arise due to the intermediate spin-flip scattering and differentiate the quantum magnetic impurity from the scalar potential by *deforming the not singular cusp* at $q = 2k_F$ in the spin-unresolved FT-LDOS (black and red lines in figure C.2 and C.4). Hence this is a consequence of its *magnetic* nature, since the scalar is non-magnetic and cannot backscatter. The cusp deformation comes from the $\Im[\Sigma^{(2)}(\tilde{\omega},J)]\Re[|\tilde{\omega}|^2\left(f_0^2(\tilde{\omega},r) - f_1^2(\tilde{\omega},r)\right)] \sim \cos(2|\tilde{\omega}|r)r^{-2}$

All these features of the surface properties induced by the impurities in the 1^{st} Born approximation are summarized in table 7.2.

In the full T-matrix expansion the induced the surface properties of the quantum magnetic impurity compared to the scalar and classical magnetic impurity:

- In the spin-unresolved/charge channel the T-matrix expansion for the two magnetic impurities, i.e the classical and quantum magnetic, becomes identical $t_{cl}(\tilde{\omega},J) = t_{qm}(\tilde{\omega},J)$ and hence the LDOS Eqn. (7.5) and FT-LDOS Eqn. (7.6) responses are equal. The LDOS

response is illustrated in 5.2 and all impurities, i.e. scalar classical and quantum magnetic, have long-distance LDOS expansion with a leading decay rate of $\alpha = 2$ as tabulated in table 7.1. The FT-LDOS responses are illustrated in figure 6.6,6.7 and 6.8. From these FT-LDOS response plots one see, that the classical magnetic impurity develop a cusp deformation identical to the quantum magnetic one.

- The full T-matrix expansion differs between the non-magnetic and magnetic impurities, so the scalar t-function is different from the magnetic ones $t_{sc}(\tilde{\omega}, J) \neq t_{cl}(\tilde{\omega}, J) = t_{qm}(\tilde{\omega}, J)$. This makes the scalar FT-LDOS response dependent on bias frequency $\tilde{\omega}$, as illustrated in figure 6.6,6.7 and 6.8 for $J > 0$, which were not the case in the 1^{st} Born approximation illustrated by the red line in figure C.4. Since $t_{sc}(\tilde{\omega}, J)$ have a $\Re$ and $\Im$ part the FT-LDOS develops a cusp deformation similar to the magnetic onces for $\tilde{\omega} < 0$ (for $J > 0$).
  - The situation is reverse for $J < 0$ where the scalar potential FT-LDOS get a cusp deformation similar to the magnetic onces for $\tilde{\omega} > 0$, but have a non-deformed cusp for $\tilde{\omega} < 0$ which differentiate the scalar from the quantum magnetic impurity.

All these features of the surface properties induced by the impurities in the full T-matrix expansion are summarized in table 7.2.

Table 7.1: Table of α for point-impurities in the Dirac model and full T-matrix.

change in LDOS	$(\mathbf{k}_f, \mathbf{k}_i)$	α for spin-unresolved $\delta\rho$	α for spin-resolved $\delta\rho^i$
scalar	TRP	2	-
classical magnetic	TRP	2	1
quantum magnetic	TRP	2	-
conv.metal		1	

Table 7.2: Table of the Dirac models LDOS and FT-LDOS responses in the 1^{st} Born Approx. and the full T-matrix for the scalar on a conventional metal and the scalar and magnetic impurities on a helical metal. A blank entry means that the response is not calculated whereas a '-' means that the response is vanishing and $s(J) \equiv sign(J)$.

		LDOS		FT-LDOS at $\mathbf{q} = 2\mathbf{k}_F$	
		$r^{-\alpha} : \delta\rho(\mathbf{r})$	$r^{-\alpha} : \delta\rho^i(\mathbf{r})$	$\delta\rho(\mathbf{q})$	$\delta\rho^i(\mathbf{q})$
sc,conv.	1.BA	1		singl.	
	full T	1		singl.	
sc,hel.	1.BA	2	-	not singl. cusp for $\tilde{\omega} = \pm s(J)$	-
	full T	2	-	not singl. but defm. cusp for $\tilde{\omega} = -s(J)$	-
qm,hel.	1.BA	2	-	not singl. but defm. cusp for $\tilde{\omega} = \pm s(J)$	-
	full T	2	-	not singl. but defm. cusp for $\tilde{\omega} = \pm s(J)$,$t_{cl}(\tilde{\omega}, J) = t_{qm}(\tilde{\omega}, J)$	-
cl,hel.	1.BA	-	1	-	singl.
	full T	2	1	not singl. but defm. cusp for $\tilde{\omega} = \pm s(J)$, $t_{cl}(\tilde{\omega}, J) = t_{qm}(\tilde{\omega}, J)$	singl.

The argument presented in section 3.1.1 and 3.1.2 declare, that,

> For scattering upon a scalar impurity (i.e. a time-reversal invariant perturbation) on a helical metal surface, backscattering is suppressed and hence the FT-LDOS response at backscattering vector $\mathbf{q} = 2\mathbf{k}_F$ is *not singular* as is exhibited in figure 6.2. Likewise is the decay rate fast $\alpha = 2$, because the backscattering vector is forbidden and

> hence the standing wave oscillations (i.e. interference of the scattering vectors) strongly attenuated. Conversely, the presence of a singularity at $\mathbf{q} = 2\mathbf{k}_F$ in the spin-unresolved FT-LDOS response signal is associated with a slow $\alpha = 1$ decay rate because the backscattering vector is allowed, and therefore the standing waves is not attenuated.

This argument is only correct if one know the impurity to be a scalar. Because the argument use the knowledge, that a $\alpha = 1$ from a backscattering vector gives a singularity in the FT-LDOS. This much is true. But one is not entitle to conclude, that just because the LDOS oscillation decay with $\alpha = 2$ and correspondingly no singularity in the FT-LDOS, then no backscattering has occurred. Because both time-reveal preserving impurities have $\alpha = 2$ (and the Fourier transform of that has no singularity), and since we now know that the quantum impurity in fact backscatter. So the quantum impurity is a counter example against the argument. It indeed backscatter in the intermediate scatterings, but have a fast decay rate $\alpha = 2$ and correspondingly no singularity in FT-LDOS response because the overall scattering vector between the incoming and outgoing vectors is like the scalar $\Sigma^{(2)} \propto U^\dagger(\phi_{\mathbf{k}})U(\phi_{\mathbf{k}'})$ The intermediate scattering information is hidden in the energy dependence of $\Sigma^{(2)} \propto g(\tilde{\omega})$ which the decay rate do not take into account, because only the distance dependence matter. But Eqn. 7.1 show that this information can be separated from the energy dependence, which gives the *cusp deformation*.

The flaw of the argument presented above happens in the following case: By just knowing that a *single local* and *time-reversal invariant* impurity is present (ex. by STM maps or performing ARPES of the dispersion) on the surface of a helical metal, one cannot deduce that it is a scalar potential by measure a decay rate $\alpha = 2$. This is because the quantum magnetic impurity is also time-reversal invariant and its LDOS decay with the same rate.

However, one can identify which of the time-reversal impurities is present on the helical metal by measureing the LDOS response resonances for probe frequencies $\tilde{\omega} > 0$ *and* $\tilde{\omega} < 0$. Figure 5.2 show that the quantum magnetic impurity have symmetric resonance peaks, whereas the scalar potential only have a single peak at $\tilde{\omega} < 0$ for a repulsive potential. If the potential is attracthive then tha resonance peak would occur at $\tilde{\omega} > 0$.

This difference in the LDOS responses are reflected in the FT-LDOS where probing $\tilde{\omega} < 0$ a small *cusp deformation* at $q = 2k_F$ occur, depending on whether the time-reversal invariant perturbation is a scalar or a quantum magnetic impurity, as seen on figure 6.6, 6.7 and 6.8. For a attractive scalar $J < 0$, the situation is reversed, so probing $\tilde{\omega} > 0$ has a small FT-LDOS *cusp deformation* at $q = 2k_F$ but the $\tilde{\omega} < 0$ only has a cusp.

Neither can the spin-resolved FL-LDOS distinguish between the scalar potential and quantum magnetic impurity, because the FT-LDOS response of them both is zero, as derived by ref [22]. Actually ref [22] only derived the results for a scalar and classical magnetic impurity, but since the scalar and quantum impurity is derived here to be proportional to each other, then the spin-resolved FT-LDOS of the scalar, will also be the same for the quantum magnetic impurity. The spin-resolved LDOS and FT-LDOS responses can exclusively differentiate between time-reversal preserving and breaking impurities, because the form have vanishing responses whereas the latter not.

By the spin-unresolved LDOS and FT-LDOS responses no difference among the magnetic impurities exist because their t-functions $t_{qm}(\tilde{\omega}, J) = t_{cl}(\tilde{\omega}, J)$ are identical. This cause the symmetric resonance peaks in the LDOS response and the symmetric cusp deformations in the FT-LDOS response. Hence it would be tempting to use the cusp deformation as a signature of backscattering, but since the scalar also develop one, such a signature would be ambiguous.

The resonance peaks of the spin-unresolved LDOS and FT-LDOS are *all* determined by the t-functions Eqn. 4.56, 4.57 and (4.58) for the respective impurities. A general feature is that *all* the resonances of the scalar, classical magnetic impurity and the quantum magnetic impurity (when 2^{nd} order T-matrix $\tilde{T}^{qm}(\tilde{\omega}, J)$ is used) derived in this thesis depend on probe energy/frequency $\tilde{\omega} = \omega + \mu$. This has the consequence that, two different systems prepared such that $\tilde{\omega}_1 = \tilde{\omega}_2 = \tilde{\omega}_0$ for some fixed energy $\tilde{\omega}_0$. For two systems where:
System 1. has half-filling, i.e. $\mu_1 = 0$, and probing away/not directly on the Fermi surface, i.e. $\omega_1 \neq 0$,
System 2. has finite-filling, i.e. $\mu_2 \neq 0$, and probing on the Fermi surface, i.e. $\omega_2 = 0$. Now if it happen that the values $\tilde{\omega}_0, \omega_1$ and μ_2 are such that $\tilde{\omega}_0 = \omega_1 = \mu_2$, i.e $\tilde{\omega}_0 = \tilde{\omega}_1 = \tilde{\omega}_2$, then both systems have identical LDOS and FT-LDOS observables.

The feature just mentioned has the consequence that for the quantum impurity (when $\tilde{\Sigma^{(2)}}^{qm}(\tilde{\omega}, J)$ is used) all resonance peaks appear symmetric around $\tilde{\omega} = 0$ determined by the t^{imp}-function, which is a result of the Dirac model having a symmetric band cut-off. This is not the case for real Bi_2Se_3 and Bi_2Te_3 material and further the Fermi level may be $\mu \neq 0$. Both are causes, that cause the resonance peaks not to be situated symmetric on the electron and hole side.

When the quantum impurity induced 3^{rd} order self-energy is taking into account, the above feature is *not* the case any more, and in this sense, it captures the effect of the Fermi level μ and the states that is being probed, i.e. $\omega < 0$,$\omega = 0$ or $\omega > 0$. However the band cut-off is still symmetric and in this respect the $\tilde{T}^{qm,(3)}(\mu, \omega, J, T)$ do not look identical to the real Bi_2Se_3 and Bi_2Te_3 materials. But as argued in defend of the Dirac model in section 2, is not a big worry since it captures the low-energy physics of these material and later generations of material can be doped in such a way that the Dirac model becomes very close to a real material.

Recall from section A.3 on the symmetry of $\tilde{\Sigma}^{(3)}(\mu, \omega, J, T)$ for $\mu \neq 0$ and $\omega \neq 0$. Symmetry consideration of Eqn. (4.40) and (4.39) show that the retarded
$\Sigma^{(3)}$, for a certain $\tilde{\omega} = \tilde{\omega}(\omega, \mu) = \tilde{\omega}(\omega_0, \mu_0) = \tilde{\omega}_0$, have to obey

$$\Re\Sigma^{(3)}(\tilde{\omega}(\omega_0, \mu_0)) = -\Re\Sigma^{(3)}(\tilde{\omega}(-\omega_0, -\mu_0)) \tag{7.7}$$

$$\Im\Sigma^{(3)}(\tilde{\omega}(\omega_0, \mu_0)) = +\Im\Sigma^{(3)}(\tilde{\omega}(-\omega_0, -\mu_0)) \tag{7.8}$$

This is supposed to be understood such that two same-valued $\tilde{\omega}_1$ and $-\tilde{\omega}_0$ are parametrized such $\tilde{\omega}_1 = \tilde{\omega}(\omega_1, \mu_1) = \tilde{\omega}(-\omega_0, -\mu_0) = -\tilde{\omega}_0$ do *not* (of cause unless $\omega_1 = -\omega_0$ and $\mu_1 = -\mu_0$ simultaneously) have the above derived asymmetry and symmetry relations respectively, i.e

$$\Re\Sigma^{(3)}(\tilde{\omega}(\omega_0, \mu_0)) \neq -\Re\Sigma^{(3)}(\tilde{\omega}(\omega_1, \mu_1)) \tag{7.9}$$

$$\Im\Sigma^{(3)}(\tilde{\omega}(\omega_0, \mu_0)) \neq +\Im\Sigma^{(3)}(\tilde{\omega}(\omega_1, \mu_1)) \tag{7.10}$$

To conclude, the symmetry-feature here is explicit dependent on the parameters ω_0, μ_0 entering the parametrization $\tilde{\omega}(\omega_0, \mu_0) = \tilde{\omega}_0$. This is a new feature arising in the 3.order self-energy that is *not* present in the 2.order self-energy, where $\Sigma^{(2)}(\tilde{\omega})$ *only* depends on the value of $\tilde{\omega} = \omega + \mu$. I.e. any two different systems prepared such that $\tilde{\omega}_1 = \tilde{\omega}_2 = \tilde{\omega}_0$ for some fixed energy $\tilde{\omega}_0$ have $\Sigma^{(2)}(\tilde{\omega}_1) = \Sigma^{(2)}(\tilde{\omega}_2)$. This means the $\Sigma^{(3)}(\omega, \mu)$ depends highly on the Fermi level μ and which state is probed i.e. on ω. In $\Sigma^{(2)}(\tilde{\omega})$ it is any $\tilde{\omega}$ and hence no specific reference to the Fermi level. Notice that this is only for the quantum magnetic impurity.

Before one gets too excited about the quantum magnetic impurity on the helical metal, one should notice that it actually might not exist at all. The helical metal has very large spin-orbit coupling in the bulk, because that was the very reason why, the band inversion could take place in the first instance, and hence drive it to the non-trivial $v_0 = 1$ topological phase. But it happens,

that a surface which has a large spin-orbit coupling also has a strong *anisotropy*, i.e. an easy axis in the surface plane. So it cost some energy to align a spin in a different direction that this east axis, and hence the concept of a free localized spin do not make sense anymore. The Kondo/exchange Hamiltonian that was used in this thesis, exactly rely on the existence of such a free spin. But if the Kondo temperature is larger, than the energy cost to flip against the easy axis, then the free localized spin concept is restored.

Chapter 8

Conclusion

In this thesis the first and basic question was, what are the restrictions on the electron scattering imposed by the helical spin-momentum locking, when a helical electron scatter off a *single local* impurity. The impurities considered are a scalar potential (time-reversal preserving and non-magnetic), a classical magnetic (time-reversal breaking and magnetic) and assuming the existence of a quantum magnetic (time-reversal preserving and magnetic) impurity. It was further investigated how these imposed restrictions influenced the spin-unersolved and spin-resolved LDOS and FT-LDOS responses, which are measureable by a STM probe. The results presented for the scalar and classical magnetic impurity was derived in ref [9, 22, 31], but those of the quantum magnetic impurity are not published except for the LDOS oscillation decay rate in ref [39].

In order to determine the restrictions on the scattering, the 1^{st} Born approximation of Fermi's golden rule for the scalar potential and quantum magnetic impurity were calculated for an incoming + helicity cone surface electron with momentum $\mathbf{k}$. In section 3.1.1 the squared matrix element for the scalar potential Eqn. (3.9) $w^{sc}_{+,\mathbf{k}\to+,\mathbf{k}'}$ is illustrated in figure 4.2. Especially the scalar are allowed to forward scatter, but direct backward scattering is suppressed as expected.

In section 3.1.2 the possible matrix elements squared for a spin-half $S = \frac{1}{2}$ quantum magnetic impurity were calcluated. The 'impurity non spin-flip' transition rate Eqn. (3.10) $w^{qm}_{M;+,\mathbf{k}\to M;+,\mathbf{k}'}$ is highly scattering angle dependent, and in particular the direct forward scattering is forbidden but backward scattering allowed. On the other hand the 'impurity spin-flip' matrix element squared Eqn. (3.14) $w^{qm}_{M;+,\mathbf{k}\to 1+M;+,\mathbf{k}'}$ is independent of angles.
Summing over the impurity spin-polarizations $w^{qm}_{\mathbf{k},+\to\mathbf{k}',\eta'} = \sum_{M,M'=\frac{1}{2},-\frac{1}{2}} w^{qm}_{M;\mathbf{k},+\to M';\mathbf{k}',\eta'}$ is illustrated in figure 4.2, and note especially that the quantum magnetic impurity is allow to scatter *any* angle.

These matrix elements squared enter the inverse transport time $\frac{1}{\tau^{tr}}$, i.e. the time entering the expression for the conductivity, and it is given by Eqn. (4.23) and (4.22) on the helical metal for the scalar potential and quantum magnetic impurity, respectively. Likewise on the conventional Dirac metal the transport time Eqn. (4.24) and (4.25), respectively. In section 4.1 it was derived that in the case of a scalar potential, the transport lifetime on the helical metal is a factor 4 larger than on the conventional Dirac metal. For the quantum impurity this difference is not quite that remarkable, but a factor $\frac{12}{7}$ larger on the helical metal than the conventional Dirac metal. In any case, this enhancement is solely due to the helical metal Fermi surface, which in the 'Dirac model' has non-degenerate surface states with spin locked tangentially to the Fermi surface momentum.

For the quantum magnetic impurity the first non-vanshing irreducible self energy contribution is the second order diagram illustrated in figure 7.1. It is second order in the coupling J, and hence the surface electron interacts with it twice. Upon scattering with the impurity, the electron is allowed to scatter *any* angle due to the calculated square matrix element $w^{qm}_{\mathbf{k},+\to\mathbf{k}',+}$ which is plotted in figure 4.2. However, averaging the time ordered impurity spin $\langle S^i S^j \rangle \propto \delta_{i,j}$ cause the the overall incoming and outgoing momentum dependence to be *exactly* as the scalar potential. The intermediate scattering - in any direction - is summed to a complex energy dependece $g(\tilde{\omega})$ given by Eqn. (4.13). Hence the second order irreducible self energy for the quantum magnetic impurity $\tilde{\Sigma}^{(2)}_{\mathbf{k},\mathbf{k}'}(\tilde{\omega}) = -\frac{3}{4} g(\tilde{\omega}) J^2 U^\dagger(\phi_{\mathbf{k}}) U(\phi_{\mathbf{k}'})$ is just a *complex scalar*. Hence despite a arbitrary intermediate scattering, the overall backscattering is suppressed. This has several consequences for the measured LDOS and FT-LDOS responses as will be described next.

By measuring *both* spin-unresolved and spin-resolved LDOS (see figure 5.3, 5.4, 5.5, 5.6, 5.7 and 5.7) and FT-LDOS responses, it is possible to identify which single local impurity is present on the helical surface, i.e. whether it is a scalar potential, a classical or quantum magnetic impurity. In table 7.2 all the responses of a surface with one of the respective impurities are summarized.

With spin-resolved LDOS and FT-LDOS it is possible to distinguish between a impurity that *break or preserve time-reversal symmetry*, since the former has non-vanshing responces whereas the latter due to time-reversal preservation vanish. This was showed by ref [22] in the case of the scalar potential and the classical magnetic impurity, but the case of a quantum magnetic impurity is derived here in section 5.1.2 for the LDOS response and FT-LDOS response in appendix B.2.2. It simply follows since the T-matrix for the scalar and quantum magnetic impurity has the same momentum dependence and is given by Eqn. (4.2) and (4.12), respectively.

With *only* spin-unresolved LDOS (see figure 5.2) and FT-LDOS responses (see figure 6.2, 6.6, 6.7 and 6.8) it is more complicated to distinguish between the impurities.
In case the classical magnetic impurity *is* strong enough to open a gap in the dispersion, then by ARPES or STM measurements of the surface state dispersion, it would be possible to infer that the impurity present is time-reversal breaking, since the time-reversal preserving impurities cannot open a gap.
In case the classical magnetic impurity is *not* strong enough to open a gap in the dispersion, then *no* ARPES or STM measurements of the surface state dispersion would possibly reveal that the impurity present is a time-reversal breaking or preserving impurity. With spin-unresolved LDOS and FT-LDOS responses it is *not* possible to distinguis between the magnetic impurities. That is because the the energy dependence of the T-matrix (see Eqn. (4.58)) for the classical and quantum magnetic impurites $t_{cl}(\tilde{\omega}, J) = t_{qm}(\tilde{\omega}, J)$ are identical in the spin-unresolved probe. Further, it is only possible to distinguish between the non-magnetic (scalar potential) and magnetic (classical and quantum) impurities by probing $\tilde{\omega} > 0$ for a repulsive potental. For these probe frequiencies the LDOS response for the magnetic impurities have a resonance peak, whereas the non-magnetic potential has no resonanse peak. In the FT-LDOS response at $q = 2\mu$, i.e. twice the Fermi energy, this leads to a cusp deformation for the magnetic impurities, whereas the non-magnetic has a cusp. For a attractive potental one has to probe $\tilde{\omega} < 0$.

Since the quantum magnetic impurity is a complex scalar, then the decay rate (see table 7.1 and table 7.2) $r^{-\alpha}$ of the spin-unresolved LDOS Friedel ocillation is fast $\alpha = 2$, like that induced by the scalar potential and classical magnetic impurity. So since the quantum magnetic impurity is explicity showed by $w^{qm}_{\mathbf{k},+\to\mathbf{k}',\eta'}$ to allow *any* intermediate scattering, then one *cannot* conclude, that a fast $\alpha = 2$ imply that no backscatter occur. It only imply that a *overall* backscattering is suppressed in the case of the quantum magnetic impurity.

If the temperature is lowered to the Kondo regime, then the spin-unresolved LDOS response resonance amplitude induced by the quantum magnetic impurity enhances due to an effectively larger coupling $|J_{eff}| > |J|$. This will also shift the position of the resonances due to inclusion of Eqn. 4.47 $\Im\Sigma^{(3)}(\mu, \omega, J_{eff}, T)$, which is strongly dependent on the Fermi level μ and the probing/bias frequency ω.

Due to the linear density of states (DOS) Eqn (2.17) of a helical metal, the Kondo problem on a helical metal is largely influenced by the Fermi level μ. This is unlike the conventional metal because of its constant DOS Eqn. (2.13). When complete symmetry of holes and electrons $\mu = 0$ the Kondo problem vanish, whereas it is present for arbitraty assymetry $|\mu| \leqq |D|$. At $|\mu| = |D|$ the Kondo problem is present for any temperature and do not arise due to a log-singularity, but from the ultraviolet energy band cut-off. This seems to be an unphysical artifact of the Dirac model used in this thesis. However, for $0 < |\mu| << |D|$ and low temperatures this artifact becomes negligible, and the 3^{rd} order contribution is the log-singularity only. This give rise to the Kondo problem & temperature Eqn. (4.55) in the helical metal, which is very similar to that Eqn. (4.48) on a conventional Metal. Both depends exponentially on the inverse coupling-and DOS at the Fermi level of the respective metals, but on the helical metal the Kondo temperature is inverse proportional to the DOS at the Fermi level, whereas on the conventional metal it depends linearly.

Chapter 9

Prospect

As illustrated in figure 6.4(f), one see that, based on experiments, the FT-LDOS cusp of the scalar and magnetic cannot be distinguished. Therefore in prospect; it would be interesting to do an impurity averaging over many uniformly distributed impurities (of the same type) placed at $\delta(\mathbf{r}_i)$ on the surface. This might change the FT-LDOS of the magnetic-impurity, so that the small cusp deformation would either disappear of smoothly deforms to look like the cusp for the scalar in the 1^{st} Born approximation. In that case it show that one will not see any difference between them.

Calculate the squared matrix elements in the 2^{nd} order Born approximation Eqn. (3.8). This should be a consistency check on the 3^{rd} order self-energy. It will show which $w^{qm}_{M\to M}$ or $w^{qm}_{M\to M+1}$ matrix elements, that will dominate when approaching the Kondo temperature. Further by the angle dependence in $w^{qm}_{M\to M}$ and $w^{qm}_{M\to M+1}$ will tell which scattering angles that also get enhanced by approaching the Kondo temperature.

Calculate the matrix element squared in the 1^{st} order Born approximation in Eqn. (3.8), but including warping ($\lambda \neq 0$) It would tell the same as mentioned just above, but more interestingly, notice that in the warping model the spin-expectation value on the Fermi surface becomes

$$\langle +,\mathbf{k}|\bar{s}|\mathbf{k},+\rangle_{\lambda\neq 0} = \frac{1}{2}\begin{pmatrix} 2\sin\phi_{\mathbf{k}}\cos\frac{\theta_{\mathbf{k}}}{2}\sin\frac{\theta_{\mathbf{k}}}{2} \\ -2\cos\phi_{\mathbf{k}}\cos\frac{\theta_{\mathbf{k}}}{2}\sin\frac{\theta_{\mathbf{k}}}{2} \\ \cos\theta_{\mathbf{k}} \end{pmatrix} \tag{9.1}$$

where $\tan\theta_{\mathbf{k}} = k_c^2/(k^2\cos 3\phi_{\mathbf{k}})$. So $\langle +,\mathbf{k}|\bar{s}|\mathbf{k},+\rangle_{\lambda\neq 0} = \cos\theta_{\mathbf{k}} \neq \langle +,\mathbf{k}|\bar{s}|\mathbf{k},+\rangle|_{\lambda=0} = 0$, which for angles $\cos\theta_{\mathbf{k}} = 1$, the state $\tau^z|\mathbf{k},+\rangle$ is parallel to $\langle +,\mathbf{k}|$, which mean that the quantum impurity in the 1^{st} order Born approximation is allowed to forward scatter for some angles $\phi_{\mathbf{k}}$ such that $\cos\theta_{\mathbf{k}} = 1$. Remember the 'impurity non spin-flip' matrix element squared in the Dirac model ($\lambda = 0$)

$$w^{qm}_{M;+,\mathbf{k}\to M;+,\mathbf{k}'}|_{\lambda=0} = \frac{\pi}{2\hbar}J^2\sin\left(\frac{\phi_{\mathbf{k}}-\phi_{\mathbf{k}'}}{2}\right)^2 \tag{9.2}$$

but this is not the case any more in the warping model where

$$w^{qm}_{M;+,\mathbf{k}\to M;+,\mathbf{k}'}|_{\lambda\neq 0} = ? \tag{9.3}$$

which for sure have an impact on the inverse lifetime and the inverse transport time. One might speculate that the result would approach, that of the scalar, since it is allowed to forward scatter which it was not allowed in the Dirac Model.

Appendix A

3^{rd} oder self energy

The dependence of $\Im\Sigma^{(3)}$ and $\Re\Sigma^{(3)}$ on the parameters λ and μ have to reflect that $\Im\rho$ and $\Re\rho$ respectively. Therefore symmetry considerations on $\Im\rho$ and $\Re\rho$ with respect to the parameters mount to clerify the symmetry-structure of the self-energy but also a consistency controle of the calculation. In order to survey the resulting $\Im\Sigma^{(3),R}(\lambda,\mu)$ and $\Re\Sigma^{(3),R}(\lambda,\mu)$ in the relevant limits $\lambda \to 0$ and $\mu \to 0$ in the cases where both limits are taking simultaneously or singly, the derivations are devided into three cases which should transform into eachother in the relevant limits.

A.1 For $\mu = 0, \omega \neq 0$

Since $\omega \neq 0$ and $\mu = 0$ then $\phi \neq 0$ and $\lambda = 0$ thus $\tilde{\phi} = \phi \neq 0$. Symmetry consideration of Eqn. (4.40) and Eqn. (4.39) show that the retarded ρ have to obey

$$\Re\rho(\phi) = -\Re\rho(-\phi) \tag{A.1.1}$$
$$\Im\rho(\phi) = +\Im\rho(-\phi) \tag{A.1.2}$$

A.1.1 $\Im\rho(\phi)$

Define notation $sgn(\cdot) = s(\cdot)$ and

$$\begin{aligned}\rho(i\phi_n) &= \sum_{\eta_1\eta_3} \frac{\eta_3}{\eta_1 q_1 - \eta_3 q_3} \frac{1}{i\phi_n - \eta_1 q_1} \\ &= \left(\frac{1}{q_1 - q_3} - \frac{1}{q_1 + q_3}\right)\left(\frac{1}{i\phi_n - q_1} + \frac{1}{i\phi_n + q_1}\right)\end{aligned}$$

Using that

$$q_3\left(\frac{1}{q_1 - q_3} - \frac{1}{q_1 + q_3}\right) = -2 + q_1\left(\frac{1}{q_3 + q_1} - \frac{1}{q_3 - q_1}\right)$$

simplify the first integration to yield

$$\int_0^1 \frac{\mathrm{d}q_3}{2\pi} q_3\,\rho(i\phi) = \frac{1}{2\pi}\left[-2 + q_1\left(\log\left(1 + \frac{1}{q_1}\right) - \log\left(-1 + \frac{1}{q_1}\right)\right)\right]\left(\frac{1}{i\phi_n - q_1} + \frac{1}{i\phi_n + q_1}\right)$$

focusing on the imaginary part, the second integral becomes

$$\int_0^1 \frac{\mathrm{d}q_1}{2\pi} q_1 \int_0^1 \frac{\mathrm{d}q_3}{2\pi} q_3 \, \Im\rho(\phi) = \frac{|\phi|}{2\pi}\left[1 - \frac{|\phi|}{2}\log\left(\frac{|\phi|+1}{1-|\phi|}\right)\right]$$

thus

$$\Im R(\omega) = \frac{D|\omega|}{2\pi}\left[1 - \frac{|\omega|}{D}\frac{1}{2}\log\frac{D+|\omega|}{D-|\omega|}\right] \tag{A.1.3}$$

A.1.2 $\Re\rho(\phi)$

$$\Re\rho(\phi) = \left(\frac{1}{q_1 - q_3} - \frac{1}{q_1 + q_3}\right)\left(\frac{1}{\phi - q_1} + \frac{1}{\phi + q_1}\right)$$

Using

$$q_1 \frac{1}{q_1 - q_3} = 1 + q_3 \frac{1}{q_1 - q_3} \tag{A.1.4}$$

and

$$q_1 \frac{1}{q_1 + q_3} = 1 - q_3 \frac{1}{q_3 + q_1}$$

together with

$$\left(\frac{1}{\phi - q_1} + \frac{1}{\phi + q_1}\right) = s(\phi)\left(\frac{1}{|\phi| - q_1} + \frac{1}{|\phi| + q_1}\right)$$

then

$$\begin{aligned}\int \mathrm{d}q_1 \, q_1 \, \Re\rho(\phi) &= s(\phi) q_3 \int \mathrm{d}q_1 \, \left(\frac{1}{q_1 - q_3} + \frac{1}{q_1 + q_3}\right)\left(\frac{1}{|\phi| - q_1} + \frac{1}{|\phi| + q_1}\right) \\ &= s(\phi) q_3 \Big(\Gamma(\phi, q_3) + \Omega(\phi, q_3)\Big)\end{aligned}$$

Here we encounter two equations that will appear several times. Henceforth define

$$\Gamma(a, q_3) = \int \mathrm{d}q_1 \, \frac{1}{|a| - q_1}\frac{1}{q_1 - q_3} + \frac{1}{|a| + q_1}\frac{1}{q_1 + q_3} = \frac{\log\left(\frac{|a|(1-q_3)}{q_3(1-|a|)}\right)}{|a| - q_3} + \frac{\log\left(\frac{|a|(1+q_3)}{q_3(1+|a|)}\right)}{|a| - q_3} \tag{A.1.5}$$

and

$$\Omega(a, q_3) = \int \mathrm{d}q_1 \, \frac{1}{|a| + q_1}\frac{1}{q_1 - q_3} + \frac{1}{|a| - q_1}\frac{1}{q_1 + q_3} = \frac{\log\left(\frac{|a|(1-q_3)}{q_3(1+|a|)}\right)}{|a| + q_3} + \frac{\log\left(\frac{|a|(1+q_3)}{q_3(1-|a|)}\right)}{|a| + q_3} \tag{A.1.6}$$

both for $a, b \in]-1, 1[/\{0\}$. At last

$$\Re R(\omega) = D^2 \int_0^1 \frac{\mathrm{d}q_3}{2\pi} q_3 \frac{\mathrm{d}q_1}{2\pi} q_1 \, \Re\rho(\omega) = \left(\frac{D}{2\pi}\right)^2 \int_0^1 \mathrm{d}q_3 \, s(\omega) q_3^2 \, \Big(\Gamma(\frac{\omega}{D}, q_3) + \Omega(\frac{\omega}{D}, q_3)\Big) \tag{A.1.7}$$

which is left to be calculated numerically.

A.2 For $\mu \neq 0, \omega = 0$

Since $\mu \neq 0$ and $\omega = 0$ then $\phi = 0$, $\lambda \neq 0$ and $\tilde{\phi} = \lambda \neq 0$. The symmetry of Eqn. (4.40) and Eqn. (4.39) show that the retarded ρ have to obey

$$\Re\rho(\lambda) = -\Re\rho(-\lambda) \tag{A.2.1}$$
$$\Im\rho(\lambda) = +\Im\rho(-\lambda) \tag{A.2.2}$$

A.2.1 $\Im\rho(\lambda)$

$$\begin{aligned}\Im\rho(\lambda) &= \sum_{\eta_1\eta_3} \frac{s(\eta_3 q_3 - \lambda)}{\eta_1 q_1 - \eta_3 q_3}(-\pi)\delta(\lambda - \eta_1 q_1) \\ &= -\pi\left[\left(\frac{s(q_3-\lambda)}{q_1-q_3} - \frac{s(q_3+\lambda)}{q_1+q_3}\right)\delta(\lambda - q_1) + \left(\frac{s(q_3-\lambda)}{-q_1-q_3} - \frac{s(q_3+\lambda)}{-q_1+q_3}\right)\delta(\lambda + q_1)\right]\end{aligned}$$

then

$$\int_0^1 \frac{\mathrm{d}q_1}{2\pi} q_1\, \Im\rho(\lambda) = -|\lambda|\left[\frac{s(q_3-|\lambda|)}{|\lambda|-q_3} - \frac{s(q_3+|\lambda|)}{|\lambda|+q_3}\right]$$

the first term of which gives rise to a log-singularity from the principal value as

$$\int_0^1 \frac{\mathrm{d}q_3}{2\pi} q_3 \frac{s(q_3-|\lambda|)}{|\lambda|-q_3} = \frac{1}{2\pi}\left[-1 + 2|\lambda| - |\lambda|\log|\lambda| - |\lambda|\log(1-|\lambda|) + 2|\lambda|\log\delta\right]$$

whereas the second term is finite

$$\int_0^1 \frac{\mathrm{d}q_3}{2\pi} q_3 \frac{s(q_3+|\lambda|)}{|\lambda|+q_3} = \frac{1}{2\pi}\left[1 + |\lambda|\log|\lambda| - |\lambda|\log(1+|\lambda|)\right]$$

thus

$$\Im R(\mu) = \frac{D|\mu|}{2\pi}\left[1 - \frac{|\mu|}{D} - \frac{|\mu|}{D}\left(\frac{1}{2}\log\frac{D+|\mu|}{D-|\mu|} + \log\frac{T}{D} - \log\frac{|\mu|}{D}\right)\right] \tag{A.2.3}$$

where T/D mathematically is the Cauchy-principal infinitesimal parameter (δ) that gives the log-singularity but physically is the 'dimensionless temperature'.

A.2.2 $\Re\rho(\lambda)$

$$\begin{aligned}\Re\rho(\lambda) &= \sum_{\eta_1\eta_3} \frac{s(\eta_3 q_3 - \lambda)}{\eta_1 q_1 - \eta_3 q_3}\frac{1}{\lambda - \eta_1 q_1} \\ &= \frac{s(\lambda)}{|\lambda| - q_1}\left(\frac{s(q_3-|\lambda|)}{q_1-q_3} - \frac{s(q_3+|\lambda|)}{q_1+q_3}\right) + \frac{s(\lambda)}{|\lambda|+q_1}\left(\frac{s(q_3+|\lambda|)}{q_1-q_3} - \frac{s(q_3-|\lambda|)}{q_1+q_3}\right)\end{aligned}$$

Using Eqn. (A.1.4) then

$$\begin{aligned}\int \mathrm{d}q_1\, q_1\, \Re\rho(\lambda) &= s(\lambda)\left(s(q_3+|\lambda|)-s(q_3-|\lambda|)\right)\int \mathrm{d}q_1 \left(\frac{1}{|\lambda|-q_1}-\frac{1}{|\lambda|-q_1}\right)\\ &\quad +s(\lambda)q_3\left[s(q_3-|\lambda|)\Gamma(\lambda,q_3)+s(q_3+|\lambda|)\Omega(\lambda,q_3)\right]\\ &= s(\lambda)\left(s(q_3+|\lambda|)-s(q_3-|\lambda|)\right)\log\left(\frac{|\lambda|^2}{1-|\lambda|^2}\right)\\ &\quad +s(\lambda)q_3\left[s(q_3-|\lambda|)\Gamma(\lambda,q_3)+s(q_3+|\lambda|)\Omega(\lambda,q_3)\right]\end{aligned}$$

At last

$$\begin{aligned}\Re R(\mu) &= D^2\int_0^1 \frac{\mathrm{d}q_3}{2\pi}q_3\,\frac{\mathrm{d}q_1}{2\pi}q_1\,\Re\rho(\mu)\\ &= s(\mu)\left(\frac{D}{2\pi}\right)^2\left(\int_0^1\frac{\mathrm{d}q_3}{2\pi}q_3\,\left(s(q_3+|\mu|)-s(q_3-|\mu|)\right)\right)\log\left(\frac{|\mu|^2}{D^2-|\mu|^2}\right)\\ &\quad +s(\mu)\left(\frac{D}{2\pi}\right)^2\int_0^1\frac{\mathrm{d}q_3}{2\pi}q_3^2\left[s(q_3-|\mu|)\Gamma(\frac{\mu}{D},q_3)+s(q_3+|\mu|)\Omega(\frac{\mu}{D},q_3)\right]\\ &= -s(\mu)\left(\frac{D}{2\pi}\right)^2\mu^2\log\left(\frac{|\mu|^2}{D^2-|\mu|^2}\right)\\ &\quad +s(\mu)\left(\frac{D}{2\pi}\right)^2\int_0^1\mathrm{d}q_3\,q_3^2\left[s(q_3-|\mu|)\Gamma(\frac{\mu}{D},q_3)+s(q_3+|\mu|)\Omega(\frac{\mu}{D},q_3)\right]\end{aligned}\tag{A.2.4}$$

which is left to be calculated numerically.

A.3 For $\mu \neq 0, \omega \neq 0$

Since $\mu \neq 0$ and $\omega \neq 0$ then $\phi \neq 0$, $\lambda \neq 0$ and $\tilde{\phi} = \phi + \lambda$ is allowed to take any value between $-1 < \tilde{\phi} < 1$. Symmetry consideration of Eqn. (4.40) and Eqn. (4.39) show that the retarded ρ, for a certain $\tilde{\phi} = \tilde{\phi}(\phi,\lambda) = \tilde{\phi}(\phi_0,\lambda_0) = \tilde{\phi}_0$, have to obey

$$\Re\rho(\tilde{\phi}(\phi_0,\lambda_0)) = -\Re\rho(\tilde{\phi}(-\phi_0,-\lambda_0)) \tag{A.3.1}$$

$$\Im\rho(\tilde{\phi}(\phi_0,\lambda_0)) = +\Im\rho(\tilde{\phi}(-\phi_0,-\lambda_0)) \tag{A.3.2}$$

This is supposed to be understood such that two same-valued $\tilde{\phi}_1 = \tilde{\phi}(\phi_1,\lambda_1) = \tilde{\phi}(-\phi_0,-\lambda_0) = -\tilde{\phi}_0$ do *not* (of cause unless $\phi_1 = -\phi_0$ and $\lambda_1 = -\lambda_0$ simultaneously) have the above derived asymmetry and symmetry relations respectively, i.e

$$\Re\rho(\tilde{\phi}(\phi_0,\lambda_0)) \neq -\Re\rho(\tilde{\phi}(\phi_1,\lambda_1)) \tag{A.3.3}$$

$$\Im\rho(\tilde{\phi}(\phi_0,\lambda_0)) \neq +\Im\rho(\tilde{\phi}(\phi_1,\lambda_1)) \tag{A.3.4}$$

and further generally

$$\Re\rho(\tilde{\phi}_1) \neq \Re\rho(\tilde{\phi}_2) \tag{A.3.5}$$

$$\Im\rho(\tilde{\phi}_1) \neq \Im\rho(\tilde{\phi}_2) \tag{A.3.6}$$

even for those same-valued $\tilde{\phi}_1 = \tilde{\phi}(\phi_1, \lambda_1) = \tilde{\phi}(\phi_2, \lambda_2) = \tilde{\phi}_2$ if $\phi_1 \neq \phi_2$ and $\mu_1 \neq \mu_2$. To conclude, the symmetry-feature here is explicit dependent on the parameters ϕ_0, λ_0 entering the parametrization $\tilde{\phi}(\phi_0, \lambda_0) = \tilde{\phi}_0$. This is a new feature arising in the 3.order self-energy that is *not* present in the 2.order self-energy, where $\Sigma^{(2),R}(\tilde{\phi})$ *only* depends on the value of $\tilde{\phi} = \phi + \lambda$. I.e. any two different systems prepared such that $\tilde{\phi}_1 = \tilde{\phi}_2 = \tilde{\phi}_0$ for some fixed energy $\tilde{\phi}_0$ have $\Sigma^{(2),R}(\tilde{\phi}_1) = \Sigma^{(2),R}(\tilde{\phi}_2)$. This means the $\Sigma^{(3),R}(\omega, \mu)$ depends highly on the Fermi level μ and which state is probed i.e. on ω. In $\Sigma^{(2),R}(\tilde{\omega})$ it is any $\tilde{\omega}$ and hence no specific reference to the Fermi level.

A.3.1 $\Im\rho(\phi, \lambda)$

$$\begin{aligned}\Im\rho(\phi,\lambda) &= \sum_{\eta_1\eta_3} \frac{s(\eta_3 q_3 - \lambda)}{\eta_1 q_1 - \eta_3 q_3}(-\pi)\delta(\tilde{\phi} - \eta_1 q_1) \\ &= -\pi\left[\left(\frac{s(q_3-\lambda)}{q_1-q_3} - \frac{s(q_3+\lambda)}{q_1+q_3}\right)\delta(\tilde{\phi}-q_1) + \left(\frac{s(q_3-\lambda)}{-q_1-q_3} - \frac{s(q_3+\lambda)}{-q_1+q_3}\right)\delta(\tilde{\phi}+q_1)\right]\end{aligned}$$

First integration yield

$$\int_0^1 \frac{\mathrm{d}q_1}{2\pi} q_1\, \Im\rho(\phi,\lambda) = -\frac{|\tilde{\phi}|}{2}\left[\left(\frac{s(q_3-\lambda)}{|\tilde{\phi}|-q_3} - \frac{s(q_3+\lambda)}{|\tilde{\phi}|+q_3}\right)\Theta(\tilde{\phi}) + \left(\frac{s(q_3+\lambda)}{|\tilde{\phi}|-q_3} - \frac{s(q_3-\lambda)}{|\tilde{\phi}|+q_3}\right)\Theta(-\tilde{\phi})\right]$$

Using

$$\left(\frac{q_3}{|\tilde{\phi}|-q_3}\right) = -\left(\frac{q_3}{q_3-|\tilde{\phi}|}\right) = -\left(\frac{q_3-|\tilde{\phi}|}{q_3-|\tilde{\phi}|} + \frac{|\tilde{\phi}|}{q_3-|\tilde{\phi}|}\right) = -1 - \frac{|\tilde{\phi}|}{q_3-|\tilde{\phi}|}$$

and

$$\frac{q_3}{|\tilde{\phi}|+q_3} = \frac{q_3+|\tilde{\phi}|}{q_3+|\tilde{\phi}|} - \frac{|\tilde{\phi}|}{q_3+|\tilde{\phi}|} = 1 - \frac{|\tilde{\phi}|}{q_3+|\tilde{\phi}|}$$

then

$$\begin{aligned}&\int_0^1 \frac{\mathrm{d}q_3}{2\pi} q_3 \int_0^1 \frac{\mathrm{d}q_1}{2\pi} q_1\, \Im\rho(\phi,\lambda) \\ &= -\frac{|\tilde{\phi}|}{2}\left[-\int_0^1 \frac{\mathrm{d}q_3}{2\pi}\left(s(q_3-\lambda)+s(q_3+\lambda)\right) + \frac{|\tilde{\phi}|}{2}\int_0^1 \frac{\mathrm{d}q_3}{2\pi}\left(\frac{s(q_3+\lambda)}{|\tilde{\phi}|+q_3} - \frac{s(q_3-\lambda)}{q_3-|\tilde{\phi}|}\right)\Theta(\tilde{\phi})\right. \\ &\quad \left. + \frac{|\tilde{\phi}|}{2}\int_0^1 \frac{\mathrm{d}q_3}{2\pi}\left(\frac{s(q_3-\lambda)}{|\tilde{\phi}|+q_3} - \frac{s(q_3+\lambda)}{q_3-|\tilde{\phi}|}\right)\Theta(-\tilde{\phi})\right]\end{aligned}$$

the first integral

$$-\int_0^1 \frac{\mathrm{d}q_3}{2\pi}\left(s(q_3-\lambda)+s(q_3+\lambda)\right) = 2 - 2|\lambda|$$

the second

$$\int_0^1 \frac{\mathrm{d}q_3}{2\pi}\left(\frac{s(q_3+\lambda)}{|\tilde{\phi}|+q_3} - \frac{s(q_3-\lambda)}{q_3-|\tilde{\phi}|}\right)\Theta(\tilde{\phi}) = \left[\log\frac{1+|\tilde{\phi}|}{1-|\tilde{\phi}|} - s(\lambda)\left(2\log|\tilde{\phi}| - 2\log\left||\tilde{\phi}|-\lambda\right|\right)\right]\Theta(\tilde{\phi})$$

the third

$$\int_0^1 \frac{\mathrm{d}q_3}{2\pi}\left(\frac{s(q_3-\lambda)}{|\tilde{\phi}|+q_3}-\frac{s(q_3+\lambda)}{q_3-|\tilde{\phi}|}\right)\Theta(-\tilde{\phi})=\left[\log\frac{1+|\tilde{\phi}|}{1-|\tilde{\phi}|}+s(\lambda)\left(2\log|\tilde{\phi}|-2\log\left||\tilde{\phi}|+\lambda\right|\right)\right]\Theta(-\tilde{\phi})$$

thus

$$\begin{aligned}\Im R(\mu,\omega) &= \frac{|\tilde{\omega}|D}{2\pi}\Theta(D-|\tilde{\omega}|)\left[1-\frac{|\mu|}{D}-\frac{|\tilde{\omega}|}{D}\frac{1}{2}\log\frac{D+|\tilde{\omega}|}{D-|\tilde{\omega}|}\right.\\ &\quad\left.-s(\mu)\frac{|\tilde{\omega}|}{D}\left[\left(\log\left|\frac{|\tilde{\omega}|-\mu}{D}\right|-\log\frac{|\tilde{\omega}|}{D}\right)\Theta(\tilde{\omega})-\left(\log\left|\frac{|\tilde{\omega}|+\mu}{D}\right|-\log\frac{|\tilde{\omega}|}{D}\right)\Theta(-\tilde{\omega})\right]\right] \quad \text{(A.3.7)}\\ &= \frac{|\tilde{\omega}|D}{2\pi}\Theta(D-|\tilde{\omega}|)\left[1-\frac{|\mu|}{D}-\frac{|\tilde{\omega}|}{D}\frac{1}{2}\log\frac{D+|\tilde{\omega}|}{D-|\tilde{\omega}|}-s(\mu)\frac{\tilde{\omega}}{D}\left(\log\frac{|\omega|}{D}-\log\frac{|\tilde{\omega}|}{D}\right)\right] \quad \text{(A.3.8)}\\ &= \frac{|\tilde{\omega}|D}{2\pi}\Theta(D-|\tilde{\omega}|)\left[1-\frac{|\mu|}{D}-\frac{|\tilde{\omega}|}{D}\frac{1}{2}\log\frac{D+|\tilde{\omega}|}{D-|\tilde{\omega}|}-s(\mu)\frac{\tilde{\omega}}{D}\left(\log\frac{\sqrt{\omega^2+T^2}}{D}-\log\frac{\sqrt{\tilde{\omega}^2+T^2}}{D}\right)\right] \quad \text{(A.3.9)}\end{aligned}$$

for $D > |\tilde{\omega}|$. The three different forms Eqn. (A.3.7),Eqn. (A.3.8) and Eqn. (A.3.9) of $\Im R(\mu,\omega)$ are all identical but each eludiciate features the others don't. As will be discussed below the Eqn. (A.3.7) illustrates well the limits $\mu \to 0$ and $\tilde{\omega} \to 0$ when $\omega \neq 0$. The Eqn. (A.3.8) explictly reveal the log-singularity when probing the fermi-surface, i.e. the limit $\omega \to 0(\ \tilde{\omega} \to \mu\ )$, and the arise of a temperature (T) dependence is explcitly inserted in Eqn. (A.3.9).
Contourplots of $\Im R(\mu,\omega,T)$ as function of μ and ω for two extreme temperatures, $T = 1\,D$ and $T = 0.0005\,D$, are shown in figure A.1(a) and (b) respectively.

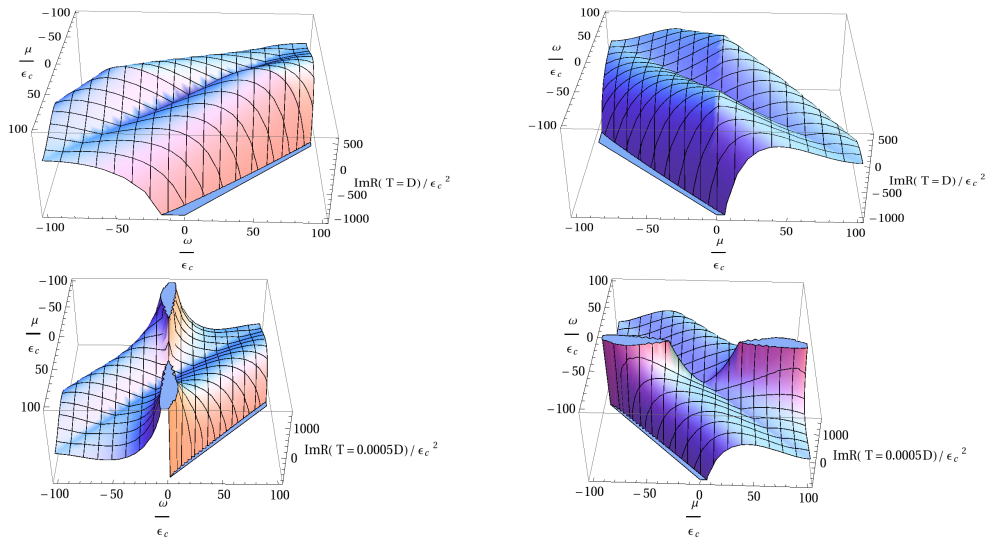

Figure A.1: Plot of $\Im R(\mu,\omega,T)/\epsilon_c^2$ as a function of μ/ϵ_c and ω/ϵ_c for a given temperature and all have $D/\epsilon_c = 100$. The upper row (a) and (b) have $T = 1D$, the lower row (c) and (d) have $T = 0.0005D$. Note that this plot is also a plot of $\frac{\Im\Sigma^{(3),R}(\mu,\omega,T)}{(-(s(s+1)/4)J^3)/\epsilon_c^{-4}}$

A.3.2 Consistency check of $\Im\rho(\mu,\omega)$

Symmetry: The general expressions Eqn. (A.3.7),Eqn. (A.3.8) and Eqn. (A.3.9) obey the symmtry of Eqn. (A.3.2), likewise those of Eqn. (A.1.3) on Eqn. (A.1.2) and Eqn. (A.2.3) on Eqn. (A.2.2).
The symmetry of $\Im R(\mu,\omega)$ and therefore $\Im\Sigma^{(3),R}(\mu,\omega)$ has the symmetry Eqn. (A.3.2) which $\Im\Sigma^{(2),R}(\mu,\omega)$ respects. This has to be so for every order $\Im\Sigma^{(n),R}(\mu,\omega)$ for $n\in\mathbf{Z}$ which is easily realized by notning that the total self-energy for arbitary number of multiple scatterings entering the total T-matrix for the corresponding scatterings. For example the first order in the total T-Matrix $\tilde{T}^{(1)+(2)+(3)+\cdots}=\tilde{\Sigma}^{(1)}+\tilde{\Sigma}^{(2)}+\tilde{\Sigma}^{(3)}+\cdots$ determines the symmetry and hence each i^{th} self-energy $\tilde{\Sigma}^{(i)}$ have to respect the symmetry of the T-matrix and the rest of orders in the self-energy. This is also the case of the real part $\Re R(\mu,\omega)$ and hence also $\Im\Sigma^{(3),R}(\mu,\omega)$.

Limit $\mu\to 0$: In the topological transport regime approaching the spin-degenerate point. For $\mu,\omega>0$ the limit reduces $\tilde{\omega}\to\omega$. Only the $\Theta(\tilde{\omega})$-part of Eqn. (A.3.7) is picked up and

$$\left(\log\left|\frac{|\tilde{\omega}|-\mu}{D}\right|-\log\frac{|\tilde{\omega}|}{D}\right)\to 0$$

thus Eqn. (A.3.7) reduces to Eqn. (A.1.3). Likewise for $\mu,\omega<0$ except it is the $\Theta(-\tilde{\omega})$-part. This is illustrated in figure A.2(a) for a frequency $\omega=\omega_0=3$; the red line $\Im R(\mu,\omega_0=3)$, Eqn. (A.3.7), intersect the blue dashed line $\Im R(\omega_0=3)$,Eqn. (A.1.3), when turning $\mu=\mu_0=0$.
The reason for the second intersection, i.e. $\mu=\mu_0=-6$, between the two, in figure A.2(a), is of a different nature. This is because when the frequency is set $\omega_0=3$ and turing $\mu=\mu_0=-6$ makes $|\tilde{\omega}_0|=|\omega_0+\mu_0|=|3-6|=3=\omega_0$ and the $\Theta(-\tilde{\omega})$-part (the other do not contribute) $\log\left|\frac{|\tilde{\omega}_0|+\mu_0}{D}\right|-\log\frac{|\tilde{\omega}_0|}{D}=0$ thus Eqn. (A.3.7) reduces to Eqn. (A.1.3) which is the intersection.

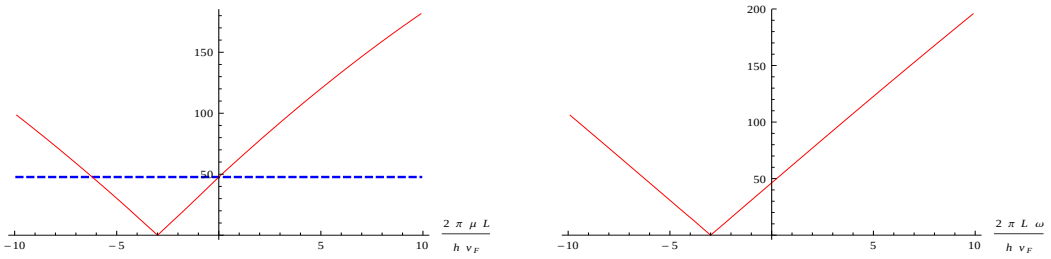

Figure A.2: Plot (a) The red line $\Im R(\mu,\omega_0=3)/\epsilon_c^2$ and blue dashed line $\Im R(\omega_0=3)/\epsilon_c^2$ as a function of μ/ϵ_c. (b) The red line $\Im R(\mu_0)/\epsilon_c^2=3,\omega)$ as a function of ω/ϵ_c.

Limit $\tilde{\omega}\to 0$: Probing the *half-filled state* corresponds to $\tilde{\omega}=0$ which can be approched from two directions for a certain-sign chemical potential. For $\mu>0$(and analog for $\mu<0$), the limit $\tilde{\omega}\to 0$ can be approched from the direction $\omega\to-\mu^+$ ($\tilde{\omega}=0^+$) and $\omega\to-\mu^-$ ($\tilde{\omega}=0^-$) both from a initial frequency $\omega<0$. The former pick up the $\Theta(\tilde{\omega})$-part and latter the $\Theta(-\tilde{\omega})$-part of Eqn. (A.3.7). The $\Theta(\pm\tilde{\omega})$-part respectively have $|\tilde{\omega}|\to|\mu-\mu^{\pm}|\approx|0|=0$ and

$$\left(\log\left|\frac{|\tilde{\omega}|\mp\mu}{D}\right|-\log\frac{|\tilde{\omega}|}{D}\right)\Theta(\pm\tilde{\omega})\to\left(\log\left|\frac{|\mu-\mu^{\pm}|\mp\mu}{D}\right|-\log\frac{|\mu-\mu^{\pm}|}{D}\right)\Theta(\pm(\mu-\mu^{\pm}))$$

This tend towards a log-singularity but a factor $|\tilde{\omega}|^2 \to |\mu - \mu^{\pm}|^2$ in Eqn. (A.3.7) kills it. Consequently

$$\Im R(\mu, \omega) \to 0, \text{ for } \tilde{\omega} \to 0 \tag{A.3.10}$$

This is illustrated in both figure A.2(a) and (b). Figure A.2(a) is for at certain $\omega = \omega_0 = 3$ and turning $\mu \to \mu_0 = -3$ thus $\tilde{\omega}_0 \to 0$ and $\Im R(\mu, \omega_0) \to 0$. The reverse is illustrated in figure A.2(b) for a certain $\mu_0 = 3$ but turning $\omega \to \omega_0 = -3$ thus $\tilde{\omega}_0 \to 0$ and $\Im R(\mu, \omega) \to 0$.

Limit $|\tilde{\omega}| \to |\mu|$: Probing the *fermi surface* corresponds to $\tilde{\omega} = \mu$ which occur when turning $\omega \to 0$. The fermi surface can be approched from two directions for a certain-sign chemical potential.
For $\mu > 0$ the limit $\tilde{\omega} \to \mu$ can be approched from the direction $\omega \to 0^+$ ($\tilde{\omega} \to \mu^+$) and $\omega \to 0^-$ ($\tilde{\omega} \to \mu^-$), the former from a initial frequency $\omega > 0$ whereas the latter from $\omega < 0$ but both directions pick up the same $\Theta(\tilde{\omega})$-part of Eqn. (A.3.7). The limits $\omega \to 0^{\pm}$ makes $\tilde{\omega} \to \mu^{\pm} \approx \mu$ thus

$$-s(\mu)\left(\log\left|\frac{|\tilde{\omega}| - \mu}{D}\right| - \log\frac{|\tilde{\omega}|}{D}\right)\Theta(\tilde{\omega}) \to -\left(\log\left|\frac{|\mu^{\pm}| - \mu}{D}\right| - \log\frac{|\mu^{\pm}|}{D}\right)\Theta(\mu^{\pm}) \approx -\left(\log\left|\frac{T}{D}\right| - \log\frac{|\mu|}{D}\right)\Theta(\mu)$$

which reduces Eqn. (A.3.7) to Eqn. (A.2.3) as required. For $\mu < 0$ a factor $+s(\mu) = -$ in front of the $\Theta(-\tilde{\omega})$-part ensures the right signs of $\log|\frac{T}{D}|$ and $\log\frac{|\mu|}{D}$.

A.3.3 $\Re\rho(\lambda, \phi)$

$$\begin{aligned}\Re\rho(\phi, \lambda) &= \sum_{\eta_1\eta_3} \frac{s(\eta_3 q_3 - \lambda)}{\eta_1 q_1 - \eta_3 q_3} \frac{1}{\tilde{\phi} - \eta_1 q_1} \\ &= \frac{1}{\tilde{\phi} - q_1}\left(\frac{s(q_3 - \lambda)}{q_1 - q_3} - \frac{s(q_3 + \lambda)}{q_1 + q_3}\right) + \frac{1}{\tilde{\phi} + q_1}\left(\frac{s(q_3 + \lambda)}{q_1 - q_3} - \frac{s(q_3 - \lambda)}{q_1 + q_3}\right)\end{aligned}$$

Using Eqn. (A.1.4) then

$$\begin{aligned}&\int \mathrm{d}q_1\, q_1\, \Re\rho(\phi, \lambda) \\ &= (s(q_3 - |\lambda|) - s(q_3 + |\lambda|)) \int \mathrm{d}q_1 \left(\frac{1}{|\tilde{\phi}| - q_1} - \frac{1}{|\tilde{\phi}| + q_1}\right) \\ &\quad + q_3\Theta(\tilde{\phi})\big[s(q_3 - \lambda)\Gamma(\tilde{\phi}, q_3) + s(q_3 + \lambda)\Omega(\tilde{\phi}, q_3)\big] - q_3\Theta(-\tilde{\phi})\big[s(q_3 - \lambda)\Omega(\tilde{\phi}, q_3) + s(q_3 + \lambda)\Gamma(\tilde{\phi}, q_3)\big] \\ &= (s(q_3 - |\lambda|) - s(q_3 + |\lambda|)) \log\left(\frac{|\tilde{\phi}|^2}{1 - |\tilde{\phi}|^2}\right) \\ &\quad + q_3\Theta(\tilde{\phi})\big[s(q_3 - \lambda)\Gamma(\tilde{\phi}, q_3) + s(q_3 + \lambda)\Omega(\tilde{\phi}, q_3)\big] - q_3\Theta(-\tilde{\phi})\big[s(q_3 - \lambda)\Omega(\tilde{\phi}, q_3) + s(q_3 + \lambda)\Gamma(\tilde{\phi}, q_3)\big]\end{aligned}$$

At last

$$
\begin{aligned}
&\Re R(\mu,\omega) \\
&= D^2 \int_0^1 \frac{\mathrm{d}q_3}{2\pi} q_3 \, \frac{\mathrm{d}q_1}{2\pi} q_1 \, \Re\rho(\mu,\omega) \\
&= -s(\mu) \left(\frac{D}{2\pi}\right)^2 \mu^2 \log\left(\frac{|\tilde{\omega}|^2}{D^2 - |\tilde{\omega}|^2}\right) \\
&\quad + \left(\frac{D}{2\pi}\right)^2 \int_0^1 \mathrm{d}q_3 \, q_3^2 \, \Big(\Theta(\tilde{\omega})\big[s(q_3-\mu)\Gamma(\tilde{\omega},q_3) + s(q_3+\mu)\Omega(\tilde{\omega},q_3)\big] - \Theta(-\tilde{\omega})\big[s(q_3-\mu)\Omega(\tilde{\omega},q_3) + s(q_3+\mu)\Gamma(\tilde{\omega},q_3)\big]
\end{aligned}
\tag{A.3.1}
$$

which is calculated numerically and exhibited in figure A.3

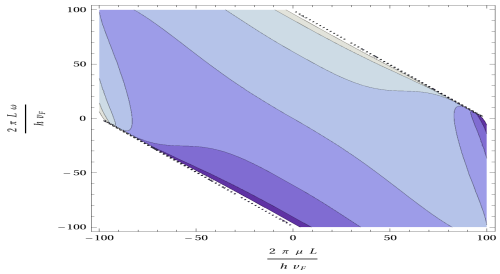

Figure A.3: Plot of $\Re R(\mu,\omega)/\epsilon_c^2$ as a function of μ/ϵ_c and ω/ϵ_c and both have $D/\epsilon_c = 100$.

A.3.4 Consistency check of $\Re\rho(\mu,\omega)$

Symmetry: The general expression Eqn. (A.3.11) obey the symmtry of Eqn. (A.3.1), likewise those of Eqn. (A.1.7) on Eqn. (A.1.1) and Eqn. (A.2.4) on Eqn. (A.2.1).

Limits $\mu \to 0$ and $\tilde{\omega} \to 0$: Figure A.4 plot the blue contour $\Re R(\mu,\omega) = \Re R(\mu)$ and red contour $\Re R(\mu,\omega) = \Re R(\omega)$, thus illustrates the two limits. This is to be understood such that for a given chemical potential $\mu = \mu_0$ then Eqn. (A.3.11), $\Re R(\mu_0,\omega)$, reduces to that of Eqn. (A.2.4), $\Re R(\mu_0)$, for $\omega \to 0$ illustrated by the blue curve. For a given frequency $\omega = \omega_0$ then Eqn. (A.3.11), $\Re R(\mu,\omega_0)$, reduces to that of Eqn. (A.1.7), $\Re R(\omega_0)$, for $\mu \to 0$ is illustrated by the red curve.

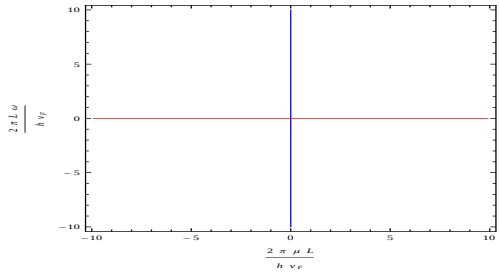

Figure A.4: Plot of $\Re R(\mu,\omega)/\epsilon_c^2 = \Re R(\mu)/\epsilon_c^2$(blue contour) and $\Re R(\mu,\omega)/\epsilon_c^2 = \Re R(\omega)/\epsilon_c^2$ (red contour).

A.3.5 Real part of the 3^{rd} order self-energy

The real part of the retarded *3. order self-energy* in the σ-basis is finally (Eqn. (4.38) with Eqn. (A.3.11))

$$\Re\Sigma^{(3),R}_{\mathbf{k},\mathbf{k}'}(\tilde{\omega}) = \frac{S(S+1)}{2} J^3 \left(\frac{L}{\hbar v_F}\right)^4 \frac{D^2}{4\pi^2} \left[-s(\mu)\mu^2 \log\left(\frac{|\tilde{\omega}|^2}{D^2-|\tilde{\omega}|^2}\right) + \Xi(\mu,\omega)\right] \tau^0 \tag{A.3.12}$$

where

$$\begin{aligned}\Xi(\mu,\omega) = \int_0^1 \mathrm{d}q_3\, q_3^2 \Big(&\Theta(\tilde{\omega})\big[s(q_3-\mu)\Gamma(\tilde{\omega},q_3) + s(q_3+\mu)\Omega(\tilde{\omega},q_3)\big] \\ &-\Theta(-\tilde{\omega})\big[s(q_3-\mu)\Omega(\tilde{\omega},q_3) + s(q_3+\mu)\Gamma(\tilde{\omega},q_3)\big]\Big)\end{aligned} \tag{A.3.13}$$

The real part of the retarded 2. order self-energy in the σ-basis is

$$\Re\Sigma^{(2),R}_{\mathbf{k},\mathbf{k}'}(\mu,\omega) = -\frac{S(S+1)}{4\pi} J^2 \left(\frac{L}{\hbar v_F}\right)^2 \tilde{\omega} \log\left(\frac{D^2}{\tilde{\omega}^2} - 1\right) \Theta(D-|\tilde{\omega}|)\, \tau^0 \tag{A.3.14}$$

The real part of the *total irreducible self-energy upto 3. order* is

$$\begin{aligned}\Re\Sigma^{(1,2,3),R}_{\mathbf{k},\mathbf{k}'}(\mu,\omega) = &-\frac{S(S+1)}{4\pi} J^2 \left(\frac{L}{\hbar v_F}\right)^2 \left[\tilde{\omega}\log\left(\frac{D^2}{|\tilde{\omega}|^2}-1\right)\right. \\ &\left.\frac{D^2}{2\pi} J \left(\frac{L}{\hbar v_F}\right)^2 \left(s(\mu)\mu^2 \log\left(\frac{D^2}{|\tilde{\omega}|^2}-1\right) - \Xi(\mu,\omega)\right)\right] \tau^0\end{aligned} \tag{A.3.15}$$

Appendix B

Spin-unresolved FT-LDOS

Per definition

$$
\begin{aligned}
\delta\rho(\mathbf{q},i\tilde{\omega}_n) &\equiv \int \mathrm{d}\mathbf{r}\exp\left(i\,\mathbf{q}\cdot\mathbf{r}\right) Tr\left[\delta\rho(\mathbf{r},\mathbf{r};i\tilde{\omega}_n)\right] \\
&= \int \mathrm{d}\mathbf{r}\, e^{i\,\mathbf{q}\cdot\mathbf{r}}\, Tr\left[\Im\left[\left(\frac{L}{\hbar v_F}\right)^2\int\frac{\mathrm{d}^2\mathbf{k}}{(2\pi)^2}\left(\frac{L}{\hbar v_F}\right)^2\int\frac{\mathrm{d}^2\mathbf{k}^{'}}{(2\pi)^2}\, e^{i\,\mathbf{k}\cdot\mathbf{r}}e^{-i\,\mathbf{k}^{'}\cdot\mathbf{r}}\delta\, G(\mathbf{k},\mathbf{k}^{'};i\tilde{\omega}_n)\right]\right] \\
&= \int \mathrm{d}\mathbf{r}\, e^{i\,\mathbf{q}\cdot\mathbf{r}}\left(\frac{L}{\hbar v_F}\right)^2\int\frac{\mathrm{d}^2\mathbf{k}}{(2\pi)^2}\left(\frac{L}{\hbar v_F}\right)^2\int\frac{\mathrm{d}^2\mathbf{k}^{'}}{(2\pi)^2}\, Tr\left[\Im\left[e^{i\,\mathbf{k}\cdot\mathbf{r}}e^{-i\,\mathbf{k}^{'}\cdot\mathbf{r}}\,\delta\, G(\mathbf{k},\mathbf{k}^{'};i\tilde{\omega}_n)\right]\right] \\
&= \int \mathrm{d}\mathbf{r}\, e^{i\,\mathbf{q}\cdot\mathbf{r}}\left(\frac{L}{\hbar v_F}\right)^2\int\frac{\mathrm{d}^2\mathbf{k}}{(2\pi)^2}\left(\frac{L}{\hbar v_F}\right)^2\int\frac{\mathrm{d}^2\mathbf{k}^{'}}{(2\pi)^2}\,\frac{1}{2\,i}Tr\left[e^{i\,\mathbf{k}\cdot\mathbf{r}}e^{-i\,\mathbf{k}^{'}\cdot\mathbf{r}}\,\delta\, G(\mathbf{k},\mathbf{k}^{'};i\tilde{\omega}_n)\right. \\
&\left.-e^{-i\,\mathbf{k}\cdot\mathbf{r}}e^{i\,\mathbf{k}^{'}\cdot\mathbf{r}}\left(\delta\, G(\mathbf{k},\mathbf{k}^{'};i\tilde{\omega}_n)\right)^*\right] \\
&= \frac{1}{2\,i}\left(\frac{L}{\hbar v_F}\right)^2\int\frac{\mathrm{d}^2\mathbf{k}}{(2\pi)^2}\int\mathrm{d}^2\mathbf{k}^{'}\, Tr\left[\delta(\mathbf{q}+\mathbf{k}-\mathbf{k}^{'})\delta\, G(\mathbf{k},\mathbf{k}^{'};i\tilde{\omega}_n)-\delta(\mathbf{q}-\mathbf{k}+\mathbf{k}^{'})\left(\delta\, G(\mathbf{k},\mathbf{k}^{'};i\tilde{\omega}_n)\right)^*\right] \\
&= \frac{1}{2\,i}\left(\frac{L}{\hbar v_F}\right)^2\int\frac{\mathrm{d}^2\mathbf{k}}{(2\pi)^2}Tr\left[\delta\, G(\mathbf{k},\mathbf{k}+\mathbf{q};i\tilde{\omega}_n)-(\delta\, G(\mathbf{k},\mathbf{k}-\mathbf{q};i\tilde{\omega}_n))^*\right] \qquad \text{(B.0.1)}
\end{aligned}
$$

so $\delta\rho(\mathbf{q},i\tilde{\omega}_n)$ is in units of energy^{-1}.

The definition of the Fourier transform was $f(\mathbf{r})=\frac{1}{L^2}\sum_{\mathbf{k}} f_{\mathbf{k}}\, e^{-i\mathbf{k}\cdot\mathbf{r}} \to \left(\frac{1}{\hbar v_F}\right)^2\int\frac{\mathrm{d}^2\mathbf{k}}{(2\pi)^2}f(\mathbf{k})e^{-i\mathbf{k}\cdot\mathbf{r}}$ in units of L^{-2}energy^{-1} and $f(\mathbf{k})=\int\mathrm{d}\mathbf{r}\, f(\mathbf{r})\, e^{-i\mathbf{k}\cdot\mathbf{r}}$ in units of energy^{-1} with $\int\mathrm{d}\mathbf{r}\, e^{-i\mathbf{k}\cdot\mathbf{r}}=(2\pi)^2\left(\hbar v_F\right)^2\delta(\mathbf{k})$.

B.1 For the scalar potential and quantum magnetic impurity

Both can be expressed as $\tilde{T}(\mathbf{k},\mathbf{k}\pm\mathbf{q};i\tilde{\omega}_n)=t(i\tilde{\omega}_n)\,U^{\dagger}_{\phi_{\mathbf{k}}}U_{\phi_{\mathbf{k}\pm\mathbf{q}}}$ so

$$
\begin{aligned}
\delta\, G(\mathbf{k},\mathbf{k}\pm\mathbf{q};i\tilde{\omega}_n) &= t(i\tilde{\omega}_n)U_{\phi_{\mathbf{k}}}\tilde{G}^0(k;i\tilde{\omega}_n)U^{\dagger}_{\phi_{\mathbf{k}}}U_{\phi_{\mathbf{k}\pm\mathbf{q}}}\tilde{G}^0(k\pm\mathbf{q};i\tilde{\omega}_n)\,U^{\dagger}_{\phi_{\mathbf{k}\pm\mathbf{q}}} \\
&= t(i\tilde{\omega}_n)G^0(k;i\tilde{\omega}_n)G^0(k\pm q;i\tilde{\omega}_n)d \qquad \text{(B.1.1)}
\end{aligned}
$$

which is inserted in

$$\begin{aligned}\Lambda(\mathbf{q};i\tilde{\omega}_n) &\equiv \int \frac{\mathrm{d}^2\mathbf{k}}{(2\pi)^2} Tr\left[\delta\, G(k,k+q;i\tilde{\omega}_n)\right] \\ &= t(i\tilde{\omega}_n)\int \frac{\mathrm{d}^2\mathbf{k}}{(2\pi)^2} Tr\left[G^0(k;i\tilde{\omega}_n)G^0(k+q;i\tilde{\omega}_n)\right] \end{aligned} \tag{B.1.2}$$

which is the first term in Eqn. (B.0.1) and the second term

$$\begin{aligned}&\int \frac{\mathrm{d}^2\mathbf{k}}{(2\pi)^2} Tr\left[\left(\delta\, G(k,k-q;i\tilde{\omega}_n)\right)^*\right] \\ &= \int \frac{\mathrm{d}^2\mathbf{k}}{(2\pi)^2} Tr\left[\left(t(i\tilde{\omega}_n)\, G^0(k;i\tilde{\omega}_n)G^0(k-q;i\tilde{\omega}_n)\right)^*\right] \\ &= \int \frac{\mathrm{d}^2\mathbf{k}}{(2\pi)^2} Tr\left[\left(t(i\tilde{\omega}_n)\right)^*\, \left(G^0(k;i\tilde{\omega}_n)G^0(k-q;i\tilde{\omega}_n)\right)^*\right] \\ &= \left(t(i\tilde{\omega}_n)\right)^* \int \frac{\mathrm{d}^2\mathbf{k}}{(2\pi)^2} Tr\left[\left(G^0(k;i\tilde{\omega}_n)G^0(k-q;i\tilde{\omega}_n)\right)^*\right] \\ &= \left(t(i\tilde{\omega}_n)\right)^* \left(\int \frac{\mathrm{d}^2\mathbf{k}}{(2\pi)^2} Tr\left[G^0(k;i\tilde{\omega}_n)G^0(k-q;i\tilde{\omega}_n)\right]\right)^* \\ &\overset{*}{=} \left(t(i\tilde{\omega}_n)\right)^* \left(\int \frac{\mathrm{d}^2\mathbf{k}}{(2\pi)^2} Tr\left[G^0(k;i\tilde{\omega}_n)G^0(k+q;i\tilde{\omega}_n)\right]\right)^* \\ &= \left(\int \frac{\mathrm{d}^2\mathbf{k}}{(2\pi)^2} Tr\left[t(i\tilde{\omega}_n)\, G^0(k;i\tilde{\omega}_n)G^0(k+q;i\tilde{\omega}_n)\right]\right)^* \\ &= \left(\Lambda(\mathbf{q};i\tilde{\omega}_n)\right)^* \end{aligned} \tag{B.1.3}$$

where in (*) it was used that $Tr\left[G^0(k;i\tilde{\omega}_n)G^0(k+q;i\tilde{\omega}_n)\right] = Tr\left[G^0(k;i\tilde{\omega}_n)G^0(k-q;i\tilde{\omega}_n)\right]$ as will be evident further below but can be understood by shiting $\mathbf{k}\to-\mathbf{k}$.
To conclude the spin-unresolved FT-LDOS, Eqn. (B.0.1), for a scalar potential and a quantum impurity becomes

$$\begin{aligned}\delta\rho(\mathbf{q},i\tilde{\omega}_n) &= \frac{1}{2\,i}\left(\Lambda(\mathbf{q};i\tilde{\omega}_n) - \left(\Lambda(\mathbf{q};i\tilde{\omega}_n)\right)^*\right)\left(\frac{L}{\hbar v_F}\right)^2 = Im\left[\Lambda(\mathbf{q};i\tilde{\omega}_n)\right]\left(\frac{L}{\hbar v_F}\right)^2 \\ &= Im\left[t(i\tilde{\omega}_n)\int \frac{\mathrm{d}^2\mathbf{k}}{(2\pi)^2} Tr\left[G^0(k;i\tilde{\omega}_n)G^0(k+q;i\tilde{\omega}_n)\right]\right]\left(\frac{L}{\hbar v_F}\right)^2 \\ &= Im\left[t(i\tilde{\omega}_n)\Omega(\mathbf{q};i\tilde{\omega}_n)\right]\left(\frac{L}{\hbar v_F}\right)^2 \end{aligned} \tag{B.1.4}$$

with (See next subsection
'Derivation $\int \mathrm{d}^2\mathbf{k}\, Tr[G_0(\mathbf{k};i\tilde{\omega}_n)G_0(\mathbf{k}-\mathbf{q};i\tilde{\omega}_n)]$')

$$\Omega(\mathbf{q};i\tilde{\omega}_n) = \int \frac{\mathrm{d}^2\mathbf{k}}{(2\pi)^2}\, Tr[G_0(k;i\tilde{\omega}_n)G_0(k+q;i\tilde{\omega}_n)] = \frac{1}{2\pi}\left(-F(z) + \ln\left(\frac{\mathrm{D}^2}{\tilde{\omega}_n^2}+1\right)\right) \tag{B.1.5}$$

and the t-factor for a scalar potential

$$t_{sc}(\tilde{\omega}, v_0) = \frac{v_0}{1+v_0 g^R(\tilde{\omega})} \tag{B.1.6}$$

and for the quantum impurity:

$$t_{qm}(\tilde{\omega}, J) = \frac{-\frac{3}{4}J^2 g(\tilde{\omega})}{1 - \frac{3}{4}J^2 g(\tilde{\omega})^2} \tag{B.1.7}$$

B.2 For the classical magnetic impurity

The T-matrix

$$\tilde{T}_{\mathbf{k},\mathbf{k}\pm\mathbf{q}} = U^{\dagger}_{\phi_{\mathbf{k}}} \left(\frac{\bar{S}\cdot\bar{\tau} - g(i\tilde{\omega}_n)|S|^2}{1 - g(i\tilde{\omega}_n)^2|S|^2} \right) U_{\phi_{\mathbf{k}\pm\mathbf{q}}}$$

$$\begin{aligned}
\delta G(\mathbf{k}, \mathbf{k}\pm\mathbf{q}; i\tilde{\omega}_n) &= U_{\phi_{\mathbf{k}}} \tilde{G}^0(k; i\tilde{\omega}_n) U^{\dagger}_{\phi_{\mathbf{k}}} \left(\frac{\bar{S}\cdot\bar{\tau} - g(i\tilde{\omega}_n)|S|^2}{1 - g(i\tilde{\omega}_n)^2|S|^2} \right) U_{\phi_{\mathbf{k}\pm\mathbf{q}}} \tilde{G}^0(k\pm q; i\tilde{\omega}_n)\, U^{\dagger}_{\phi_{\mathbf{k}\pm\mathbf{q}}} \\
&= t_1^i(i\tilde{\omega}_n) G^0(k; i\tilde{\omega}_n)\, \tau^i\, G^0(k\pm q; i\tilde{\omega}_n) + t_2(i\tilde{\omega}_n) G^0(k; i\tilde{\omega}_n) G^0(k\pm q; i\tilde{\omega}_n)
\end{aligned} \tag{B.2.1}$$

where the Einstein sumconvention is implicit and of cause in accord with the no. of compotents in the magnetic Hamilton $V_{cl} = S^i\tau^i$. The t-functions $t_1^i(i\tilde{\omega}_n) = \frac{S^i}{1-g(i\tilde{\omega}_n)^2|S|^2}$ and $t_2(i\tilde{\omega}_n) = \frac{-|S|^2 g(i\tilde{\omega}_n)}{1-g(i\tilde{\omega}_n)^2|S|^2}$. It will be evident below (See next subsection 'Derivation $\int \mathrm{d}^2\mathbf{k}\, Tr[G_0(k; i\tilde{\omega}_n)\, \tau^i\, G_0(k-q; i\tilde{\omega}_n)]$')

$$\begin{aligned}
0 &= \int \frac{\mathrm{d}^2\mathbf{k}}{(2\pi)^2} Tr\left[t_1^i(i\tilde{\omega}_n)\, G^0(k; i\tilde{\omega}_n)\, \tau^i\, G^0(k+q; i\tilde{\omega}_n) \right] \\
&= \int \frac{\mathrm{d}^2\mathbf{k}}{(2\pi)^2} Tr\left[t_1^i(i\tilde{\omega}_n)\, G^0(k; i\tilde{\omega}_n)\, \tau^i\, G^0(k-q; i\tilde{\omega}_n) \right]
\end{aligned} \tag{B.2.2}$$

So what's left is this

$$\begin{aligned}
\Lambda_2(\mathbf{q}; i\tilde{\omega}_n) &= \int \frac{\mathrm{d}^2\mathbf{k}}{(2\pi)^2} Tr\left[\delta G(\mathbf{k}, \mathbf{k}+\mathbf{q}; i\tilde{\omega}_n) \right] \\
&= t_2(i\tilde{\omega}_n) \int \frac{\mathrm{d}^2\mathbf{k}}{(2\pi)^2} Tr\left[G^0(k; i\tilde{\omega}_n) G^0(k+q; i\tilde{\omega}_n) \right] \\
&= t_2(i\tilde{\omega}_n) \Omega(\mathbf{q}; i\tilde{\omega}_n)
\end{aligned} \tag{B.2.3}$$

and finally redefine $t_2(i\tilde{\omega}_n) \equiv t_{cl}(i\tilde{\omega}_n)$. To conclude the spin-unresolved FT-LDOS, Eqn. (B.0.1), for a classical magnetic impurity

$$\begin{aligned}
\delta\rho(\mathbf{q}, i\tilde{\omega}_n) &= \frac{1}{2\,i} \left(\Lambda_2(\mathbf{q}; i\tilde{\omega}_n) - (\Lambda_2(\mathbf{q}; i\tilde{\omega}_n))^* \right) = Im\left[\Lambda_2(\mathbf{q}; i\tilde{\omega}_n) \right] \\
&= \Im\left[t_{cl}(i\tilde{\omega}_n) \int \frac{\mathrm{d}^2\mathbf{k}}{(2\pi)^2} Tr\left[G^0(k; i\tilde{\omega}_n) G^0(k+q; i\tilde{\omega}_n) \right] \right] \\
&= \Im\left[t_{cl}(i\tilde{\omega}_n) \Omega(\mathbf{q}; i\tilde{\omega}_n) \right]
\end{aligned} \tag{B.2.4}$$

where the Ω-structure is the same as for the scalar and qm-impurity, but the t-function for the magnetic impurity

$$\begin{aligned}
t_{cl}(\tilde{\omega}, S) &= \left(\frac{-g^R(\tilde{\omega}_n) S^2}{1 - g(\tilde{\omega}_n)^2 S^2} \right) \\
&= t_{qm}(\tilde{\omega}, J)
\end{aligned} \tag{B.2.5}$$

when the strength is scaled $S^2 = \frac{3}{4}J^2$.

B.2.1 Derivation $\int \mathrm{d}^2\mathbf{k}\, Tr[G_0(\mathbf{k}; i\tilde{\omega}_n)G_0(\mathbf{k}-\mathbf{q}; i\tilde{\omega}_n)]$

$$\begin{aligned} G_0(\mathbf{k}; i\tilde{\omega}_n) &= [i\tilde{\omega}_n\tau^0 - H_0]^{-1} = [i\tilde{\omega}_n\tau^0 - (k_x\tau^y - k_y\tau^x)]^{-1} \\ &= \frac{i\tilde{\omega}_n\tau^0 + k_x\tau^y - k_y\tau^x}{(i\tilde{\omega}_n)^2 - k^2} = -1\,\frac{i\tilde{\omega}_n\tau^0 + k_x\tau^y - k_y\tau^x}{\tilde{\omega}_n^2 + k^2} \end{aligned} \tag{B.2.6}$$

with $k^2 = k_x^2 + k_y^2$. Likewise

$$\begin{aligned} G_0(k-q; i\tilde{\omega}_n) &= [i\tilde{\omega}_n\tau^0 - H_0]^{-1} = [i\tilde{\omega}_n\tau^0 - ((k_x-q_x)\tau^y - (k_y-q_y)\tau^x)]^{-1} \\ &= \frac{i\tilde{\omega}_n\tau^0 + (k_x-q_x)\tau^y - (k_y-q_y)\tau^x}{(i\tilde{\omega}_n)^2 - k^2} \\ &= -1\,\frac{i\tilde{\omega}_n\tau^0 + (k_x-q_x)\tau^y - (k_y-q_y)\tau^x}{\tilde{\omega}_n^2 + (k-q)^2} \end{aligned} \tag{B.2.7}$$

with $(k-q)^2 = (k_x-q_x)^2 + (k_y-q_y)^2$. The quantity

$$\begin{aligned} \int \mathrm{d}^2\mathbf{k}\, Tr[G_0(\mathbf{k}; i\tilde{\omega}_n)G_0(\mathbf{k}-\mathbf{q}; i\tilde{\omega}_n)] &= 2\int \mathrm{d}^2\mathbf{k}\, \frac{-\tilde{\omega}_n^2 + k_x(k_x-q_x) + k_y(k_y-q_y)}{(\tilde{\omega}_n^2 + k^2)(\tilde{\omega}_n^2 + (k-q)^2)} \\ &= 2\Gamma_{11}\int_0^1 \mathrm{d}x \int \mathrm{d}^2\mathbf{k}\, \frac{k^2}{(k^2+\Delta^2)^2} \\ &\quad - 2\Gamma_{11}\int_0^1 \mathrm{d}x\, \Delta^2 \int \mathrm{d}^2\mathbf{k}\, \frac{1}{(k^2+\Delta^2)^2} \\ &= 2\cdot 1\cdot (I_1 - I_2) \end{aligned} \tag{B.2.8}$$

with $\Delta^2 = \tilde{\omega}_n^2 + x(1-x)q^2$ and x being the Feynman-Schwinger parameter. The last equallity came about invoking the Feynman-Schwinger parametrization $\frac{1}{A^\alpha B^\beta} = \Gamma_{\alpha\beta}\int_0^1 \mathrm{d}x\, \frac{x^{\alpha-1}(1-x)^{\beta-1}}{(xA+(1-x)B)^{\alpha+\beta}}$, $\Gamma_{\alpha\beta} = \frac{\Gamma(\alpha+\beta)}{\Gamma(\alpha)\Gamma(\beta)}$ and shifting momentum $\mathbf{k} \to \mathbf{k} + (1-x)\mathbf{q}$ and retaning only equal powers of $\mathbf{k}_i$ since odd powers will vanish when integrating. The factor arose as $2 = Tr[\tau^2]$ and $\Gamma_{\alpha\beta}$ with $\Gamma(n)$ being the usual Gamma-function taking integer argument n evaluates to $\Gamma_{11} = \frac{\Gamma(2)}{\Gamma(1)\Gamma(1)} = 1$.

Since the integrals I_1 and I_2 only depend on the magnitude of the momentum they're easily calculated by shifting to 2-dim polar coordinates: $\int \mathrm{d}^2\mathbf{k} = \int \mathrm{d}\phi_{\mathbf{k}} \int_0^{\mathrm{D}} \mathrm{d}k = 2\pi \int_0^{\mathrm{D}} \mathrm{d}k\, k$

$$\begin{aligned} I_1 &= \int_0^1 \mathrm{d}x \int \mathrm{d}^2\mathbf{k}\, \frac{k^2}{(k^2+\Delta^2)^2} = \pi \int_0^1 \mathrm{d}x \left(\ln\left(\frac{\mathrm{D}^2+\Delta^2}{\Delta^2}\right) - \frac{\mathrm{D}^2}{\mathrm{D}^2+\Delta^2}\right) \\ &= \pi \Bigg(-2\sqrt{-1-z^2}\tan^{-1}\left(\frac{1}{\sqrt{-1-z^2}}\right) + \underbrace{2\sqrt{-1-z^2-z_*^2}\tan^{-1}\left(\frac{1}{\sqrt{-1-z^2-z_*^2}}\right)}_{=2} \\ &\quad + \ln\left(\frac{\mathrm{D}^2}{\tilde{\omega}_n^2}+1\right)\Bigg) - \pi \\ &= \pi\left(-2\sqrt{-1-z^2}\tan^{-1}\left(\frac{1}{\sqrt{-1-z^2}}\right) + 1 + \ln\left(\frac{\mathrm{D}^2}{\tilde{\omega}_n^2}+1\right)\right) \\ &= \pi\left(-F(z) + 1 + \ln\left(\frac{\mathrm{D}^2}{\tilde{\omega}_n^2}+1\right)\right) \end{aligned} \tag{B.2.9}$$

with definitions $z = \frac{2\tilde{\omega}_n}{q}$, $F(z) = (-1-z^2)g(z)$ and $g(z) = \frac{2}{\sqrt{-1-z^2}}\tan^{-1}(\frac{1}{\sqrt{-1-z^2}})$. The integral was simplified by following approximation $\sqrt{-1-z^2-z_*^2} = |z_*|\sqrt{-\frac{1}{z_*^2}-\frac{z^2}{z_*^2}-1} \approx i\,|z_*|$ when the ultraviolet band cut-off D $>>$ q and D $>>$ $\tilde{\omega}_n$ hence $z_* = \frac{\mathrm{D}}{q} >> 1$ and $z_* >> z$. Therefore

$$\begin{aligned} &2\sqrt{-1-z^2-z_*^2}\tan^{-1}(\frac{1}{\sqrt{-1-z^2-z_*^2}}) \approx 2\,i\,|z_*|\tan^{-1}(\frac{1}{i\,|z_*|}) \\ &= 2\,|z_*|\tanh^{-1}(\frac{1}{|z_*|}) \approx 2\,|z_*|\left(\frac{1}{|z_*|}+O(|z_*|^{-3})+\cdots\right) \approx 2 \end{aligned} \tag{B.2.10}$$

in the limit of small probing frequencies $\tilde{\omega}_n$ compared to the ultraviolet cut-off D as given above. A similar approximation has been done in $\int_0^1 \mathrm{d}x - \frac{\mathrm{D}^2}{\mathrm{D}^2+\Delta^2} = -\pi$. Letting the cut-off approch infinity the integral

$$I_2 = 2\pi\int_0^1 \mathrm{d}x\,\Delta^2\int_0^\infty \mathrm{d}k\,\frac{k^2}{(k^2+\Delta^2)^2} = 2\pi\int_0^1 \mathrm{d}x\,\Delta^2\frac{1}{2\Delta^2} = \pi \tag{B.2.11}$$

To conclude

$$\int \mathrm{d}^2\mathbf{k}\,Tr[G_0(\mathbf{k};i\tilde{\omega}_n)G_0(\mathbf{k}-\mathbf{q};i\tilde{\omega}_n)] = 2\pi\left(-F(z)+\ln(\frac{\mathrm{D}^2}{\tilde{\omega}_n^2}+1)\right) = 2\pi\Lambda_{00}(\mathbf{q},i\tilde{\omega}) \tag{B.2.12}$$

the last equality expressed the same quantity in notation of ref [22].

In the derivation of the spin-unresloved FT-LDOS it was used that $\int \mathrm{d}^2\mathbf{k}\,Tr[G_0(\mathbf{k};i\tilde{\omega}_n)G_0(\mathbf{k}-\mathbf{q};i\tilde{\omega}_n)] = \Omega(\mathbf{q};i\tilde{\omega}_n)$. That this is so can easily be seen by shifting $\mathbf{k}\to-\mathbf{k}$

$$\begin{aligned} &\int \mathrm{d}^2\mathbf{k}\,Tr[G_0(\mathbf{k};i\tilde{\omega}_n)G_0(\mathbf{k}-\mathbf{q};i\tilde{\omega}_n)] \\ &\to \int \mathrm{d}^2\mathbf{k}\,Tr[G_0(-\mathbf{k};i\tilde{\omega}_n)G_0(-(\mathbf{k}+\mathbf{q});i\tilde{\omega}_n)] \\ &= 2\int \mathrm{d}^2\mathbf{k}\,\frac{-\tilde{\omega}_n^2+(k_x)(-(k_x+q_x))+(-k_y)(-(k_y+q_y))}{(\tilde{\omega}_n^2+(-k)^2)(\tilde{\omega}_n^2+(-(k+q))^2)} \\ &= 2\int \mathrm{d}^2\mathbf{k}\,\frac{-\tilde{\omega}_n^2+k_x(k_x+q_x))+k_y(k_y+q_y)}{(\tilde{\omega}_n^2+k^2)(\tilde{\omega}_n^2+(k+q)^2)} \\ &= \int \mathrm{d}^2\mathbf{k}\,Tr[G_0(\mathbf{k};i\tilde{\omega}_n)G_0(\mathbf{k}+\mathbf{q};i\tilde{\omega}_n)] = \Omega(\mathbf{q};i\tilde{\omega}_n) \end{aligned}$$

B.2.2 Derivation $\int \mathrm{d}^2\mathbf{k}\, Tr[G_0(\mathbf{k}; i\tilde{\omega}_n)\, \tau^i\, G_0(\mathbf{k}-\mathbf{q}; i\tilde{\omega}_n)]$

The quantity

$$
\begin{aligned}
&\int \frac{\mathrm{d}^2\mathbf{k}}{(2\pi)^2}\, Tr[G_0(k; i\tilde{\omega}_n)\, \tau^i\, G_0(k-q; i\tilde{\omega}_n)] \\
=&2\int \frac{\mathrm{d}^2\mathbf{k}}{(2\pi)^2}\, \frac{i\tilde{\omega}_n\left((2k_x-q_x)\,\delta_{i\,y}-(2k_y-q_y)\,\delta_{i\,x}\right)+i\left(k_y(k_x-q_x)-k_x(k_y-q_y)\right)\delta_{i\,z}}{(\tilde{\omega}_n^2+k^2)(\tilde{\omega}_n^2+(k-q)^2)} \\
=&2\Gamma_{11}\int_0^1 \mathrm{d}x\, \frac{\mathrm{d}^2\mathbf{k}}{(2\pi)^2}\, i\tilde{\omega}_n \frac{(1-2x)q_x\delta_{i\,y}-(1-2x)q_y\delta_{i\,x}}{(k^2+\Delta^2)^2} \\
=&2\Gamma_{11}\, i\tilde{\omega}_n\left(q_x\delta_{i\,y}-q_y\delta_{i\,x}\right)\int_0^1 \mathrm{d}x\,(1-2x)\int \frac{\mathrm{d}^2\mathbf{k}}{(2\pi)^2}\,\frac{1}{(k^2+\Delta^2)^2} \\
=&2\Gamma_{11}\, i\tilde{\omega}_n\left(q_x\delta_{i\,y}-\mathbf{q}_y\delta_{i\,x}\right)\int_0^1 \mathrm{d}x\,(1-2x)\left(\frac{2\pi}{(2\pi)^2}\frac{1}{2}\frac{1}{\Delta^2}\right) \\
=&2\Gamma_{11}\,\frac{2\pi}{(2\pi)^2}\frac{1}{2}\, i\tilde{\omega}_n\left(q_x\delta_{i\,y}-q_y\delta_{i\,x}\right)\underbrace{\int_0^1 \mathrm{d}x\,\frac{(1-2x)}{\tilde{\omega}_n+x(1-x)q^2}}_{=0}=0
\end{aligned}
\tag{B.2.13}
$$

with $\Delta^2=\tilde{\omega}_n^2+x(1-x)q^2$, x the Feynman-Schwinger parameter.

The last equallity came about invoking the Feynman-Schwinger parametrization $\frac{1}{A^\alpha B^\beta}=\Gamma_{\alpha\beta}\int_0^1 \mathrm{d}x\,\frac{x^{\alpha-1}(1-x)^{\beta-1}}{(xA+(1-x)B)^{\alpha+\beta}}$, $\Gamma_{\alpha\beta}=\frac{\Gamma(\alpha+\beta)}{\Gamma(\alpha)\Gamma(\beta)}$ and shifting momentum $\mathbf{k}\to\mathbf{k}+(1-x)\mathbf{q}$ and retaning only equal powers of $\mathbf{k}_i$. $\Gamma_{\alpha\beta}$ was evaluated to $\Gamma_{11}=\frac{\Gamma(2)}{\Gamma(1)\Gamma(1)}=1$ with $\Gamma(n)$ being the usual Gamma-function taking integer argument n and the factor arose as $2=Tr[\tau^0]$.

In the derivation of the spin-unresloved FT-LDOS it was used that

$$
\int \frac{\mathrm{d}^2\mathbf{k}}{(2\pi)^2}\, Tr[G_0(k; i\tilde{\omega}_n)\, \tau^i\, G_0(k+q; i\tilde{\omega}_n)] = \int \frac{\mathrm{d}^2\mathbf{k}}{(2\pi)^2}\, Tr[G_0(k; i\tilde{\omega}_n)\, \tau^i\, G_0(k-q; i\tilde{\omega}_n)] = 0
$$

. That this is so can easily be seen by shifting $\mathbf{k}\to-\mathbf{k}$

$$
\begin{aligned}
&\int \frac{\mathrm{d}^2\mathbf{k}}{(2\pi)^2}\, Tr[G_0(k; i\tilde{\omega}_n)\, \tau^i\, G_0(k+q; i\tilde{\omega}_n)] \\
=&2\int \frac{\mathrm{d}^2\mathbf{k}}{(2\pi)^2}\, \frac{(-i\tilde{\omega}_n)\left((2k_x+q_x)\,\delta_{i\,y}-(2k_y+q_y)\,\delta_{i\,x}\right)+i\left(k_y(k_x+q_x)-k_x(k_y+q_y)\right)\delta_{i\,z}}{(\tilde{\omega}_n^2+k^2)(\tilde{\omega}_n^2+(k+q)^2)} \\
=&2\Gamma_{11}\int_0^1 \mathrm{d}x\, \frac{\mathrm{d}^2\mathbf{k}}{(2\pi)^2}\, i\tilde{\omega}_n \frac{(1-2x)q_x\delta_{i\,y}-(1-2x)q_y\delta_{i\,x}}{(k^2+\Delta^2)^2} \\
=&\int \frac{\mathrm{d}^2\mathbf{k}}{(2\pi)^2}\, Tr[G_0(k; i\tilde{\omega}_n)\, \tau^i\, G_0(k-q; i\tilde{\omega}_n)] = 0
\end{aligned}
\tag{B.2.14}
$$

So after involking the Feynman-Schwinger parametrization technique and the shift in momentum $\mathbf{k}\to\mathbf{k}-(1-x)\mathbf{q}$ the two integrals are shown to be identical and zero.

B.3 FT-LDOS on the conventional metal

In principle all that is needed is the *spin-unresolved FT-LDOS* defined as the retarded quantity

$$\delta\rho(q,\omega) = \delta\rho(q, i\omega_n \to \omega + i\,0^+) \tag{B.3.1}$$

where by defintion

$$\begin{aligned}\delta\rho(q,i\omega_n) &\equiv \int \mathrm{d}\mathbf{r}\exp\left(i\,\mathbf{q}\cdot\mathbf{r}\right) Tr\left[\delta\rho(\mathbf{r},\mathbf{r};i\omega_n)\right] \\ &= \frac{1}{2\,i}\int\frac{\mathrm{d}^2\mathbf{k}}{(2\pi)^2} Tr\left[\delta\,G(\mathbf{k},\mathbf{k}+\mathbf{q};i\omega_n) - (\delta\,G(\mathbf{k},\mathbf{k}-\mathbf{q};i\omega_n))^*\right]\end{aligned} \tag{B.3.2}$$

and $*$ denotes complex conjugation.

The conventional metal dispersion relation reads $\epsilon(k) = \frac{k^2}{2\,m}$ and $\xi(k) = \epsilon(k) - \mu$ and each $\mathbf{k}$-state is double spin degenerate. If the states up to the chemical potential μ is filled and this level defined to be zero energy then $0 = \xi(k_F) = \frac{k_F^2}{2\,m} - \mu \leftrightarrow \mu = \frac{k_F^2}{2\,m}$. The momentum of a test fermion with probe energy/frequency ω is $\omega = \xi(k_\omega) = \frac{k_\omega^2}{2\,m} - \mu \leftrightarrow k_\omega = k_F\sqrt{\frac{\omega}{\mu}+1}$, with $k_F = \sqrt{2\,m\mu}$. When probing the Fermi surface i.e. $\omega = 0$ then $k_\omega = k_F$. The free conventional 2 dimensional electron gas propegator

$$G^0(k,i\omega_n) = \frac{1}{i\,\omega_n - \xi(k)} \tag{B.3.3}$$

is diagonal in momentum and spin. Hence

$$\begin{aligned}\delta\,G(\mathbf{k},\mathbf{k}\pm\mathbf{q};i\omega_n) &= G^0(\mathbf{k};i\omega_n)T(\mathbf{k},\mathbf{k}\pm\mathbf{q};i\omega_n)G^0(\mathbf{k}\pm\mathbf{q};i\omega_n) \\ &= t^{imp}(i\omega_n)G^0(k;i\omega_n)G^0(k\pm q;i\omega_n)\end{aligned} \tag{B.3.4}$$

since the T-matrix is diagonal. Now Eqn. (B.3.2) the same form for any impurity

$$\delta\rho_{conv.metal}(q;i\omega_n,J) = \Im[t^{imp}(i\omega_n,J)\Omega_{conv.metal}(q;i\omega_n)] \tag{B.3.5}$$

with the impurity t-function discussed in section 4.3. Consider the quantity

$$\begin{aligned}\Omega(q;i\omega) &= \int\frac{\mathrm{d}^2\mathbf{k}}{(2\pi)^2}\,Tr[G_0(k;i\omega_n)G_0(k-q;i\omega_n)] = 2\int\frac{\mathrm{d}^2\mathbf{k}}{(2\pi)^2}\,\frac{1}{i\,\omega_n-\xi(k)}\,\frac{1}{i\,\omega_n-\xi(k+q)} \\ &= 2\int\frac{\mathrm{d}^2\mathbf{k}}{(2\pi)^2}\,\frac{1}{i\,\varpi_n-\epsilon(k)}\,\frac{1}{i\,\varpi_n-\epsilon(k+q)} = 2\int_0^1\mathrm{d}x\int\frac{\mathrm{d}^2\mathbf{k}}{(2\pi)^2}\,\frac{1}{(\Delta^2-\frac{k^2}{2\,m})^2}\end{aligned} \tag{B.3.6}$$

with $\Delta^2 = i\,\varpi_n - \frac{x(1-x)q^2}{2\,m}$, $\varpi_n = \omega_n - i\mu$ and x being the Feynman-Schwinger parameter.
The prefactor factor arose as $2 = Tr[\tau^0]$ and the last equallity came about invoking the Feynman-Schwinger parametrization $\frac{1}{A^\alpha B^\beta} = \Gamma_{\alpha\beta}\int_0^1\mathrm{d}x\,\frac{x^{\alpha-1}\,(1-x)^{\beta-1}}{(xA+(1-x)B)^{\alpha+\beta}}$, $\Gamma_{\alpha\beta} = \frac{\Gamma(\alpha+\beta)}{\Gamma(\alpha)\Gamma(\beta)}$ and shifting momentum $\mathbf{k}\to\mathbf{k}-(1-x)\mathbf{q}$ only in the denominator, since the nominator is momentum independent. $\Gamma(n)$ denote the usual Gamma-function taking an integer argument n and $\Gamma_{\alpha\beta}$ is evaluated to $\Gamma_{11} = \frac{\Gamma(2)}{\Gamma(1)\Gamma(1)} = 1$.

Note that

$$\int\frac{\mathrm{d}^2\mathbf{k}}{(2\pi)^2}\,Tr[G_0(k;i\omega_n)G_0(k+q;i\omega_n)] = \int\frac{\mathrm{d}^2\mathbf{k}}{(2\pi)^2}\,Tr[G_0(k;i\omega_n)G_0(k-q;i\omega_n)] = \Omega(q;i\omega)$$

and continuing Eqn. (B.3.6) by integrating in scaled momentum 2 dimensional polar (since no angular dependence) coordinates $\int \frac{\mathrm{d}^2\mathbf{k}}{(2\pi)^2} = \int_0^{2\pi} \frac{\mathrm{d}\phi_k}{(2\pi)} \int_0^\infty \frac{\mathrm{d}k\, k}{(2\pi)} = \int_0^\infty \frac{\mathrm{d}k\, k}{(2\pi)} = 2\,m \int_0^\infty \frac{\mathrm{d}\kappa\, \kappa}{(2\pi)}$, with $\kappa = \frac{k}{\sqrt{2\,m}}$ then

$$\Omega(q; i\omega) = 2 \cdot 2\,m \int_0^1 \mathrm{d}x \int_0^\infty \frac{\mathrm{d}\kappa\, \kappa}{(2\pi)} \frac{1}{\Delta^2 - \kappa^2} = -\frac{2 \cdot 2\,m}{2 \cdot 2\pi} \int_0^1 \mathrm{d}x \frac{1}{i\,\varpi_n - \frac{x(1-x)q^2}{2\,m}} \tag{B.3.7}$$

The retarded Ω-structure is $\Omega(q;\omega) = \Omega(q; i\omega_n \to i0^+)$ with real and imaginary components as given (some algebra is left out) right below. The real component of the retarded Ω-structure (below $\mathbb{P}$ define the Cauchy principal value)

$$\begin{aligned}
\Re\Omega_{Conv.Metal}(q;\omega) &= \frac{2 \cdot 2\,m}{2 \cdot 2\pi} \mathbb{P} \int_0^1 \mathrm{d}x \frac{1}{i\,\varpi_n - \frac{x(1-x)q^2}{2\,m}} \\
&= \begin{cases} \frac{16\pi N_0^2}{|q|\sqrt{q^2 - 4\,k_\omega^2}} \ln\left(\frac{q^2 + |q|\sqrt{q^2 - 4\,k_\omega^2}}{-q^2 + |q|\sqrt{q^2 - 4\,k_\omega^2}} \right) & \text{for } q > 2k_\omega \\ -\frac{32\pi N_0^2}{|q|\sqrt{4\,k_\omega^2 - q^2}} \tan^{-1}\left(\frac{q}{\sqrt{4\,k_\omega^2 - q^2}} \right) & \text{for } q < 2k_\omega \end{cases} \\
&= \begin{cases} \frac{16\pi N_0^2}{|q||k_\omega|\sqrt{x^2-4}} \ln\left(\frac{x + \sqrt{x^2-4}}{-x + \sqrt{x^2-4}} \right) & \text{for } x > 2 \\ -\frac{32\pi N_0^2}{|q||k_\omega|\sqrt{4-x^2}} \tan^{-1}\left(\frac{x}{\sqrt{4-x^2}} \right) & \text{for } x < 2 \end{cases}
\end{aligned} \tag{B.3.8}$$

as a function of the dimensionless parameter $x = q/k_\omega$ and $N_0 = \frac{m}{2\pi}$ being the single electron density of states Eqn. (2.13). The imaginary component of the retarded Ω-structure

$$\begin{aligned}
\Im\,\Omega_{Conv.Metal}(q;\omega) &= \frac{2 \cdot 2\,m}{2 \cdot 2\pi} \pi \int_0^1 \mathrm{d}x\, \delta(\varpi_n - \frac{x(1-x)q^2}{2\,m}) \\
&= \begin{cases} \frac{8\pi^2 N_0^2}{|q|\sqrt{q^2 - 4\,k_\omega^2}} & \text{for } q > 2k_\omega \\ 0 & \text{for } q < 2k_\omega \end{cases} \\
&= \begin{cases} \frac{8\pi^2 N_0^2}{|q||k_\omega|\sqrt{x^2-4}} & \text{for } x > 2 \\ 0 & \text{for } x < 2 \end{cases}
\end{aligned} \tag{B.3.9}$$

In the Born approximation i.e. $T \approx J$ and probing the Fermi surface $\omega = 0$ then $k_\omega = k_F$ the FT-LDOS responce Eqn. (B.3.5) $\rho_{Conv.Metal}(q,0)/8\pi^2 N_0^2 v_0$ as a function of q/k_F is plotted in figure 6.1. The *singular* responce in $\Omega_{Conv.Metal}(q;\omega)$ arise at momenta q_ω for which $\xi(\frac{q_\omega}{2}) = \omega$ at probe bias ω

$$\begin{aligned}
\xi(\frac{q_\omega}{2}) = \omega \leftrightarrow \\
q_\omega = 2k_\omega
\end{aligned} \tag{B.3.10}$$

momenta for which the real and imaginary part of $\Omega(q;\omega)$ has a *singularity*.

Appendix C

Connection between LDOS and FT-LDOS

In this chapter the connection between the long distance expansion of the LDOS oscillations with leading decay rate α and the FT-LDOS will be elaborated. Hence it connects the chapters 5 and 6.

C.1 Long distance asymptotic expansion - spin unresolved probes

The spin-unresolved/charge LDOS of the impurities are Eqn. (5.28), (5.30) and (5.32) all have the form

$$\delta\rho_{sc}(\mathbf{r};\tilde{\omega},J) = -\frac{2}{\pi}\Im\left[t^{sc/qm/cl}(\tilde{\omega},J)\frac{|\tilde{\omega}|^2}{16}\left(f_0^2(\tilde{\omega},r)-f_1^2(\tilde{\omega},r)\right)\left(\frac{L}{v_F\hbar}\right)^4\right] \tag{C.1.1}$$

with $t^{sc/qm/cl}$ differentiating the impurities, but all sharing $\frac{|\tilde{\omega}|^2}{16}\left(f_0^2(\tilde{\omega},r)-f_1^2(\tilde{\omega},r)\right)$ where the functions

$$\begin{aligned} f_0(\tilde{\omega},r) &= s(\tilde{\omega})Y_0(|\tilde{\omega}|r) - iJ_0(|\tilde{\omega}|r)\Theta(D-|\tilde{\omega}|),\\ f_1(\tilde{\omega},r) &= iY_1(|\tilde{\omega}|r) + s(\tilde{\omega})J_1(|\tilde{\omega}|r)\Theta(D-|\tilde{\omega}|) \end{aligned} \tag{C.1.2}$$

with $J_{0/1}$ and $Y_{0/1}$ denoting the Bessel functions of first and second[1] kind, respectively, to zeroth or first order.

The $J_n(x)$ and $Y_n(x)$ Bessel function of the first and second kind of order n has the asymptotic expansion

$$J_n(x) \sim \sqrt{\frac{2}{\pi x}}\cos\left(x-\frac{n\pi}{2}-\frac{\pi}{4}\right) \tag{C.1.3}$$

$$Y_n(x) \sim \sqrt{\frac{2}{\pi x}}\sin\left(x-\frac{n\pi}{2}-\frac{\pi}{4}\right) \tag{C.1.4}$$

[1] note that this is called the Neuman function in the thesis

for large x. In the long distance $|\tilde{\omega}|r \sim \frac{D}{\epsilon_c}$ then $\frac{|\tilde{\omega}|}{r} \sim \frac{D}{\epsilon_c r^2}$ and therefore

$$|\tilde{\omega}|^2 \left(f_0^2(\tilde{\omega}, r) - f_1^2(\tilde{\omega}, r)\right) \to -\frac{2}{\pi}\left(\frac{\cos\left(2|\tilde{\omega}|r\right)}{r^2} - i\frac{\sin\left(2|\tilde{\omega}|r\right)}{r^2}\right) \tag{C.1.5}$$

for $\tilde{\omega} \geq 0$ which will be the assumption in the rest.

In the 1^{st} Born approximation the t-function for the scalar potential becomes

$$t^{sc}(\tilde{\omega}, J) = J$$

a real constant. Hence the spin-unresolved LDOS Eqn. (C.1.1) for the scalar potential becomes

$$\delta\rho_{sc}(\mathbf{r}; \tilde{\omega}, J) \sim J\,\frac{2}{16\pi}\frac{2}{\pi}\frac{\sin\left(2|\tilde{\omega}|r\right)}{r^2}\left(\frac{L}{v_F\hbar}\right)^4 = J\frac{1}{4\pi^2}\frac{\sin\left(2|\tilde{\omega}|r\right)}{r^2}\left(\frac{L}{v_F\hbar}\right)^4 \tag{C.1.6}$$

which is a 'fast' decay rate of $\alpha = 2$. Therefore the LDOS long-distance expansion generically goes as

$$h_{sc}(\mathbf{r}, \mu) = \frac{\sin\left(2|\mu|r\right)}{\epsilon_c^2 r^2} \tag{C.1.7}$$

which is plotted in figure C.1 as the red curve and it is seen that it follow the cyan curve $\beta_{sc}(\epsilon_c r)^{-2}$ with $\gamma_{sc} = 1$.

In the 1^{st} Born approximation the classical magnetic impurity has T-matrix $T_{cl}(\tilde{\omega}, J) = J\tau^i$, with $i = x, y, z$ and the spin-unresolved LDOS and FT-LDOS responses become[2]

$$\delta\rho_{cl}(\mathbf{r}; \tilde{\omega}, J) = 0 \quad , \quad \delta\rho_{cl}(\mathbf{q}; \tilde{\omega}, J) = 0 \tag{C.1.8}$$

The quantum magnetic impurity is more subtle, because the first order irreducible self-energy $\Sigma^{(1)} = 0$ vanish and hence in the 1^{st} Born approximation the t-function becomes

$$t^{qm}(\tilde{\omega}, J) = \Sigma^{(2)}(\tilde{\omega}, J) = -\frac{3}{4}J^2 g(\tilde{\omega})$$

which now have a imaginary and real part due to the g-function Eqn. (4.13)

$$g(\tilde{\omega}) = \left(\frac{L}{\hbar v_F}\right)^2 \left(\frac{\tilde{\omega}}{4\pi}\ln\left[\frac{\mathrm{D}^2}{\tilde{\omega}^2} - 1\right] + \frac{i\,|\tilde{\omega}|}{4}\right)\Theta(\mathrm{D} - |\tilde{\omega}|) \tag{C.1.9}$$

Hence the spin-unresolved LDOS Eqn. (C.1.1) for the quantum magnetic impurity consist of two parts.

The first part

$$\Im t^{qm}(\tilde{\omega}, J)\Re\left[|\tilde{\omega}|^2\left(f_0^2(\tilde{\omega}, r) - f_1^2(\tilde{\omega}, r)\right)\right] \sim \frac{-3}{4}\frac{J^2\tilde{\omega}}{4\epsilon_c^2}\frac{2}{\pi}\frac{\cos\left(2|\tilde{\omega}|r\right)}{\epsilon_c^2 r^2} \tag{C.1.10}$$

The second part

$$\Re t^{qm}(\tilde{\omega}, J)\Im\left[|\tilde{\omega}|^2\left(f_0^2(\tilde{\omega}, r) - f_1^2(\tilde{\omega}, r)\right)\right] \sim \frac{-3}{4}\frac{J^2\tilde{\omega}}{4\pi\epsilon_c^2}\frac{2}{\pi}\ln\left((D/\tilde{\omega})^2 - 1\right)\frac{\sin\left(2|\tilde{\omega}|r\right)}{\epsilon_c^2 r^2} \tag{C.1.11}$$

[2] The spin-unresolved LDOS and FT-LDOS response for the classical magnetic impurity is Eqn. (7.5) and (7.6) respectively in the full T-matrix expansion, since only the part $\tilde{T}_{\mathbf{k}\mathbf{k}'} \propto t_{cl}(\tilde{\omega}, J)U^\dagger(\phi_{\mathbf{k}})U(\phi_{\mathbf{k}'})$ of its T-matrix is picked out and $t_{cl}(\tilde{\omega}, J) = t_{qm}(\tilde{\omega}, J)$. However, in the 1^{st} Born approximation where the T-matrix in not proportional to the identity matrix, then Eqn. (7.5) and (7.6) cannot be used, but one have to derive the LDOS and FT-LDOS by their definitions.

which adds corrections of orders r^{-j} with $j = 2, 3, 4, 5\ldots$ due to the log-correction. Therefore the spin-unresolved LDOS Eqn. (C.1.1) becomes

$$\delta\rho_{qm}(\mathbf{r};\tilde{\omega},J) \to -J^2\frac{2}{16\pi}\frac{2}{\pi}\frac{3}{4}\tilde{\omega}\left[\frac{\cos\left(2|\tilde{\omega}|r\right)}{4r^2} - \frac{\log\left((D/\tilde{\omega})^2-1\right)}{4\pi}\frac{\sin\left(2|\tilde{\omega}|r\right)}{r^2}\right]\left(\frac{L}{\hbar v_F}\right)^6$$
$$= -J^2\frac{1}{4\pi^2}\frac{3\tilde{\omega}}{4}\left[\frac{\cos\left(2|\tilde{\omega}|r\right)}{4r^2} - \frac{\log\left((D/\tilde{\omega})^2-1\right)}{4\pi}\frac{\sin\left(2|\tilde{\omega}|r\right)}{r^2}\right]\left(\frac{L}{\hbar v_F}\right)^6 \qquad \text{(C.1.12)}$$

which is also a 'fast' decay rate of $\alpha = 2$ as the leading rate. Therefore the LDOS long-distance expansion generically goes as

$$h_{qm}(\mathbf{r},\mu) = \frac{3\tilde{\omega}J}{4\epsilon_c^2}\left(\frac{\cos\left(2|\tilde{\omega}|r\right)}{4\epsilon_c^3 r^2} - \frac{\log\left((D/\tilde{\omega})^2-1\right)}{4\pi}\frac{\sin\left(2|\tilde{\omega}|r\right)}{\epsilon_c^2 r^2}\right) \qquad \text{(C.1.13)}$$

which is plotted in figure C.1 as the black curve and it is seen that it follow the white curve $\gamma_{qm}(\epsilon_c r)^{-2}$ with $\gamma_{qm} = \frac{3\tilde{\omega}J}{4\epsilon_c^2}\frac{\log\left((D/\tilde{\omega})^2-1\right)}{4\pi}$. In table 5.3 in section 5.2 the decay rates are summarized and also in table C.1.

Table C.1: Table of α for point-impurities in the Dirac model and 1^{st} Born approximation.

change in LDOS	$(\mathbf{k}_f, \mathbf{k}_i)$	α for spin-unresolved $\delta\rho$	α for spin-resolved $\delta\rho^i$
scalar	TRP	2	-
classical magnetic	TRP	-	1
quantum magnetic	TRP	2	-
conv.metal		1	

In figure C.2 is plotted the Fourier transform modulus $h_{imp.}(\mathbf{q},\tilde{\omega})|_{\omega=0} = h_{imp.}(\mathbf{q},\mu) = \left|\int \mathrm{d}\mathbf{r} e^{-i\mathbf{q}\cdot\mathbf{r}} h_{imp.}(\mathbf{r},\mu)\right|$ of the LDOS long-distance asymptotic expansion (plotted in figure C.1) of: the scalar on a conventional metal with $h_{sc,conv.}(\mathbf{r},\mu) = \frac{\cos\left(2|\mu|r\right)}{\epsilon_c r}$ and decay rate $\alpha = 1$, the scalar on a helical metal with Eqn. (C.1.7) $h_{sc}(\mathbf{r},\mu) = \frac{\sin\left(2|\mu|r\right)}{\epsilon_c^2 r^2}$ which has $\alpha = 2$ and the quantum magnetic impurity on a helical metal with Eqn.(C.1.13) $h_{qm}(\mathbf{r},\mu) = \frac{3\tilde{\omega}J}{4\epsilon_c^2}\left(\frac{\cos\left(2|\tilde{\omega}|r\right)}{4\epsilon_c^3 r^2} - \frac{\log\left((D/\tilde{\omega})^2-1\right)}{4\pi}\frac{\sin\left(2|\tilde{\omega}|r\right)}{\epsilon_c^2 r^2}\right)$ which has $\alpha = 2$.

The $h_{imp.}(\mathbf{q},\mu)$ Fourier transform of the long-distance LDOS expansion $h_{imp.}(\mathbf{r},\mu)$ with leading decay-rate α plotted in figure C.2 should resemble the FT-LDOS in 1^{st} Born Approximation (derived in section 6.1.1 and 6.1.2 on the conventional and helical metal respectively) illustrated in figure C.3 and C.4. For all impurities the response signature at $q = 1$ (i.e. $q = 2k_F$) agree well.

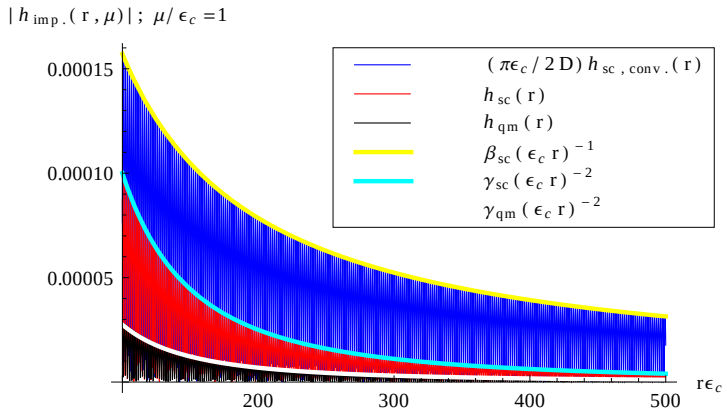

Figure C.1: The long distance LDOS expansion $h_{imp.}(\mathbf{r},\mu)$. The scalar on a conventional metal (blue line) is $\frac{\pi}{2}\frac{\epsilon_c}{D}\,h_{sc,conv.}(\mathbf{r},\mu)$ which follow the yellow line $\beta_{sc}(\epsilon_c r)^{-1}$ with $\beta_{sc}=\frac{\pi}{2}\frac{\epsilon_c}{D}$. The scalar on a helical metal (red line) is $h_{sc}(\mathbf{r},\mu)$ which follow the cyan line $\gamma_{sc}(\epsilon_c r)^{-2}$ with $\gamma_{sc}=1$ and the quantum magnetic impurity (black line) is $h_{qm}(\mathbf{r},\mu)$ which follow the white line $\gamma_{qm}(\epsilon_c r)^{-2}$ with $\gamma_{qm}=\frac{3\tilde{\omega}J}{4}\frac{\log\left((D/\tilde{\omega})^2-1\right)}{4\pi\epsilon_c^3 r^3}$. The cut-off is $D/\epsilon_c=100$ and the impurity strength $J/\epsilon_c=1/2$

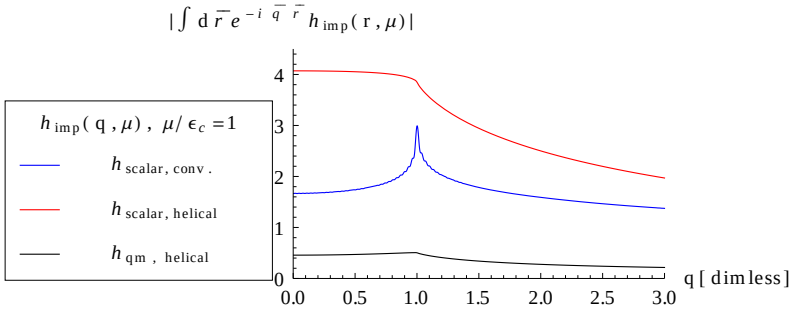

Figure C.2: The Fourier transform modulus $|h_{imp.}(\mathbf{q},\mu)|$ of the long-distance LDOS expansion $h_{imp}(\mathbf{r},\mu)$ with leading decay-rate α. The scalar on a conventional metal (blue line) is $h_{sc,conv.}(\mathbf{q},\mu)$, the scalar on a helical metal (red line) is $h_{sc}(\mathbf{q},\mu)$ and quantum magnetic impurity (black line) is $h_{qm}(\mathbf{q},\mu)$. The cut-off is $D/\epsilon_c=100$ and the impurity strength $J/\epsilon_c=1/2$

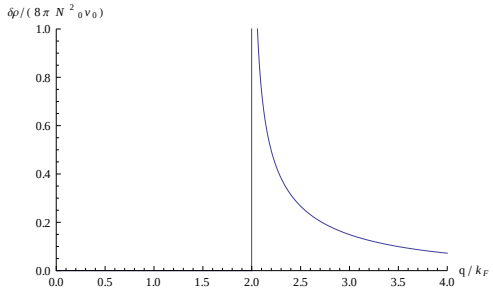

Figure C.3: Plot of scalar FT-LDOS $\rho_{Conv.Metal}(q,0)/8\pi^2 N_0^2 J$ as a function of q/k_F in the 1^{st} Born Approx. This is figure 6.1 in thesis.

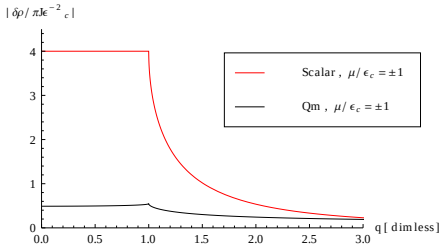

Figure C.4: Plot of scalar on a helical metal (red line) $|\rho_{sc}(q\,2\mu)/J\pi\epsilon_c^{-2}|$ and quantum magnetic imp. FT-LDOS modulus (black line) $|\rho_{qm}(q\,2\mu)/J\pi\epsilon_c^{-2}|$ as a function of dimensionless q and $\mu/\epsilon_c = \pm 1$ in the 1^{st} Born Approx.

Appendix D

The T-matrix for the scalar potential and classical magnetic impurities

D.1 T-matrix for a scalar potential

The scalar scattering matrix in η-basis $\tilde{V}_{\mathbf{k}',\mathbf{k}} = U^{\dagger}_{\mathbf{k}'} V_0 \tau^0 U_{\mathbf{k}}$ is used to calculate the T-matrix in η-basis

$$\begin{aligned}
\tilde{T}_{\mathbf{k}'\mathbf{k}} &= \tilde{V}_{\mathbf{k}'\mathbf{k}} + \tilde{V}_{\mathbf{k}'\mathbf{k}_1}\tilde{G}_{\mathbf{k}_1}\tilde{V}_{\mathbf{k}_1\mathbf{k}} + \tilde{V}_{\mathbf{k}'\mathbf{k}_1}\tilde{G}_{\mathbf{k}_1}\tilde{V}_{\mathbf{k}_1\mathbf{k}_2}\tilde{G}_{\mathbf{k}_2}\tilde{V}_{\mathbf{k}_2\mathbf{k}} + \cdots \\
&= \sum_{\mathbf{k}_1\mathbf{k}_2\cdots} U^{\dagger}_{\mathbf{k}'} \Bigg(V_0\tau^0 + V_0\tau^0 \underbrace{U_{\mathbf{k}_1}\tilde{G}_{\mathbf{k}_1}U^{\dagger}_{\mathbf{k}_1}}_{=-g(i\tilde{\omega}_n)\tau^0} V_0\tau^0 \\
&\qquad + V_0\tau^0 \underbrace{U_{\mathbf{k}_1}\tilde{G}_{\mathbf{k}_1}U^{\dagger}_{\mathbf{k}_1}}_{=-g(i\tilde{\omega}_n)\tau^0} V_0\tau^0 \underbrace{U_{\mathbf{k}_2}\tilde{G}_{\mathbf{k}_2}U^{\dagger}_{\mathbf{k}_2}}_{=-g(i\tilde{\omega}_n)\tau^0} V_0\tau^0 + \cdots \Bigg) U_{\mathbf{k}} \\
&= U^{\dagger}_{\mathbf{k}'} \left(V_0\tau^0 + V_0\tau^0(-g(i\tilde{\omega}_n))\tau^0 V_0\tau^0 \right. \\
&\qquad \left. + V_0\tau^0(-g(i\tilde{\omega}_n)\tau^0)V_0\tau^0(-g(i\tilde{\omega}_n)\tau^0)V_0\tau^0 + \cdots \right) U_{\mathbf{k}} \\
&= V_0 U^{\dagger}_{\mathbf{k}'}\tau^0 \left(1 + V_0(-g(i\tilde{\omega}_n))\tau^0 + (V_0)^2(-g(i\tilde{\omega}_n))^2(\tau^0)^2 + \cdots\right) U_{\mathbf{k}} \\
&= V_0 U^{\dagger}_{\mathbf{k}'}\tau^0 \left(\sum_{n=0}^{\infty} x^n\right) U_{\mathbf{k}} \\
&= V_0 U^{\dagger}_{\mathbf{k}'}\tau^0 \left(\frac{\tau^0}{1 - V_0(-g(i\tilde{\omega}_n))}\right) U_{\mathbf{k}}
\end{aligned} \tag{D.1.1}$$

where the relation

$$\sum_{\mathbf{k}_i} U_{\mathbf{k}_i}\tilde{G}_{\mathbf{k}_i}U^{\dagger}_{\mathbf{k}_i} = -g(i\tilde{\omega}_n)\tau^0 \tag{D.1.2}$$

was used several times. In the second-to-last equality the matrix $x = V_0(-g(i\tilde{\omega}_n))\tau^0$ was defined and the geometric serie becomes

$$[\tau^0 - x]^{-1} = [\tau^0 - V_0(-g(i\tilde{\omega}_n))\tau^0]^{-1} = \frac{\tau^0}{1 - V_0(-g(i\tilde{\omega}_n))}$$

Hence the the T-matrix in σ-basis is

$$T_{\mathbf{k}'\mathbf{k}} = U_{\mathbf{k}'}\tilde{T}_{\mathbf{k}'\mathbf{k}}U^\dagger_{\mathbf{k}} = \frac{V_0\tau^0}{1 - V_0(-g(i\tilde{\omega}_n))} \tag{D.1.3}$$

D.2 T-matrix for a classical magnetic impurity

The classical megnetic scattering matrix in η-basis $\tilde{V}_{\mathbf{k}'\mathbf{k}} = S_i U^\dagger_{\mathbf{k}'}\tau^i U^\dagger_{\mathbf{k}'}$ and the Einstein sum conventionen is implicit. It is used to calculate the T-matrix in η-basis

$$\begin{aligned}
\tilde{T}_{\mathbf{k}'\mathbf{k}} &= \tilde{V}_{\mathbf{k}'\mathbf{k}} + \tilde{V}_{\mathbf{k}'\mathbf{k}_1}\tilde{G}_{\mathbf{k}_1}\tilde{V}_{\mathbf{k}_1\mathbf{k}} + \tilde{V}_{\mathbf{k}'\mathbf{k}_1}\tilde{G}_{\mathbf{k}_1}\tilde{V}_{\mathbf{k}_1\mathbf{k}_2}\tilde{G}_{\mathbf{k}_2}\tilde{V}_{\mathbf{k}_2\mathbf{k}} + \cdots \\
&= \sum_{\mathbf{k}_1\mathbf{k}_2\cdots} U^\dagger_{\mathbf{k}'}\Bigg(S_i\tau^i + S_i\tau^i \underbrace{U_{\mathbf{k}_1}\tilde{G}_{\mathbf{k}_1}U^\dagger_{\mathbf{k}_1}}_{=-g(i\tilde{\omega}_n)\tau^0} S_j\tau^j \\
&\qquad + S_i\tau^i \underbrace{U_{\mathbf{k}_1}\tilde{G}_{\mathbf{k}_1}U^\dagger_{\mathbf{k}_1}}_{=-g(i\tilde{\omega}_n)\tau^0} S_j\tau^j \underbrace{U_{\mathbf{k}_2}\tilde{G}_{\mathbf{k}_2}U^\dagger_{\mathbf{k}_2}}_{=-g(i\tilde{\omega}_n)\tau^0} S_l\tau^l + \cdots \Bigg) U_{\mathbf{k}} \\
&= U^\dagger_{\mathbf{k}'}\big(S_i\tau^i + S_i\tau^i(-g(i\tilde{\omega}_n))\tau^0 S_j\tau^j \\
&\qquad + S_i\tau^i(-g(i\tilde{\omega}_n)\tau^0)S_j\tau^j(-g(i\tilde{\omega}_n)\tau^0)S_l\tau^l + \cdots\big) U_{\mathbf{k}} \\
&= U^\dagger_{\mathbf{k}'}\big(\bar{S}\cdot\bar{\tau} + \bar{S}\cdot\bar{\tau}(-g(i\tilde{\omega}_n))\tau^0\bar{S}\cdot\bar{\tau} \\
&\qquad + \bar{S}\cdot\bar{\tau}(-g(i\tilde{\omega}_n)\tau^0)\bar{S}\cdot\bar{\tau}(-g(i\tilde{\omega}_n)\tau^0)\bar{S}\cdot\bar{\tau} + \cdots\big) U_{\mathbf{k}} \\
&= U^\dagger_{\mathbf{k}'}\bar{S}\cdot\bar{\tau}\left(1 + (-g(i\tilde{\omega}_n))\tau^0\bar{S}\cdot\bar{\tau} + (-g(i\tilde{\omega}_n))^2(\tau^0)(\bar{S}\cdot\bar{\tau})(\tau^0)(\bar{S}\cdot\bar{\tau}) + \cdots\right) U_{\mathbf{k}} \\
&= U^\dagger_{\mathbf{k}'}\bar{S}\cdot\bar{\tau}\left(\sum_{n=0}^{\infty} x^n\right) U_{\mathbf{k}} \\
&= U^\dagger_{\mathbf{k}'}\left(\frac{\bar{S}\cdot\bar{\tau} - g(i\tilde{\omega}_n)|S|^2}{1 - g(i\tilde{\omega}_n)^2|S|^2}\right) U_{\mathbf{k}}
\end{aligned} \tag{D.2.1}$$

Again the relation (D.1.2) was used in each $\mathbf{k}$-sum and the matrix $x = (-g(i\tilde{\omega}_n))\tau^0\bar{S}\cdot\bar{\tau} = -g(i\tilde{\omega}_n)\bar{S}\cdot\bar{\tau}$ in the second to last equality sign give the geometric serie $[\tau^0 - x]^{-1} = [\tau^0 - (-g(i\tilde{\omega}_n))\bar{S}\cdot\bar{\tau}]^{-1} = \frac{\tau^0 - g(i\tilde{\omega}_n)\bar{S}\cdot\bar{\tau}}{1 - g(i\tilde{\omega}_n)^2|S|^2}$. In the last equality sign the relation $(\bar{\tau}\cdot\mathbf{a})(\bar{\tau}\cdot\mathbf{b}) = \mathbf{a}\cdot\mathbf{b} + i\,\bar{\tau}\,(\mathbf{a}\times\mathbf{b})$ for any Pauli matrix τ and vectors $\mathbf{a}$ and $\mathbf{b}$ which makes $(\bar{S}\cdot\bar{\tau})(\bar{S}\cdot\bar{\tau}) = \bar{S}\cdot\bar{S} + i\tau\cdot(\bar{S}\times\bar{S}) = \bar{S}\cdot\bar{S} = |S|^2$ was used. Hence the T-matrix in σ-bais is

$$T^{mag}_{\mathbf{k}'\mathbf{k}} = U_{\mathbf{k}'}\tilde{T}_{\mathbf{k}'\mathbf{k}}U^\dagger_{\mathbf{k}} = \frac{\bar{S}\cdot\bar{\tau} - g(i\tilde{\omega}_n)|S|^2}{1 - g(i\tilde{\omega}_n)^2|S|^2} \tag{D.2.2}$$

Note that it was really not necessary to calculate $\tilde{T}^{mag}_{\mathbf{k}'\mathbf{k}}$ and $\tilde{T}^{scalar}_{\mathbf{k}'\mathbf{k}}$ in η-basis. The η-basis is only introduced in order to be able to calculate the self-energy induced by the quantum mechanical impurity.

Bibliography

[1] Z. Alpichshev, J. G. Analytis, J. H. Chu, I.R. Fisher, Y.L. Chen, Z.X. Shen, A. Fang, and A. Kapitulnik. STM Imaging of Electronic Waves on the Surface of Bi2Te3: Topologically Protected Surface States and Hexagonal Warping Effects. *Physical Review Letters*, 104(1), 2010.

[2] Zhanybek Alpichshev, J. G. Analytis, J. H. Chu, I. R. Fisher, and A. Kapitulnik. STM imaging of a bound state along a step on the surface of the topological insulator Bi$_2$Te$_3$. *ArXiv1003.2233*, page 5, March 2010.

[3] Zhanybek Alpichshev, Rudro R. Biswas, Alexander V. Balatsky, James G. Analytis, Jiun-Haw Chu, Ian R. Fisher, and Aharon Kapitulnik. STM imaging of impurity resonances on Bi$_2$Se$_3$. *ArXiv1108.0022*.

[4] A. Balatsky, I. Vekhter, and Jian-Xin Zhu. Impurity-induced states in conventional and unconventional superconductors. *Reviews of Modern Physics*, 78(2):373–433, May 2006.

[5] J. Bardeen. Tunnelling from a Many-Particle Point of View. *Physical Review Letters*, 6(2):57–59, January 1961.

[6] Haim Beidenkopf, Pedram Roushan, Jungpil Seo, Lindsay Gorman, Ilya Drozdov, Yew San Hor, R. J. Cava, and Ali Yazdani. Spatial Fluctuations of Helical Dirac Fermions on the Surface of Topological Insulators. *ArXiv1108.2089*.

[7] Marco Bianchi, Dandan Guan, Shining Bao, Jianli Mi, Bo Brummerstedt Iversen, Philip D. C. King, and Philip Hofmann. Coexistence of the topological state and a two-dimensional electron gas on the surface of Bi2Se3. *ArXiv1009.2879*.

[8] G BIHLMAYER, Y KOROTEEV, P ECHENIQUE, E CHULKOV, and S BLUGEL. The Rashba-effect at metallic surfaces. *Surface Science*, 600(18):3888–3891, September 2006.

[9] Rudro Biswas and A. Balatsky. Impurity-induced states on the surface of three-dimensional topological insulators. *Physical Review B*, 81(23), June 2010.

[10] Rudro R. Biswas and Alexander V. Balatsky. Scattering from Surface Step Edges in Strong Topological Insulators. *ArXiv0912.4477*.

[11] L. Capriotti, D. Scalapino, and R. Sedgewick. Wave-vector power spectrum of the local tunneling density of states: Ripples in a d-wave sea. *Physical Review B*, 68(1), July 2003.

[12] Y L Chen, J G Analytis, J-H Chu, Z K Liu, S-K Mo, X L Qi, H J Zhang, D H Lu, X Dai, Z Fang, S C Zhang, I R Fisher, Z Hussain, and Z-X Shen. Experimental realization of a three-dimensional topological insulator, Bi2Te3. *Science (New York, N.Y.)*, 325(5937):178–81, July 2009.

[13] M. F. Crommie, C. P. Lutz, and D. M. Eigler. Imaging standing waves in a two-dimensional electron gas. *Nature*, 363(6429):524–527, June 1993.

[14] Xiao-Yong Feng, Wei-Qiang Chen, Jin-Hua Gao, Qiang-Hua Wang, and Fu-Chun Zhang. Anderson impurity in a helical metal. *Physical Review B*, 81(23), June 2010.

[15] Xiao-Yong Feng and Fu-Chun Zhang. Kondo Spin Screening Cloud in Two-dimensional Electron Gas with Spin-orbit Couplings. *ArXiv1102.2947*, February 2011.

[16] Ø ystein Fischer, Martin Kugler, Ivan Maggio-Aprile, Christophe Berthod, and Christoph Renner. Scanning tunneling spectroscopy of high-temperature superconductors. *Reviews of Modern Physics*, 79(1):353–419, March 2007.

[17] Flensberg. *Many-Body Quantum Theory in Condensed Matter Physics*. Oxford university Press, 2007.

[18] Liang Fu. Hexagonal Warping Effects in the Surface States of the Topological Insulator Bi_{2}Te_{3}. *Physical Review Letters*, 103(26), December 2009.

[19] Liang Fu and C. Kane. Topological insulators with inversion symmetry. *Physical Review B*, 76(4), July 2007.

[20] A K Geim and K S Novoselov. The rise of graphene. *Nature materials*, 6(3):183–91, March 2007.

[21] Kenjiro K. Gomes, Wonhee Ko, Warren Mar, Yulin Chen, Zhi-Xun Shen, and Hari C. Manoharan. Quantum Imaging of Topologically Unpaired Spin-Polarized Dirac Fermions. *ArXiv0909.0921*, September 2009.

[22] H. M. Guo and M. Franz. Theory of quasiparticle interference on the surface of a strong topological insulator. *ArXiv0910.4946*, page 4, October 2009.

[23] M. Hasan and C. Kane. Colloquium: Topological insulators. *Reviews of Modern Physics*, 82(4):3045–3067, November 2010.

[24] M. Hoesch. Spin structure of the Shockley surface state on Au(111). *Physical Review B*, 69(241401), 2004.

[25] D Hsieh, Y Xia, D Qian, L Wray, J H Dil, F Meier, J Osterwalder, L Patthey, J G Checkelsky, N P Ong, A V Fedorov, H Lin, A Bansil, D Grauer, Y S Hor, R J Cava, and M Z Hasan. A tunable topological insulator in the spin helical Dirac transport regime. *Nature*, 460(7259):1101–5, August 2009.

[26] D. Hsieh, Y. Xia, D. Qian, L. Wray, F. Meier, J. Dil, J. Osterwalder, L. Patthey, A. Fedorov, H. Lin, A. Bansil, D. Grauer, Y. Hor, R. Cava, and M. Hasan. Observation of Time-Reversal-Protected Single-Dirac-Cone Topological-Insulator States in Bi2Te3 and Sb2Te3. *Physical Review Letters*, 103(14), September 2009.

[27] D Hsieh, Y Xia, L Wray, D Qian, A Pal, J H Dil, J Osterwalder, F Meier, G Bihlmayer, C L Kane, Y S Hor, R J Cava, and M Z Hasan. Observation of unconventional quantum spin textures in topological insulators. *Science (New York, N.Y.)*, 323(5916):919–22, February 2009.

[28] Jun Kondo. Resistance Minimum in Dilute Magnetic Alloys. *Progress of Theoretical Physics*, 32(1):37–49, July 1964.

[29] Wei-Cheng Lee, Congjun Wu, Daniel P. Arovas, and Shou-Cheng Zhang. Quasiparticle interference on the surface of the topological insulator Bi_{2}Te_{3}. *Physical Review B*, 80(24), December 2009.

[30] Chao-Xing Liu, Xiao-Liang Qi, HaiJun Zhang, Xi Dai, Zhong Fang, and Shou-Cheng Zhang. Model Hamiltonian for topological insulators. *Physical Review B*, 82(4), July 2010.

[31] Qin Liu. Stationary phase approach to the quasiparticle interference on the surface of three dimensional strong topological insulators. *ArXiv1108.6051*.

[32] L. Petersen, P. Sprunger, Ph. Hofmann, E. Læ gsgaard, B. Briner, M. Doering, H.-P. Rust, A. Bradshaw, F. Besenbacher, and E. Plummer. Direct imaging of the two-dimensional Fermi contour: Fourier-transform STM. *Physical Review B*, 57(12):R6858–R6861, March 1998.

[33] X. L. Qi and S. C. Zhang. Topological insulators and superconductors. *arXiv1008.2026v1*, 2010.

[34] Xiao-Liang Qi, Rundong Li, Jiadong Zang, and Shou-Cheng Zhang. Inducing a magnetic monopole with topological surface States. *Science (New York, N.Y.)*, 323(5918):1184–7, February 2009.

[35] Pedram Roushan, Jungpil Seo, Colin V Parker, Y S Hor, D Hsieh, Dong Qian, Anthony Richardella, M Z Hasan, R J Cava, and Ali Yazdani. Topological surface states protected from backscattering by chiral spin texture. *Nature*, 460(7259):1106–9, August 2009.

[36] B. Seradjeh, J. Moore, and M. Franz. Exciton Condensation and Charge Fractionalization in a Topological Insulator Film. *Physical Review Letters*, 103(6):4, August 2009.

[37] L. Simon, C. Bena, F. Vonau, M. Cranney, and D. Aubel. Fourier Transform Scanning Tunneling Spectroscopy: the possibility to obtain constant energy maps and the band dispersion using a local measurement. *ArXiv1107.3648*, page 33, July 2011.

[38] J. Tersoff and D. R. Hamann. Theory of the scanning tunneling microscope. *Physical Review B*, 31(2):805–813, January 1985.

[39] Minh-Tien Tran and Ki-Seok Kim. Probing surface states of topological insulators: Kondo effect and Friedel oscillations in a magnetic field. *Physical Review B*, 82(15), October 2010.

[40] M. Vojta. *Bulk and boundary quantum phase transitions in d-wave superconductors*. Habilitationsschrift, Augsburg, 2002.

[41] Rok Žitko. Quantum impurity on the surface of a topological insulator. *Physical Review B*, 81(24):241414, June 2010.

[42] Jing Wang, Wei Li, Peng Cheng, Canli Song, Tong Zhang, Peng Deng, Xi Chen, Xucun Ma, Ke He, Jin-Feng Jia, Qi-Kun Xue, and Bang-Fen Zhu. Power-Law Decay of Standing Waves on the Surface of Topological Insulators. *ArXiv1105.1957*, page 4, May 2011.

[43] D Withoff and E Fradkin. Phase transitions in gapless Fermi systems with magnetic impurities. *Physical review letters*, 64(15):1835–1838, April 1990.

[44] Y. Xia, D. Qian, D. Hsieh, R. Shankar, H. Lin, A. Bansil, A. V. Fedorov, D. Grauer, Y. S. Hor, R. J. Cava, and M. Z. Hasan. Topological Control: Systematic control of topological insulator Dirac fermion density on the surface of Bi2Te3. *ArXiv0907.3089*, page 12, July 2009.

[45] Y. Xia, D. Qian, R. Shankar, H. Lin, A. Bansil, A V. Fedorov, D. Grauer, Y.S. Hor, R. J. Cava, and M.Z. Hasan. Topological control: Systematic control of topological Dirac fermion density on the surface of Bi2Te3. *arXiv0907.3089*, 2009.

[46] Su-Yang Xu, L. A. Wray, Y. Xia, F. von Rohr, Y. S. Hor, J. H. Dil, F. Meier, B. Slomski, J. Osterwalder, M. Neupane, H. Lin, A. Bansil, A. Fedorov, R. J. Cava, and M. Z. Hasan. Realization of an isolated Dirac node and strongly modulated Spin Texture in the topological insulator Bi2Te3. *ArXiv1101.3985*.

[47] Su-Yang Xu, Y Xia, L A Wray, S Jia, F Meier, J H Dil, J Osterwalder, B Slomski, A Bansil, H Lin, R J Cava, and M Z Hasan. Topological phase transition and texture inversion in a tunable topological insulator. *Science (New York, N.Y.)*, 332(6029):560–4, April 2011.

[48] Haijun Zhang, Chao-Xing Liu, Xiao-Liang Qi, Xi Dai, Zhong Fang, and Shou-Cheng Zhang. Topological insulators in Bi2Se3, Bi2Te3 and Sb2Te3 with a single Dirac cone on the surface. *Nature Physics*, 5(6):438–442, May 2009.

[49] Tong Zhang, Peng Cheng, Xi Chen, Jin-Feng Jia, Xucun Ma, Ke He, Lili Wang, Haijun Zhang, Xi Dai, Zhong Fang, Xincheng Xie, and Qi-Kun Xue. Experimental demonstration of the topological surface states protected by the time-reversal symmetry. *ArXiv0908.4136*, August 2009.

[50] Xiaoting Zhou, Chen Fang, Wei-Feng Tsai, and JiangPing Hu. Theory of quasiparticle scattering in a two-dimensional system of helical Dirac fermions: Surface band structure of a three-dimensional topological insulator. *Physical Review B*, 80(24), December 2009.